

# **Modulating Electronic Structure and Reactivity of Cr Nitride Complexes *via* Oxidation**

**by**  
**Diego Martelino**

B.Sc. (Hons.), University of Victoria, 2016

Thesis Submitted in Partial Fulfillment of the  
Requirements for the Degree of  
Master of Science

in the  
Department of Chemistry  
Faculty of Science

© Diego Martelino 2020  
SIMON FRASER UNIVERSITY  
Fall 2020

Copyright in this work rests with the author. Please ensure that any reproduction  
or re-use is done in accordance with the relevant national copyright legislation.

## Declaration of Committee

**Name:** Diego Martelino

**Degree:** Master of Science (Chemistry)

**Title:** *Modulating Electronic Structure and Reactivity of Cr Nitride Complexes via Oxidation*

**Committee:**

**Chair: Robert Britton**  
Professor, Chemistry

**Tim Storr**  
Supervisor  
Professor, Chemistry

**Daniel Leznoff**  
Committee Member  
Professor, Chemistry

**Charles Walsby**  
Committee Member  
Associate Professor, Chemistry

**Loren Kaake**  
Examiner  
Associate Professor, Chemistry

## Abstract

Metal nitride complexes exhibit interesting structure and bonding properties that are invoked when discussing the reactivity of these systems. The nitride ( $\text{N}^{3-}$ ) moiety can be either nucleophilic or electrophilic based on a variety of factors such as metal identity, oxidation state, and nature of the ancillary ligands. Herein, the electronic tuning of Cr salen nitride complexes is investigated *via* modulation of phenolate *para*-R substituents of varying electron donating ability ( $\text{R} = \text{CF}_3$ , tBu,  $\text{NMe}_2$ ) in order to influence reactivity. Salen ligands can exhibit non-innocent behavior, implying that redox processes can either be metal or ligand-based. This feature allows the ligand to help facilitate difficult substrate transformations uncommon to Earth-abundant first-row metals. Depending on the *para*-R group, the locus of oxidation in Cr nitride salen complexes (metal vs. ligand) can be influenced. The electronic structure of oxidized compounds is detailed, allowing for rationalization of nitride reactivity based on oxidation locus.

**Keywords:** Cr; metal nitride; salen; ligand design; ligand non-innocence; electronic structure.

## **Dedication**

*para sa aking mga magulang – ang aking mga unang guro*

## Acknowledgements

The completion of this Thesis would not have been possible without the unwavering support of several people, who have guided me both academically and personally throughout the years. To my parents, Virginia and Manuel, no words can amount to how thankful I am for everything you have done – you provided the Martelino kids with everything and so much more. The struggles of dropping our comfortable life in Manila and flying halfway across the world to live in Vancouver was done so with the intent of securing a better future for us, and for that I am truly grateful. I hope this Thesis can serve as a testament to the success of that story.

Being the eldest of 5 kids certainly brings about a very interesting childhood. To Julio, your philosophical nature continues to fascinate me and has led us to engage in many interesting and equally hilarious conversations. I eagerly await the day you cash in your stockpile of gold and we can go off and buy another 10 sets of 20-piece McNuggets with Louie. To the goofball middle child Bea, you're the glue that holds us together. Never stop pursuing your passions, and I might just fill up your car one day... To Emilio, I see tremendous potential in you. Continue asking the difficult questions in life that occasionally stump me. To Natalia, you have a heart too big to comprehend. I have no doubt that your caring nature and artistic abilities will take you very far in life. And finally, to the goodest boy Timmy, this Thesis would have been much more stressful if it wasn't for your furry companionship.

To my senior supervisor Dr. Tim Storr, your mentorship cannot be overstated. You have provided me the opportunity to explore my interests and conduct research in France. You have constantly helped guide my projects toward the right direction. Thank you for making this degree a truly amazing experience by providing a challenging yet motivating atmosphere within the Storr group. Much of this work would not have been possible without the guidance of several other faculty members. To Dr. Chares Walsby and Dr. Daniel Leznoff, thank you for taking the time to serve on my supervisory committee and for our insightful discussions during committee meetings. To Dr. Fabrice Thomas, you have been very accommodating during my research term in France. I have learned a tremendous amount by working with you and all the members of the DCM team. To Dr. Olivier Jarjayes, thank you for your assistance on several synthetic procedures. Your

guidance has helped smoothen the transition of working in a foreign country. To Dr. Nicolas Leconte, thank you for buying me my first beer upon arriving in Grenoble!

I have had the privilege of working closely with many talented people within the Storr group. To past and present members, thank you all for our friendship and collaborations. To Ryan Clarke, you're a brilliant scientist and I thank you for providing me with the knowledge and tools for success at the beginning of my degree. You will make a fine professor one day, however there will come a time where I eventually defeat you at beer pong. To Khrystyna Herasymchuk, thank you for all the unsung logistical work you do around the lab and for your assistance with EPR – you have no doubt helped inform my chemical intuition greatly. To Jessica Miller, I am glad there was someone in the group who enjoyed dancing to bad club music as much as I do. To Romain Kunert, we've had some epic nights out. Hopefully we can hit up a music festival again soon. To Samyadeb Mahato, I'm grateful for our discussions relating to DFT. To Janaina Bataglioli, Luiza Gomez, Nick Hein and Jason Smith, I am very fortunate to have worked alongside you all and I look forward to our continued friendship. And finally, to our summer exchange student Hector Gonzalez, you are gifted synthetically – I am very pleased with what you managed to accomplish during your stay. *Hasta la vista, Paco!*

To Declan McKearney, Bryton Varju, Curtis Gibbs, David Weber, Soumalya Sinha and Ana Sonea, our lab space has been much more enjoyable with you all in it. Its been great sharing the (more than) occasional beer with you guys to relieve much of the stress that grad school has to offer. To my friends outside of SFU, Clementina, Brandon, Rodney, and many more, thank you for constantly reminding me that there is a life outside of chemistry.

And finally, Kate Fraser. Although I went into this program seeking a degree, I did not expect to also find a partner. You are my support system, travel buddy and best friend, even though you roll your eyes whenever I tell people we have good *chemistry*. I hope you are as proud of me as I am of you, and that we continue to bring out the best in each other. I promise to take you to down to Mexico in our dream van one day for that perfect Instagram pic.

# Table of Contents

Declaration of Committee .....	ii
Abstract.....	iii
Dedication .....	iv
Acknowledgements .....	v
Table of Contents.....	vii
List of Tables.....	x
List of Figures.....	xi
List of Schemes.....	xvi
List of Acronyms.....	xvii
<b>Chapter 1. Introduction .....</b>	<b>1</b>
1.1. Bonding and Relationship to Reactivity.....	2
1.2. Transition Metal Nitride Reactivity .....	7
1.2.1. Early transition metals .....	7
1.2.2. Late Transition Metals .....	7
1.2.3. Mid-Transition Metals .....	9
1.2.4. C—H Activation .....	12
1.2.5. Intermetal Reactivity .....	13
1.3. Non-Innocent Ligands .....	14
1.3.1. Non-innocent Ligands in Nature and Synthesis .....	14
1.3.2. Salens as Non-Innocent Ligands .....	17
1.4. Cr Salen Complexes.....	22
1.5. Thesis Outline .....	24
<b>Chapter 2. Synthesis and Characterization of CrNSal<sup>CF3</sup>, CrNSal<sup>tBu</sup> and CrNSal<sup>NMe2</sup> .....</b>	<b>25</b>
2.1. Introduction.....	25
2.2. Results .....	27
2.2.1. Synthesis.....	27
2.2.2. Solid-State Structure Determination.....	28
2.2.3. Electron Paramagnetic Resonance Spectroscopy .....	30
2.2.4. Electronic Absorption Spectroscopy .....	32
2.2.5. Theoretical Analysis.....	33
2.3. Discussion and Summary .....	34
2.4. Experimental .....	35
2.4.1. Materials.....	35
2.4.2. Synthesis.....	35
2.4.3. Instrumentation.....	36
2.4.4. X-ray Structure Determination .....	36
2.4.5. Theoretical Analysis.....	37
<b>Chapter 3. Oxidation of CrNSal<sup>CF3</sup>, CrNSal<sup>tBu</sup> and CrNSal<sup>NMe2</sup> and Electronic Structure Determination.....</b>	<b>38</b>

3.1.	Introduction.....	38
3.2.	Electronic Structure Determination .....	40
3.2.1.	Electrochemistry .....	40
3.2.2.	Electronic Absorption Spectroscopy .....	44
3.2.3.	Electron Paramagnetic Resonance Spectroscopy .....	47
3.2.4.	Theoretical Analysis.....	51
3.2.5.	Discussion and Summary .....	53
3.3.	Experimental .....	55
3.3.1.	Materials.....	55
3.3.2.	Instrumentation.....	55
3.3.3.	Theoretical Analysis.....	55
3.3.4.	Oxidation Protocol .....	56
<b>Chapter 4.</b>	<b>Investigation of Reactivity Differences upon Oxidation.....</b>	<b>57</b>
4.1.	Introduction.....	57
4.2.	Results .....	59
4.2.1.	Electronic Absorption Spectroscopy .....	59
4.2.2.	Electron Paramagnetic Resonance.....	61
4.2.3.	Theoretical Analysis.....	65
4.3.	Discussion and Summary .....	72
4.4.	Experimental .....	73
4.4.1.	Materials.....	73
4.4.2.	Instrumentation.....	73
4.4.3.	Reactivity Studies of Complexes with Tris(pentafluorophenyl) Borane monitored by Electronic Absorption Spectroscopy .....	74
4.4.4.	Reactivity Studies of Complexes with Tris(pentafluorophenyl) Borane monitored by Electronic Paramagnetic Resonance Spectroscopy .....	74
4.4.5.	Theoretical Analysis.....	75
<b>Chapter 5.</b>	<b>Ongoing and Future Directions.....</b>	<b>76</b>
5.1.	Thesis Summary.....	76
5.2.	Chapter 2 and Chapter 3 .....	76
5.2.1.	Variable Temperature Evans Method on $[\text{Cr}^{\text{V}}\text{NSal}^{\text{NMe}_2}]^{+}$ .....	76
5.2.2.	Infrared Spectroscopy.....	78
5.2.3.	X-ray Absorption Spectroscopy .....	79
5.3.	Chapter 4 .....	80
5.3.1.	X-ray Crystallography .....	80
5.3.2.	Reactivity Profile of Cr Complexes with Tris(pentafluorophenyl) Borane.....	81
5.3.3.	Reactivity of $[\text{Cr}^{\text{VI}}\text{NSal}^{\text{CF}_3}]^{+}$ and $[\text{Cr}^{\text{VI}}\text{NSal}^{\text{tBu}}]^{+}$ with Nucleophiles .....	82
5.4.	Conclusion.....	86
5.5.	Experimental .....	86
5.5.1.	Materials.....	86
5.5.2.	Instrumentation.....	86
5.5.3.	Theoretical Analysis.....	87



<b>References.....</b>	<b>88</b>
<b>Appendix A. Supplementary Material for Chapter 2.....</b>	<b>110</b>
<b>Appendix B. Supplementary Material for Chapter 3.....</b>	<b>119</b>
<b>Appendix C. Supplementary Material for Chapter 4.....</b>	<b>130</b>
<b>Appendix D. Supplementary Material for Chapter 5.....</b>	<b>140</b>

## List of Tables

Table 2.1.	Selected crystallographic data for CrNSal <sup>tBu</sup> and CrNSal <sup>NMe2</sup> .....	29
Table 2.2.	Spectroscopic properties of CrNSal <sup>CF3</sup> , CrNSal <sup>tBu</sup> and CrNSal <sup>NMe2</sup> . ....	33
Table 2.3.	Calculated and experimental (in parentheses) coordination sphere metrical parameters for complexes in Å.....	34
Table 3.1.	Redox potentials for complexes versus F <sub>c</sub> <sup>+</sup> /F <sub>c</sub> . <sup>a,b</sup> .....	42
Table 3.2.	Spectroscopic properties of oxidized Cr complexes. ....	46
Table 3.3.	Relative spin state energetics upon oxidation in kcal mol <sup>-1</sup> . ....	51
Table 3.4.	Calculated coordination sphere metrical parameters for oxidized complexes in Å. Bracketed values correspond to difference (oxidized – neutral <sup>a</sup> ) in calculated bond lengths.....	52
Table 4.1.	Comparison of simulation parameters <sup>a</sup> between CrNSal <sup>R</sup> and Cr(N—B(C <sub>6</sub> F <sub>5</sub> ) <sub>3</sub> )Sal <sup>R</sup> .....	62
Table 4.2.	Calculated bonding parameters that influence nitride reactivity. Bracketed values correspond to the difference between oxidized and neutral values. ....	66
Table 4.3.	Relative orbital energies in kcal mol <sup>-1</sup> . Bracketed values correspond to the difference (oxidized – neutral values). <sup>a</sup> .....	67
Table 4.4.	Calculated values for neutral and oxidized Cr(N—B(C <sub>6</sub> F <sub>5</sub> ) <sub>3</sub> )Sal <sup>R</sup> . Bracketed values indicate difference (adduct – free nitride). <sup>a</sup> .....	69
Table 4.5.	Total energy change upon reactivity of CrNSal <sup>R</sup> with tris(pentafluorophenyl) borane.....	70
Table 4.6.	Total energy change upon reactivity of oxidized complexes with tris(pentafluorophenyl) borane.....	71
Table 5.1.	Tentative assignment of nitride stretching frequencies of neutral and oxidized CrNSal <sup>CF3</sup> , CrNSal <sup>tBu</sup> , and CrNSal <sup>NMe2</sup> in cm <sup>-1</sup> . Bracketed values correspond to the difference (oxidized – neutral).....	79
Table 5.2.	Relative energies of π* and σ* antibonding interactions in kcal mol <sup>-1</sup> . Bracketed values correspond to the difference (oxidized – neutral values). <sup>a</sup> .....	85

## List of Figures

Figure 1.1.	Examples of Mo and Fe complexes as synthetic model compounds in catalytic N <sub>2</sub> reduction. Details: HIPT = hexa-iso-propyl-terphenyl, iPr = isopropyl, tBu = tert-butyl.....	2
Figure 1.2.	Partial MO diagram for a <i>d</i> <sup>0</sup> metal-oxo complex in an octahedral field in which metal <i>d</i> -orbitals and oxo atomic orbitals are considered. A similar MO diagram applies to metal nitrides. The diagram predicts a σ ( <i>d</i> <sub>z<sup>2</sup></sub> + <i>sp</i> <sub>z</sub> ) and two π bonds ( <i>d</i> <sub>xz</sub> + <i>p</i> <sub>x</sub> , <i>d</i> <sub>yz</sub> + <i>p</i> <sub>y</sub> ) that form to afford a metal-oxo triple bond as well as a lone pair on the oxo. ....	3
Figure 1.3.	The “oxo wall” for tetragonal metal oxo complexes.....	4
Figure 1.4.	Partial MO diagram for an early <i>d</i> <sup>0</sup> transition metal nitride complex in a square pyramidal geometry where the metal <i>d</i> -orbitals and nitride atomic orbitals are considered.....	5
Figure 1.5.	Simplified MO diagram of the π interaction of nitride <i>p</i> and metal <i>d</i> orbitals. Case 1 represents an early transition metal in which metal <i>d</i> AO's are higher in energy than nitride <i>p</i> AO's. The result is a nucleophilic nitride due to the prevalence of nitride character in the HOMO (π). Case 2 represents a late transition metal where instead metal <i>d</i> AO's are lower in energy than nitride <i>p</i> AOs. The result is an electrophilic nitride due to the prevalence of nitride character in the LUMO (π*). ....	6
Figure 1.6.	(A) General scheme for the nucleophilic reactivity of early transition metal nitride complexes. (B) A nucleophilic Mo nitride porphyrin complex.....	7
Figure 1.7.	Examples of late metal nitride decomposition pathways. (A) Proposed Ni nitride species undergoing intermolecular ligand insertion and (B) A Rh nitride species homocoupling to afford N <sub>2</sub> . ....	8
Figure 1.8.	(A) General scheme for electrophilic reactivity of mid-to-late transition metal nitride complexes. (B) An ambiphilic Os nitride complex that reacts with both bromotrimethylsilane and trimethylphosphine.....	9
Figure 1.9.	(A) An Fe nitride species that readily forms an adduct with triphenylphosphine. (B) The dual-nature transition state proposed by Smith. (1) The low-lying σ* LUMO of nitride character accepts electron density from the phosphine lone pair. (2) The π HOMO of Fe character back-donates into the P–aryl σ* bond and accounts for the enhanced rate for more electron-withdrawing aryl substituents. The nitride thus exhibits both nucleophilic and electrophilic properties. ....	10
Figure 1.10.	Select examples of N–transfer reactions upon activation with Lewis acids. (A) aziridination of cyclooctene, (B) aziridation of a styrene with a nitrido Mn salen complex and (C) amination of silyl enol ethers with a nitrido Ru porphyrin. Mes = mesityl, py = pyridine, Ts <sub>2</sub> O = <i>p</i> -toluenesulfonic anhydride. ....	11
Figure 1.11.	Insertion of the nitride into (A) C—H bond of xanthene, and (B) C=C bond of 2,3-dimethyl-2-butene. ....	12
Figure 1.12.	Examples of intermetal N-atom transfer as a preparative tool to form new metal nitride complexes.....	13

Figure 1.13.	The relative ordering of metal and ligand frontier orbitals dictates whether the ligand will undergo reduction or oxidation and be classified as “non-innocent”. .....	14
Figure 1.14.	(A) Pymol rendering of CytochromeP450. <sup>114</sup> (B) Reaction scheme for the hydroxylation of C–H bonds. ....	15
Figure 1.15.	(A) Pymol rendering of GOase. <sup>114</sup> (B) Reaction scheme for the oxidation of primary alcohols. ....	16
Figure 1.16.	Fe-catalyzed [2 $\pi$ + 2 $\pi$ ] cycloaddition of dienes employing a redox-active bis(imino)pyridine Fe complex. X = CH <sub>2</sub> , N-alkyl, C(CO <sub>2</sub> )Et) <sub>2</sub> . ....	17
Figure 1.17.	(A) General scheme for the preparation of salen complexes. (B) Structures of asymmetric, imino-half reduced and salan derivatives. Semi-circle in Figure depicts general diamine backbone. ....	18
Figure 1.18.	Examples of factors that can affect the degree of ligand radical involvement in the electronic structure of 1-electron oxidized salen complexes. (A) Effect of changing the metal ion, <sup>175,176</sup> (B) addition of axially binding ligands, <sup>176</sup> (C) temperature-dependent valence tautomerism in solution. <sup>177</sup> .....	19
Figure 1.19.	The effect of the <i>para</i> -ring substituent on ligand radical delocalization visualized by DFT-generated spin density (SD) plots. Greater spin density on the Ni ion is observed for more electron-withdrawing groups (R = CF <sub>3</sub> > tBu) due to involvement of the metal <i>d</i> orbitals in the SOMO of the complex facilitating radical delocalization. <sup>179</sup> Electron donating groups (R = NMe <sub>2</sub> ) result in less spin density on the Ni and localization of the radical to one side of the salen. <sup>180</sup> .....	20
Figure 1.20.	The oxidation of Mn(V) nitride salen complexes. Activation of the Mn–N bond is dependent on <i>para</i> -R electronics .....	21
Figure 1.21.	(A) The proposed mechanism for the decomposition of the Mn(VI) complex proceeds through a nitridyl radical species that favours N–N homocoupling. (B) An example of an Ir complex with a large degree of nitridyl radical character. ....	21
Figure 1.22.	Mn and Cr salens used in alkene epoxidation. (A) commercially available Jacobsen's catalyst for epoxidation of asymmetric alkenes. (B) First example of a structurally characterized Cr oxo active species. <sup>201</sup> (C) Proposed mechanism for metal salen catalyzed alkene epoxidation. ....	23
Figure 1.23.	Nitrido Cr(V) complexes bearing salen ligands with <i>para</i> -ring substituents from electron-withdrawing (R = CF <sub>3</sub> ) to electron-donating (R = NMe <sub>2</sub> )....	23
Figure 2.1.	First reported cases for the synthesis of Cr nitride complexes by (A) photolysis of an azide precursor <sup>225</sup> and (B) Intermetallic N-atom transfer. <sup>226</sup> .....	26
Figure 2.2.	POV-Ray representation of CrNSal <sup>tBu</sup> .....	28
Figure 2.3.	POV-Ray representation of CrNSal <sup>NMe2</sup> .....	29
Figure 2.4.	Room temperature EPR of CrNSal <sup>CF3</sup> , CrNSal <sup>tBu</sup> , and CrNSal <sup>NMe2</sup> in dichloromethane. Fitted parameter values are the same for all compounds: <i>g</i> <sub>iso</sub> = 1.978; <i>A</i> <sup>53Cr</sup> = 78.00 MHz, <i>A</i> <sup>14N, imine</sup> = 6.34 MHz, <i>A</i> <sup>14N, nitride</sup> = 6.28 MHz. Conditions: 0.33 mM complex; freq. = 9.85 GHz; power = 2.0 mW; mod. freq. = 100 kHz; mod. amp. = 0.6 mT; T = 298 K.....	30

Figure 2.5.	Low temperature EPR spectrum of CrNSal <sup>CF3</sup> , CrNSal <sup>tBu</sup> , and CrNSal <sup>NMe2</sup> in dichloromethane. Fitted parameter values are identical for all compounds: $g_{\perp} = 1.992$ , $A^{53\text{Cr}} = 53$ MHz; $g_{\parallel} = 1.950$ , $A^{53\text{Cr}} = 130$ MHz. Inset corresponds to a zoomed in region of the high-field signals that contain the resolved Cr hyperfine interactions to the $g_{\parallel}$ . Conditions: 0.33 mM complex; 0.1 M TBAP; freq. = 9.387 GHz; power = 2.0 mW; mod. freq. = 100 kHz; mod. amp. = 6 GHz; T = 77 K.....	31
Figure 2.6.	UV-vis absorption spectra of CrNSal <sup>CF3</sup> , CrNSal <sup>tBu</sup> and CrNSal <sup>NMe2</sup> . Inset: observable $d \rightarrow d$ transitions. The CrNSal <sup>NMe2</sup> $d \rightarrow d$ transition is likely hidden by the LMCT band. Conditions: 0.45 mM complex; T = 298 K; CH <sub>2</sub> Cl <sub>2</sub> .....	32
Figure 2.7.	DFT-generated plots for CrNSal <sup>tBu</sup> . (A) Visualization of the $d_{xy}$ SOMO. (B) Spin density plot. Nitride Cr SD values: R = CF <sub>3</sub> : -0.431, R = tBu: -0.427, R = NMe <sub>2</sub> : -0.425. Cr SD values: : R = CF <sub>3</sub> : 1.454, R = tBu: 1.448, R = NMe <sub>2</sub> : 1.444. See Appendix A – Fig. A2 & A3 for SOMO and SD plots of CrNSal <sup>CF3</sup> and CrNSal <sup>NMe2</sup> . ....	33
Figure 3.1.	Examples of mixed-valence systems. (A) Creutz-Taube ion. (B) An oxidized metal salen complex.....	39
Figure 3.2.	Cyclic voltammogram of CrNSal <sup>NMe2</sup> , CrNSal <sup>tBu</sup> and CrNSal <sup>CF3</sup> . Only the 1 <sup>st</sup> redox wave is shown for tBu and CF <sub>3</sub> derivatives. Conditions: 1.0 mM complex; 0.1 M <sup>n</sup> Bu <sub>4</sub> NClO <sub>4</sub> ; scan rate: 100 mV/s; T = 298 K; CH <sub>2</sub> Cl <sub>2</sub> .....	41
Figure 3.3.	(A) 1 <sup>st</sup> and 2 <sup>nd</sup> redox waves for CrNSal <sup>NMe2</sup> (black) resolved by DPV (red). (B) Comparison of CrNSal <sup>NMe2</sup> (black) and MnNSal <sup>NMe2</sup> (red). <sup>181</sup> Conditions: 1.0 mM complex; 0.1 M <sup>n</sup> Bu <sub>4</sub> NClO <sub>4</sub> ; scan rate: 100 mV/s; T = 298 K; CH <sub>2</sub> Cl <sub>2</sub> . ....	42
Figure 3.4.	(A) Comparison of CrNSal <sup>tBu</sup> (black) and MnNSal <sup>tBu</sup> (red) <sup>181</sup> by CV. (B) Comparison of CrNSal <sup>CF3</sup> (black) and MnNSal <sup>CF3</sup> (red) <sup>181</sup> by CV. Conditions: 1.0 mM complex; 0.1 M <sup>n</sup> Bu <sub>4</sub> NClO <sub>4</sub> ; scan rate: 100 mV/s; T = 298 K; CH <sub>2</sub> Cl <sub>2</sub> .....	44
Figure 3.5.	Chemical oxidation of CrNSal <sup>CF3</sup> and CrNSal <sup>tBu</sup> using ([N(C <sub>6</sub> H <sub>3</sub> Br <sub>2</sub> ) <sub>3</sub> ] <sup>+</sup> [SbF <sub>6</sub> ] <sup>-</sup> ) monitored by UV-vis-NIR spectroscopy. Black: neutral; red: oxidized. Intermediate grey lines represent increasing aliquots of oxidant added until 1 equivalent was reached. Conditions: 0.45 mM complex; T = 233 K; CH <sub>2</sub> Cl <sub>2</sub> . Analysis of the red band over time indicated minimal changes at T = 233 K, further demonstrating the stability of oxidized complexes in solution. ....	45
Figure 3.6.	Chemical oxidation of CrNSal <sup>NMe2</sup> monitored by UV-vis-NIR spectroscopy. Black: neutral; red: oxidized. Intermediate grey lines represent increasing aliquots of oxidant added until 1 equivalent was reached. Conditions: 0.45 mM complex; T = 233 K; CH <sub>2</sub> Cl <sub>2</sub> . Analysis of the red band over time indicated minimal changes at T = 233 K, further demonstrating the stability of oxidized complex in solution. ....	46
Figure 3.7.	Frozen solution EPR spectra of concentration-matched neutral (black) and oxidized samples (red) of CrNSal <sup>CF3</sup> , CrNSal <sup>tBu</sup> and CrNSal <sup>NMe2</sup> in dichloromethane. Insets are a magnification of the corresponding oxidized complex signal. Conditions: 0.45 mM complex; 0.1 M TBAP; freq. = 9.4 GHz; power = 2.0 mW; mod. freq. = 100 kHz; mod. amp. = 6 GHz; T = 20 K. ....	48

Figure 3.8.	$^1\text{H}$ NMR spectra of chemically oxidized complexes in $\text{CD}_2\text{Cl}_2$ . R = $\text{CF}_3$ : green; tBu: purple; blue: $\text{NMe}_2$ . * Denotes solvent peaks. $\blacktriangle$ Denotes resonances from $\text{N}(\text{C}_6\text{H}_3\text{Br}_2)_3$ which is the reduced form of the aminium chemical oxidant. $\text{CrNSal}^{\text{NMe}_2}$ was oxidized using $\text{AgSbF}_6$ (0.65 V vs $\text{Fc}^+/\text{Fc}$ ). <sup>266</sup> $\dagger$ Denotes the paramagnetically shifted solvent peak used as a reference for magnetic susceptibility via Evans Method. ....49
Figure 3.9.	EPR of a sample of $[\text{Cr}^{\text{V}}\text{NSal}^{\text{NMe}_2}]^{\bullet+}$ (bottom). The corresponding simulation (red) was accomplished by summing the simulation parameters obtained for neutral $\text{CrNSal}^{\text{NMe}_2}$ and bis-oxidized $[\text{Cr}^{\text{V}}\text{NSal}^{\text{NMe}_2}]^{\bullet+2+}$ complexes. Conditions: 0.45 mM complex; 0.1 M TBAP; freq. = 9.4 GHz; power = 2.0 mW; mod. freq. = 100 kHz; mod. amp. = 6 GHz; T = 20 K; $\text{CH}_2\text{Cl}_2$ . ....50
Figure 3.10.	Spin density plots for possible $[\text{Cr}^{\text{V}}\text{NSal}^{\text{NMe}_2}]^{\bullet+}$ structures. (A) Broken-symmetry singlet case. (B) Triplet case. ....52
Figure 3.11.	Plots of the $[\text{Cr}^{\text{V}}\text{NSal}^{\text{NMe}_2}]^{\bullet+}$ magnetic orbitals in the broken-symmetry singlet state. ....53
Figure 4.1.	Examples of computationally studied nitride complexes to describe nucleophilicity based on nitride partial charges. (A) Salen and chloro complexes (M = V, Cr, Mn, Fe) by Sauer. <sup>280</sup> (B) triazo-acetylacetonate complex (M = V, Cr, R = H; M = Mn, R = $\text{CH}_3$ ) by Bachler. <sup>279</sup> ....58
Figure 4.2.	UV-vis titration of neutral complexes with tris(pentafluorophenyl) borane. Black: $\text{CrNSal}^{\text{R}}$ ; red: 1 equivalent tris(pentafluorophenyl) borane added. Intermediate grey lines represent increasing aliquots of borane until 1 equivalent is reached. Conditions: 0.45 mM complex; T = 233 K; $\text{CH}_2\text{Cl}_2$ . Complexes are stable and spectra appear identical after 1 hour. Free tris(pentafluorophenyl) borane does not exhibit any absorption peaks within the energy range of studied. ....59
Figure 4.3.	Interaction of tris(pentafluorophenyl) borane with the oxidized complexes monitored by UV-vis-NIR spectroscopy. Black: oxidized $\text{CrNSal}^{\text{R}}$ ; red: 1 equivalent borane added. Conditions: 0.45 mM complex; T = 233 K; $\text{CH}_2\text{Cl}_2$ . Complexes are stable and spectra appear identical after 1 hr. Addition of over 1 equivalent borane yields no further changes for all spectra (see Appendix C – Fig. C2). ....60
Figure 4.4.	Titration of $[\text{Cr}^{\text{V}}\text{NSal}^{\text{NMe}_2}]^{\bullet+}$ with tris(pentafluorophenyl) borane. Black: $[\text{Cr}^{\text{V}}\text{NSal}^{\text{NMe}_2}]^{\bullet+}$ ; red: 1 equivalent borane added. Intermediate grey lines represent increasing aliquots of borane added until 1 equivalent was reached. Conditions: 0.45 mM complex; T = 233 K; $\text{CH}_2\text{Cl}_2$ . Complexes are stable and spectra appear identical after 1 hr. ....61
Figure 4.5.	Room temperature EPR spectra of $\text{Cr}(\text{N}=\text{B}(\text{C}_6\text{F}_5)_3)\text{Sal}^{\text{R}}$ . Conditions: 0.50 mM complex; freq. = 9.85 GHz; power = 2.0 mW; mod. freq. = 100 kHz; mod. amp. = 0.6 mT; T = 298 K; $\text{CH}_2\text{Cl}_2$ . ....62
Figure 4.6.	Solution EPR of concentration matched Cr samples. Black: $\text{CrNSal}^{\text{NMe}_2}$ ; red: $[\text{Cr}^{\text{V}}\text{NSal}^{\text{NMe}_2}]^{\bullet+}$ ; Inset represents a magnification of the signal in red. Conditions: 0.50 mM complex; freq. = 9.428 GHz; power = 2.0 mW; mod. freq. = 100 kHz; mod. amp. = 0.6 mT; T = 298 K. ....63
Figure 4.7.	Low temperature EPR analysis of the addition of tris(pentafluorophenyl) borane to a solution of $[\text{Cr}^{\text{V}}\text{NSal}^{\text{NMe}_2}]^{\bullet+}$ . Black: $[\text{Cr}^{\text{V}}\text{NSal}^{\text{NMe}_2}]^{\bullet+}$ ; red: 1 equivalent borane added. Conditions: 0.29 mM complex; 0.1 M TBAP; freq.

	= 9.388 GHz; power = 1.0 mW; mod. freq. = 100 kHz; mod. amp. = 6 GHz; T = 100 K. ....	64
Figure 4.8.	Visualization of the alpha orbitals of the Cr—N $\pi$ bonding interactions for CrNSal <sup>CF<sub>3</sub></sup> , CrNSal <sup>tBu</sup> and CrNSal <sup>NMe<sub>2</sub></sup> in the xz and yz planes from NBO analysis. See Appendix C – Fig. C7–C12 for visualization of the $\pi$ -interactions for oxidized complexes as well as visualization of the $\sigma$ -interactions and lone pairs for all complexes. ....	67
Figure 4.9.	Spin density plots of (A) Cr(N—B(C <sub>6</sub> F <sub>5</sub> ) <sub>3</sub> )Sal <sup>NMe<sub>2</sub></sup> and (B) broken-symmetry singlet [Cr <sup>V</sup> (N—B(C <sub>6</sub> F <sub>5</sub> ) <sub>3</sub> )Sal <sup>NMe<sub>2</sub></sup> ] <sup>•+</sup> . See Appendix C – Fig. C13 for spin density plots of Cr(N—B(C <sub>6</sub> F <sub>5</sub> ) <sub>3</sub> )Sal <sup>tBu</sup> , Cr(N—B(C <sub>6</sub> F <sub>5</sub> ) <sub>3</sub> )Sal <sup>CF<sub>3</sub></sup> as well as triplet [Cr <sup>V</sup> (N—B(C <sub>6</sub> F <sub>5</sub> ) <sub>3</sub> )Sal <sup>NMe<sub>2</sub></sup> ] <sup>•+</sup> . ....	68
Figure 5.1.	<sup>1</sup> H NMR analysis of [Cr <sup>V</sup> NSal <sup>NMe<sub>2</sub></sup> ] <sup>•+</sup> at 298 K in CD <sub>2</sub> Cl <sub>2</sub> oxidized using AgSbF <sub>6</sub> (0.65 V vs F <sub>c</sub> <sup>+</sup> /F <sub>c</sub> ). <sup>266</sup> * Denotes the solvent peak. † Denotes the paramagnetically shifted solvent peak used as a reference for magnetic susceptibility <i>via</i> Evans Method. ....	77
Figure 5.2.	Solution IR spectra showing the nitride stretching frequency of (A) neutral (*) and (B) oxidized (†) CrNSal <sup>CF<sub>3</sub></sup> (green), CrNSal <sup>tBu</sup> (purple), and CrNSal <sup>NMe<sub>2</sub></sup> (blue). Compounds were oxidized using [N(C <sub>5</sub> H <sub>3</sub> Br <sub>2</sub> ) <sub>3</sub> ][SbF <sub>6</sub> ]. Conditions: 0.5 mM, CH <sub>2</sub> Cl <sub>2</sub> . See Appendix D – Fig. D1 & D2 for full spectra. ....	79
Figure 5.3.	Lennard-Jones-type reaction profile for the N—B interaction. <i>r</i> <sub>eq</sub> represents the equilibrium N—B distance in adducts. ....	81
Figure 5.4.	Interaction of filled Cr-nitride molecular orbitals with the empty borane p orbital. (A) A bent approach suggests involvement of the Cr—N $\pi$ bonding orbitals in adduct formation. (B) A linear approach suggests involvement of the nitride lone pair in adduct formation. ....	82
Figure 5.5.	Reactivity of (A) neutral and (B) cationic Re(V) oxo complexes by triphenyl phosphine. ....	83
Figure 5.6.	The orbitals involved in the reactivity of Re(V) oxo complexes by Brown include the Re—O $\pi^*$ combination and phosphine lone pair. <sup>310</sup> ....	84

## List of Schemes

Scheme 2.1.	Synthesis of Cr nitride salen complexes (R = CF <sub>3</sub> , tBu, NMe <sub>2</sub> ). .....	27
Scheme 2.2.	Synthetic strategy for Cr nitride salen complexes. ....	27
Scheme 4.1.	Interaction of CrNSal <sup>R</sup> with tris(pentafluorophenyl) borane to form N—B adducts. ....	58
Scheme 4.2.	Reactivity of CrNSal <sup>CF<sub>3</sub></sup> , CrNSal <sup>tBu</sup> and CrNSal <sup>NMe<sub>2</sub></sup> with tris(pentafluorophenyl) borane.....	70
Scheme 4.3.	Reactivity of [Cr <sup>VI</sup> NSal <sup>CF<sub>3</sub></sup> ] <sup>+</sup> and [Cr <sup>VI</sup> NSal <sup>tBu</sup> ] <sup>+</sup> with tris(pentafluorophenyl) borane (R = CF <sub>3</sub> , tBu).....	71
Scheme 4.4.	Reactivity of [Cr <sup>V</sup> NSal <sup>NMe<sub>2</sub></sup> ] <sup>•+</sup> with tris(pentafluorophenyl) borane (R = NMe <sub>2</sub> ).....	71
Scheme 5.1.	Potential reactivity of [Cr <sup>VI</sup> NSal <sup>CF<sub>3</sub></sup> ] <sup>+</sup> and [Cr <sup>VI</sup> NSal <sup>tBu</sup> ] <sup>+</sup> with phosphines (R = alkyl, aryl).....	85



## List of Acronyms

A	Hyperfine coupling constant
Å	Ångström, $10^{-10}$ meters
AO	Atomic orbital
BDE	Bond dissociation energy
BSS	Broken symmetry singlet (DFT)
$c_A$	Analyte concentration
cm	Centimeters
$\text{cm}^{-1}$	Wavenumbers
$\chi_d$	Diamagnetic correction factor
$\chi_m$	Molar susceptibility
CT	Charge transfer
CV	Cyclic voltammetry
$\Delta v_{1/2}$	Peak width at half height
DCM	Dichloromethane
$\Delta E_{ox}$	Difference in potential
DFT	Density functional theory
DPV	Differential pulse voltammetry
E	Energy
$\varepsilon$	Dielectric constant
$\varepsilon$	Molar extinction coefficient
EA	Elemental analysis
ee	Enantiomeric excess
Elec	Electrophilic substrate
$E_{pa}$	Anodic peak potential
$E_{pc}$	Cathodic peak potential
EPR	Electron paramagnetic resonance
ESI	Electrospray ionization
eV	Electron volts
F	Faraday's constant
$F_c$	Ferrocene
$F_c^+$	Ferrocenium
g	Grams

$g_e$	Free electron g value (2.0023)
GHz	Gigahertz
$g_{iso}$	Isotropic g value
GOase	Galactose Oxidase
GO <sub>ox</sub>	Oxidized form of galactose oxidase
GO <sub>red</sub>	Reduced form of galactose oxidase
HIPT	Hexa-iso-propyl-terphenyl
HOMO	Highest occupied molecular orbital
$I$	Nuclear spin quantum number
IVCT	Intervalence charge transfer
K	Kelvin
$K_c$	Comproportionation constant
kcal	Kilocalorie
kHz	Kilohertz
L	Ligand
LLCT	Ligand-to-ligand charge transfer
$\lambda_{max}$	Wavelength at maximum absorbance
LMCT	Ligand-to-metal charge transfer
LP	Lone pair
LUMO	Lowest unoccupied molecular orbital
M	Metal
M	Molar
$M_a$	Molar mass
$\mu A$	Microamperes
$\mu_{eff}$	Effective magnetic moment
mL	Millilitres
mM	Millimolar
mm	Millimeter
MO	Molecular orbital
Mod. amp.	Modulation amplitude
mol	Moles
MS	Mass spectrometry
mT	Milliteslas
mV	Millivolts

mW	Milliwatts
$\nu$	Frequency
NBO	Natural bond order (DFT)
NIR	Near-infrared
nm	Nanometers
NMR	Nuclear magnetic resonance
Nuc	Nucleophilic substrate
OA	Oxidative addition
PCM	Polarized continuum model
PES	Potential energy surface
ppm	Chemical shift
py	Pyridine
pyz	Pyrazine
R	Ideal gas constant
RE	Reductive elimination
S	Electron spin quantum number
s	Seconds
Salen (Sal)	Bis-(Shiff base) bis(phenol)
SD	Spin Density
SOMO	Singularly occupied molecular orbital
T	Temperature
TBAP	Tetra- <i>n</i> -butyl ammonium perchlorate
TD-DFT	Time-dependant density functional theory
TFAA	Trifluoroacetic anhydride
THF	Tetrahydrofuran
UV-vis	Ultraviolet-visible spectroscopy
V	Volts
VT	Variable temperature
XAS	X-ray absorption spectroscopy
ZFS	Zero-field splitting

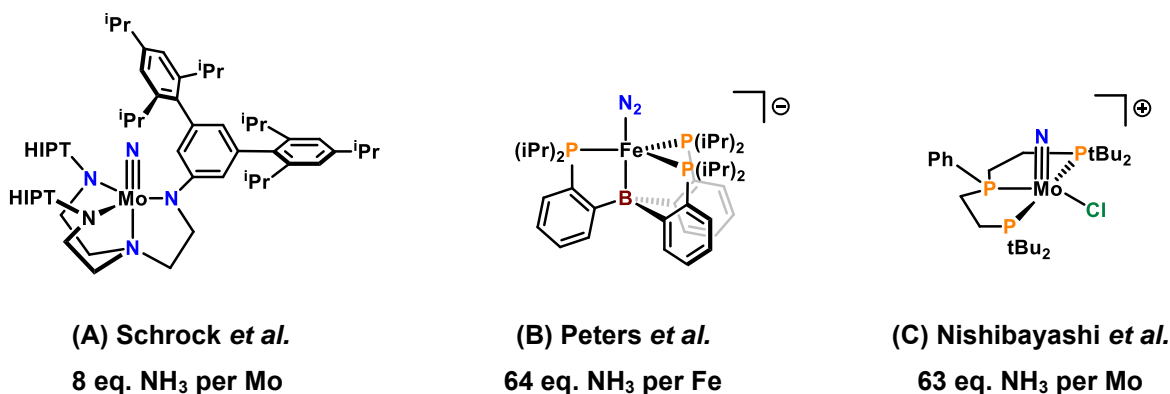
## Chapter 1. Introduction

Transition metal complexes bearing terminal nitride ( $\text{N}^{3-}$ ) ligands have been known for over 170 years.<sup>1</sup> The electronic structure and bonding of metal-nitrogen multiple bonds has since been a long-standing topic of interest. In general, the marked kinetic and thermodynamic stability of nitride-containing compounds make them attractive candidates for use in thermo and piezoelectric materials for energy harvesting<sup>2</sup> and thin films.<sup>3</sup> Nitride bonds to main group elements, such as boron nitrides, represent an extremely resilient and versatile class of materials (sometimes harder than diamond) which are traditionally used as components in high-temperature equipment.<sup>4</sup> Only relatively recently have nitrides been given serious consideration as important reactive synthons.<sup>5,6</sup>

The vast majority of metal nitride complexes are unreactive at the nitride, and thus the ability to generate a reactive nitride fragment is of considerable interest.<sup>7</sup> Additionally, the relevance of these compounds in biological and industrial nitrogen fixation continues to garner appeal.<sup>8</sup> For example, the Haber-Bosch process combines  $\text{H}_2$  and  $\text{N}_2$  over metal catalysts at high temperature and pressure to form ammonia on an industrial scale.<sup>9</sup> The nature of the catalyst is paramount to the efficiency of the overall process, which normally consists of an Fe surface embedded with potassium additives to promote adsorption and cleavage of dinitrogen into nitride intermediates.<sup>10–13</sup> Interestingly, biological  $\text{N}_2$  fixation is achieved by the nitrogenase enzyme under ambient conditions.<sup>14,15</sup> Catalytic  $\text{N}_2$  reduction is achieved within active sites consisting of multi-metallic cofactors containing Fe and Mo (or V), with the formation of a terminal nitrido intermediate hypothesized to form.<sup>16,17</sup> This elegant enzymatic chemistry has inspired research into the development of small molecule model systems that catalytically transform dinitrogen to ammonia at ambient temperatures and pressures.<sup>18–20</sup>

With Fe nitrides hypothesized to form in both the industrial and biological dinitrogen to ammonia processes, there have been a number of interesting reports of the characterization and reactivity of these species.<sup>11,20–28</sup> In addition to Fe, Schrock first demonstrated the catalytic reduction of dinitrogen to ammonia using a Mo complex, in which a Mo nitride is formed in the process (Fig. 1.A).<sup>18</sup> Subsequent work by Peters<sup>21</sup> using Fe and Nishibayashi<sup>19</sup> using Mo (Fig. 1B and Fig. 1C respectively) have elegantly advanced this chemistry by achieving higher turnovers in  $\text{NH}_3$  production. Thus, the study

of such complexes and their corresponding reactivities provide insight into the mechanistic details of  $N_2$  activation.

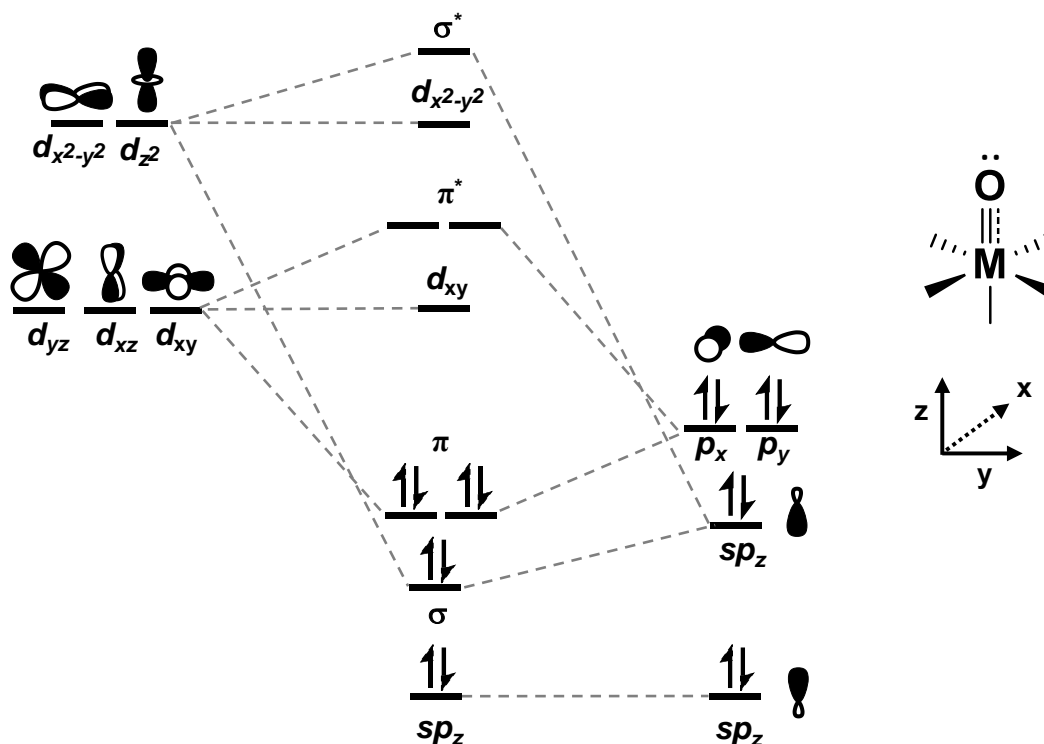


**Figure 1.1.** Examples of Mo and Fe complexes as synthetic model compounds in catalytic  $N_2$  reduction. Details: HIPT = hexa-iso-propyl-terphenyl, iPr = isopropyl, tBu = tert-butyl.

Metal nitrides are also utilized synthetically in substrate oxidations, as will be discussed herein. This includes group and N-atom transfer reactions, C–H activation, and alkene aziridination. The diverse reactivity of metal nitrides can be rationalized by structure and bonding analysis.

## 1.1. Bonding and Relationship to Reactivity




Generally, transition metal nitrides are classified as nucleophilic or electrophilic depending on the relative energy of metal versus nitride fragment orbitals.<sup>7</sup> This can be rationalized by simplified molecular orbital (MO) bonding considerations. The nitride bonding scheme was originally derived from the isoelectronic oxo ( $O^{2-}$ ) system following Gray's detailed MO description of the vanadyl ion ( $VO^{2+}$ ) in 1962.<sup>29</sup> This work details the general bonding in metal oxo (and nitride) complexes which is represented by a partial MO diagram in an octahedral ligand field, in which the metal  $d$ -orbitals and oxo orbitals are considered (Fig. 1.2).<sup>30</sup> Filled orbitals on the oxo effectively overlap with vacant orbitals of appropriate symmetry and energy on the metal ion to afford short metal-oxygen distances ( $1.5 - 1.7 \text{ \AA}$ ) indicative of multiple bond character.<sup>31</sup>



**Figure 1.2.** Partial MO diagram for a  $d^0$  metal-oxo complex in an octahedral field in which metal  $d$ -orbitals and oxo atomic orbitals are considered. A similar MO diagram applies to metal nitrides. The diagram predicts a  $\sigma$  ( $d_{z^2} + sp_z$ ) and two  $\pi$  bonds ( $d_{xz} + p_x$ ,  $d_{yz} + p_y$ ) that form to afford a metal-oxo triple bond as well as a lone pair on the oxo.

The diagram in Figure 1.2. also defines the criteria for forming stable terminal oxo and nitride complexes. Complexes of tetragonal symmetry can contain no more than four  $d$  electrons while still maintaining multiple-bond character. In the above diagram, a triple bond is the proper formulation for  $d^0$ ,  $d^1$ , and low spin  $d^2$  electronic structures. The diagram also predicts the presence of a lone pair due to the non-bonding  $sp_z$  hybrid. This hybrid is calculated to contain significant  $s$ -character (~80 %) and is therefore usually considered energetically unsuitable for reactivity.<sup>29</sup> A decrease in metal-oxo bond order arises for higher electron counts (represented by the dashed M—O bond in Fig. 1.2) due to the population of  $\pi^*$  orbitals within the MO manifold. In the absence of  $\pi$ -bonding, the oxo ligand becomes exceptionally basic and susceptible to protonation or electrophilic attack.<sup>32</sup> Thus, oxo and nitride complexes are favoured by early transition metals and/or metals in high oxidation states. It becomes more difficult to stabilize late transition metals due to the exceedingly high oxidation states needed to maintain no more than four  $d$  electrons. The

“oxo wall” (Fig. 1.3) proposed by Winkler and Gray describes the theoretical boundary between groups 8 and 9 in the periodic table. The concept states that oxo complexes of group 9 or later with tetragonal symmetry are unstable.<sup>33</sup> These complexes however have been invoked as highly reactive transient intermediates in late transition metal C–H activation reactions.<sup>34</sup> Attempts to isolate such species to this day have been largely unsuccessful and have even eluded spectroscopic detection. Indeed, work published in *Science* claiming preparation of a tetragonal Pt–oxo complex in direct violation of this principal has subsequently been retracted.<sup>35</sup>

3	4	5	6	7	8		9	10	11	10
Sc	Ti	V	Cr	Mn	Fe		Co	Ni	Cu	Zn
Y	Zr	Nb	Mo	Tc	Ru		Rh	Pd	Ag	Cd
Lu	Hf	Ta	W	Re	Os		Ir	Pt	Au	Hg

**Figure 1.3.** The “oxo wall” for tetragonal metal oxo complexes.

Similar MO descriptions apply to complexes containing terminal nitride ligands, which are isoelectronic with the oxo ion. Figure 1.4 depicts the MO diagram for the interaction of a single terminal nitride unit with an arbitrary  $d^0$  early transition metal ion supported by four coplanar  $\sigma$ -donating ligands.<sup>36</sup> The coordination environment represented here is akin to that of salen complexes discussed in subsequent chapters. The M–N interaction contains a  $\sigma$  bond ( $\sigma$ ) formed from the favorable overlap of a filled nitride  $sp_z$  hybrid with the empty  $d_{z^2}$  orbital. The interaction is also predicted to exhibit two  $\pi$  bonds ( $\pi$ ) formed by the overlap of filled  $p$  orbitals on the nitride with empty  $d$  orbitals of correct symmetry on the metal centre. The qualitative metal nitride MO bears a striking resemblance to the metal oxo MO in Figure 1.2. Thus, nitride complexes are favoured by early transition metals in high oxidation states in the same manner as oxo derivatives, as the “oxo wall” principle extends to nitrides. The strong  $\sigma$  and  $\pi$  donating ability of the nitride ligand confers an exceptionally strong *trans* effect that results in the stabilization of lower coordination numbers. Indeed, square pyramidal geometries are commonly observed, with the nitride at the apical position.

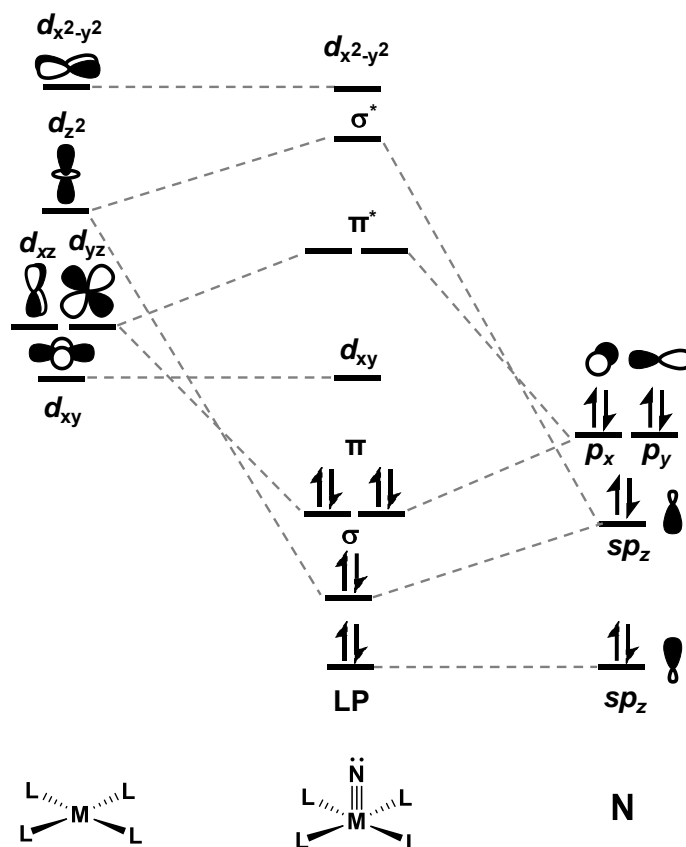


**Figure 1.4.** Partial MO diagram for an early  $d^0$  transition metal nitride complex in a square pyramidal geometry where the metal  $d$ -orbitals and nitride atomic orbitals are considered.

The reactivity of metal nitrides can be rationalized from the above diagram. As depicted in Figure 1.4, early transition metal complexes are generally nucleophilic because the highest occupied molecular orbitals (HOMOs), represented by  $\pi$ , are predominantly nitride in character and can interact with suitable electrophilic substrates. The lowest unoccupied molecular orbitals (LUMOs) in this scenario are metal-based, represented by  $\pi^*$ , and thus the metal centre is rendered electrophilic in comparison to the nitride. From the bonding diagram,  $\pi$  is typically cited when discussing nitride nucleophilicity due to energetic accessibility.<sup>7,37</sup> Similar to the vanadyl case in Figure 1.2, a lone pair (LP) on the nitride is predicted to form due to a non-bonding  $sp_z$  hybrid orbital that contains a large component of N s AO character. This has been supported by detailed computational analysis suggesting that the LP is typically contracted and much lower in energy in comparison to the metal-nitride bonding / antibonding orbitals.<sup>36,38</sup>



Reactivity can be influenced by the metal identity, oxidation state and auxiliary ligands. These factors directly influence the  $\pi$  interaction between nitride  $p$  and metal  $d$  orbitals. As an example, Figure 1.5 depicts a further simplified MO picture, taking into consideration only metal-nitride  $\pi$  interactions. Case 1 features an early transition metal analogous to the system in Figure 1.4, in which the nitride moiety is nucleophilic. An electrophilic nitride is in turn predicted for late transition metals (Case 2), as the  $\pi^*$  MOs are predominantly nitride in character.<sup>37</sup> In situations where the  $\pi^*$  orbitals contain similar metal and nitride character, ambiphilic reactivity is observed.<sup>39,40</sup> This typically occurs for mid-transition metal nitride complexes.

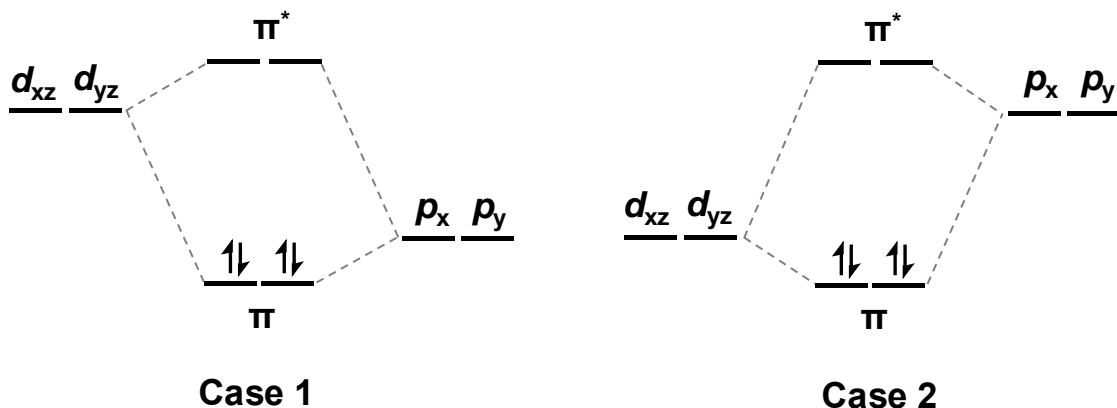


**Figure 1.5.** Simplified MO diagram of the  $\pi$  interaction of nitride  $p$  and metal  $d$  orbitals. Case 1 represents an early transition metal in which metal  $d$  AO's are higher in energy than nitride  $p$  AO's. The result is a nucleophilic nitride due to the prevalence of nitride character in the HOMO ( $\pi$ ). Case 2 represents a late transition metal where instead metal  $d$  AO's are lower in energy than nitride  $p$  AOs. The result is an electrophilic nitride due to the prevalence of nitride character in the LUMO ( $\pi^*$ ).

## 1.2. Transition Metal Nitride Reactivity

### 1.2.1. Early transition metals

Early transition metal nitrides are nucleophilic and react with electrophilic substrates (Elec) such as alkylating agents<sup>41–49</sup> and boranes ( $\text{BX}_3$ ; X = halide, alkyl,  $\text{C}_6\text{F}_5$ , etc.)<sup>50–55</sup> to afford adducts (Fig. 1.6A). For example, a Mo tetraphenylporphyrin nitride complex reacts with boron trifluoride to form the corresponding imido complex (Fig 1.6B).<sup>39</sup> Adduct formation indicates nucleophilicity, and typically occurs without a change in oxidation state. The imido species maintains  $sp$  hybridization in most cases and results in linearity of the  $\text{M}\equiv\text{N}\text{--}\text{Elec}$  bond. Bent  $sp^2$  hybridized imido complexes are less common ( $\text{M}=\text{N}\text{--}\text{Elec}$ ), and can occur when there is competing  $\pi$ -basicity with ancillary ligands.<sup>37</sup> Thus,  $sp^2$  imides are usually formed when other multiply bonded ligands, such as alkylidenes or oxo groups are present.<sup>56</sup>

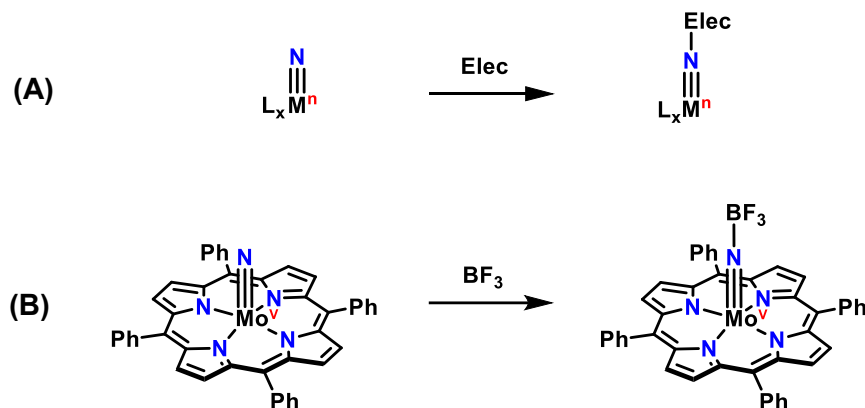


**Figure 1.6.** (A) General scheme for the nucleophilic reactivity of early transition metal nitride complexes. (B) A nucleophilic Mo nitride porphyrin complex.

### 1.2.2. Late Transition Metals

Contrary to early transition metals, late transition metal nitrides are electrophilic and significantly less stable. This is due to the lack of empty  $d$  orbitals of appropriate energy and symmetry to accommodate nitride  $\pi$  electron density.<sup>57</sup> Highly reactive complexes of group 9-10 metals have been reported and are susceptible to rapid decomposition *via* intramolecular ligand insertion reactions.<sup>58,59</sup> In one study by the van

der Vlugt group, the reactivity of a transient Ni nitride complex was described (Figure 1.7A).<sup>60</sup> Theoretical analysis predicted the formation of a nitrido species upon photolysis of an azide precursor in benzene (1). The reactive nitrido species (2) is subsequently ‘trapped’ by nucleophilic attack from an adjacent phosphine ligand to afford the Ni–P insertion complex (3). C–H activation of benzene results in the formation of a new phosphino-amido ligand (4). Late transition metal nitride complexes can also decay *via* intermolecular N–N coupling.<sup>61</sup> As an example, the Schneider group reported a Rh nitride complex prepared from a frozen toluene solution (5). This species rapidly decays to the dinitrogen complex (7) upon thawing of the solution under an atmosphere of N<sub>2</sub> (Fig. 1.7B).<sup>62</sup> The dimeric  $\mu$ -(N<sub>2</sub>) bridged species (6) is an intermediate detected by mass spectrometry and <sup>31</sup>P NMR.

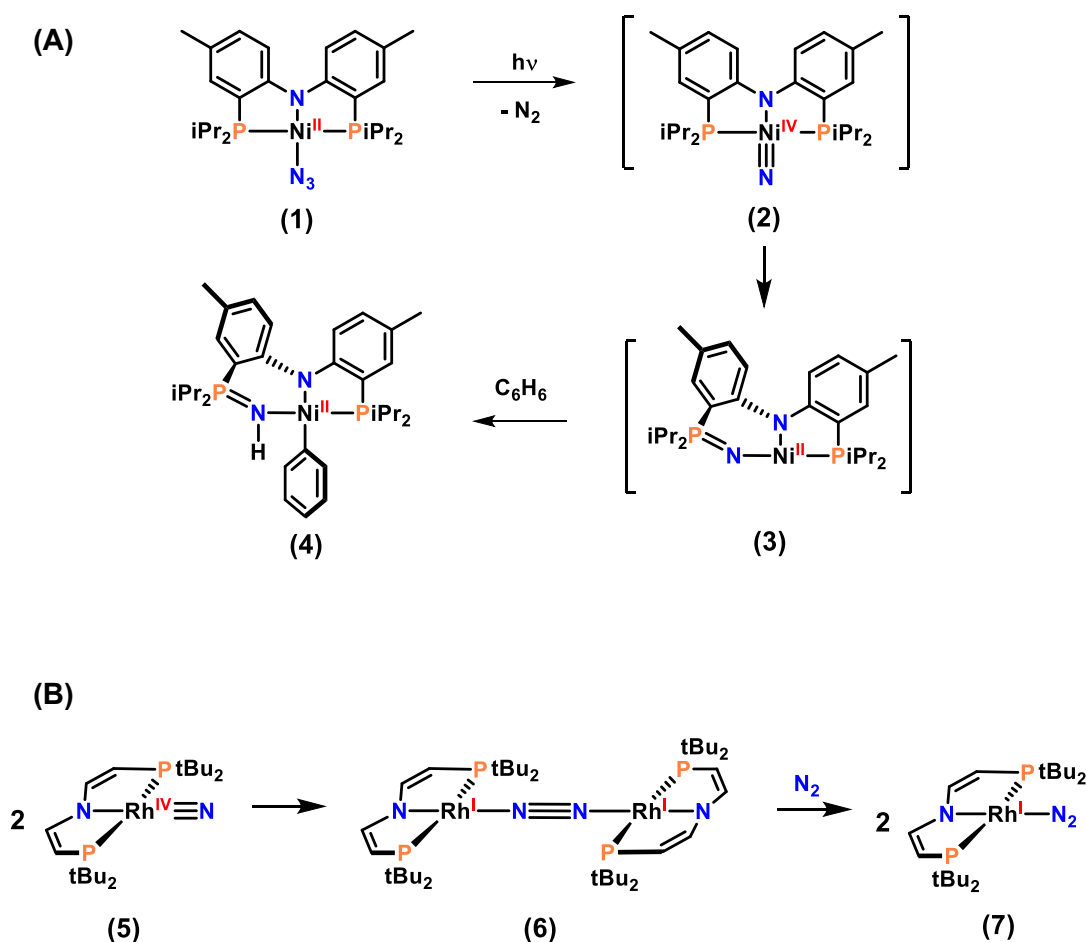


**Figure 1.7.** Examples of late metal nitride decomposition pathways. **(A)** Proposed Ni nitride species undergoing intermolecular ligand insertion and **(B)** A Rh nitride species homocoupling to afford N<sub>2</sub>.

### 1.2.3. Mid-Transition Metals

The above examples highlight the highly reactive and electrophilic nature of late transition metal nitride complexes. Mid-transition metals of group 7-8 exhibit reactivity intermediate between early and late transition metal analogues. Group 8 nitrides such as Fe are appealing due to their involvement in several model reactions relevant to nitrogen fixation and frequently exhibit electrophilic behavior.<sup>20–28,63–70</sup> A simple representation of electrophilicity is conveyed in Figure 1.8A. The addition of nucleophilic substrates (Nuc) results in reduction at the metal centre and a decrease in metal-nitride bond order due to the population of  $\pi^*$  MO's to accommodate additional electron density.<sup>71,72</sup> Reactivity with phosphines is most commonly observed for Group 8 metals and results in the formation of a phosphoraniminato ligand ( $\text{N}=\text{PR}_3$ ).<sup>73–77</sup> In rare cases, complete N-atom transfer to the nucleophilic substrate can occur.<sup>22,63</sup> Additionally, ambiphilic reactivity can arise where the nitride is regarded as both nucleophilic and electrophilic. For example, an Os nitride supported by a P–N–P type pincer ligand prepared by the Schneider group was observed to react with both bromotrimethylsilane as well as trimethylphosphine to form the respective adducts (Fig. 1.8B).<sup>78</sup>

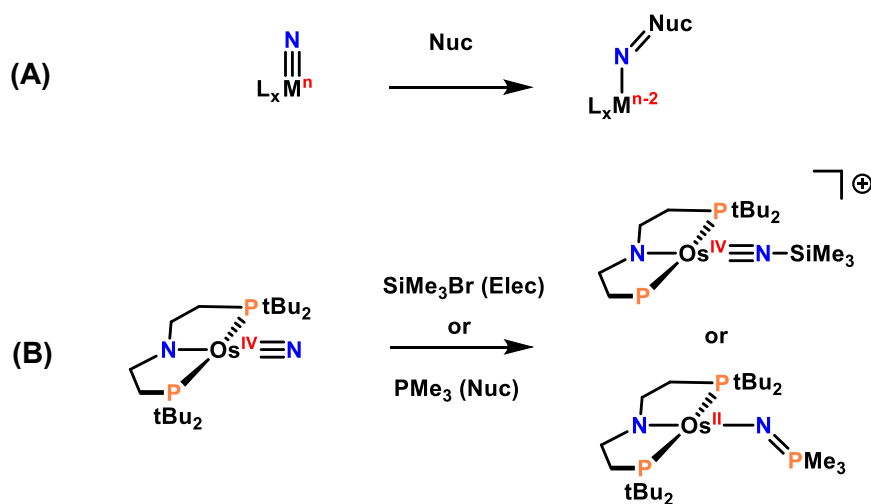


**Figure 1.8.** (A) General scheme for electrophilic reactivity of mid-to-late transition metal nitride complexes. (B) An ambiphilic Os nitride complex that reacts with both bromotrimethylsilane and trimethylphosphine.

Ambiphilic character is not always straightforward to interpret but can be important in addressing paradoxical experimental results. For example, the Smith group reported an Fe nitride complex supported by a tris(carbene)borate ligand that readily forms an adduct with triphenylphosphine, however this complex was not reported to interact with electrophilic substrates (Fig. 1.9A).<sup>23</sup> Computational analysis predicted a low-lying nitride-based  $\sigma^*$  LUMO that served as the site of nucleophilic attack by the phosphine. Hammett studies however using various *para*-substituted aryl phosphines revealed that an increase in the rate of the N—P interaction was associated with an increase in the electron-withdrawing ability of the aryl group. The result was inconsistent with an electrophilic nitride species. Smith addressed this issue by describing a dual-nature transition state (Fig. 1.9B)<sup>24</sup> that involves  $\sigma$ -donation from the phosphine into the nitride LUMO (1), as well as  $\pi$ -backdonation from the nitride HOMO into an empty P–aryl  $\sigma^*$  orbital (2). The synergistic effect of the two donor-acceptor interactions gave rise to a unique case of nitride ambiphilicity.

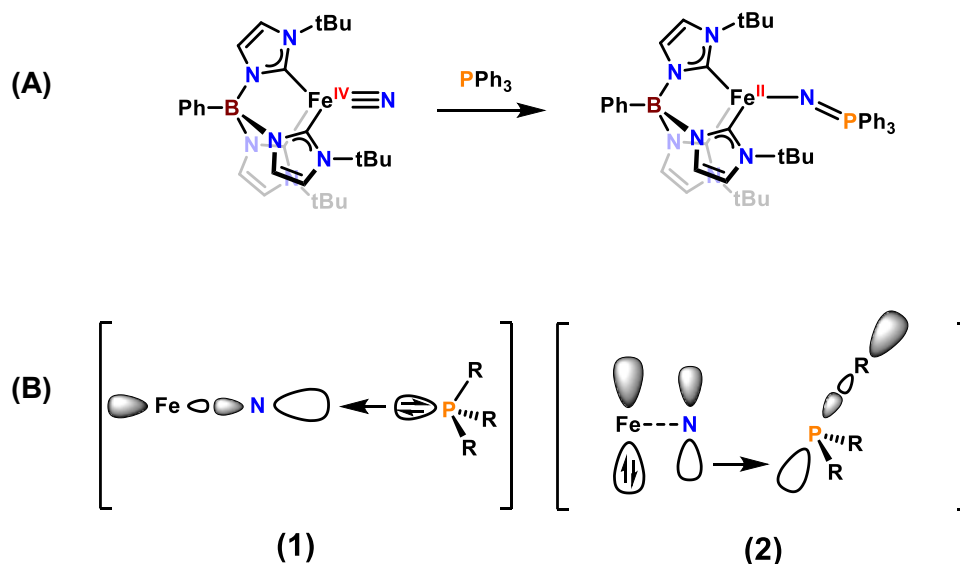


**Figure 1.9.** (A) An Fe nitride species that readily forms an adduct with triphenylphosphine. (B) The dual-nature transition state proposed by Smith. (1) The low-lying  $\sigma^*$  LUMO of nitride character accepts electron density from the phosphine lone pair. (2) The  $\pi$  HOMO of Fe character back-donates into the P–aryl  $\sigma^*$  bond and accounts for the enhanced rate for more electron-withdrawing aryl substituents. The nitride thus exhibits both nucleophilic and electrophilic properties.

Group 7 metals such as manganese nitrides are often nucleophilic and are frequently utilized in synthesis as amination reagents.<sup>79–84</sup> The reactivity of analogous metal oxo complexes for O-atom transfer is well established, but the utility of nitride complexes in this regard is significantly less explored.<sup>85–87</sup> Pioneering work by Groves and co-workers features a Mn nitride porphyrin complex that inserts into the C–C double bond of cyclooctene, and is the first reported case of olefin aziridination by a metal nitride complex.<sup>88</sup> The addition of a Lewis acid such as trifluoroacetic anhydride (TFAA) was necessary to drive reactivity as it converts the nitride into a transient imide species that is active towards group transfer (Fig. 1.10A).<sup>89</sup> This was later expanded to include amination of styrenes and silyl enol ethers using salen ancillary ligands<sup>90–92</sup> (Fig.10B), as well as other mid-transition metals such as Ru (Fig. 1.10C).<sup>93</sup> In the absence of substrate, the reactive imido species is susceptible to N–N coupling.<sup>94</sup>

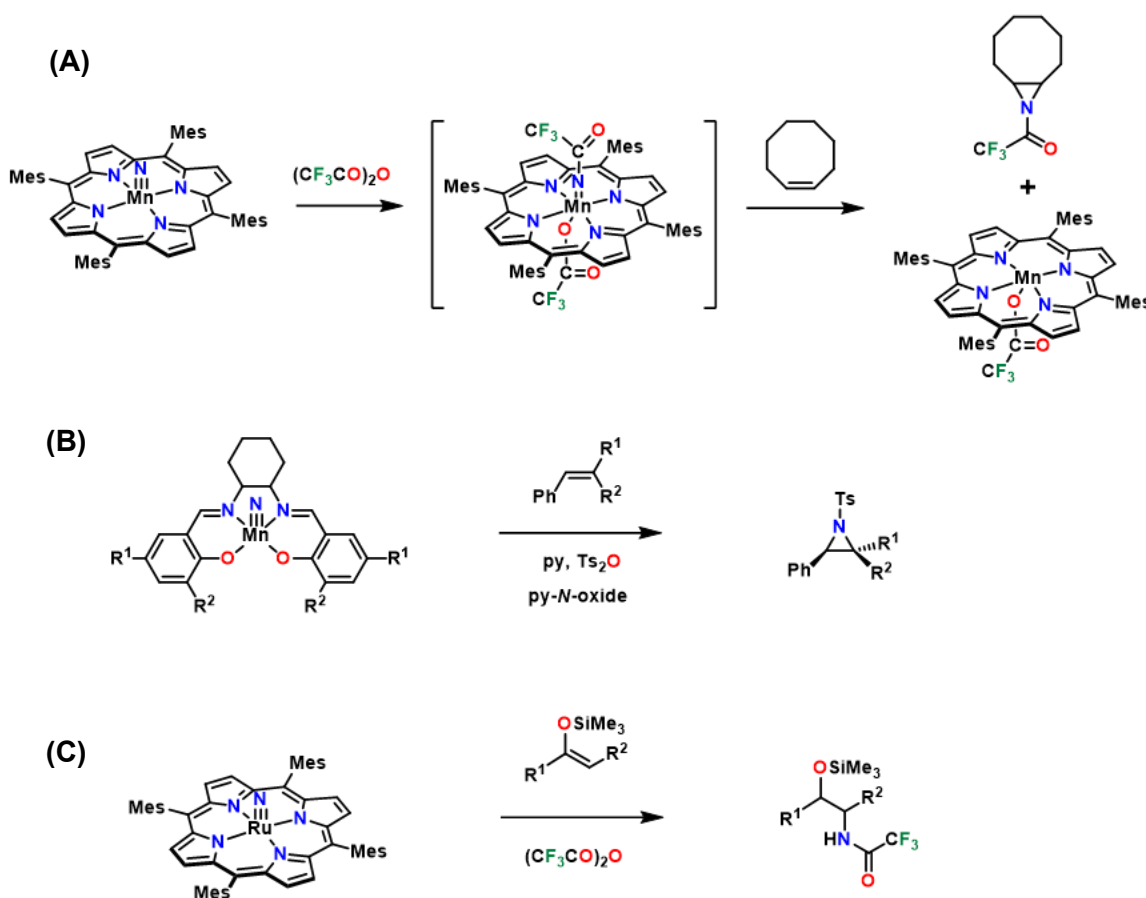


**Figure 1.10.** Select examples of N-transfer reactions upon activation with Lewis acids. **(A)** aziridination of cyclooctene, **(B)** aziridation of a styrene with a nitrido Mn salen complex and **(C)** amination of silyl enol ethers with a nitrido Ru porphyrin. Mes = mesityl, py = pyridine, Ts<sub>2</sub>O = *p*-toluenesulfonic anhydride.

### 1.2.4. C—H Activation

C—H activation of organic substrates by metal nitrides has also been investigated. This is often achieved *via* generation of a highly reactive nitrido species *in situ* by thermolysis, photolysis or gas-phase electrospray ionization.<sup>95–100</sup> In many cases, the active nitride species was not isolated. Lau and coworkers successfully isolated and characterized a high-valent nitrido Ru salen complex that activates organic substrates with low bond dissociation energies (BDE) such as xanthene (75.5 kcal mol<sup>-1</sup>)<sup>101</sup> or 9,10-dihydroanthracene (78.0 kcal mol<sup>-1</sup>)<sup>102</sup> (Fig. 1.11A).<sup>103</sup> The addition of ligands such as pyridine (py) that bind *trans* to the nitride results in a more reactive complex capable of activating C—H bonds as strong as cyclohexane (95.4 kcal mol<sup>-1</sup>).<sup>104</sup> This species also readily inserts into simple alkenes without Lewis acidic activating agents (Fig. 1.11B).<sup>105</sup>

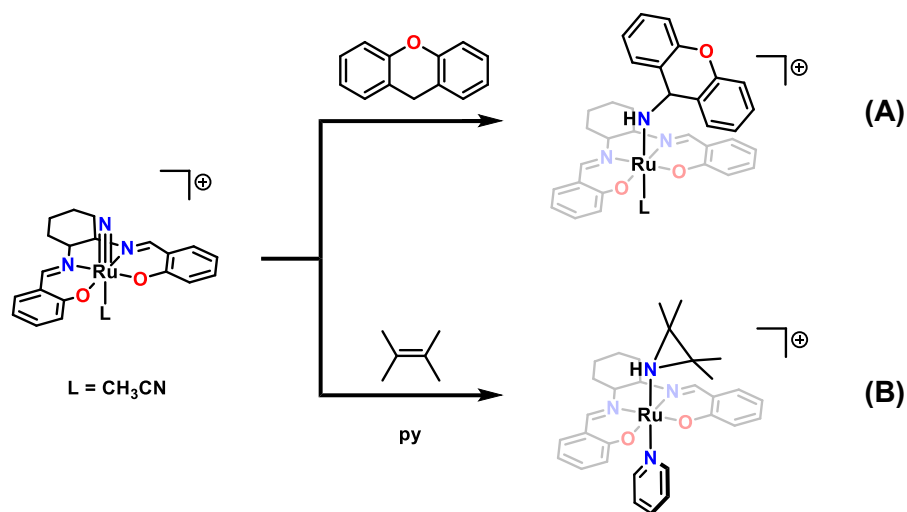


**Figure 1.11.** Insertion of the nitride into **(A)** C—H bond of xanthene, and **(B)** C=C bond of 2,3-dimethyl-2-butene.

### 1.2.5. Intermetal Reactivity

Finally, metal nitride compounds also serve as synthons in the preparation of other metal nitride complexes. For example, treatment of a known nitrido Mn salen species with Mn porphyrins results in oxidative N–atom transfer from the salen complex to the porphyrin affording a nitrido Mn(V) porphyrin with subsequent reduction of the Mn(V) salen species to Mn(III) (Fig. 1.12A).<sup>106</sup> This has since been extended to include N–transfer between other ligand sets such as corroles, and between hetero-metal centres (Fig. 1.12B).<sup>107–109</sup>

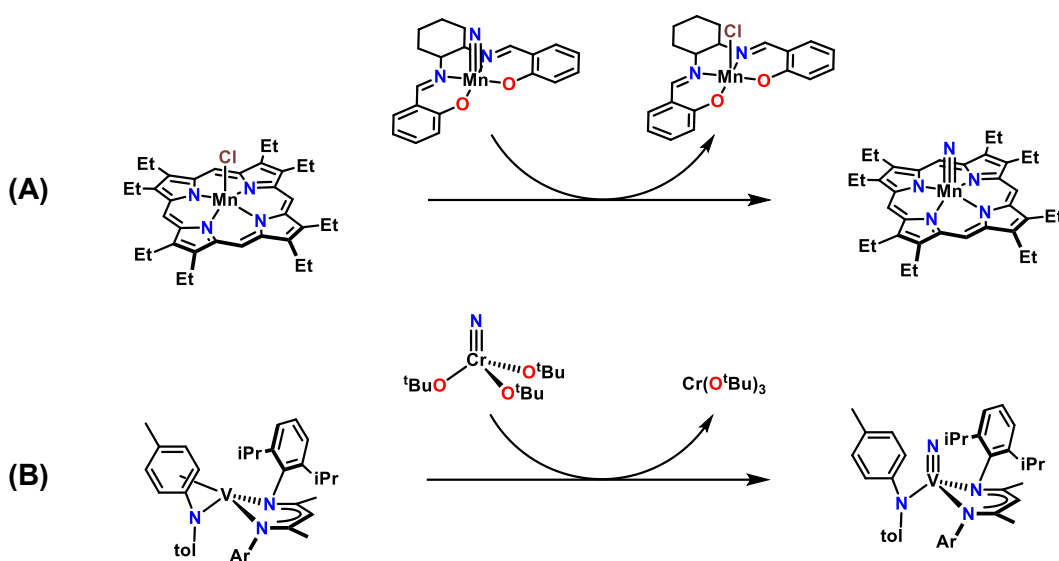


**Figure 1.12.** Examples of intermetal N-atom transfer as a preparative tool to form new metal nitride complexes.

In some of the examples discussed, salen ligands are frequently used as spectator ligands in metal nitride chemistry. This is largely due to their ability to stabilize a range of different metals in varying oxidation states.<sup>110</sup> As will be discussed below, salen ligands can also participate in the overall redox chemistry of the system, allowing for ligand redox activity that can potentially be exploited in reactivity.<sup>111</sup>



## 1.3. Non-Innocent Ligands

### 1.3.1. Non-innocent Ligands in Nature and Synthesis

The overwhelming majority of compounds in coordination chemistry utilize spectator or ‘innocent’ ligands, whose primary purpose is to offer structural and electronic support to the central metal atom. Ligands were first deemed to be ‘innocent’ or ‘non-innocent’ by Jørgenson in 1966 based on whether the oxidation state of the metal centre could be determined.<sup>112</sup> Currently, the term ‘non-innocent’ is mostly associated with ligands that can be oxidized or reduced within the redox processes of a transition metal complex, and hence the term ‘redox-active’ can be used interchangeably.<sup>113</sup> The ability of the ligand to participate in the redox activity of the complex depends on the relative ordering of metal (M) versus ligand (L) frontier orbitals. Figure 1.13 depicts the two situations in which ligand non-innocence can take place. In the first scenario, if the LUMO is predominantly ligand in character, *reduction* will be ligand-based. Alternatively, if the HOMO is ligand in character, then *oxidation* of the complex will be ligand-based. The latter will be the primary focus of this thesis, however in both cases, a ligand radical is formed.

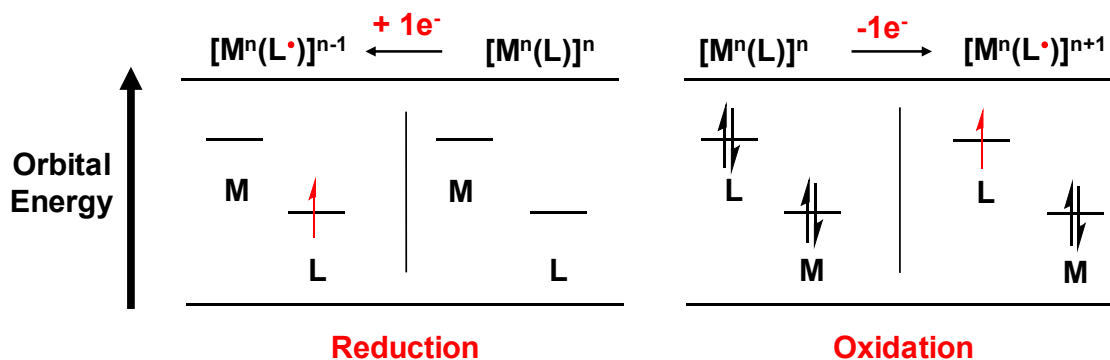


**Figure 1.13.** The relative ordering of metal and ligand frontier orbitals dictates whether the ligand will undergo reduction or oxidation and be classified as “non-innocent”.

Ligand non-innocence is critical to the functioning of certain biological metalloenzymes. In these enzymes, the ligands facilitate difficult substrate transformations by assisting the metal in multielectron chemistry. Among these systems, Cytochrome P450 remains one of the most notable (Fig. 1.14A)<sup>114</sup> and features a heme active site to oxidize C—H bonds.<sup>115</sup> The active oxidant (Compound I), is spectroscopically characterized as an Fe(IV) oxo species with a ligand radical delocalized across the porphyrin scaffold.<sup>116</sup> The non-innocence of the porphyrin is essential to the enzyme's function, as it serves to aid the metal in the 2-electron transformation of alkanes into alcohols *via* insertion of the oxo into C—H bonds (Fig 1.14B).

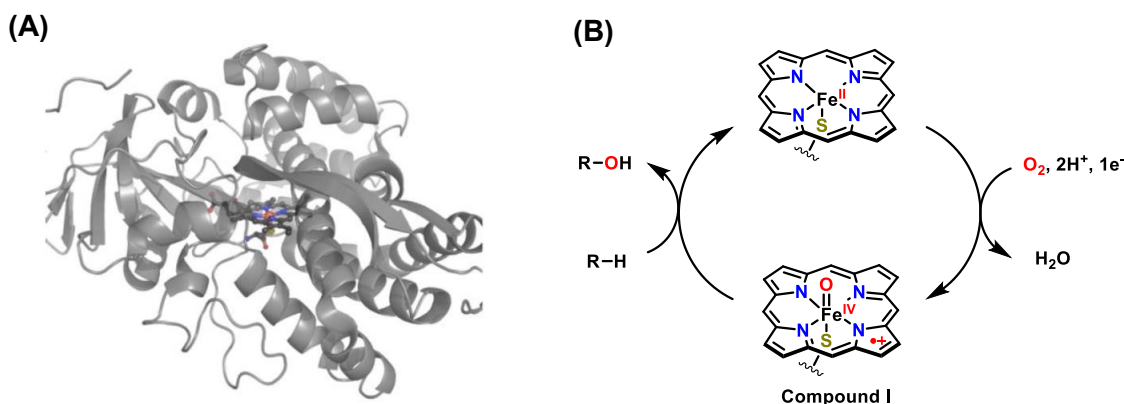


**Figure 1.14.** (A) Pymol rendering of CytochromeP450.<sup>114</sup> (B) Reaction scheme for the hydroxylation of C—H bonds.

A second example is galactose oxidase (GOase), a copper-containing metalloenzyme (Fig. 1.15A)<sup>114</sup> that catalyzes the oxidation of primary alcohols to aldehydes with concomitant reduction of dioxygen to H<sub>2</sub>O<sub>2</sub> (Fig. 1.15B).<sup>117,118</sup> The Cu in the active site is bound equatorially to two histidine residues (His<sub>496</sub> and His<sub>581</sub>) and to a post-translationally modified tyrosine residue (Tyr<sub>272</sub>) cross-linked with a cysteine residue (Cys<sub>228</sub>), while a tyrosine residue (Tyr<sub>495</sub>) occupies the axial position. The active oxidant (GO<sub>ox</sub>) incorporates a Cu(II) centre and a tyrosine radical that both undergo 1-electron reduction upon substrate oxidation.<sup>119</sup>

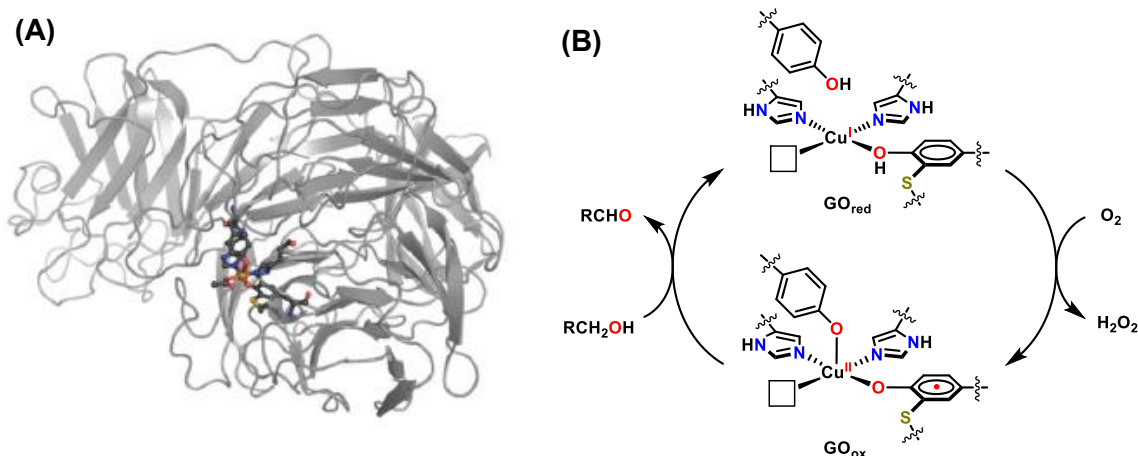


**Figure 1.15.** (A) Pymol rendering of GOase.<sup>114</sup> (B) Reaction scheme for the oxidation of primary alcohols.

The enzymes highlighted in the above examples have served as inspiration in the design of synthetic analogues that can facilitate difficult substrate transformations by harnessing ligand non-innocence. These systems offer an attractive alternative to rare and expensive noble metals in catalysis.<sup>120,121</sup> Generally, catalytic transformations are based on bond breaking/making events in which multiple electrons (usually 2) are shuttled across the substrate and metal centre. Such is the case for elementary processes such as oxidative addition (OA) and reductive elimination (RE). This type of chemistry is common to expensive (noble) metals such as Pd, Pt, Ir, Rh, etc. but not readily accessible to the cheaper earth-abundant first-row transition metals that typically engage in 1-electron chemistry.<sup>122</sup>

Non-innocent ligands can compliment metal reactivity by functioning as electron reservoirs during catalysis.<sup>120,123–125</sup> Multielectron chemistry can thus be achieved in a controlled manner by common 1<sup>st</sup> row transition metals. Chirik and coworkers have elegantly advanced the field by applying this concept to the Fe-catalyzed  $[2\pi + 2\pi]$  cycloaddition of olefins.<sup>126,127</sup> In their model depicted in Figure 1.16, an Fe(II) complex in the reduced form employing a non-innocent (bis)iminopyridine ligand forms a  $\pi$  complex with a diene upon the release of two nitrogen ligands (1). A 2-electron OA subsequently takes place, with the ligand acting as the electron source as opposed to the metal (2). This allows Fe to remain in the Fe<sup>II</sup> state, bypassing a less energetically favourable Fe<sup>IV</sup> intermediate. A RE then forms the cyclized product whilst the ligand is reduced back to the dianionic state (3). The overall ability of the ligand to function as an electron reservoir

allows the Fe complex to facilitate an important catalytic transformation traditionally executed by noble metals.<sup>122</sup> This concept has been applied to other earth-abundant metal complexes incorporating redox-active ligands in both catalysis<sup>128–134</sup> and in stoichiometric multi-electron reactions.<sup>135–138</sup>

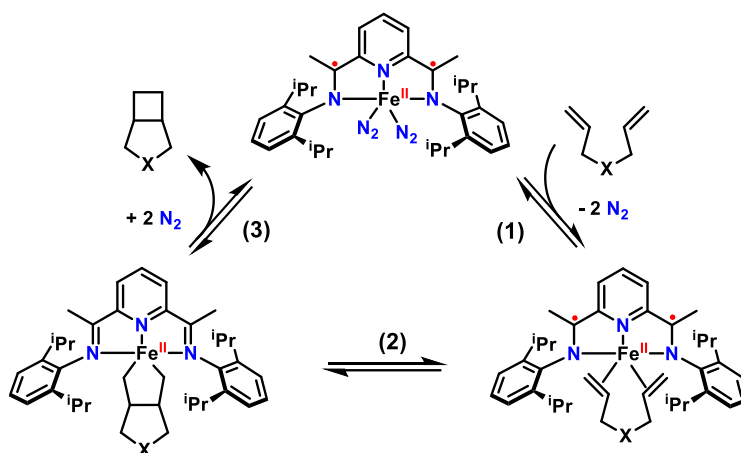


**Figure 1.16.** Fe-catalyzed [2π + 2π] cycloaddition of dienes employing a redox-active bis(imino)pyridine Fe complex. X = CH<sub>2</sub>, N-alkyl, C(CO<sub>2</sub>)Et)<sub>2</sub>.

### 1.3.2. Salens as Non-Innocent Ligands

Salen ligands ('salen' being a common abbreviation for N<sub>2</sub>O<sub>2</sub> bis-phenoxide bis-Schiff-base ligands) are of interest due to their significance in asymmetric catalysis,<sup>139–148</sup> and potential versatility for material<sup>149–152</sup> and medicinal applications.<sup>153–155</sup> Furthermore, salen ligands can exhibit ligand non-innocence.<sup>111</sup> Phenolate oxidation affords metal complexes that resemble the active site of galactose oxidase, and can serve as a platform in the advancement of biomimetic chemistry.<sup>156–164</sup> Typically, salen complexes are prepared by the condensation of a salicylaldehyde with a diamine, followed by complexation to a metal salt (MX<sub>2</sub>) upon deprotonation with a suitable base (Fig. 1.17A). Due to the abundance of readily available salicylaldehydes and diamine backbones, a number of salen-type ligands can be readily prepared. In addition, asymmetric, imino-reduced (salan), and half-reduced analogues are well known (Fig. 1.17B).<sup>158,165–168</sup>

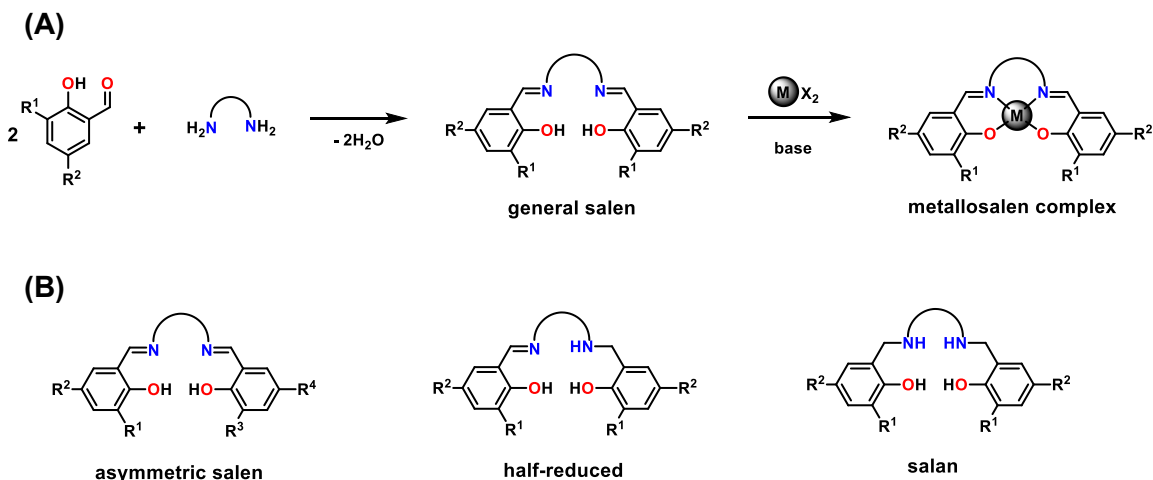


**Figure 1.17.** **(A)** General scheme for the preparation of salen complexes. **(B)** Structures of asymmetric, imino-half reduced and salen derivatives. Semi-circle in Figure depicts general diamine backbone.

The modular synthesis of salen ligands provides a straightforward approach for tuning steric and electronic properties about the metal centre.<sup>169</sup> Furthermore, these ligands can stabilize various metals in a wide range of oxidation states.<sup>110</sup> As mentioned, salens have the potential to undergo oxidation in place of the metal. While outside the scope of this thesis, reduction of the salen scaffold is also possible with strong alkali metal reducing agents (Li, Na, K).<sup>170</sup> In some cases, oxidation can be strictly metal or ligand-based. Contribution from both the metal and the ligand to the singularly occupied molecular orbital (SOMO) is also possible, resulting in delocalization of the oxidation locus across the complex.<sup>171–173</sup> The identity of the metal ion and oxidation state imparts a strong influence in this case, while various exogenous factors such as the addition of axially binding ligands and temperature can lead to valence tautomerism (Fig. 1.18).<sup>174–178</sup>

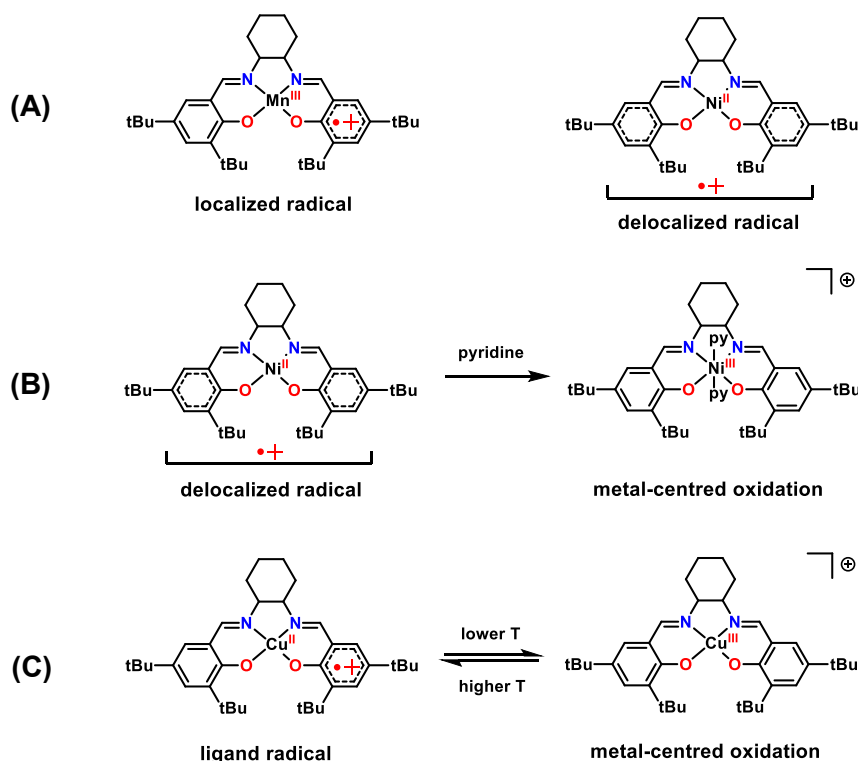


**Figure 1.18.** Examples of factors that can affect the degree of ligand radical involvement in the electronic structure of 1-electron oxidized salen complexes. **(A)** Effect of changing the metal ion,<sup>175,176</sup> **(B)** addition of axially binding ligands,<sup>176</sup> **(C)** temperature-dependent valence tautomerism in solution.<sup>177</sup>

How different phenolate *para*-R phenoxide substituents influence the overall electronic structure of oxidized metal salen complexes has been extensively studied in the Storr group.<sup>179–184</sup> The alteration of *para*-R substituents provides a means of electronic tuning whilst maintaining a constant geometry about the metal centre. As an example, the donating ability of the *para*-R substituent was modulated in Ni salen complexes and the extent of ligand radical delocalization upon oxidation was explored.<sup>175,176,179,180</sup> Complete delocalization across the two redox-active phenoxides was determined to be of lowest energy in complexes with electron-withdrawing or weakly donating *para*-R substituents (CF<sub>3</sub> and tBu) due to the participation of the metal ion in the SOMO. A shift towards a localized electronic structure was observed upon substitution with more electron-donating groups (NMe<sub>2</sub>), in which the lowest energy electronic structure includes significant radical character on one of the electron-donating *para*-ring substituents. (Fig 1.19).<sup>179,180</sup>

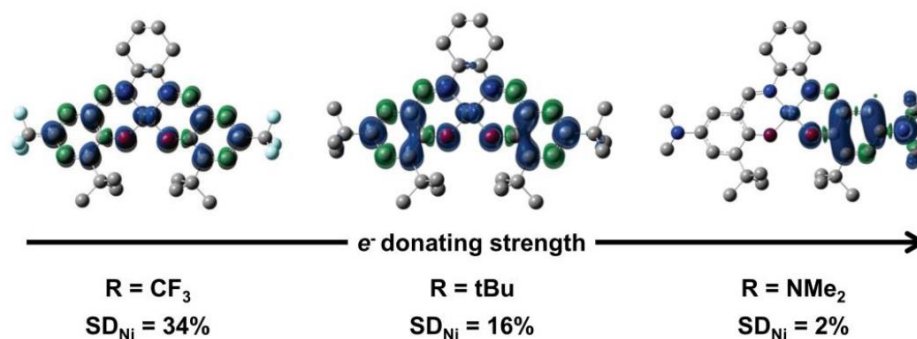


**Figure 1.19.** The effect of the *para*-ring substituent on ligand radical delocalization visualized by DFT-generated spin density (SD) plots. Greater spin density on the Ni ion is observed for more electron-withdrawing groups ( $\text{R} = \text{CF}_3 > \text{tBu}$ ) due to involvement of the metal *d* orbitals in the SOMO of the complex facilitating radical delocalization.<sup>179</sup> Electron donating groups ( $\text{R} = \text{NMe}_2$ ) result in less spin density on the Ni and localization of the radical to one side of the salen.<sup>180</sup>

Ligand electronics can also affect the reactivity of metal salen complexes.<sup>183,185</sup> For example, Thomas and Shimazaki have collectively demonstrated that the rate and mechanism of benzyl alcohol oxidation to benzaldehyde by an oxidized Cu(II) salen species can be influenced by phenolate *para*-R substitution.<sup>186–189</sup> Jacobsen reported that the enantiomeric excess (ee) values in Mn salen catalyzed epoxidation of alkenes was found to be larger for electron-donating *para*-R groups.<sup>190,191</sup> A similar effect was observed for Cr salen catalyzed copolymerization of cyclohexene oxide and  $\text{CO}_2$ , in that polymerization rates were enhanced with *para*-R electron-donating ability.<sup>192,193</sup> The Storr group has investigated the effect of *para*-R substituent electronic tuning on metal nitride chemistry. In recent work, a series of Mn(V) nitride salen complexes were prepared with varying *para*-R substituents.<sup>181</sup> Oxidation of complexes with mildly electron-donating ( $\text{R} = \text{tBu}$ ) and strongly withdrawing groups ( $\text{R} = \text{CF}_3$ ) resulted in metal-based oxidation. This species exhibited a highly reactive Mn(VI)–nitride unit that rapidly decays *via* N–N coupling to afford  $\text{N}_2$  and a Mn<sup>III</sup> decay product (Fig. 1.20). The rate of coupling was found to be dependent on the electron-withdrawing ability of the R group, with the  $\text{CF}_3$  substituent affording a faster coupling rate compared to the tBu derivative. In contrast, oxidation of the Mn(V) nitride employing a strongly electron-donating *para*-R substituent ( $\text{R} = \text{NMe}_2$ ) resulted in ligand-based oxidation, forming a stable ligand radical that was remarkably resistant to the homocoupling pathway.

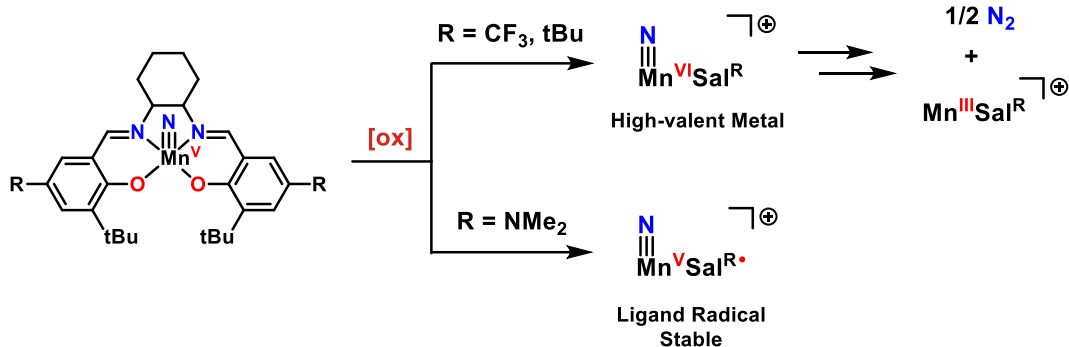
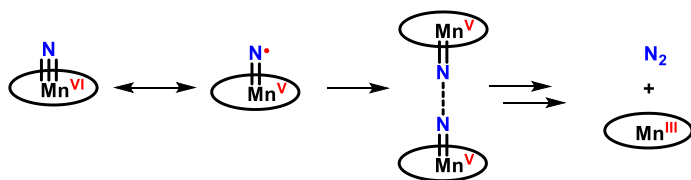
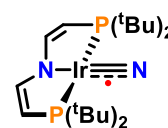


**Figure 1.20.** The oxidation of Mn(V) nitride salen complexes. Activation of the Mn—N bond is dependent on *para*-R electronics

The current hypothesis for the observed reactivity is that the high-valent metal species contains a degree of nitridyl radical character that favours a radical coupling pathway (Fig. 1.21A).<sup>181</sup> Direct spectroscopic evidence of nitridyl radicals are uncommon but known in the literature (Fig. 1.21B).<sup>41,61,62</sup> Although N—N coupling remains a common pathway for various high-valent metal nitrides, they are also suitable candidates for the amination of unactivated C—H bonds due to their H-atom abstraction ability.<sup>194</sup>



**(A) Storr *et al.***



**(B) Schneider *et al.***

**Figure 1.21.** **(A)** The proposed mechanism for the decomposition of the Mn(VI) complex proceeds through a nitridyl radical species that favours N—N homocoupling. **(B)** An example of an Ir complex with a large degree of nitridyl radical character.



## 1.4. Cr Salen Complexes

The results highlighted in the Mn study above demonstrate that oxidation and subsequent activation of the metal–nitride bond can be influenced by ligand electronics. In unpublished work from the Storr group, the reactive Mn(VI) species shows precedence for amination of organic small molecules. While this remains an ongoing area of research in the group, preliminary work suggests that the rapid homocoupling pathway significantly outcompetes substrate interactions. In an alternative approach, we have changed the metal ion to Cr in order to investigate the changes to the overall electronic structure and reactivity upon oxidation. We postulated that the Cr nitride complexes would be inherently more stable in comparison to Mn following the general trend of greater stability for early transition metal nitrides, where the oxidized Cr(VI) complexes are relatively inert towards homocoupling. This would allow for more detailed investigations of electronic structure as well as reactivity studies with organic substrates.

This principal was exemplified by Kochi who evaluated the active species in metal salen catalyzed enantioselective epoxidation of alkenes. In the early 1990's, Jacobsen<sup>195,196</sup> and Katsuki<sup>197</sup> independently demonstrated that Mn(III) salen complexes can catalytically transform pro-chiral alkenes into epoxides using PhIO or NaClO as a stoichiometric oxidant. Currently, different versions of the catalyst are commercially available, with the most popular (and versatile) colloquially referred to as Jacobsen's catalyst (Fig. 1.22A).<sup>198</sup> Cr versions are also readily available. In their work, the Kochi group proposed that the active oxidant was a Mn(V) oxo species generated *in situ* by treatment of Mn(III) with PhIO.<sup>199</sup> Attempts to isolate this species however have been largely unsuccessful.<sup>200</sup> When Cr was instead used, a cationic Cr(V) oxo complex was successfully isolated and structurally characterized (Fig 1.22B).<sup>201</sup> Despite enhanced stability, this complex was still highly active towards epoxidation, as treatment with one equivalent of alkene resulted in complete epoxide formation and quantitative recovery of the Cr(III) reduced product, signalling a 1:1 stoichiometry. It was on this basis, along with detailed kinetic and spectroscopic data, that the active oxidant in Cr salen catalyzed epoxidation was unambiguously assigned as the oxo species. These findings have since been translated to Mn in which a transient Mn oxo intermediate is invoked as the active species in the catalytic epoxidation of alkenes, despite unsuccessful isolation and spectroscopic detection of this intermediate (Fig. 1.22C).<sup>143,202</sup>

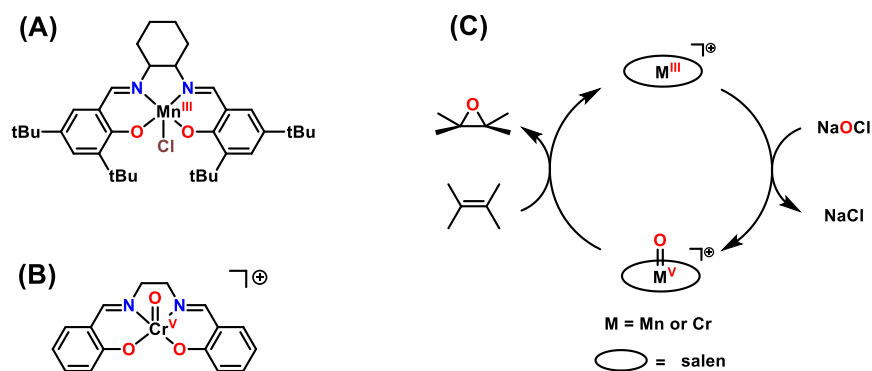


**Figure 1.22.** Mn and Cr salen used in alkene epoxidation. **(A)** commercially available Jacobsen's catalyst for epoxidation of asymmetric alkenes. **(B)** First example of a structurally characterized Cr oxo active species.<sup>201</sup> **(C)** Proposed mechanism for metal salen catalyzed alkene epoxidation.

Cr salen complexes are frequently reported in the literature as highly efficient epoxidation catalysts.<sup>143,203</sup> Apart from this, they are also regarded as suitable catalysts in epoxide ring-opening reactions,<sup>204–207</sup> CO<sub>2</sub> copolymerization with various small molecules<sup>208–214</sup> and in alcohol oxidation.<sup>215</sup> Phenoxyl radicals bound to Cr are scarce in the literature,<sup>216,217</sup> and despite the potentially rich chemistry, the formation and reactivity of Cr complexes bearing salen-based phenoxyl radicals have not yet been reported. This thesis describes the synthesis and characterization of a series of Cr(V) nitride complexes bearing non-innocent salen ligands (Fig. 1.23). Ligand electronics were tuned by modulation of phenolate *para*-R substituents to influence the locus of oxidation. The electronic structure of the oxidized species was assessed by various spectroscopic and theoretical techniques, and factors affecting nitride reactivity were investigated.

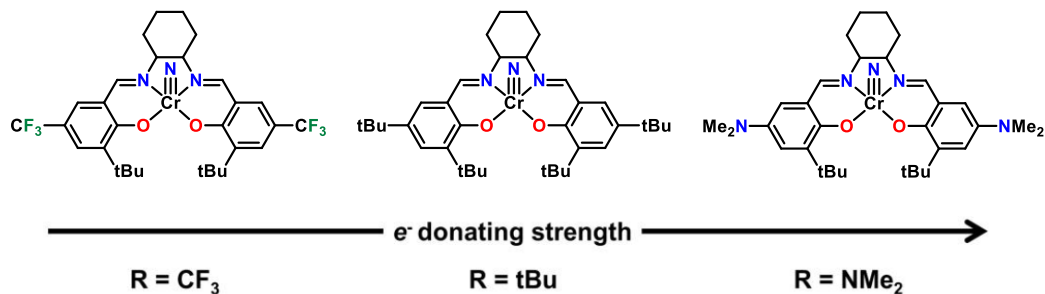


**Figure 1.23.** Nitrido Cr(V) complexes bearing salen ligands with para-ring substituents from electron-withdrawing (R = CF<sub>3</sub>) to electron-donating (R = NMe<sub>2</sub>).

## 1.5. Thesis Outline

In an effort to gain a deeper understanding of the electronic nature of metal nitride complexes and how this relates to reactivity, a series of Cr nitride salen complexes employing *para*-R phenoxide substituents of varying electron donating ability have been prepared. Chapter 2 outlines the synthetic strategies for the preparation of **CrNSal**<sup>CF<sub>3</sub></sup>, **CrNSal**<sup>tBu</sup> and **CrNSal**<sup>NMe<sub>2</sub></sup>, and a combination of spectroscopic and theoretical techniques permitted detailed characterization.

Chapter 3 details how the modulation of *para*-R phenoxide substituents influences the locus of oxidation. It was observed that strongly withdrawing and moderately donating R groups (R = CF<sub>3</sub>, tBu) favour metal-based oxidation, while employing strongly donating groups (R = NMe<sub>2</sub>) affords a ligand radical species.

In Chapter 4, the reactivities of neutral and oxidized complexes is discussed. Nucleophilicity was found to be a general property for neutral Cr(V) compounds, however this is effectively *switched off* upon metal-based oxidation. Interestingly, oxidation at the ligand does not appear to impart significant changes in the Cr—N unit as this species remains nucleophilic. Extensive theoretical analysis is employed to rationalize these reactivity differences.

Finally, Chapter 5 outlines the ongoing work and future directions geared at building off of the results discussed herein. In all, this thesis provides significant new information on the intricate interplay between ligand electronics and metal nitride reactivity.

## Chapter 2. Synthesis and Characterization of $\text{CrNSal}^{\text{CF}_3}$ , $\text{CrNSal}^{\text{tBu}}$ and $\text{CrNSal}^{\text{NMe}_2}$

D. Martelino performed the synthesis and carried out UV-vis and theoretical analysis. R. M. Clarke collected X-ray data. K. Herasymchuk and G. McNeil collected EPR data and Diego Martelino simulated the data.

### 2.1. Introduction

The synthetic strategies for the preparation of Cr nitride complexes are reported in a number of reviews.<sup>5,6</sup> Select examples include ammonia oxidation<sup>218</sup> and nitrosyl deoxygenation.<sup>219</sup> A versatile synthetic route is photochemical decomposition of an azide precursor, in which the major driving force is the liberation of  $\text{N}_2$ .<sup>220–224</sup> This was initially reported by Arshankow and Poznjak in 1982, who demonstrated that photolysis of a Cr(III) azide salen complex afforded the Cr(V) nitride product (Fig. 2.1A).<sup>225</sup> This was the first reported case of a terminal nitride ligand bonded to a first row transition metal. Herein, the method in which the complexes  $\text{CrNSal}^{\text{CF}_3}$ ,  $\text{CrNSal}^{\text{tBu}}$  and  $\text{CrNSal}^{\text{NMe}_2}$  were prepared was through N-atom transfer from a nitrido Mn species to a Cr(III) precursor. This reactivity was introduced in Section 1.2.5 and is a commonly used procedure in transition metal nitride synthesis. The ability to transfer a single nitrogen atom between two metal centres was first reported by Bottomley and Neely who found that complete N-transfer from a nitrido Mn(V) porphyrin to a Cr(III) porphyrin was possible (Fig. 2.1B).<sup>226</sup>

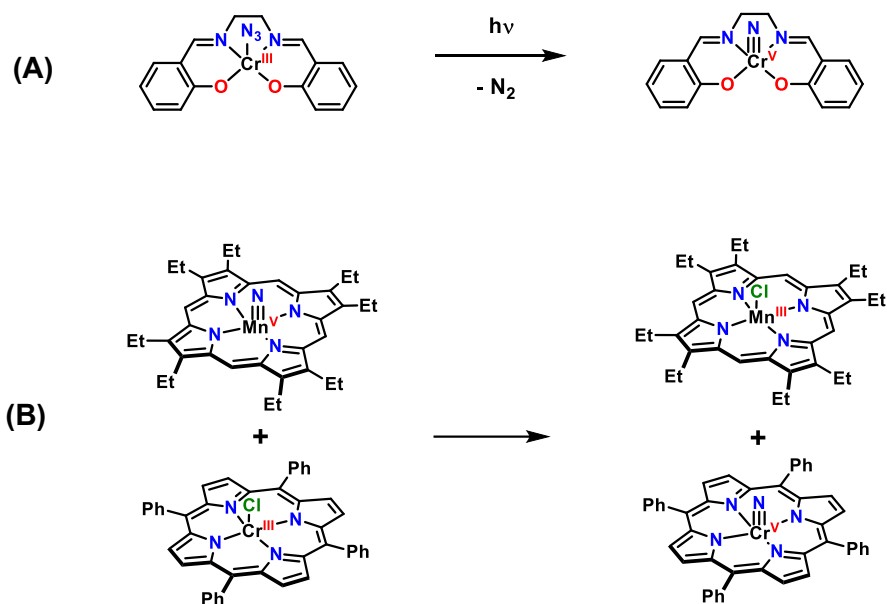
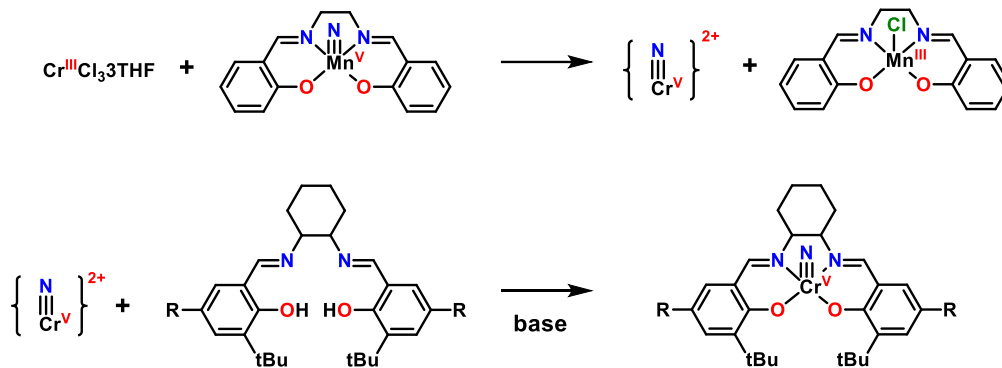


**Figure 2.1.** First reported cases for the synthesis of Cr nitride complexes by **(A)** photolysis of an azide precursor<sup>225</sup> and **(B)** Intermetallic N-atom transfer.<sup>226</sup>

The N-atom transfer procedure was elegantly advanced by Bendix and coworkers who devised a general route for the preparation of a number of Cr nitride complexes.<sup>227</sup> This preparation involves reaction of a nitrido Mn salen complex with  $\text{CrCl}_3(\text{THF})_3$ . Oxidative N-transfer from Mn(V) to the Cr(III) starting material occurs readily. The resulting reaction mixture contains a species in solution that has been described as a  $[\text{Cr}\equiv\text{N}]^{2+}$  unit complexed by a labile coordination sphere (Scheme 2.1). The room temperature electron paramagnetic resonance (EPR) spectrum of this solution consists of a broad and featureless isotropic signal ( $g_{\text{iso}} = 1.98$ ) that is consistent with a Cr(V)  $d^1$  species.<sup>228,229</sup> The Mn complex is effectively reduced to a Mn(III) by-product and readily precipitates in acetonitrile solvent. The filtrate containing  $[\text{Cr}\equiv\text{N}]^{2+}$  is an excellent template that coordinates to a wide variety of both simple and multidentate ligands.<sup>230–232</sup> Salen ligands readily coordinate to this species under basic conditions, allowing for the isolation of air-stable **CrNSal<sup>NMe2</sup>**, **CrNSal<sup>tBu</sup>** and **CrNSal<sup>CF3</sup>**.

**Scheme 2.1.** Synthesis of Cr nitride salen complexes (R = CF<sub>3</sub>, tBu, NMe<sub>2</sub>).



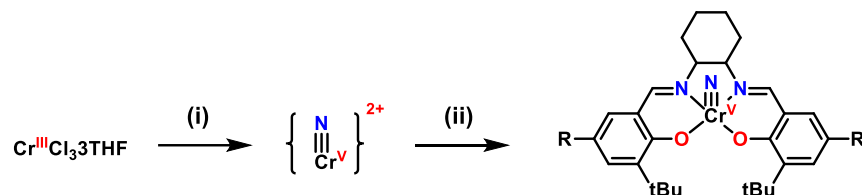
This chapter outlines the preparation and characterization of **CrNSal<sup>NMe<sub>2</sub></sup>**, **CrNSal<sup>tBu</sup>** and **CrNSal<sup>CF<sub>3</sub></sup>**. Synthesis was accomplished using the N-atom transfer method with a nitrido Mn salen complex (MnNSalen). Characterization using spectroscopic and computational methods will be discussed.

## 2.2. Results

### 2.2.1. Synthesis

All Cr compounds were synthesized according to the general preparation outlined by Bendix,<sup>227</sup> in which the appropriate substituted salen ligand was added to a solution containing  $[\text{Cr}\equiv\text{N}]^{2+}$ . All three complexes were isolated as coloured microcrystalline solids in reasonable yield (R = CF<sub>3</sub>: rose gold, 75 %; tBu: brownish-yellow, 80 % NMe<sub>2</sub>: dark orange, 82 %) and exhibited good fits to elemental analysis (EA) data.

**Scheme 2.2.** Synthetic strategy for Cr nitride salen complexes.



Reaction conditions: (i)  $\text{CH}_3\text{CN}$ , 1 eq.  $\text{MnNSalen}$ ; (ii)  $\text{CH}_3\text{CN}$ , ~ 3 drops  $\text{Et}_3\text{N}$ , 1 eq.  $\text{H}_2\text{Sal}^{\text{R}}$ .

## 2.2.2. Solid-State Structure Determination

The solid-state structures of **CrNSal<sup>tBu</sup>** and **CrNSal<sup>NMe<sub>2</sub></sup>** are presented in Fig. 2.2 and Fig. 2.3 respectively and selected crystallographic data is presented in Table 2.1. X-ray quality crystals were grown by slow evaporation of complexes in a 1:1 mixture of dichloromethane and acetonitrile. Attempts to isolate suitable crystals of **CrNSal<sup>CF<sub>3</sub></sup>** for analysis were unsuccessful due to a high degree of twinning and relatively small crystal morphology. Nevertheless, the structures obtained for **CrNSal<sup>tBu</sup>** and **CrNSal<sup>NMe<sub>2</sub></sup>** feature a pseudo-square pyramidal geometry with the nitride at the apical position and the central Cr ion above the salen plane by  $\sim 0.5$  Å (R = tBu: 0.595 Å, R = NMe<sub>2</sub>: 0.518 Å). The short Cr-nitride bond length of ca. 1.5 Å (R = tBu: 1.549 Å, NMe<sub>2</sub>: 1.544 Å) is indicative of triple bond character and is in close agreement with other Cr complexes containing terminal nitride ligands.<sup>219,228,232</sup>

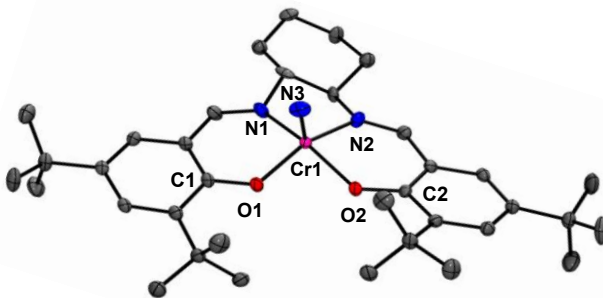


**Figure 2.2.** POV-Ray representation of **CrNSal<sup>tBu</sup>**. Thermal ellipsoids shown at 50% probability level. Hydrogen atoms omitted for clarity. Cr, pink; C, grey; O, red; N, blue. Select interatomic distances [Å] and angles [deg]: Cr(1)-O(1): 1.909(3), Cr(1)-O(2): 1.898(2), Cr(1)-N(1): 2.008(3), Cr(1)-O(2): 2.019(2), Cr(1)-N(3): 1.549(3), O(1)-C(1): 1.314(4), O(2)-C(2): 1.307(4). Angles: O(1)-Cr(1)-O(2): 87.47, O(1)-Cr(1)-N(1): 88.12, O(1)-Cr(1)-N(2): 144.72, O(1)-Cr(1)-N(3): 110.13, O(2)-Cr(1)-N(2): 105.88, O(2)-Cr(1)-N(1): 153.50, O(2)-Cr(1)-N(3): 105.88, N(1)-Cr(1)-N(2): 80.58, N(1)-Cr(1)-N(3): 100.17, N(2)-Cr(1)-N(3): 104.74.

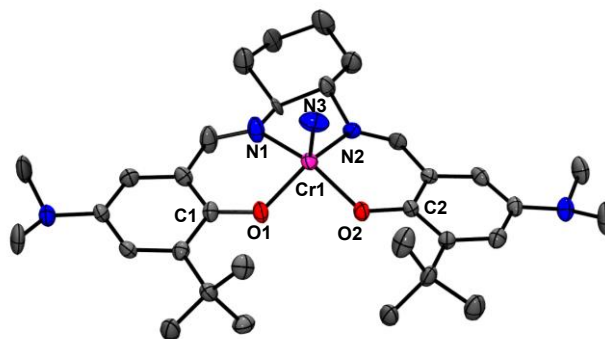


**Figure 2.3.** POV-Ray representation of **CrNSal<sup>NMe2</sup>**. Thermal ellipsoids shown at 50% probability level. Hydrogen atoms omitted for clarity. Cr, pink; C grey; O, red; N, blue. Select interatomic distances [Å] and angles [deg]: Cr(1)-O(1): 1.911(4), Cr(1)-O(2): 1.906(4), Cr(1)-N(1): 2.013(5), Cr(1)-O(2): 2.004(4), Cr(1)-N(3): 1.544(5), O(1)-C(1): 1.305(6), O(2)-C(2): 1.323(6). Angles: O(1)-Cr(1)-O(2): 87.81, O(1)-Cr(1)-N(1): 88.79, O(1)-Cr(1)-N(2): 149.28, O(1)-Cr(1)-N(3): 108.04, O(2)-Cr(1)-N(2): 88.57, O(2)-Cr(1)-N(1): 150.52, O(2)-Cr(1)-N(3): 107.51, N(1)-Cr(1)-N(2): 79.65, N(1)-Cr(1)-N(3): 101.38, N(2)-Cr(1)-N(3): 102.13.

**Table 2.1.** Selected crystallographic data for **CrNSal<sup>tBu</sup>** and **CrNSal<sup>NMe2</sup>**.

	<b>CrNSal<sup>tBu</sup></b>	<b>CNSal<sup>NMe2</sup></b>
<b>Formula</b>	C <sub>36</sub> H <sub>52</sub> CrN <sub>3</sub> O <sub>2</sub>	C <sub>32</sub> H <sub>46</sub> CrN <sub>5</sub> O <sub>2</sub>
<b>Formula weight</b>	610.8	584.72
<b>Space group</b>	P -1	P 2 <sub>1</sub> /n
<b>a (Å)</b>	9.99(3)	9.27(2)
<b>b (Å)</b>	13.51(3)	27.81(6)
<b>c (Å)</b>	14.70(3)	12.04(3)
<b>α (deg)</b>	63.0(1)	90
<b>β (deg)</b>	78.2(2)	102.8(10)
<b>γ (deg)</b>	71.4(10)	90
<b>V (Å<sup>3</sup>)</b>	1672.83	3027.11
<b>Z</b>	4	6
<b>T (K)</b>	150	150
<b>ρ<sub>calcd</sub> (g cm<sup>-3</sup>)</b>	1.213	1.283
<b>λ (Å)</b>	1.54178	1.54178
<b>μ (cm<sup>-1</sup>)</b>	3.072	3.393
<b>R indices<sup>a</sup> with I &gt; 2.0σ(I) (data)</b>	0.0586	0.0927
<b>wR<sub>2</sub></b>	0.1548	0.2069
<b>R<sub>1</sub></b>	0.0601	0.0985
<b>Goodness-of-fit on F<sup>2</sup></b>	1.303	1.267

<sup>a</sup>Goodness-of-fit on F



### 2.2.3. Electron Paramagnetic Resonance Spectroscopy

Electron paramagnetic resonance (EPR) spectroscopy was used to confirm the  $3d^1$  ( $S = 1/2$ ) electronic ground state. All compounds, regardless of R group, were found to exhibit identical experimental spectra and simulation parameters. Figure 2.4 shows the room temperature EPR spectrum of **CrNSal**<sup>CF<sub>3</sub></sup>, **CrNSal**<sup>tBu</sup>, and **CrNSal**<sup>NMe<sub>2</sub></sup> in dichloromethane. Each signal is composed of a sharp isotropic resonance centred at  $g_{\text{iso}} = 1.978$ . The intense central feature is due to Cr isotopes with nuclear spin  $I = 0$  (totalling 90.5 % abundance). This signal is flanked by a quartet pattern due to hyperfine splitting from <sup>53</sup>Cr with nuclear spin  $I = 3/2$  (9.5 % abundant). These signals are further split into a septet line pattern due to similar hyperfine splitting values with three nitrogen atoms (two imines on the salen and the nitride,  $I = 1$ ). The degeneracy in splitting values, despite chemical non-equivalence, is a characteristic feature for Cr nitride complexes containing equatorial imino-donating ligands.<sup>220,233,234</sup>

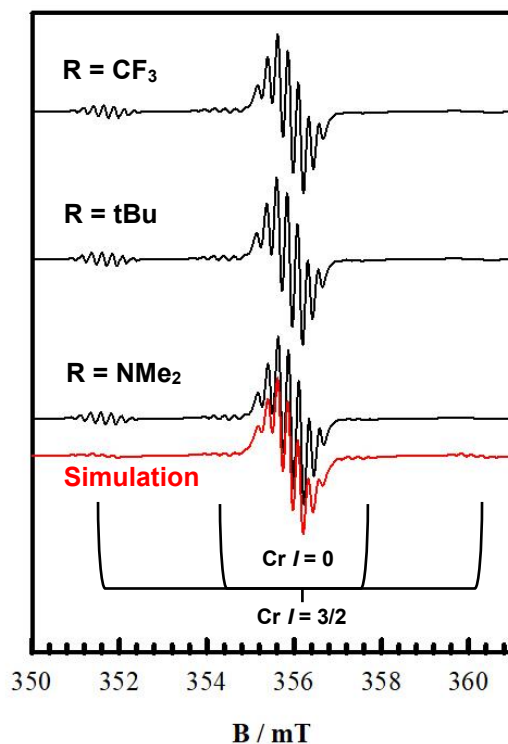


**Figure 2.4.** Room temperature EPR of **CrNSal**<sup>CF<sub>3</sub></sup>, **CrNSal**<sup>tBu</sup>, and **CrNSal**<sup>NMe<sub>2</sub></sup> in dichloromethane. Fitted parameter values are the same for all compounds:  $g_{\text{iso}} = 1.978$ ;  $A^{53\text{Cr}} = 78.00$  MHz,  $A^{14\text{N, imine}} = 6.34$  MHz,  $A^{14\text{N, nitride}} = 6.28$  MHz. Conditions: 0.33 mM complex; freq. = 9.85 GHz; power = 2.0 mW; mod. freq. = 100 kHz; mod. amp. = 0.6 mT; T = 298 K.

Samples were then frozen and analyzed at 77 K (Fig. 2.5). Again, all three derivatives exhibited identical spectra. Each signal is composed of a uniaxial line shape with hyperfine coupling to a single Cr centre, in close agreement with other Cr(V) systems.<sup>222,233,235</sup> The addition of a large excess of tetrabutylammonium perchlorate (TBAP) supporting electrolyte was necessary in order to minimize intermolecular interactions. In the absence of supporting electrolyte, the signal intensity was significantly reduced and afforded line patterns that could not be accounted for in simulations (Appendix A – Fig. A1).

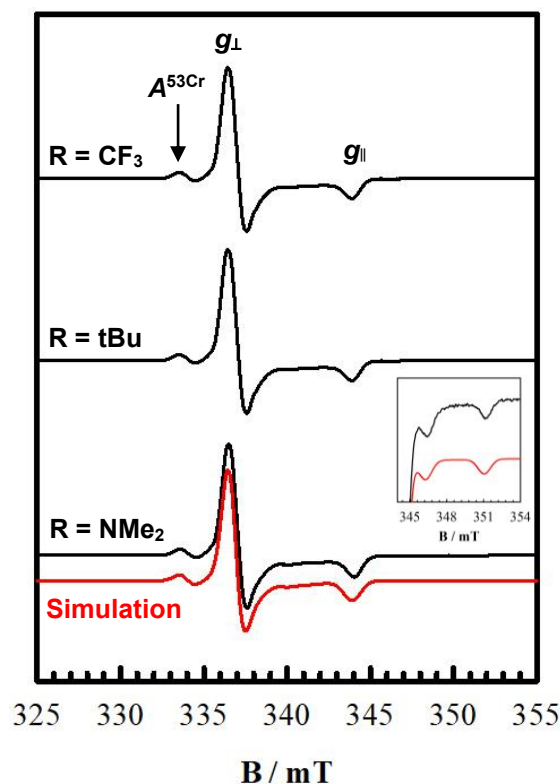


**Figure 2.5.** Low temperature EPR spectrum of **CrNSal<sup>CF3</sup>**, **CrNSal<sup>tBu</sup>**, and **CrNSal<sup>NMe2</sup>** in dichloromethane. Fitted parameter values are identical for all compounds:  $g_{\perp} = 1.992$ ,  $A^{53\text{Cr}} = 53$  MHz;  $g_{\parallel} = 1.950$ ,  $A^{53\text{Cr}} = 130$  MHz. Inset corresponds to a zoomed in region of the high-field signals that contain the resolved Cr hyperfine interactions to the  $g_{\parallel}$ . Conditions: 0.33 mM complex; 0.1 M TBAP; freq. = 9.387 GHz; power = 2.0 mW; mod. freq. = 100 kHz; mod. amp. = 6 GHz; T = 77 K.

## 2.2.4. Electronic Absorption Spectroscopy

UV-vis absorption spectroscopy was used to further probe the ground state electronic structure. Figure 2.6 depicts the absorption spectra for the three derivatives. Similar spectral features are observed and are typical of a  $d^1$  Cr(V) complex in a square pyramidal geometry.<sup>221,233</sup> The intense transition at high energy exhibits R group dependence (Table 2.2, energy of transition decreases in the order  $\text{CF}_3 > \text{tBu} > \text{NMe}_2$ ). This is consistent with ligand to metal charge transfer (LMCT) character due to the influence of R-group electronics on the corresponding ligand orbital energy. The increased electron-withdrawing ability of the  $\text{CF}_3$  substituent is a key factor in facilitating the stabilization of the ligand orbital energy in comparison to the tBu and  $\text{NMe}_2$  derivatives. A similar trend was observed for a series of Mn nitride complexes employing the same salen ligands.<sup>181</sup>

The energy of the weak transition (Fig. 2.6 inset) at  $18,000\text{ cm}^{-1}$  does not appear to exhibit R-group dependence. This is consistent with a Laporte forbidden  $d \rightarrow d$  transition ( $\epsilon \sim 300\text{ M}^{-1}\text{cm}^{-1}$ ) from the non-bonding  $d_{xy}$  into empty  $d_{xz}$  or  $d_{yz} \pi^*$  orbitals.<sup>228</sup> The transition can only be observed for **CrNSal**<sup>CF<sub>3</sub></sup> and **CrNSal**<sup>tBu</sup>. The **CrNSal**<sup>NMe<sub>2</sub></sup> LMCT band described above is relatively broad and lower in energy in comparison to the tBu and  $\text{CF}_3$  derivatives. Thus, this feature likely obstructs detection of the  $d \rightarrow d$  band for **CrNSal**<sup>NMe<sub>2</sub></sup>.

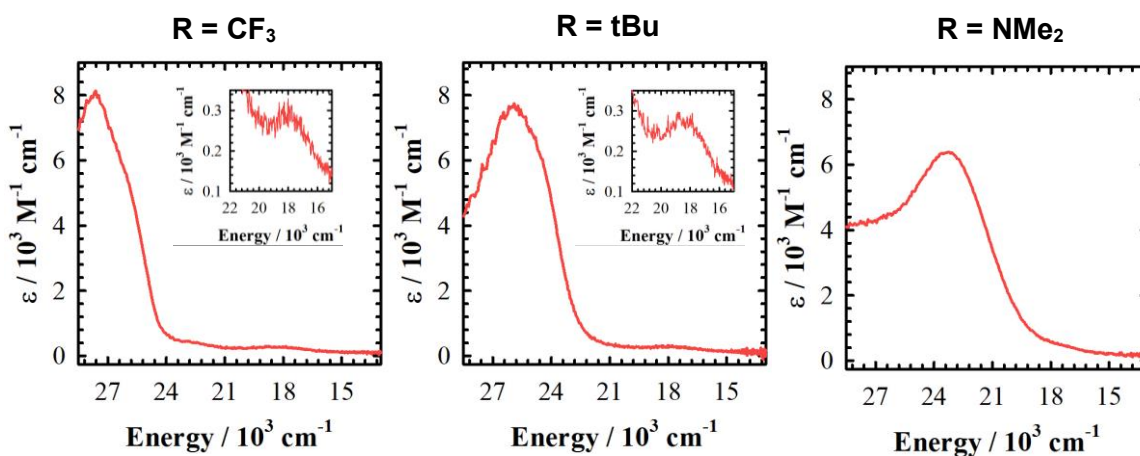


**Figure 2.6.** UV-vis absorption spectra of **CrNSal**<sup>CF<sub>3</sub></sup>, **CrNSal**<sup>tBu</sup> and **CrNSal**<sup>NMe<sub>2</sub></sup>. Inset: observable  $d \rightarrow d$  transitions. The **CrNSal**<sup>NMe<sub>2</sub></sup>  $d \rightarrow d$  transition is likely hidden by the LMCT band. Conditions: 0.45 mM complex; T = 298 K;  $\text{CH}_2\text{Cl}_2$ .

**Table 2.2.** Spectroscopic properties of **CrNSal<sup>CF3</sup>**, **CrNSal<sup>tBu</sup>** and **CrNSal<sup>NMe2</sup>**.

Complex	$\lambda_{\text{max}} / 10^3 \text{ cm}^{-1}$ ( $\epsilon / 10^3 \text{ M}^{-1} \text{ cm}^{-1}$ )
<b>CrNSal<sup>CF3</sup></b>	27.5 (8.1), 18.0 (0.3)
<b>CrNSal<sup>tBu</sup></b>	25.5 (7.8), 18.0 (0.3)
<b>CrNSal<sup>NMe2</sup></b>	23.3 (6.4)

## 2.2.5. Theoretical Analysis

Theoretical analysis using density functional theory (DFT) were employed to visualize orbital contributions to the  $S = \frac{1}{2}$  electronic ground state and characterize spin density (SD). Analysis of the singularly occupied molecular orbital (SOMO) of **CrNSal<sup>tBu</sup>** (Fig. 2.7A) depicts a predominant  $d_{xy}$  contribution and is non-bonding with respect to the nitride. Additionally, the SD plot (Fig. 2.7B) predicts significant spin localization on the metal (ca. 1.45) and a degree of negative spin on the nitride (ca. -0.43). These values do not appear to be influenced by *para*-R group and identical SOMO and SD plots are obtained for **CrNSal<sup>CF3</sup>** and **CrNSal<sup>NMe2</sup>**. Furthermore, the predicted metrical parameters were found to be in good agreement with experimental structural data (Table 2.3).

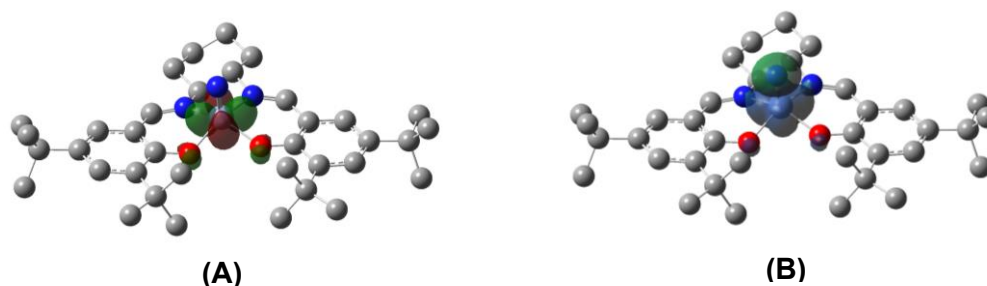


**Figure 2.7.** DFT-generated plots for **CrNSal<sup>tBu</sup>**. **(A)** Visualization of the  $d_{xy}$  SOMO. **(B)** Spin density plot. Nitride Cr SD values: R = CF<sub>3</sub>: -0.431, R = tBu: -0.427, R = NMe<sub>2</sub>: -0.425. Cr SD values: : R = CF<sub>3</sub>: 1.454, R = tBu: 1.448, R = NMe<sub>2</sub>: 1.444. See Appendix A – Fig. A2 & A3 for SOMO and SD plots of **CrNSal<sup>CF3</sup>** and **CrNSal<sup>NMe2</sup>**.

**Table 2.3.** Calculated and experimental (in parentheses) coordination sphere metrical parameters for complexes in Å.

Compound	Cr1-O1	Cr1-O2	Cr1-N1	Cr1-N2	Cr1-N3	O1-C1	O2-C2
<b>CrNSal<sup>CF3</sup></b>	1.927	1.936	2.028	2.037	1.521	1.309	1.310
<b>CrNSal<sup>tBu</sup></b>	1.922 (1.909)	1.930 (1.898)	2.029 (2.008)	2.038 (2.019)	1.524 (1.549)	1.316 (1.314)	1.316 (1.307)
<b>CrNSal<sup>NMe2</sup></b>	1.919 (1.911)	1.928 (1.906)	2.029 (2.013)	2.038 (2.004)	1.525 (1.544)	1.317 (1.305)	1.318 (1.323)

## 2.3. Discussion and Summary

Synthesis of the three nitrido Cr complexes was accomplished by employing N-atom transfer from MnNSalen to CrCl<sub>3</sub>(THF)<sub>3</sub>, followed by coordination of the derivatized H<sub>2</sub>Sal<sup>R</sup> ligand to the {Cr≡N}<sup>2+</sup> unit. This was found to be the highest yielding approach with respect to the salen ligand. Photolysis afforded comparatively low yields (for example 82 % *via* N-transfer versus 11 % *via* photolysis for **CrNSal<sup>tBu</sup>**) and required preparation of azide precursors from chloride derivatives. The mild conditions and rapid rate with which the N-transfer pathway proceeds makes this procedure highly appealing. Facile transfer of the nitride moiety from Mn to Cr is reflective of the enhanced stability of early transition metal nitrides over later transition metal analogues, and likely serves as a thermodynamic driving force. Additionally, the insolubility of the Mn(III) chloride by-product favours product formation.

Characterization by UV-vis absorption spectroscopy, X-ray crystallography and electron paramagnetic resonance confirmed the formation of the complexes. High energy transitions in the absorption spectra were found to exhibit R-group dependence consistent with a LMCT transition. The  $S = \frac{1}{2}$  electronic ground state was confirmed by EPR spectroscopy and yielded  $g$  values and splitting patterns that were accounted for in simulations. Density functional theory gave metrical parameters that were in good agreement with experimental X-ray data. Visualization of the SOMO revealed that this orbital is  $d_{xy}$  in character, as expected based on the MO description for the isoelectronic Vanadyl complex by Gray.<sup>29</sup>

Overall, this chapter details the preparation and characterization of **CrNSal**<sup>CF<sub>3</sub></sup>, **CrNSal**<sup>tBu</sup> and **CrNSal**<sup>NMe<sub>2</sub></sup>. The influence of *para*-R group electronics on the locus of oxidation and reactivity of 1-electron oxidized complexes are studied in subsequent chapters.

## 2.4. Experimental

### 2.4.1. Materials

All chemicals were of the highest quality grade and purified whenever necessary. The ligands H<sub>2</sub>Sal<sup>NMe</sup>, H<sub>2</sub>Sal<sup>tBu</sup>, H<sub>2</sub>Sal<sup>CF<sub>3</sub></sup> were synthesized following literature procedures.<sup>179,180</sup> The atom-transfer reagents MnNSalen and CrCl<sub>3</sub>(THF)<sub>3</sub> were also prepared according to published protocols.<sup>236,237</sup> Dichloromethane and acetonitrile were dried by refluxing over calcium hydride and distilled prior to use.

### 2.4.2. Synthesis

*Preparation of {Cr≡N}<sup>2+</sup> solution:* To a purple solution of 0.150 g CrCl<sub>3</sub>(THF)<sub>3</sub> (0.40 mmol) in 2 mL dry acetonitrile was added 0.134 g (0.40 mmol) solid green MnNSalen, which resulted in an instant colour change to dark-brown with the precipitation of Mn(Cl)Salen. The solution was stirred under nitrogen at room temperature for 1 hour and subsequently stirred under air for 1 hour. The solution was then filtered to remove brown Mn(Cl)Salen in quantitative yield. The resulting yellow-brown filtrate contains the {Cr≡N}<sup>2+</sup> fragment (**Sol. A**) used in further preparations as outlined below.

*Synthesis of CrNSal<sup>NMe<sub>2</sub></sup>:* A yellow solution of 0.208 g H<sub>2</sub>Sal<sup>NMe<sub>2</sub></sup> (0.40 mmol) in 2 mL acetonitrile containing a few drops of triethylamine was added to **Sol. A**. The resulting mixture was refluxed for 5 hours upon which the solution turned dark orange. The solvent was removed *in vacuo* and the crude product was purified by silica gel column chromatography using a 1% solution of Et<sub>3</sub>N in dichloromethane (R<sub>f</sub> 0.45) to obtain **CrNSal**<sup>NMe<sub>2</sub></sup> as a dark orange powder. Yield 0.194 g (0.33 mmol, 83%). ESI-MS *m/z*: 585.32 {M+H<sup>+</sup>} 100%. Anal. Calcd (%) C<sub>32</sub>H<sub>46</sub>CrN<sub>5</sub>O<sub>2</sub>: C 65.73, H 7.93, N 11.98; Found (%): C 65.47 H 7.53, N 11.91.  $\mu_{\text{eff}} = 1.70$  (Evans method).

*Synthesis of **CrNSal<sup>tBu</sup>***: A yellow solution of 0.219 g H<sub>2</sub>Sal<sup>tBu</sup> (0.40 mmol) in 2 mL acetonitrile containing a few drops of triethylamine was added to **Sol. A** and refluxed for 5 hours upon which the solution turned black. The solvent was removed *in vacuo* and the crude product was purified by silica gel column chromatography using a 1:1 mixture of hexanes and dichloromethane as the eluent (*R<sub>f</sub>* 0.4). **CrNSal<sup>tBu</sup>** was isolated as a yellow-brown powder. Yield 0.195 g (0.32 mmol, 80%). ESI-MS *m/z*: 611.36 {M+H<sup>+</sup>} 100%. Anal. Cald (%) C<sub>36</sub>H<sub>52</sub>CrN<sub>3</sub>O<sub>2</sub>: C 70.79, H 8.58, N 6.80; Found (%): C 70.70, H 8.64, N 6.92.  $\mu_{\text{eff}}$  = 1.71 (Evans method).

*Synthesis of **CrNSal<sup>CF3</sup>***: A yellow solution of 0.228 g H<sub>2</sub>Sal<sup>CF3</sup> (0.33 mmol) in 2 mL acetonitrile containing a few drops of triethylamine was added to **Sol. A** and refluxed for 5 hours upon which the solution turned dark red. The solvent was removed *in vacuo* and the crude product was purified by silica gel column chromatography using a 1:1 mixture of hexanes and dichloromethane as the eluent (*R<sub>f</sub>* 0.5). **CrNSal<sup>CF3</sup>** was isolated as a rose-gold powder. Yield 0.190 g (0.30 mmol, 75%). ESI-MS *m/z*: 635.21 {M+H<sup>+</sup>} 100%. Anal. Cald (%) C<sub>30</sub>H<sub>34</sub>CrF<sub>6</sub>N<sub>3</sub>O<sub>2</sub>: C 56.78, H 5.40, N 6.62; Found (%): C 56.21, H 5.96, N 6.39.  $\mu_{\text{eff}}$  = 1.68 (Evans method).

### 2.4.3. Instrumentation

Electronic spectra were obtained using a Cary 5000 spectrophotometer. Mass spectrometry (ESI positive mode) was performed on an Agilent 6210 TOF ESI-MS system. Nuclear magnetic resonance (NMR) for magnetic susceptibility *via* Evan's Method was carried out on a Bruker AVANCE III 500 MHz instrument. Elemental analysis (C, H, N) were performed by Mr. Paul Mulyk at Simon Fraser University on a Carlo Erba EA1110 CHN elemental analyser. All electron paramagnetic resonance (EPR) were recorded on a Bruker EMXplus spectrometer operating with a premium X-band microwave bridge and an HS resonator. EPR spectra were simulated using the EasySpin package in Matlab.<sup>238</sup>

### 2.4.4. X-ray Structure Determination

Single-crystal X-ray crystallographic analysis of a block-brown **CrNSal<sup>tBu</sup>** or block-orange **CrNSal<sup>NMe2</sup>** crystal were performed on a Bruker APEX II Duo diffractometer with graphite monochromated Cu K $\alpha$  radiation. The crystals were mounted on a 150  $\mu$ m MiteGen sample holder. The data were collected at 293 K to a maximum 2 $\theta$  of 50°. Data

were collected in a series of  $\varphi$  and  $\omega$  scans in 0.5°-1.0° widths with 10.0 – 60.0 s exposures. The crystal-to-detector distance was 40 mm. The structures were solved by intrinsic phasing<sup>239</sup> and subsequent refinements were performed using ShelXle.<sup>240</sup> All non-hydrogen atoms were refined anisotropically. All C—H hydrogen atoms were placed in calculated positions but were not refined.

#### 2.4.5. Theoretical Analysis

Geometry optimizations were performed using the Gaussian 16 program (Revision A.03)<sup>241</sup> employing the B3LYP functional with the 6-31g\* basis set.<sup>242</sup> This combination has provided good theoretical fit to experimental metrical data for a variety of similar salen systems.<sup>172,173,243,244</sup> Frequency calculations performed on the same functional/basis set confirmed optimized structures were at a global minimum. Single point calculations were performed using the B3P86 functional and TZVP basis set of Ahlrichs<sup>245,246</sup> as this functional/basis set combination was determined to predict the change in nitride spin density values upon reaction with Lewis acids (see later chapters).<sup>41</sup> All calculations employed a polarizable continuum model (PCM) for CH<sub>2</sub>Cl<sub>2</sub> ( $\epsilon=8.93$ ) for all atoms.<sup>242,247,248</sup>



## Chapter 3. Oxidation of $\text{CrNSal}^{\text{CF}_3}$ , $\text{CrNSal}^{\text{tBu}}$ and $\text{CrNSal}^{\text{NMe}_2}$ and Electronic Structure Determination

D. Martelino performed the chemical oxidation of compounds, electrochemistry, absorption spectroscopy and theoretical analysis. K. Herasymchuk and G. McNeil collected EPR data for  $\text{CrNSal}^{\text{CF}_3}$  and  $\text{CrNSal}^{\text{tBu}}$ , F. Thomas (Grenoble) collected EPR data for  $\text{CrNSal}^{\text{NMe}_2}$ , and D. Martelino simulated the data.

### 3.1. Introduction

As discussed in previous chapters, the elucidation of electronic structure in metal salen complexes is of considerable interest due to the interesting photophysical properties and potential for noble metal-like reactivity *via* ligand non-innocence.<sup>120,121,123–125</sup> The modulation of *para*-R phenoxide substituents presents a means to tune ligand orbital energies and influence the locus of oxidation. Depending on the electronic structure, this can result in an “electron hole” within the system. Questions as to *where* (ie. ligand radical or high-valent metal) and *to what extent* delocalization occurs across the metal salen scaffold can be investigated. These details can manifest as dramatic differences in spectroscopic and electrochemical properties, and there are a variety of physical and theoretical methods employed in addressing these questions.<sup>249</sup>

Oxidized metal salen complexes can be classified as mixed-valence compounds.<sup>250,251</sup> An archetypical example of a mixed-valence compound is the Creutz-Taube ion which consists of a dinuclear Ru complex bridged by an organic pyrazine linker,  $[\text{((NH}_3)_5\text{Ru)}(\mu\text{-pyz)}(\text{Ru(NH}_3)_5)]^{5+}$  (Fig. 3.1A).<sup>252</sup> The Ru oxidation states are not accurately ascertained by conventional means as the degree of electronic coupling between dinuclear sites dictates the overall electronic structure. The Creutz-Taube ion represents a strongly coupled system, where Ru valencies are averaged ( $\text{M}^{2.5+}\text{-L-M}^{2.5+}$ ) due to complete delocalization of the electronic structure. On the contrary, a scenario with limited electronic coupling results in discrete oxidation states ( $\text{M}^{2+}\text{-L-M}^{3+}$ ). Metal salen complexes represent a reverse case (Fig. 3.1B), where two redox-active phenolate ligands are bridged by a metal ion linker ( $\text{L-M}^{n+}\text{-L}$ ).

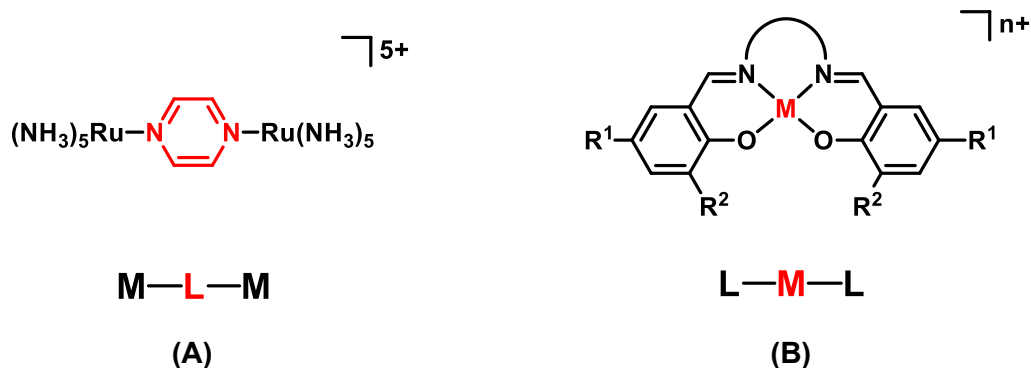


**Figure 3.1.** Examples of mixed-valence systems. **(A)** Creutz-Taube ion. **(B)** An oxidized metal salen complex.

Robin and Day established a classification system for the characterization of mixed-valence compounds.<sup>253</sup> Class I compounds exhibit no electronic communication due to inhibited intervalence charge transfer (IVCT) either by remote separation or the nature of the linker group. Class II compounds have less restricted charge transfer where valencies can interconvert thermally or through electronic excitation. Lastly, Class III compounds are best described as fully delocalized due to strong coupling. The oxidation states within Class III systems are averaged (similar to the Creutz-Taube ion example). Pro-radical salen complexes typically fall between the Class II and III regimes.<sup>111,159</sup> Distinction between a Class II localized or Class III delocalized ligand radical is paramount in characterization. Both cases exhibit IVCT transitions in the near-infrared region (800-2500 nm), and thus UV-vis-NIR (ultraviolet-visible-near-infrared) spectroscopy is routinely employed in the exploration of these systems.<sup>254–256</sup> Hush devised a theoretical model describing IVCT transitions that accounts for characteristic absorption features.<sup>257</sup> Class II compounds exhibit broad and relatively weak IVCT bands ( $\Delta\nu_{1/2} \geq 2000 \text{ cm}^{-1}$ ,  $\epsilon \leq 5000 \text{ M}^{-1} \text{ cm}^{-1}$ ), while Class III compounds exhibit sharp and intense transitions ( $\Delta\nu_{1/2} \leq 2000 \text{ cm}^{-1}$ ,  $\epsilon \geq 5000 \text{ M}^{-1} \text{ cm}^{-1}$ ).<sup>249,258,259</sup>

A variety of other analytical methods provide a wealth of information regarding the electronic structure of metal salen complexes. Electrochemical analysis is employed to probe oxidation and/or reduction events, select a suitable chemical oxidant/reductant, or determine the feasibility of electrolysis. The degree of electronic coupling can also be extrapolated from the electrochemical data, as symmetric valencies with minimal coupling will undergo oxidation at approximately equal potential.<sup>260</sup> On the other hand,

delocalization of the singularly occupied molecular orbital (SOMO) manifests as discrete redox processes.<sup>261–263</sup> Electron paramagnetic resonance (EPR) spectroscopy is also commonly used as it is sensitive to the generation or loss of a paramagnetic species. In addition, EPR is useful in discriminating between a ligand or metal-based oxidation. Ligand radicals will typically exhibit  $g$  values close to that of a free electron ( $g_e = 2.002319$ ) and can be sensitive to metal ion contribution to the SOMO.<sup>184,264</sup> In systems featuring a pre-existing paramagnetic metal ion, the generation of a ligand radical can complicate the analysis due to magnetic coupling.<sup>159,177</sup> Thus, EPR cannot be solely relied upon to draw conclusions about the detailed electronic structure of a system, highlighting the necessity of integrating information from a combination of various methods. Theoretical analysis, such as density functional theory (DFT), can be a powerful supplement to experimental data. Single point energy calculations can aid in rationalizing experimental results as the lowest energy spin state can be predicted, while visualization of the SOMO and spin density plots are useful in assessing spin localization. Time-dependent density functional theory (TD-DFT) analysis can be used to predict donor and acceptor orbitals associated with transitions in an absorption spectrum, especially diagnostic IVCT transitions in the NIR region.

In this chapter, a combination of physical and theoretical methods were employed to characterize electronic structure and investigate the influence of *para*-R substituent electronics on the oxidation of **CrNSal<sup>NMe2</sup>**, **CrNSal<sup>tBu</sup>** and **CrNSal<sup>CF3</sup>**. Experimental findings provide strong evidence for the formation of a ligand radical for strongly electron-donating R-groups (R = NMe<sub>2</sub>), while mildly donating and strongly withdrawing substituents (R = tBu, CF<sub>3</sub>) support formation of a Cr(VI) product.

## 3.2. Electronic Structure Determination

### 3.2.1. Electrochemistry

The redox processes of **CrNSal<sup>CF3</sup>**, **CrNSal<sup>tBu</sup>** and **CrNSal<sup>NMe2</sup>** were probed by cyclic voltammetry (CV) using tetrabutylammonium perchlorate (<sup>n</sup>Bu<sub>4</sub>NClO<sub>4</sub>) as the supporting electrolyte and CH<sub>2</sub>Cl<sub>2</sub> as the solvent. The lowest potential redox processes are reversible at all scan rates studied (10 – 1000 mV s<sup>-1</sup>) and no reduction waves were observed within the electrochemical window for CH<sub>2</sub>Cl<sub>2</sub> (Fig. 3.2 & Table 3.1). **CrNSal<sup>NMe2</sup>** displays two overlapping redox events that are difficult to resolve by CV. Scanning to

higher potentials reveals a third quasi-reversible redox process (Appendix B – Fig. B1). The first redox process for **CrNSal**<sup>tBu</sup> occurs at  $E_{1/2} = 0.61$  V. Scanning to higher potential reveals a second quasi-reversible process at  $E_{1/2} = 1.1$  V (Appendix B – Fig. B1). The voltammogram of **CrNSal**<sup>CF<sub>3</sub></sup> is similar to that of **CrNSal**<sup>tBu</sup> and features a single quasi-reversible redox process at  $E_{1/2} = 0.87$  V. This species exhibits a first redox process with the highest potential among the three derivatives due to the strong electron withdrawing nature of the CF<sub>3</sub> substituent. Scanning to higher potentials does not reveal additional redox processes within the scan window for CH<sub>2</sub>Cl<sub>2</sub>. In all, the oxidation potentials for the complexes are tunable by *ca.* 1V, demonstrating the profound effect of *para*-R electronics.

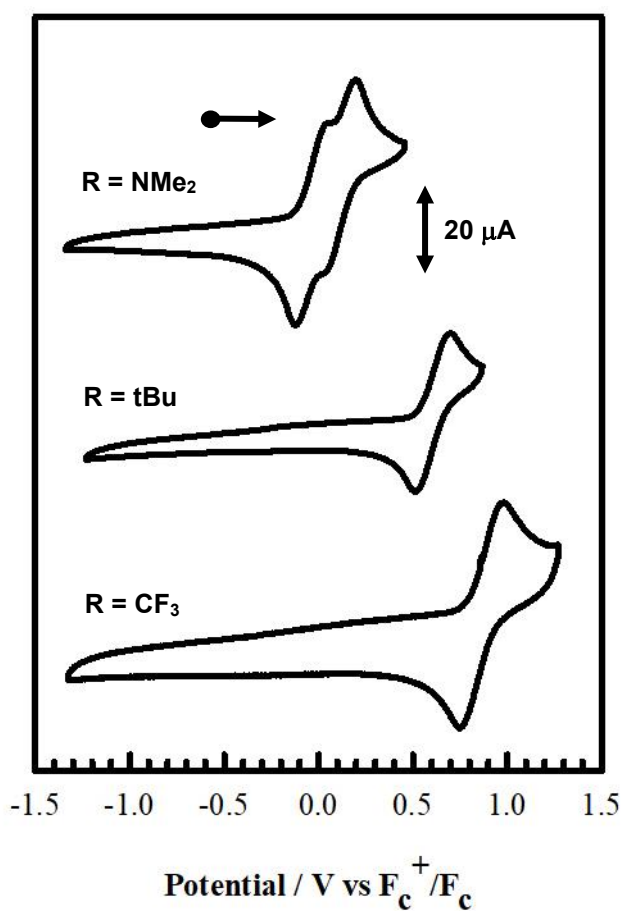


**Figure 3.2.** Cyclic voltammogram of **CrNSal**<sup>NMe<sub>2</sub></sup>, **CrNSal**<sup>tBu</sup> and **CrNSal**<sup>CF<sub>3</sub></sup>. Only the 1<sup>st</sup> redox wave is shown for tBu and CF<sub>3</sub> derivatives. Conditions: 1.0 mM complex; 0.1 M <sup>n</sup>Bu<sub>4</sub>NClO<sub>4</sub>; scan rate: 100 mV/s; T = 298 K; CH<sub>2</sub>Cl<sub>2</sub>.

**Table 3.1.** Redox potentials for complexes versus  $F_c^+/F_c$ .<sup>a,b</sup>

Compound	$E_{pa}^1$	$E_{pc}^1$	$E_{1/2}^1$	$E_{pa}^2$	$E_{pc}^2$	$E_{1/2}^2$
<b>CrNSal</b> <sup>NMe2</sup>	0.05	-0.12	-0.04 (0.17)	0.20	0.03	0.12 (0.17)
<b>CrNSal</b> <sup>tBu</sup>	0.70	0.51	0.61 (0.19)	--	--	--
<b>CrNSal</b> <sup>CF3</sup>	0.98	0.75	0.87 (0.23)	--	--	--

<sup>a</sup>Given in volts, peak-to-peak separation given in parenthesis. <sup>b</sup>Peak-to-peak separation for  $F_c^+/F_c$  couple at 298 K is 0.13 V. Redox waves were determined to be a 1-electron process by comparison of complex peak area to the peak area from 1-equivalent decamethylferrocene added.

Differential pulse voltammetry (DPV) was used to resolve the 1<sup>st</sup> and 2<sup>nd</sup> redox processes for **CrNSal**<sup>NMe2</sup> where a potential difference ( $\Delta E_{ox}$ ) of 160 mV was observed (Fig. 3.3A). Similar values have been reported by the Storr group for salen complexes employing the NMe<sub>2</sub> substituent for metal centres including Ni,<sup>180</sup> Mn nitride<sup>181</sup> and uranyl (UO<sub>2</sub>).<sup>184</sup> These features have been unambiguously assigned as sequential oxidations of both phenolate moieties. Interestingly, the voltammogram of **CrNSal**<sup>NMe2</sup> bears a striking resemblance to the voltammogram of the Mn analogue **MnNSal**<sup>NMe2</sup> (Fig. 3.3B).<sup>181</sup> These similarities provide strong evidence that the oxidations of **CrNSal**<sup>NMe2</sup> are both ligand-centred, affording [**Cr**<sup>V</sup>**NSal**<sup>NMe2</sup>]<sup>•+</sup> as the first oxidation product, matching the assignment for the Mn analogue using a number of experimental and theoretical techniques.

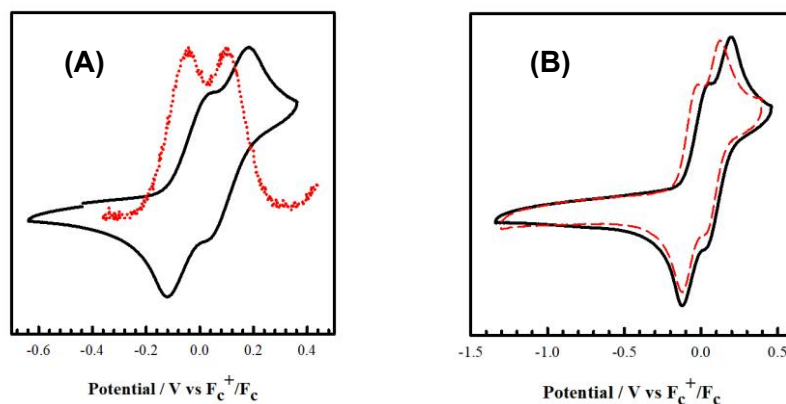


**Figure 3.3.** (A) 1<sup>st</sup> and 2<sup>nd</sup> redox waves for **CrNSal**<sup>NMe2</sup> (black) resolved by DPV (red). (B) Comparison of **CrNSal**<sup>NMe2</sup> (black) and **MnNSal**<sup>NMe2</sup> (red).<sup>181</sup> Conditions: 1.0 mM complex; 0.1 M <sup>n</sup>Bu<sub>4</sub>NClO<sub>4</sub>; scan rate: 100 mV/s; T = 298 K; CH<sub>2</sub>Cl<sub>2</sub>.

The  $\Delta E_{\text{ox}}$  value of 160 mV suggests limited electronic coupling between redox-active phenolate centres in-line with the previous reports.<sup>180,181,184</sup> The relatively small value is consistent with a Class II mixed-valence compound with significant radical localization. The stability of  $[\text{Cr}^{\text{V}}\text{NSal}^{\text{NMe}_2}]^{\bullet+}$  with respect to disproportionation can also be calculated using  $\Delta E_{\text{ox}}$ . Under the present conditions, the monocation  $[\text{Cr}^{\text{V}}\text{NSal}^{\text{NMe}_2}]^{\bullet+}$  can disproportionate to neutral  $\text{CrNSal}^{\text{NMe}_2}$  and the diradical  $[\text{Cr}^{\text{V}}\text{NSal}^{\text{NMe}_2}]^{\bullet\bullet 2+}$  as shown in Equation 1, where L represents a phenolate group and M is the metal centre. The comproportionation equilibrium constant  $K_c$  expressed in Equation 2 can be measured electrochemically using Equation 3.<sup>249,265</sup> The  $\Delta E_{\text{ox}}$  value of 160 mV affords a small  $K_c$  value of ca. 340 at 298 K. Using this value, a solution of mono-oxidized complex is calculated to be ~90%  $[\text{Cr}^{\text{V}}\text{NSal}^{\text{NMe}_2}]^{\bullet+}$ , ~5%  $\text{CrNSal}^{\text{NMe}_2}$  and ~5%  $[\text{Cr}^{\text{V}}\text{NSal}^{\text{NMe}_2}]^{\bullet\bullet 2+}$ .



$$K_c = \frac{[\text{LML}^{\bullet+}]^2}{[\text{LML}][\text{L}^{\bullet+}\text{ML}^{\bullet+}]} \quad (2)$$

$$K_c = \exp\left(\frac{\Delta E_{\text{ox}} F}{RT}\right) \quad (3)$$

The voltammograms of  $\text{CrNSal}^{\text{tBu}}$  and  $\text{CrNSal}^{\text{CF}_3}$  do not exhibit overlapping oxidation processes in contrast to  $\text{CrNSal}^{\text{NMe}_2}$ . Additionally, the 1<sup>st</sup> oxidation potentials are significantly higher in comparison to  $\text{MnNSal}^{\text{tBu}}$  and  $\text{MnNSal}^{\text{CF}_3}$  analogues (Fig. 3.4A & 3.4B) highlighting the effect of the metal ion. The 1<sup>st</sup> redox events in the Mn voltammograms have been attributed to the Mn(V)/Mn(VI) redox couple and are irreversible due to rapid N—N homocoupling.<sup>181</sup> Herein, the  $\text{CrNSal}^{\text{tBu}}$  and  $\text{CrNSal}^{\text{CF}_3}$  redox waves are best assigned as the Cr(V)/Cr(VI) couple affording  $[\text{Cr}^{\text{VI}}\text{NSal}^{\text{tBu}}]^+$  and  $[\text{Cr}^{\text{VI}}\text{NSal}^{\text{tBu}}]^+$  respectively upon oxidation. The reversibility of the Cr(V)/Cr(VI) redox process for the Cr complexes is likely due to the enhanced stability of early transition metal nitride complexes in comparison to later transition metal analogues. It unlikely that these redox features are associated with ligand-based oxidations. A large  $\Delta E_{\text{ox}}$  value (0.49 V for  $\text{CrNSal}^{\text{tBu}}$ , 2<sup>nd</sup> oxidation of  $\text{CrNSal}^{\text{CF}_3}$  falls outside the electrochemical window) would suggest significant phenoxide-phenoxyl electronic coupling.<sup>179</sup> Indeed, parallel electronic

absorption experiments do not provide evidence for the presence of a Class III mixed-valence compound (see Section 3.2.2).

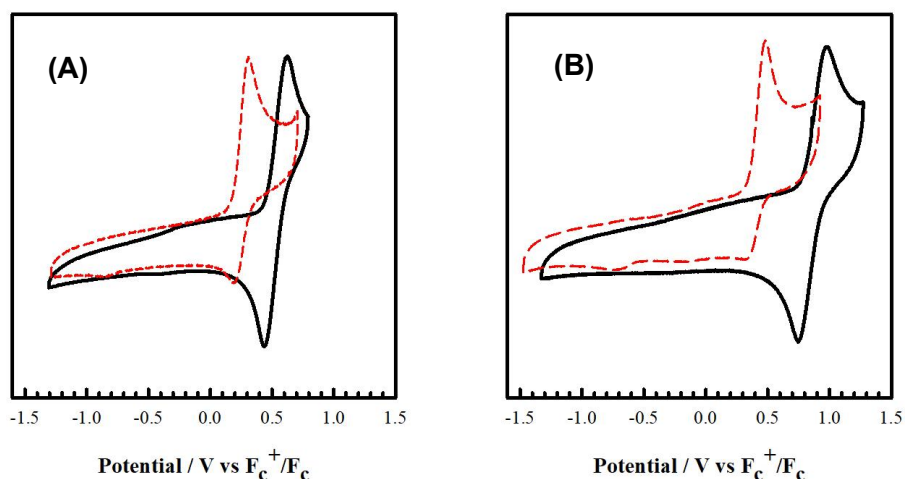


**Figure 3.4.** (A) Comparison of **CrNSal<sup>tBu</sup>** (black) and **MnNSal<sup>tBu</sup>** (red)<sup>181</sup> by CV. (B) Comparison of **CrNSal<sup>CF3</sup>** (black) and **MnNSal<sup>CF3</sup>** (red)<sup>181</sup> by CV. Conditions: 1.0 mM complex; 0.1 M <sup>n</sup>Bu<sub>4</sub>NClO<sub>4</sub>; scan rate: 100 mV/s; T = 298 K; CH<sub>2</sub>Cl<sub>2</sub>.

### 3.2.2. Electronic Absorption Spectroscopy

The high redox potential of **CrNSal<sup>CF3</sup>** (0.87 V vs. Fc<sup>+</sup>/Fc) required use of a strong chemical oxidant in order to further study the oxidized form. Tris(2,4-dibromophenyl)aminium hexafluoroantimonate ([N(C<sub>6</sub>H<sub>3</sub>Br<sub>2</sub>)<sub>3</sub>]<sup>+</sup>[SbF<sub>6</sub>]<sup>-</sup>) was selected for this purpose due to its high oxidizing potential (1.1 V vs Fc<sup>+</sup>/Fc)<sup>266</sup> and solubility in CH<sub>2</sub>Cl<sub>2</sub>. The oxidation of all three Cr complexes was monitored *via* UV-vis-NIR spectroscopy by titration with a saturated solution of oxidant until 1 equivalent was added. The oxidation of **CrNSal<sup>CF3</sup>** and **CrNSal<sup>tBu</sup>** is depicted in Figure 3.5 and features a decrease in the intensity of the high energy charge transfer band of the neutral complexes with concomitant appearance of lower energy absorbances (Table 3.2). Well defined isosbestic points indicate clean product formation. Similar spectral features are reported for the **[Mn<sup>VI</sup>NSal<sup>CF3</sup>]<sup>+</sup>** and **[Mn<sup>VI</sup>NSal<sup>tBu</sup>]<sup>+</sup>** versions, which contain low energy transitions at 11,600 and 9,300 cm<sup>-1</sup> respectively characterized as ligand-to-metal charge transfer (LMCT) events into the singularly occupied Mn(VI) *d<sub>xy</sub>* orbital.<sup>181</sup>

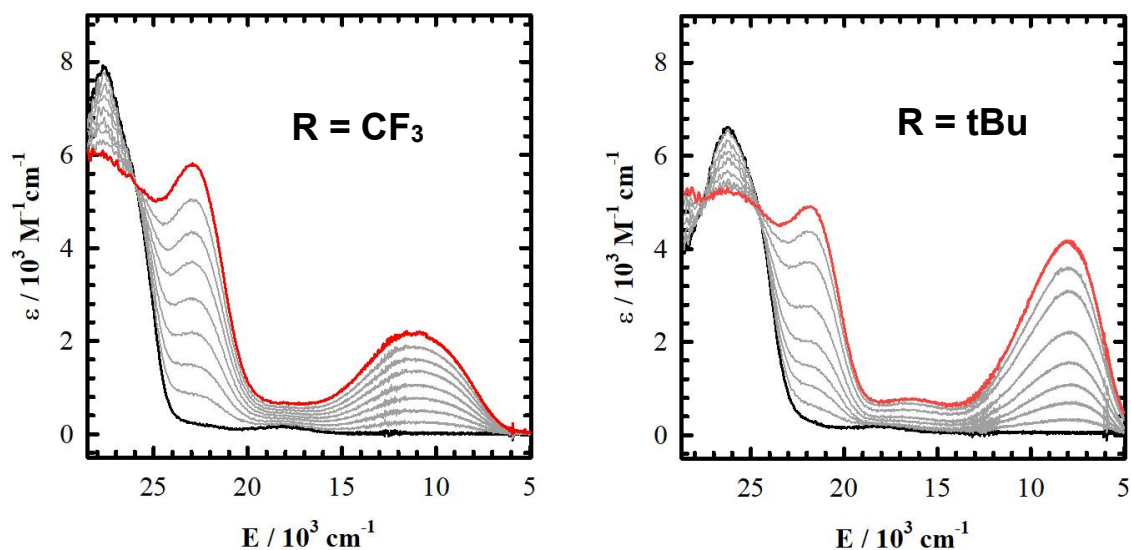


**Figure 3.5.** Chemical oxidation of **CrNSal<sup>CF<sub>3</sub></sup>** and **CrNSal<sup>tBu</sup>** using  $[\text{N}(\text{C}_6\text{H}_3\text{Br}_2)_3]^+[\text{SbF}_6]^-$  monitored by UV-vis-NIR spectroscopy. Black: neutral; red: oxidized. Intermediate grey lines represent increasing aliquots of oxidant added until 1 equivalent was reached. Conditions: 0.45 mM complex;  $T = 233 \text{ K}$ ;  $\text{CH}_2\text{Cl}_2$ . Analysis of the red band over time indicated minimal changes at  $T = 233 \text{ K}$ , further demonstrating the stability of oxidized complexes in solution.

The spectral similarities between Mn and Cr derivatives support a metal-based  $\text{Cr(V)} \rightarrow \text{Cr(VI)}$  oxidation affording **[Cr<sup>VI</sup>NSal<sup>CF<sub>3</sub></sup>]<sup>+</sup>** and **[Cr<sup>VI</sup>NSal<sup>tBu</sup>]<sup>+</sup>**. This assignment is corroborated by noting the relative energy of low energy absorption band (Energy  $\text{R} = \text{CF}_3 > \text{tBu}$ ). A blue-shift is expected upon modulation of tBu to  $\text{CF}_3$  due to the electron withdrawing ability of this substituent. It is unlikely that this transition is associated with a ligand radical-based transition. Electrochemical measurements discussed in Section 3.2.1 effectively rule out a localized regime, however it cannot rule out the possibility of a Class III delocalized ligand radical. Class III complexes contain sharp and intense ( $\Delta\nu_{1/2} \leq 2000 \text{ cm}^{-1}$ ,  $\epsilon \geq 5000 \text{ M}^{-1} \text{ cm}^{-1}$ ) NIR transitions that are a key diagnostic feature in the characterization of these complexes.<sup>249,257–259</sup> Indeed, analysis of the lowest energy transitions in the oxidized spectra do not fit the criteria for such a species (Table 3.2).



The spectral features for the oxidized **CrNSal<sup>NMe2</sup>** complex suggest a different electronic structure when compared to electron deficient derivatives (Fig. 3.6). Reduction of the high energy charge transfer band at 23,300 cm<sup>-1</sup> of the neutral species alongside the formation of an envelope of new transitions (Fig. 3.6, Table 3.2) and isosbestic points indicate clean product formation. In particular, the broad and low intensity absorbance centred at 11,500 cm<sup>-1</sup> ( $\epsilon \sim 1000 \text{ M}^{-1}\text{cm}^{-1}$ ) fits the criteria for a Class II IVCT.<sup>249,258,259</sup> Similar spectral features have been reported for other localized phenoxyl radical-containing metal salen complexes that employ the same ligand.<sup>180,181,184</sup> Furthermore, the addition of over 1 equivalent of oxidant causes this feature to decay (Appendix B – Fig. B2). These findings are consistent with the assignment of a ligand-oxidized electronic structure to form **[Cr<sup>V</sup>NSal<sup>NMe2</sup>]<sup>•+</sup>**.

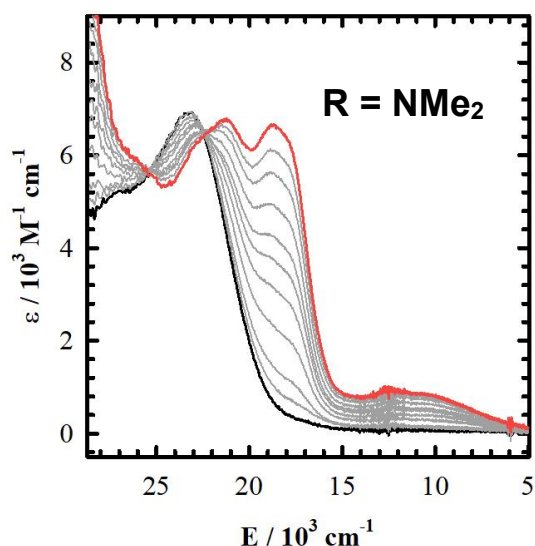


**Figure 3.6.** Chemical oxidation of **CrNSal<sup>NMe2</sup>** monitored by UV-vis-NIR spectroscopy. Black: neutral; red: oxidized. Intermediate grey lines represent increasing aliquots of oxidant added until 1 equivalent was reached. Conditions: 0.45 mM complex; T = 233 K; CH<sub>2</sub>Cl<sub>2</sub>. Analysis of the red band over time indicated minimal changes at T = 233 K, further demonstrating the stability of oxidized complex in solution.

**Table 3.2.** Spectroscopic properties of oxidized Cr complexes.

Complex	$\lambda_{\text{max}} / 10^3 \text{ cm}^{-1}$ ( $\epsilon / 10^3 \text{ M}^{-1} \text{ cm}^{-1}$ )	$\Delta\nu_{1/2}$ low energy transition / cm <sup>-1</sup>
<b>[Cr<sup>VI</sup>NSal<sup>CF3</sup>]<sup>+</sup></b>	23.0 (5.8), 11.0 (2.2)	6700
<b>[Cr<sup>VI</sup>NSal<sup>tBu</sup>]<sup>+</sup></b>	21.9 (5.0), 8.1 (4.15)	4900
<b>[Cr<sup>V</sup>NSal<sup>NMe2</sup>]<sup>•+</sup></b>	21.3 (6.8), 18.8 (6.8), 11.5 (1.0)	8700

### 3.2.3. Electron Paramagnetic Resonance Spectroscopy

The oxidized Cr complexes were analyzed by continuous wave X-band electron paramagnetic resonance (EPR) to further characterize electronic structure. A sample of **CrNSal**<sup>CF<sub>3</sub></sup> for EPR analysis was chemically oxidized using the radical oxidant [N(C<sub>6</sub>H<sub>3</sub>Br<sub>2</sub>)<sub>3</sub>]<sup>•+</sup> due to the high redox potential of this derivative (0.87 V vs. F<sub>c</sub><sup>+</sup>/F<sub>c</sub>). The milder potentials of **CrNSal**<sup>tBu</sup> and **CrNSal**<sup>NMe<sub>2</sub></sup> (0.61 and -0.04 V vs. F<sub>c</sub><sup>+</sup>/F<sub>c</sub> respectively) allowed for bulk electrolysis which afforded cleaner oxidation. EPR analysis of electrolyzed samples were also free of residual unreacted [N(C<sub>6</sub>H<sub>3</sub>Br<sub>2</sub>)<sub>3</sub>]<sup>•+</sup> signals. The EPR spectra of the neutral and oxidized complexes are depicted in Figure 3.7. Oxidation of **CrNSal**<sup>CF<sub>3</sub></sup> and **CrNSal**<sup>tBu</sup> resulted in an almost total loss of the EPR signal (ratio of doubly integrated signals of oxidized vs. neutral complex R = CF<sub>3</sub>: 5 %; tBu 2 %). The residual signals in these species are likely due to unoxidized starting material. The central feature in the oxidized **CrNSal**<sup>CF<sub>3</sub></sup> spectrum is likely due to unreacted [N(C<sub>6</sub>H<sub>3</sub>Br<sub>2</sub>)<sub>3</sub>]<sup>•+</sup>. Interestingly, oxidation of **CrNSal**<sup>NMe<sub>2</sub></sup> also leads to a significant loss of signal but still exhibits a considerable amount of spin active species (ratio of doubly integrated signal of oxidized vs. neutral complex R = NMe<sub>2</sub>: 20 %).

As discussed in Chapter 2, the EPR spectra of neutral versions unambiguously describe the Cr(V) *d*<sup>1</sup> (*S* = ½) electronic ground state. Loss of this signal upon oxidation can be due to one of three reasons.<sup>159,177,267</sup> The first and most straightforward case is the generation of diamagnetic *d*<sup>0</sup> Cr(VI).<sup>268</sup> The second possibility is a triplet species (*S* = 1) with ferromagnetic coupling between the ligand radical and electron in the *d*<sub>xy</sub> orbital. Consequently, this system can exhibit a large zero-field splitting (ZFS) component affording EPR transitions outside the X-band measurement window.<sup>161,269,270</sup> The third case is the generation of an open-shell singlet species (*S* = 0) due to antiferromagnetic coupling of the phenoxyl radical and the Cr(V) *d*<sup>1</sup> metal ion.<sup>158,271</sup> The evidence obtained from the experimental data discussed in previous sections suggests that oxidation of the complexes affords [**Cr<sup>VI</sup>NSal**<sup>CF<sub>3</sub></sup>]<sup>+</sup>, [**Cr<sup>VI</sup>NSal**<sup>tBu</sup>]<sup>+</sup> and [**Cr<sup>V</sup>NSal**<sup>NMe<sub>2</sub></sup>]<sup>•+</sup> (*S* = 0 or 1) which can all be EPR silent. The relative intensities of residual spin active species in the EPR spectra of Cr complexes suggest that there are key differences in the oxidation of **CrNSal**<sup>NMe<sub>2</sub></sup> relative to tBu and CF<sub>3</sub> derivatives.

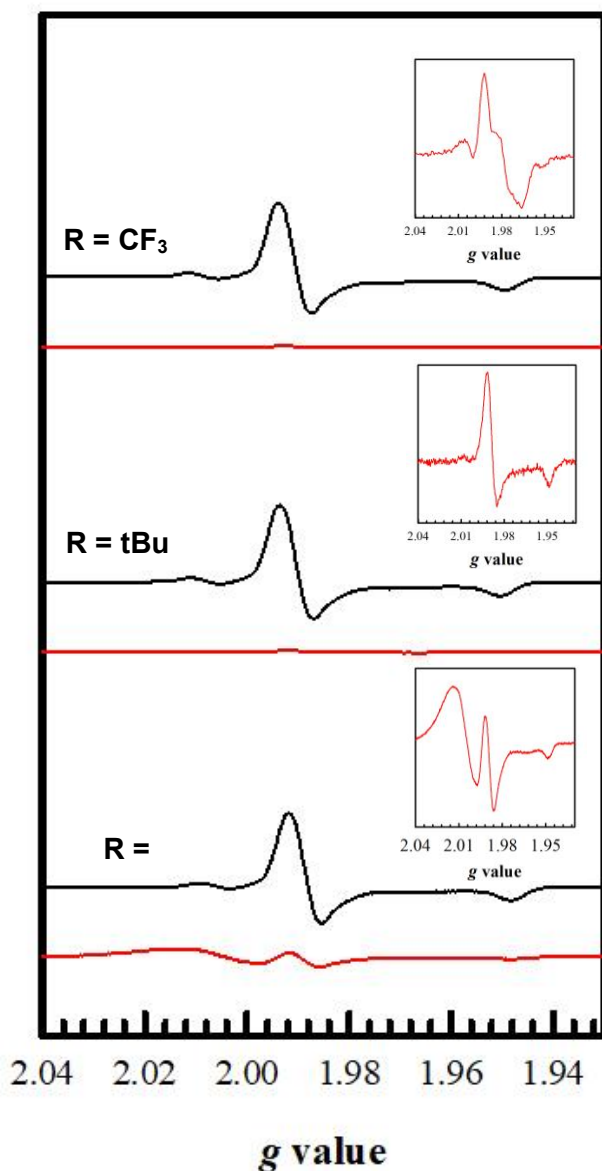


**Figure 3.7.** Frozen solution EPR spectra of concentration-matched neutral (black) and oxidized samples (red) of **CrNSal**<sup>CF<sub>3</sub></sup>, **CrNSal**<sup>tBu</sup> and **CrNSal**<sup>NMe<sub>2</sub></sup> in dichloromethane. Insets are a magnification of the corresponding oxidized complex signal. Conditions: 0.45 mM complex; 0.1 M TBAP; freq. = 9.4 GHz; power = 2.0 mW; mod. freq. = 100 kHz; mod. amp. = 6 GHz; T = 20 K.

In order to further probe the spin state, <sup>1</sup>H nuclear magnetic resonance (NMR) was conducted on chemically oxidized samples (Fig. 3.8). Sharp peaks in the 0 – 10 ppm region are observed for CF<sub>3</sub> and tBu derivatives supporting the formation of either d<sup>0</sup> Cr(VI)

or a strongly antiferromagnetically coupled Cr(V)-ligand radical. With the UV-vis-NIR and electrochemistry data suggesting Cr(VI) formation, we attribute the loss of EPR signal to the generation of diamagnetic  $d^0$   $[\text{Cr}^{\text{VI}}\text{NSal}^{\text{CF}_3}]^+$  and  $[\text{Cr}^{\text{VI}}\text{Sal}^{\text{tBu}}]^+$ . In contrast to these systems, the  $^1\text{H}$  NMR spectrum of a chemically oxidized sample of  $\text{CrNSal}^{\text{NMe}_2}$  in the 0 – 10 ppm region exhibited significant broadening indicative of a paramagnetic species. Magnetic susceptibility *via* Evans Method revealed a magnetic moment of  $\mu_{\text{eff}} = 2.82$  (2 unpaired electrons) supporting the formation of the Cr(V)  $d^1$  phenoxyl radical  $[\text{Cr}^{\text{V}}\text{NSal}^{\text{NMe}_2}]^{\bullet+}$  structure at room temperature.

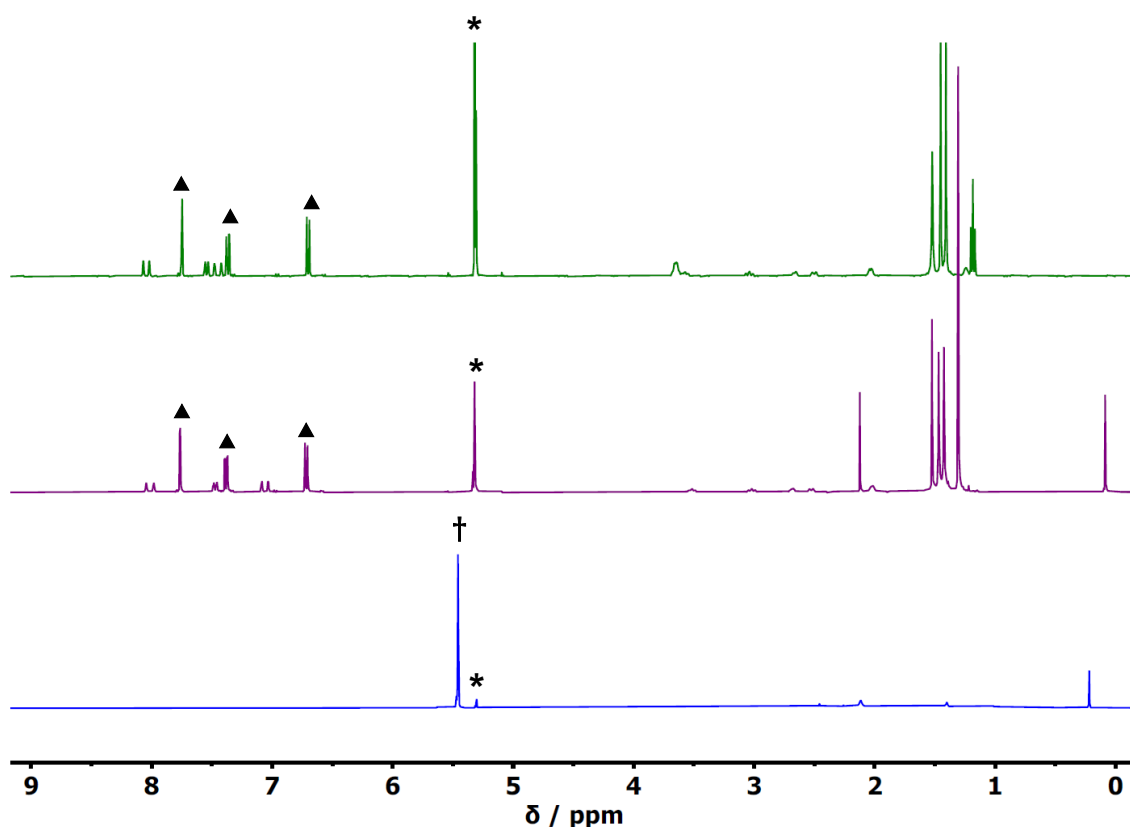


**Figure 3.8.**  $^1\text{H}$  NMR spectra of chemically oxidized complexes in  $\text{CD}_2\text{Cl}_2$ . R =  $\text{CF}_3$ : green; tBu: purple; blue:  $\text{NMe}_2$ . \* Denotes solvent peaks.  $\blacktriangle$  Denotes resonances from  $\text{N}(\text{C}_6\text{H}_3\text{Br}_2)_3$  which is the reduced form of the aminium chemical oxidant.  $\text{CrNSal}^{\text{NMe}_2}$  was oxidized using  $\text{AgSbF}_6$  (0.65 V vs  $\text{Fc}^+/\text{Fc}$ ).<sup>266</sup> † Denotes the paramagnetically shifted solvent peak used as a reference for magnetic susceptibility *via* Evans Method.

We further analyzed the EPR spectrum of  $[\text{Cr}^{\text{V}}\text{NSal}^{\text{NMe}_2}]^{\bullet+}$  by preparing the bis-oxidized diradical species  $[\text{Cr}^{\text{V}}\text{NSal}^{\text{NMe}_2}]^{\bullet\bullet 2+}$  and investigated its electronic structure by EPR. The spectrum features an isotropic signal centred at  $g = 2.0054$  characteristic of a ligand radical (Appendix B – Fig. B3). It was determined from DPV studies that the mono-oxidized complex disproportionates to give ca. 5 % neutral  $\text{CrNSal}^{\text{NMe}_2}$  and 5 % bis-oxidized  $[\text{Cr}^{\text{V}}\text{NSal}^{\text{NMe}_2}]^{\bullet\bullet 2+}$ . Interestingly, overlay of the simulation parameters of these species yields the observed EPR spectrum of the mono-oxidized sample (Fig. 3.9). This result demonstrates the EPR silence of  $[\text{Cr}^{\text{V}}\text{NSal}^{\text{NMe}_2}]^{\bullet+}$  which is likely a consequence of magnetic coupling between the  $d_{xy}$  electron and ligand radical. Unfortunately, the collective data cannot definitively discriminate between a ferromagnetic or antiferromagnetic interaction, and efforts to detect a signal at half-field corresponding to a triplet species were unsuccessful for both mono and bis-oxidized species at low temperature (9 K and 20 K respectively). (Appendix B – Fig. B4 & B5).

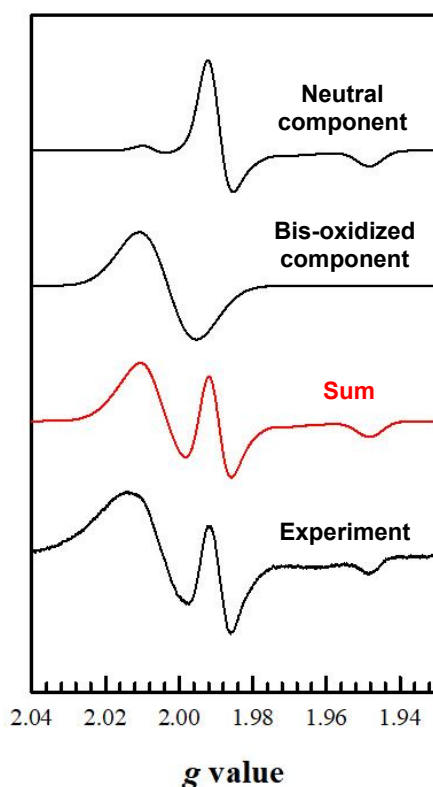


**Figure 3.9.** EPR of a sample of  $[\text{Cr}^{\text{V}}\text{NSal}^{\text{NMe}_2}]^{\bullet+}$  (bottom). The corresponding simulation (red) was accomplished by summing the simulation parameters obtained for neutral  $\text{CrNSal}^{\text{NMe}_2}$  and bis-oxidized  $[\text{Cr}^{\text{V}}\text{NSal}^{\text{NMe}_2}]^{\bullet\bullet 2+}$  complexes. Conditions: 0.45 mM complex; 0.1 M TBAP; freq. = 9.4 GHz; power = 2.0 mW; mod. freq. = 100 kHz; mod. amp. = 6 GHz; T = 20 K;  $\text{CH}_2\text{Cl}_2$ .

### 3.2.4. Theoretical Analysis

Theoretical analysis using density functional theory (DFT) calculations were performed to gain further insight into the electronic structure of the oxidized systems. Single point calculations at the b3p86/TZVP level of theory were utilized to predict the lowest energy spin state upon oxidation (Table 3.3). The possible spin states considered include singlet Cr(VI), as well as broken-symmetry singlet (BSS) and triplet species that can form upon ligand radical formation. Oxidation of **CrNSal**<sup>CF<sub>3</sub></sup> is predicted to be metal-based by 2.5 kcal mol<sup>-1</sup> affording singlet [**Cr**<sup>VI</sup>**NSal**<sup>CF<sub>3</sub></sup>]<sup>+</sup> in agreement with experimental findings. Interestingly, calculations run on the tBu derivative predict the BSS structure to be 2.4 kcal mol<sup>-1</sup> lower in energy compared to the singlet species. However, we conclude from the combined experimental data that the experimental electronic structure is more consistent with metal-based oxidation. Oxidation of **CrNSal**<sup>NMe<sub>2</sub></sup> is predicted to be ligand-based by 13.9 kcal mol<sup>-1</sup>, with the BSS and triplet structures differing by only 0.2 kcal/mol. The use of other functionals such as blyp, b3lyp and bp86 were also explored and can shift relative energetics, however theory at the b3p86 level was chosen for analysis as this functional correctly predicted a change in nitride spin density values upon reaction with Lewis acids (see later chapters).<sup>41</sup>

**Table 3.3.** Relative spin state energetics upon oxidation in kcal mol<sup>-1</sup>.

Compound	Singlet	BSS	Triplet
<b>CrNSal</b> <sup>CF<sub>3</sub></sup>	0	+ 2.5	+ 3.0
<b>CrNSal</b> <sup>tBu</sup>	+ 2.4	0	+ 0.7
<b>CrNSal</b> <sup>NMe<sub>2</sub></sup>	+ 13.9	0	+ 0.2

The changes in calculated metrical parameters were then analyzed from optimized geometries for assigned spin states (Table 3.4). Oxidation of **CrNSal**<sup>CF<sub>3</sub></sup> and **CrNSal**<sup>tBu</sup> to the singlet state is predicted to result in a symmetrically contracted coordination sphere consistent with a high-valent metal centre.<sup>111,159,267</sup> Oxidation of **CrNSal**<sup>NMe<sub>2</sub></sup> to the broken-symmetry singlet structure affords asymmetric parameters in-line with a localized ligand radical.<sup>161,174,180,184</sup> The Cr—N triple bond contracts in all cases, however the effect is significantly more pronounced upon formation of Cr(VI) (Cr—N bond contraction in Å R = CF<sub>3</sub>: - 0.018; R = tBu: -0.019; R = NMe<sub>2</sub>: -0.006) suggesting that the formation of a ligand radical has little effect on the Cr-nitride unit.

**Table 3.4.** Calculated coordination sphere metrical parameters for oxidized complexes in Å. Bracketed values correspond to difference (oxidized – neutral<sup>a</sup>) in calculated bond lengths.

Compound	Cr1-N1	Cr1-N2	Cr1-N3	Cr1-O1	Cr1-O2	O1-C1	O2-C2
<b>[Cr<sup>VI</sup>NSal<sup>CF3</sup>]<sup>+</sup></b>	2.026 (-0.002)	2.065 (+0.028)	1.503 (-0.018)	1.818 (-0.109)	1.813 (-0.123)	1.328 (+0.019)	1.340 (+0.030)
<b>[Cr<sup>VI</sup>NSal<sup>tBu</sup>]<sup>+</sup></b>	2.022 (-0.007)	2.062 (+0.024)	1.505 (-0.019)	1.819 (-0.103)	1.815 (-0.115)	1.330 (+0.014)	1.343 (+0.027)
<b>[Cr<sup>V</sup>NSal<sup>NMe2</sup>]<sup>•+</sup></b>	2.038 (+0.009)	2.015 (-0.023)	1.519 (-0.006)	1.984 (+0.065)	1.904 (-0.024)	1.279 (-0.038)	1.317 (-0.001)

<sup>a</sup>See Section 2.2.2 for details.

Spin density (SD) plots for the broken-symmetry singlet (Fig. 3.10A) and triplet (Fig. 3.10B) **[Cr<sup>V</sup>NSal<sup>NMe2</sup>]<sup>•+</sup>** solutions predict ligand radical localization and account for the asymmetry in metrical parameters. These calculations are in good agreement with results obtained from electrochemistry and UV-vis-NIR spectroscopy that provide evidence for the formation of a Class II mixed-valence compound. Calculations on metal salen complexes incorporating the same ligand also predict radical localization.<sup>180,181,184</sup>

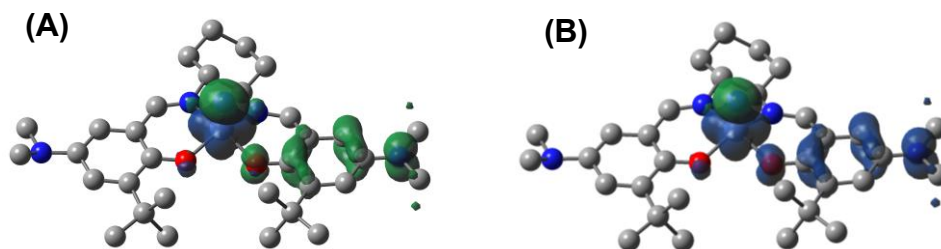


**Figure 3.10.** Spin density plots for possible **[Cr<sup>V</sup>NSal<sup>NMe2</sup>]<sup>•+</sup>** structures. **(A)** Broken-symmetry singlet case. **(B)** Triplet case.

The Cr(V)-ligand radical coupling can be calculated using the Yamaguchi equation (1) and is applicable to both strong and weak exchange systems.<sup>272,273</sup> The calculated exchange correlation ( $J = -58 \text{ cm}^{-1}$ ) corresponds to a weakly antiferromagnetically coupled system. A plot of the Cr  $d_{xy}$  and phenoxide  $\pi$  magnetic orbitals of **[Cr<sup>V</sup>NSal<sup>NMe2</sup>]<sup>•+</sup>** is depicted in Figure 3.11. The amount of net positive overlap can provide insight into the

degree of magnetic coupling.<sup>271,274</sup> A calculated value of 12% is consistent with a weakly antiferromagnetically coupled system.<sup>275</sup> This relatively small value can be rationalized based on the relative orientations of  $d_{xy}$  and phenoxide  $\pi$  magnetic orbitals, which are not suited for optimal overlap within a (pseudo)square pyramidal geometry. Slight distortions however within the metal coordination sphere can result in net positive overlap and can account for the calculated value of 12 %.

$$J = \frac{E^{BS} - E^{HS}}{\langle \hat{S}^2 \rangle^{HS} - \langle \hat{S}^2 \rangle^{BS}} \quad (1)$$

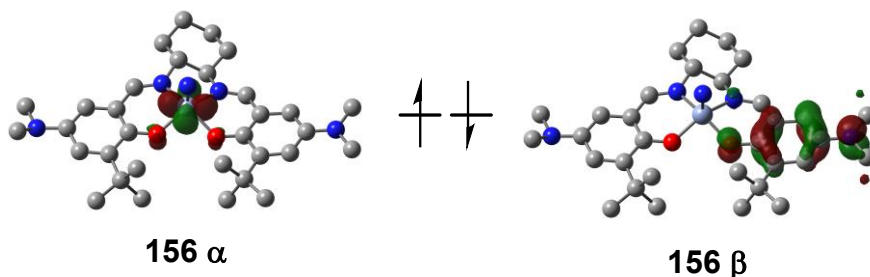


**Figure 3.11.** Plots of the  $[\text{Cr}^{\text{V}}\text{NSal}^{\text{NMe}_2}]^{+\bullet}$  magnetic orbitals in the broken-symmetry singlet state.

### 3.2.5. Discussion and Summary

This chapter illustrates that the locus of oxidation for chromium nitride salen complexes can be tuned through the modulation of phenoxide *para*-R substituents. The combined experimental and theoretical data provide strong evidence that complexes bearing electron-withdrawing to moderately electron-donating substituents ( $\text{R} = \text{CF}_3$ ,  $\text{tBu}$ ) result in metal-based oxidation, while substitution with a strongly electron-donating *para*-R group ( $\text{R} = \text{NMe}_2$ ) affords a ligand radical.

The first redox event in the CV for  $\text{CrNSal}^{\text{tBu}}$  was assigned as the  $\text{Cr(V)}/\text{Cr(VI)}$  redox couple. It is unlikely that this wave corresponds to phenoxide oxidation, as a large  $\Delta E_{\text{ox}}$  of 0.5 V would suggest *significant* electronic communication to give a Class III delocalized ligand radical species. The absorption spectrum of  $[\text{Cr}^{\text{VI}}\text{NSal}^{\text{tBu}}]^{+\bullet}$  exhibits no evidence for the presence of diagnostic IVCT absorbances associated with a delocalized



ligand radical, as the lowest observable energy transition is best described as a LMCT. The same rationale applies to  $[\text{Cr}^{\text{VI}}\text{NSal}^{\text{CF}_3}]^+$ , which also exhibits a low energy band characterized as a LMCT into the empty  $d_{xy}$  orbital. The EPR spectra for both derivatives feature a total loss of signal intensity relative to the neutral version, while the NMR spectra depict sharp resonances in the 0-10 ppm window consistent with the formation of diamagnetic  $d^0$   $[\text{Cr}^{\text{VI}}\text{NSal}^{\text{tBu}}]^+$  and  $[\text{Cr}^{\text{VI}}\text{NSal}^{\text{CF}_3}]^+$ . These results are partially corroborated by DFT calculations, which predict singlet  $[\text{Cr}^{\text{VI}}\text{NSal}^{\text{CF}_3}]^+$  as the lowest energy oxidation product, however favour the broken-symmetry singlet structure for the tBu derivative.

The electrochemical data for  $\text{CrNSal}^{\text{NMe}_2}$  suggest minimal electronic coupling based on the small  $\Delta E_{\text{ox}}$  value (0.16 V) consistent with a Class II mixed-valence compound. The absorption spectrum of  $[\text{Cr}^{\text{V}}\text{NSal}^{\text{NMe}_2}]^{\bullet+}$  features a broad and low intensity absorbance that fits the parameters for a ligand-to-ligand charge transfer.  $[\text{Cr}^{\text{V}}\text{NSal}^{\text{NMe}_2}]^{\bullet+}$  was found to be EPR silent due to magnetic coupling at low temperature (20 K), while Evans Method experiments is consistent with a species exhibiting two unpaired electrons at room temperature. The exchange correlation was calculated to be  $J = -53 \text{ cm}^{-1}$  suggesting weak antiferromagnetism rationalized by a 12 % magnetic orbital overlap. DFT analysis predicts the broken-symmetry singlet as the lowest energy structure, while the spin density plots reveal radical localization in line with a Class II mixed-valence complex.

The combined experimental and computational data provides strong evidence for the metal-based oxidation for complexes  $\text{CrNSal}^{\text{CF}_3}$  and  $\text{CrNSal}^{\text{tBu}}$ . Interestingly, substitution at the *para*-R position with electron-rich groups as demonstrated by the  $\text{CrNSal}^{\text{NMe}_2}$  complex affords a ligand radical. Interestingly, these complexes exhibit remarkable stability in comparison to Mn analogues. Although an in-depth exploration into the possible decay products for the oxidized species was not conducted, preliminary kinetic analysis in solution suggest that the slow decomposition is governed by second-order kinetics for  $[\text{Cr}^{\text{VI}}\text{NSal}^{\text{CF}_3}]^+$  and  $[\text{Cr}^{\text{VI}}\text{NSal}^{\text{tBu}}]^+$  in-line a bimolecular N—N homocoupling pathway, while the decay of  $[\text{Cr}^{\text{V}}\text{NSal}^{\text{NMe}_2}]^{\bullet+}$  is also minimal but does not follow second-order kinetics. In all, these results demonstrate that the modulation of remote ligand electronics in Cr nitride salen complexes is an effective approach in tuning the relative ordering of redox-active orbitals such that the locus of oxidation is influenced.

### 3.3. Experimental

#### 3.3.1. Materials

All chemicals were of the highest quality grade and purified whenever necessary. The tris(2,4-dibromophenyl)aminium hexafluoroantimonate radical oxidant  $[N(C_5H_3Br_2)_3][SbF_6]$  was synthesized according to published protocols.<sup>276</sup> Dichloromethane was dried by refluxing over calcium hydride and distilled prior to use.

#### 3.3.2. Instrumentation

Electronic spectra were obtained using a Cary 5000 spectrophotometer equipped with custom designed immersion fiber-optic probes with 0.1 and 1 cm path lengths. Constant temperatures were maintained with an FTS Multi-Cool Low Temperature Bath. Solvent contraction was accounted for in all low-temperature studies. Cyclic voltammetry (CV) was performed on a PAR-263A potentiometer equipped with a silver wire reference electrode, a platinum disk counter electrode and glassy carbon working electrode. Tetrabutylammonium perchlorate (0.1 M) was used as the supporting electrolyte in  $CH_2Cl_2$ . Decamethylferrocene was used as an internal standard.<sup>277</sup> Electrolysis was performed at 253 K with a Biologic SP300 potentiostat by using a carbon foam working electrode and was monitored by coulometry and rotating-disk electrode voltammetry.  $^1H$  nuclear magnetic resonance (NMR) and magnetic susceptibility *via* Evans Method was carried out on a Bruker AVANCE III 500 MHz instrument. Electron paramagnetic resonance (EPR) were recorded on a Bruker EMXplus spectrometer operating with a premium X-band microwave bridge and an HS resonator. EPR spectra were simulated using the EasySpin package in Matlab.<sup>238</sup>

#### 3.3.3. Theoretical Analysis

Geometry optimizations were all performed using the Gaussian 16 program (Revision A.03)<sup>241</sup> employing the B3LYP functional with the 6-31g\* basis set.<sup>242</sup> This combination has provided good matches to experimental metrical data for a variety of similar salen systems.<sup>172,173,243,244</sup> Frequency calculations performed on the same functional/basis set confirmed optimized structures were at a global minimum. Single point calculations were performed using the B3P86 functional and TZVP basis set of

Ahlrichs<sup>245,246</sup> as this functional/basis set combination was determined to predict the change in nitride spin density values upon reaction with Lewis acids (see later chapters).<sup>41</sup> All calculations employed a polarizable continuum model (PCM) for CH<sub>2</sub>Cl<sub>2</sub> ( $\epsilon=8.93$ ) for all atoms.<sup>242,247,248</sup> The AOMix Program was used for analysis of magnetic orbital overlap populations.<sup>275</sup>

### 3.3.4. Oxidation Protocol

Chemical oxidations for UV-vis-NIR and EPR studies were accomplished by addition of 1 equivalent of a saturated solution of the strong aminium chemical oxidant [N(C<sub>6</sub>H<sub>3</sub>Br<sub>2</sub>)<sub>3</sub>]<sup>+</sup> (1.1 V vs F<sub>4</sub>/F<sub>6</sub><sup>+</sup>).<sup>266</sup> The volume of solution needed for 1-electron oxidation was determined by titrating a sample of NiSal<sup>tBu</sup> in 3.5 mL dichloromethane (0.45 mM) with 10  $\mu$ L aliquots of oxidant and monitoring the intense absorption at 4700 cm<sup>-1</sup> ( $\epsilon = 21,600$  M<sup>-1</sup>cm<sup>-1</sup>) by UV-vis-NIR spectroscopy.<sup>180</sup> Immediate decrease of this band indicated complete 1 electron oxidation of NiSal<sup>tBu</sup>. The same volume of oxidant was then added to 0.45mM solutions of each Cr complex in 3.5 mL dichloromethane. For compounds of suitable potential including **CrNSal<sup>NMe2</sup>** and **CrNSal<sup>tBu</sup>**, bulk electrolysis allowed cleaner and more controlled oxidation. Samples were dissolved in 8 mL of dry CH<sub>2</sub>Cl<sub>2</sub> (0.5 mM) at 253 K and electrolyzed under a positive pressure of N<sub>2</sub>. The integrity of the oxidized products was assessed by recording CV curves after the first and second oxidation and ensuring that they matched with that of the unoxidized sample. 200  $\mu$ L aliquots were then placed in EPR tubes and frozen for analysis. A sample of the electrolyzed solution was also analyzed by UV-vis-NIR spectroscopy to ensure resulting spectra matched chemically oxidized samples.

## Chapter 4. Investigation of Reactivity Differences upon Oxidation

D. Martelino performed UV-vis and theoretical analysis. F. Thomas (Grenoble) collected EPR data and D. Martelino simulated the data.

### 4.1. Introduction

Despite a number Cr(V) nitride complexes reported in the literature, their reactivities have not been discussed until relatively recently. For example, Bendix *et al.* reported that Cr(V) nitrides employing salen and dibenzoylmethanolate ligands are nucleophilic and readily react with Lewis acidic substrates.<sup>41</sup> The reactivity differences between early and late transition metal nitride complexes has also been of interest from a computational standpoint.<sup>278–280</sup> Nitride partial charges have been traditionally invoked as suitable descriptors for terminal nitride reactivity. These values are derived from Mulliken analysis and predict the amount of electronic charge distribution within a particular bond.<sup>281</sup> Despite a formal N<sup>3-</sup> charge for nitride ligands, the M—N triple bond is predominantly covalent. The partial charges for individual atoms are thus calculated to be a fraction of the formal oxidation state due to a significant degree of shared electron density. In one example by Sauer and coworkers, a series of nitride complexes incorporating salen or chloride ligands were investigated by density functional theory calculations (Fig. 4.1A).<sup>280</sup> The ligand set and oxidation states were fixed while the identity of the metal was varied. It was found that the nitride negative charge decreased with increasing group number within the 3d transition metal series. This result correlates well with reported experimental trends in reactivity, and it was deduced that a negative partial charge on the nitride predicts nucleophilic properties.<sup>280</sup>

In another study by Bachler, the protonation of a series of nitride complexes were computationally modelled (Fig. 4.1B).<sup>279</sup> Experimentally, it was found that protons from trace amounts of water attack the V—N triple bond leading to decomposition, while Cr and Mn complexes were stable in up to 1.0 M perchloric acid.<sup>223</sup> Partial charge calculations predicted that the V complex would exhibit the greatest nucleophilicity at the nitride (negative N<sub>partial charge</sub> M = V > Cr > Mn) and analysis of the energy released upon protonation supported this trend ( $\Delta E$  M = V > Cr > Mn).

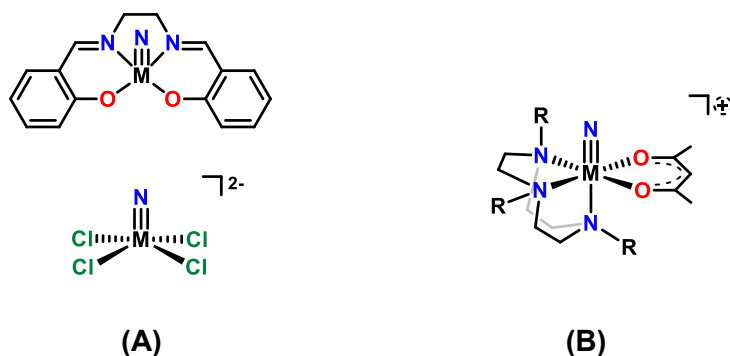
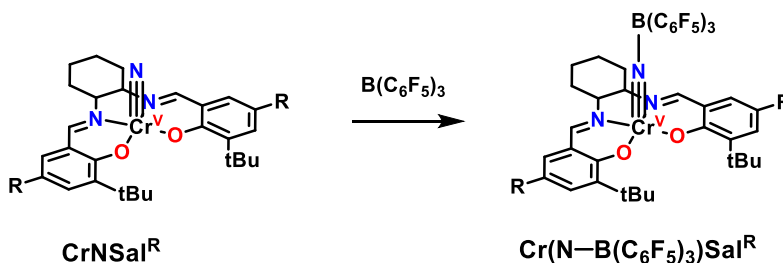


**Figure 4.1.** Examples of computationally studied nitride complexes to describe nucleophilicity based on nitride partial charges. **(A)** Salen and chloro complexes (M = V, Cr, Mn, Fe) by Sauer.<sup>280</sup> **(B)** triazo-acetylacetonate complex (M = V, Cr, R = H; M = Mn, R = CH<sub>3</sub>) by Bachler.<sup>279</sup>

This chapter outlines the effect of locus of oxidation on the reactivity of **CrNSal**<sup>CF<sub>3</sub></sup>, **CrNSal**<sup>tBu</sup> and **CrNSal**<sup>NMe<sub>2</sub></sup>. The neutral complexes are nucleophilic and readily react with the Lewis acidic tris(pentafluorophenyl) borane forming N—B adducts (Scheme 4.1). Metal-based oxidation results in a loss of nucleophilicity for tBu and CF<sub>3</sub> derivatives, while ligand-based oxidation of the NMe<sub>2</sub> derivative does not appear to retard reactivity. The nature of the N—B interaction for the oxidized complexes is difficult to rationalize experimentally, however an in-depth computational study was conducted to gain insight into the observed reactivity differences and product profiles.

**Scheme 4.1.** Interaction of **CrNSal**<sup>R</sup> with tris(pentafluorophenyl) borane to form N—B adducts.



## 4.2. Results

### 4.2.1. Electronic Absorption Spectroscopy

The reactivity of **CrNSal**<sup>NMe<sub>2</sub></sup>, **CrNSal**<sup>tBu</sup>, **CrNSal**<sup>CF<sub>3</sub></sup> as well as oxidized versions were analyzed by UV-vis-NIR spectroscopy. Tris(pentafluorophenyl) borane was titrated into a solution of **CrNSal**<sup>CF<sub>3</sub></sup>, **CrNSal**<sup>tBu</sup>, and **CrNSal**<sup>NMe<sub>2</sub></sup> and monitored by UV-vis-NIR until one equivalent was reached (Fig. 4.2). The addition of borane results in a decrease of the absorption at 23,300 cm<sup>-1</sup> for **CrNSal**<sup>NMe<sub>2</sub></sup>, and formation of band at higher energy ( $\lambda_{\text{max}}$  = 26,500 cm<sup>-1</sup>,  $\epsilon$  = 5,600 M<sup>-1</sup> cm<sup>-1</sup>). While limited changes are apparent at high energy for **CrNSal**<sup>CF<sub>3</sub></sup> and **CrNSal**<sup>tBu</sup>, new broad bands at lower energy are observed. Isosbestic points are indicative of the clean formation of **Cr(N—B(C<sub>6</sub>F<sub>5</sub>)<sub>3</sub>)Sal**<sup>R</sup>. The addition of over 1 equivalent yields no further spectral changes signalling a 1:1 stoichiometry (Appendix C – Fig. C1).

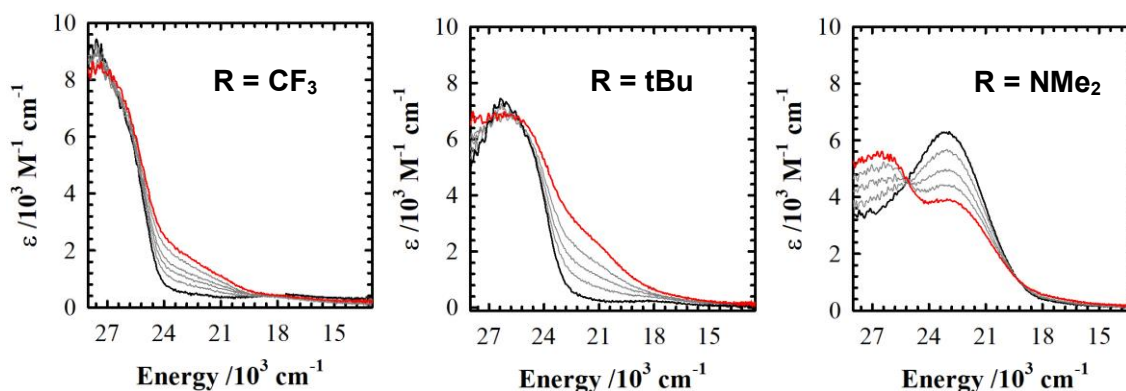


**Figure 4.2.** UV-vis titration of neutral complexes with tris(pentafluorophenyl) borane. Black: **CrNSal**<sup>R</sup>; red: 1 equivalent tris(pentafluorophenyl) borane added. Intermediate grey lines represent increasing aliquots of borane until 1 equivalent is reached. Conditions: 0.45 mM complex; T = 233 K; CH<sub>2</sub>Cl<sub>2</sub>. Complexes are stable and spectra appear identical after 1 hour. Free tris(pentafluorophenyl) borane does not exhibit any absorption peaks within the energy range of studied.

One equivalent of tris(pentafluorophenyl) borane was then added to solutions containing  $[\text{Cr}^{\text{VI}}\text{NSal}^{\text{CF}_3}]^+$ ,  $[\text{Cr}^{\text{VI}}\text{NSal}^{\text{tBu}}]^+$ , and  $[\text{Cr}^{\text{V}}\text{NSal}^{\text{NMe}_2}]^{\bullet+}$  oxidized with  $[\text{N}(\text{C}_6\text{H}_3\text{Br}_2)_3][\text{SbF}_6]$  and monitored by UV-vis-NIR under identical conditions (Fig. 4.3).  $[\text{Cr}^{\text{VI}}\text{NSal}^{\text{CF}_3}]^+$  and  $[\text{Cr}^{\text{VI}}\text{NSal}^{\text{tBu}}]^+$  do not interact with borane as evidenced by a lack of spectral changes upon addition. Interestingly, the spectrum of  $[\text{Cr}^{\text{V}}\text{NSal}^{\text{NMe}_2}]^{\bullet+}$  changes significantly, suggesting reactivity with the borane.

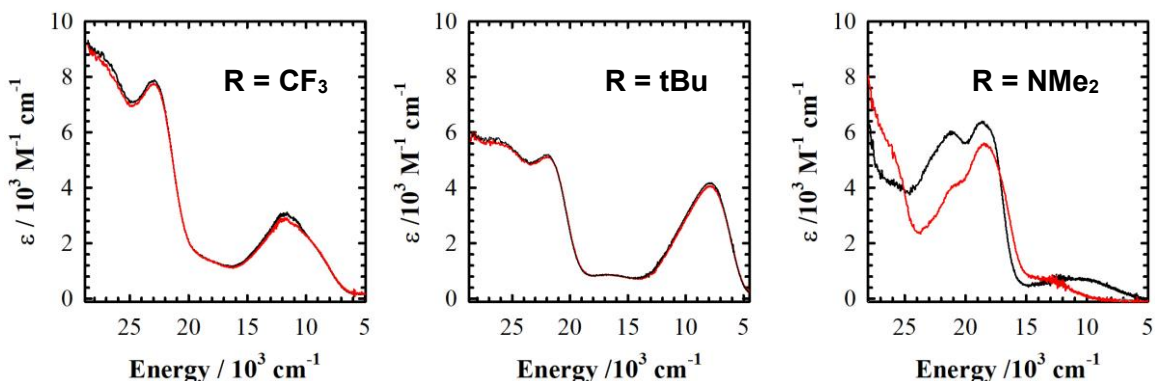


**Figure 4.3.** Interaction of tris(pentafluorophenyl) borane with the oxidized complexes monitored by UV-vis-NIR spectroscopy. Black: oxidized  $\text{CrNSal}^{\text{R}}$ ; red: 1 equivalent borane added. Conditions: 0.45 mM complex;  $T = 233 \text{ K}$ ;  $\text{CH}_2\text{Cl}_2$ . Complexes are stable and spectra appear identical after 1 hr. Addition of over 1 equivalent borane yields no further changes for all spectra (see Appendix C – Fig. C2).

Borane addition results in a decrease in intensity of the high energy features at  $21,300 \text{ cm}^{-1}$  and  $18,800 \text{ cm}^{-1}$  in the  $[\text{Cr}^{\text{V}}\text{NSal}^{\text{NMe}_2}]^{\bullet+}$  spectrum. Additionally, the broad feature at  $12,000 \text{ cm}^{-1}$  decays, and a new broad shoulder feature of similar intensity at ca.  $13,200 \text{ cm}^{-1}$  is formed. The titration of 1 equivalent of borane into a solution of  $[\text{Cr}^{\text{V}}\text{NSal}^{\text{NMe}_2}]^{\bullet+}$  shows three isosbestic points indicative of clean product formation (Fig. 4.4). These results provide strong evidence that the locus of oxidation plays a key role in modulating the nucleophilic reactivity of the Cr nitride salen complexes. It is important to mention that chemical oxidation using the aminium radical ( $[\text{N}(\text{C}_6\text{H}_3\text{Br}_2)_3]^{\bullet+}[\text{SbF}_6]^-$ ) results in the production the  $\text{N}(\text{C}_6\text{H}_3\text{Br}_2)_3$  amine by-product. While a Lewis acid-base interaction between the amine and the tris(pentafluorophenyl) borane may be possible, no evidence for this was observed by UV-vis or  $^1\text{H}$  NMR spectroscopy.

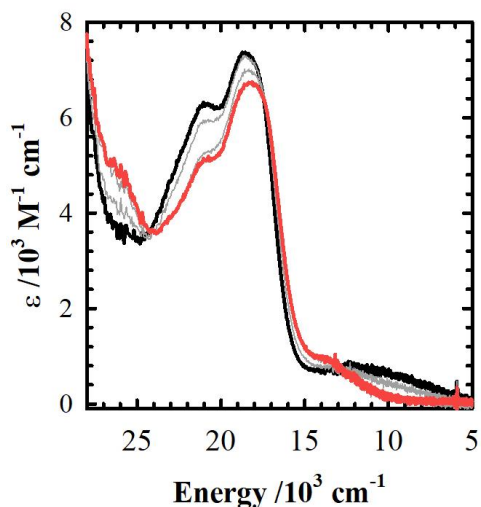


**Figure 4.4.** Titration of  $[\text{Cr}^{\text{V}}\text{NSal}^{\text{NMe}_2}]^{\bullet+}$  with tris(pentafluorophenyl) borane. Black:  $[\text{Cr}^{\text{V}}\text{NSal}^{\text{NMe}_2}]^{\bullet+}$ , red: 1 equivalent borane added. Intermediate grey lines represent increasing aliquots of borane added until 1 equivalent was reached. Conditions: 0.45 mM complex;  $T = 233\text{ K}$ ;  $\text{CH}_2\text{Cl}_2$ . Complexes are stable and spectra appear identical after 1 hr.

#### 4.2.2. Electron Paramagnetic Resonance

The reactivities of neutral and oxidized complexes were then analyzed by continuous wave X-band electron paramagnetic resonance (EPR) spectroscopy. The solution EPR spectra (298 K) for all adducts are observed to be identical and exhibit equivalent simulation parameters (Fig. 4.5). Evidence for N—B adduct formation is deduced by noting changes in nitride hyperfine interactions. Simulations reveal that the nitride  $^{14}\text{N}$  hyperfine splitting is approximately three times larger for the adducts in comparison to the free nitride (Table 4.1). This phenomenon has been previously reported by Bendix and is attributed to spin polarization of the Cr—N triple bond and is a consequence of the elongation of this bond.<sup>41</sup> The low temperature EPR spectra (100 K) of the N—B adducts resembles a broadened  $\text{CrNSal}^{\text{R}}$  signal, likely in part due to the increase in the nitride hyperfine splitting (Appendix C – Fig. C3).



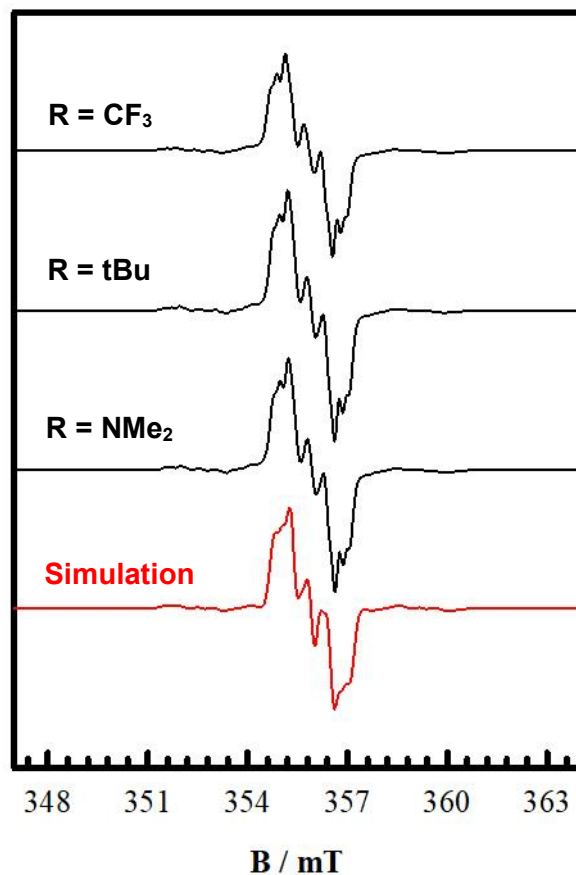


**Figure 4.5.** Room temperature EPR spectra of **Cr(N—B(C<sub>6</sub>F<sub>5</sub>)<sub>3</sub>)Sal<sup>R</sup>**. Conditions: 0.50 mM complex; freq. = 9.85 GHz; power = 2.0 mW; mod. freq. = 100 kHz; mod. amp. = 0.6 mT; T = 298 K; CH<sub>2</sub>Cl<sub>2</sub>.

**Table 4.1.** Comparison of simulation parameters<sup>a</sup> between **CrNSal<sup>R</sup>** and **Cr(N—B(C<sub>6</sub>F<sub>5</sub>)<sub>3</sub>)Sal<sup>R</sup>**.

Complex	<i>g</i> <sub>iso</sub>	<i>A</i> <sup>14N(nitride)</sup> / MHz	<i>A</i> <sup>14N(salen)</sup> / MHz	<i>A</i> <sup>53Cr</sup> / MHz
<b>CrNSal<sup>Rb</sup></b>	1.978	6.28	6.34	78.00
<b>Cr(N—B(C<sub>6</sub>F<sub>5</sub>)<sub>3</sub>)Sal<sup>R</sup></b>	1.977	16.00	6.45	61.45

<sup>a</sup>Simulation parameters are found to be identical irrespective of R group. <sup>b</sup>See Section 2.2.3 for EPR spectrum of **CrNSal<sup>R</sup>**.

The EPR spectra of  $[\text{Cr}^{\text{VI}}\text{NSal}^{\text{CF}_3}]^+$  and  $[\text{Cr}^{\text{VI}}\text{NSal}^{\text{tBu}}]^+$  exhibit a significant loss of signal due to their diamagnetic nature. The addition of borane should not afford any significant changes in the EPR spectra as the  $d^0$  spin state is expected to be conserved, even with some degree of N—B interaction.<sup>7,37,41</sup> Additionally, only a signal associated with residual unoxidized  $\text{CrNSal}^{\text{NMe}_2}$  can be observed in the room temperature spectrum of a sample of electrochemically generated  $[\text{Cr}^{\text{V}}\text{NSal}^{\text{NMe}_2}]^{.+}$  (Fig. 4.6) in agreement with the electronic structure discussed in Section 3.2.3. Furthermore, no change is observed with the addition of 1 equivalent borane to this species (Appendix C – Fig. C4A). Signals associated with the bis-oxidized complex  $[\text{Cr}^{\text{V}}\text{NSal}^{\text{NMe}_2}]^{..2+}$  were also not detected, and solution EPR measurements (298 K) of an independently prepared sample of electrochemically generated  $[\text{Cr}^{\text{V}}\text{NSal}^{\text{NMe}_2}]^{..2+}$  feature no observable signals (Appendix C – Fig. C4B). Additionally, analysis of the EPR spectrum of  $[\text{Cr}^{\text{V}}\text{NSal}^{\text{NMe}_2}]^{.+}$  and  $[\text{Cr}^{\text{V}}\text{NSal}^{\text{NMe}_2}]^{..2+}$  over time revealed regeneration of the  $\text{CrNSal}^{\text{NMe}_2}$  signal, suggesting that these species decay via reduction back to the neutral complex at room temperature (Appendix C – Fig. C5).

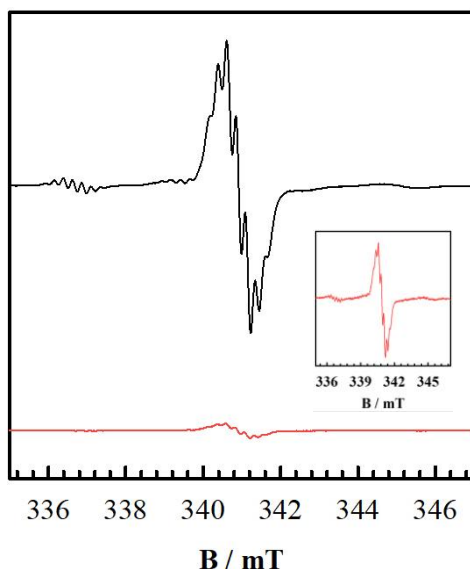


**Figure 4.6.** Solution EPR of concentration matched Cr samples. Black:  $\text{CrNSal}^{\text{NMe}_2}$ ; red:  $[\text{Cr}^{\text{V}}\text{NSal}^{\text{NMe}_2}]^{.+}$ ; Inset represents a magnification of the signal in red. Conditions: 0.50 mM complex; freq. = 9.428 GHz; power = 2.0 mW; mod. freq. = 100 kHz; mod. amp. = 0.6 mT; T = 298 K.

Interestingly, the low temperature EPR spectrum (100 K) of a frozen solution of  $[\text{Cr}^{\text{V}}\text{NSal}^{\text{NMe}_2}]^{\bullet,+}$  features an increase in the signal intensities associated with  $\text{CrNSal}^{\text{NMe}_2}$  and  $[\text{Cr}^{\text{V}}\text{NSal}^{\text{NMe}_2}]^{\bullet,2+}$  upon addition of 1 equivalent tris(pentafluorophenyl) borane (Fig. 4.7). Whether this is the result of an interaction with the borane is not yet understood and should be probed further. One possibility is that the N—B interaction facilitates the disruption of aggregation. The result is a reduction of the intermolecular spin interactions, affording signal enhancement. In Section 2.2.3, a large excess of tetrabutylammonium perchlorate (TBAP) was required for the low temperature EPR analysis of  $\text{CrNSal}^{\text{R}}$  complexes in order to minimize through-space interactions. Indeed, the addition of borane to a solution of  $\text{CrNSal}^{\text{NMe}_2}$  (in the absence of TBAP) results in a remarkable increase in signal (Appendix C – Fig. C6).

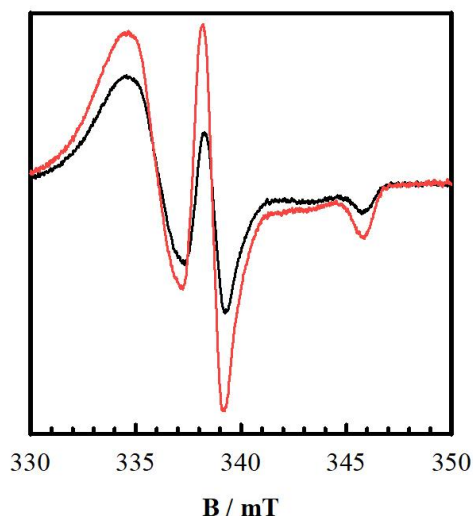


**Figure 4.7.** Low temperature EPR analysis of the addition of tris(pentafluorophenyl) borane to a solution of  $[\text{Cr}^{\text{V}}\text{NSal}^{\text{NMe}_2}]^{\bullet,+}$ . Black:  $[\text{Cr}^{\text{V}}\text{NSal}^{\text{NMe}_2}]^{\bullet,+}$ ; red: 1 equivalent borane added. Conditions: 0.29 mM complex; 0.1 M TBAP; freq. = 9.388 GHz; power = 1.0 mW; mod. freq. = 100 kHz; mod. amp. = 6 GHz; T = 100 K.

### 4.2.3. Theoretical Analysis

Theoretical analysis using DFT was conducted in order to rationalize the observed differences in reactivity. Mulliken charge analysis was used to quantify metal and nitride partial charges (Table 4.2). Neutral compounds are calculated to exhibit values of ca. - 0.4 at the nitride predicting nucleophilic character. The magnitudes scale with the electron-donating ability of the *para*-R group ( $N_{\text{partial charge R}} = \text{NMe}_2 > \text{tBu} > \text{CF}_3$ ) however all complexes exhibit similar reactivity (see above). The negative charge decreases significantly upon formation of  $[\text{Cr}^{\text{VI}}\text{NSal}^{\text{CF}_3}]^+$  and  $[\text{Cr}^{\text{VI}}\text{NSal}^{\text{tBu}}]^+$  ( $\Delta N_{\text{partial charge R}} = \text{CF}_3$ : +0.287; tBu: +0.278) consistent with a loss of reactivity with the Lewis acidic borane evidenced by UV-vis-NIR analysis. Interestingly, the partial charge for  $[\text{Cr}^{\text{V}}\text{NSal}^{\text{NMe}_2}]^{.+}$  decreases only minimally in comparison to other derivatives ( $\Delta N_{\text{partial charge R}} = \text{NMe}_2$ : +0.056) consistent with the preservation of reactivity. The differences in partial charge associated with the locus of oxidation can be rationalized by analysis of calculated bonding parameters. The neutral complexes exhibit short Cr—N bond lengths (ca. 1.52 Å as discussed in Section 2.2.5) and Mayer bond order calculations are consistent with triple bond character (bond order of ca. 2.9). The complexes  $[\text{Cr}^{\text{VI}}\text{NSal}^{\text{CF}_3}]^+$  and  $[\text{Cr}^{\text{VI}}\text{NSal}^{\text{tBu}}]^+$  are predicted to exhibit shorter and stronger bonds in comparison to neutral analogues, while the Cr—N bonding parameters for  $[\text{Cr}^{\text{V}}\text{NSal}^{\text{NMe}_2}]^{.+}$  remain relatively unchanged suggesting that formation of a ligand radical has little effect on the Cr-nitride unit ( $\Delta \text{Cr—N}_{\text{bond length}}$  upon oxidization: R = CF<sub>3</sub>: - 0.018 Å ~ tBu: - 0.019 Å > NMe<sub>2</sub>: - 0.006 Å). Consequently, strengthening of the Cr—N bond as a result of metal-based oxidation confers enhanced covalency with reduced charge separation. This idea is corroborated by analyzing the Cr partial charges in addition to the nitride partial charges. Despite Cr(V) → Cr(VI) oxidation, a significant decrease in positive charge is observed for  $[\text{Cr}^{\text{VI}}\text{NSal}^{\text{CF}_3}]^+$  and  $[\text{Cr}^{\text{VI}}\text{NSal}^{\text{tBu}}]^+$  ( $\Delta \text{Cr}_{\text{partial charge R}} = \text{CF}_3$ : - 0.171; tBu: - 0.177) in comparison to  $[\text{Cr}^{\text{V}}\text{NSal}^{\text{NMe}_2}]^{.+}$  ( $\Delta \text{Cr}_{\text{partial charge R}} = \text{NMe}_2$ : - 0.016) consistent with the covalency assignment.

**Table 4.2.** Calculated bonding parameters that influence nitride reactivity. Bracketed values correspond to the difference between oxidized and neutral values.

Compound	Partial charge	Partial charge	Cr—N
	Cr	N	Bond Order <sup>a</sup>
<b>CrNSal<sup>CF3</sup></b>	0.617	- 0.355	2.909
<b>CrNSal<sup>tBu</sup></b>	0.617	- 0.387	2.897
<b>CrNSal<sup>NMe2</sup></b>	0.617	- 0.392	2.893
<b>[Cr<sup>VI</sup>NSal<sup>CF3</sup>]<sup>+</sup></b>	0.446 (- 0.171)	- 0.068 (+ 0.287)	2.981 (+ 0.072)
<b>[Cr<sup>VI</sup>NSal<sup>tBu</sup>]<sup>+</sup></b>	0.440 (- 0.177)	- 0.109 (+ 0.278)	2.976 (+ 0.079)
<b>[Cr<sup>V</sup>NSal<sup>NMe2</sup>]<sup>•+</sup></b>	0.601 (- 0.016)	- 0.336 (+ 0.056)	2.895 (+ 0.002)

<sup>a</sup>Values are obtained from Mayer bond order calculations.

Analysis of the  $\pi$  bonding MOs for the metal nitride triple bond is typically invoked when discussing nucleophilicity due to the energetic accessibility of these orbitals.<sup>7,37</sup> Natural bond order (NBO) calculations were used to visualize Cr—N  $d_{\pi}-p_{\pi}$  interactions and interpret changes upon oxidation. NBO analysis uses the wavefunction generated from a geometry optimization and forms orthonormal sets of ‘maximum occupancy’ orbitals.<sup>282</sup> The result is a Lewis-like interpretation for a particular interaction which resembles familiar chemical bonding concepts. Recently, Bullock *et al.* have employed NBO to characterize trends in N—N homocoupling for a series of metal nitride complexes.<sup>283</sup> Herein, NBO analysis of the Cr—N  $\pi$  bonding interactions reveal important factors that can influence reactivity differences. A plot of these orbitals in the xz and yz planes for **CrNSal<sup>CF3</sup>**, **CrNSal<sup>tBu</sup>** and **CrNSal<sup>NMe2</sup>** is depicted in Figure 4.8. NBO calculations predict a *decrease* in the  $\pi$  orbital energy upon oxidation. Table 4.3 denotes, however, that the degree of stabilization is more pronounced in **[Cr<sup>VI</sup>NSal<sup>CF3</sup>]<sup>+</sup>** and **[Cr<sup>VI</sup>NSal<sup>tBu</sup>]<sup>+</sup>** in comparison to **[Cr<sup>V</sup>NSal<sup>NMe2</sup>]<sup>•+</sup>** ( $\Delta E_{\pi}$  in kcal mol<sup>-1</sup>: CF<sub>3</sub>: -41.9 > tBu: -41.4 >> NMe<sub>2</sub>: -16.3) consistent with experimental findings that suggest the Cr(VI) complexes exhibit a loss of nucleophilicity. The  $\sigma$ -bonding interaction and nitride lone pairs for all complexes are not expected to be of immediate importance for reactivity (calculated to be ca. 200 and 230 kcal mol<sup>-1</sup> lower in energy in comparison to the  $\pi$  orbitals respectively). Furthermore, the nitride lone pairs are calculated to be comprised of ca. 80 % s-atomic orbital character similar to other accounts and is often viewed as part of the core electron

set.<sup>29,36,38</sup> Nonetheless, these orbital manifolds follow the same trend in stabilization with the locus of oxidation (Table 4.3).

**Table 4.3.** Relative orbital energies in kcal mol<sup>-1</sup>. Bracketed values correspond to the difference (oxidized – neutral values).<sup>a</sup>

Compound	$\pi$	$\sigma$	Lone pair
<b>CrNSal</b> <sup>CF<sub>3</sub></sup>	-207.12	-406.23	-436.03
<b>CrNSal</b> <sup>tBu</sup>	-200.17	-402.30	-427.31
<b>CrNSal</b> <sup>NMe<sub>2</sub></sup>	-198.90	-401.82	-425.52
<b>[Cr<sup>VI</sup>NSal</b> <sup>CF<sub>3</sub></sup> ] <sup>+</sup>	-249.02 (-41.90)	-441.60 (-35.37)	-479.83 (-43.80)
<b>[Cr<sup>VI</sup>NSal</b> <sup>tBu</sup> ] <sup>+</sup>	-241.56 (-41.40)	-432.32 (-30.02)	-478.71 (-51.40)
<b>[Cr<sup>V</sup>NSal</b> <sup>NMe<sub>2</sub></sup> ] <sup>•+</sup>	-215.20 (-16.30)	-412.56 (-10.74)	-444.38 (-18.76)

<sup>a</sup>See Appendix C – Table C1-C10 for relative atomic orbital contributions to  $\pi$ ,  $\sigma$  and lone pair molecular orbitals.

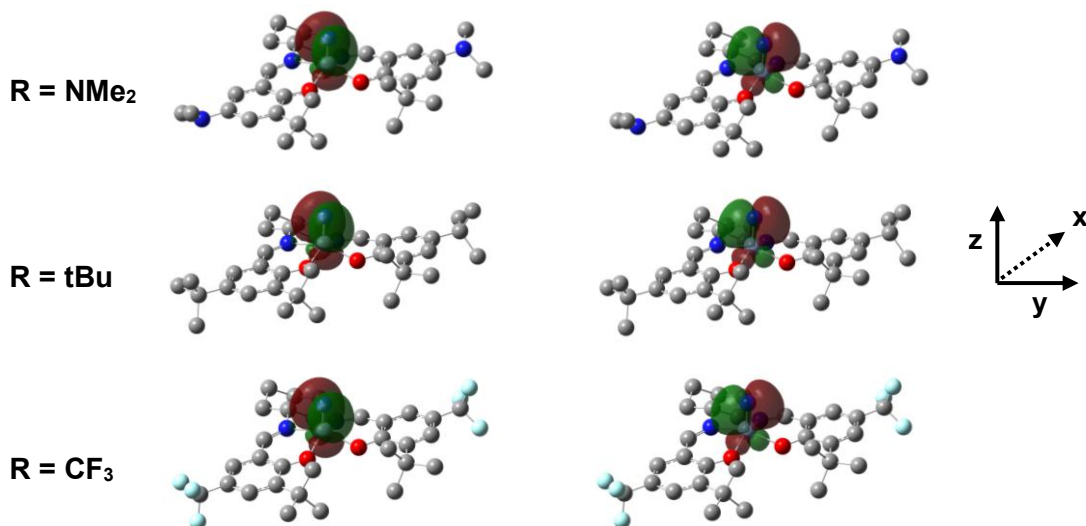


**Figure 4.8.** Visualization of the alpha orbitals of the Cr—N  $\pi$  bonding interactions for **CrNSal**<sup>CF<sub>3</sub></sup>, **CrNSal**<sup>tBu</sup> and **CrNSal**<sup>NMe<sub>2</sub></sup> in the xz and yz planes from NBO analysis. See Appendix C – Fig. C7–C12 for visualization of the  $\pi$ -interactions for oxidized complexes as well as visualization of the  $\sigma$ -interactions and lone pairs for all complexes.

DFT analysis was then used to investigate the structural and electronic nature of neutral and oxidized adducts (Table 4.4). All optimized geometries exhibit approximately linear Cr—N—B angles (ca. 175 °) suggesting similar N—B interactions in both neutral and oxidized compounds. Adduct formation is also predicted to elongate the Cr—N bond by ca. 0.05 Å in all cases. A corresponding increase in nitride spin density is predicted for neutral derivatives upon adduct formation (Fig. 4.9A). These results are corroborated by solution EPR measurements (298 K) that reveal an increase in nitride  $^{14}\text{N}$  hyperfine splitting as a result of spin polarization of the elongated Cr—N bond (see previous section).<sup>41</sup> Interestingly, this effect is also predicted for the ligand radical complex. The spin density plot of this species also reveals radical localization suggesting that reactivity with the borane has little effect on the phenoxyl radical (Fig. 4.9B). Although adduct formation is not experimentally observed for the Cr(VI) species, DFT optimizations suggest an adduct with similar bonding

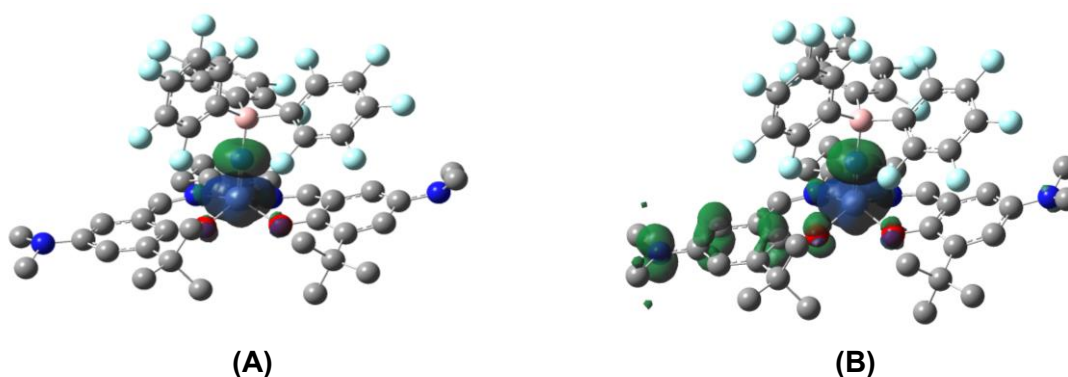


**Figure 4.9.** Spin density plots of (A)  $\text{Cr}(\text{N}-\text{B}(\text{C}_6\text{F}_5)_3)\text{Sal}^{\text{NMe}_2}$  and (B) broken-symmetry singlet  $[\text{Cr}^{\text{V}}(\text{N}-\text{B}(\text{C}_6\text{F}_5)_3)\text{Sal}^{\text{NMe}_2}]^{\cdot+}$ . See Appendix C – Fig. C13 for spin density plots of  $\text{Cr}(\text{N}-\text{B}(\text{C}_6\text{F}_5)_3)\text{Sal}^{\text{tBu}}$ ,  $\text{Cr}(\text{N}-\text{B}(\text{C}_6\text{F}_5)_3)\text{Sal}^{\text{CF}_3}$  as well as triplet  $[\text{Cr}^{\text{V}}(\text{N}-\text{B}(\text{C}_6\text{F}_5)_3)\text{Sal}^{\text{NMe}_2}]^{\cdot+}$ .

**Table 4.4.** Calculated values for neutral and oxidized **Cr(N—B(C<sub>6</sub>F<sub>5</sub>)<sub>3</sub>)Sal<sup>R</sup>**. Bracketed values indicate difference (adduct – free nitride).<sup>a</sup>

Compound	Nitride SD	Cr SD	Cr—N Bond length / Å	Cr—N—B Bond angle / °
<b>Cr(N—B(C<sub>6</sub>F<sub>5</sub>)<sub>3</sub>)Sal<sup>CF<sub>3</sub></sup></b>	-0.517 (+0.086)	1.574 (+0.120)	1.576 (+0.055)	176.6
<b>Cr(N—B(C<sub>6</sub>F<sub>5</sub>)<sub>3</sub>)Sal<sup>tBu</sup></b>	-0.515 (+0.088)	1.574 (+0.126)	1.581 (+0.057)	175.1
<b>Cr(N—B(C<sub>6</sub>F<sub>5</sub>)<sub>3</sub>)Sal<sup>NMe<sub>2</sub></sup></b>	-0.499 (+0.074)	1.552 (+0.108)	1.582 (+0.057)	174.9
<b>[Cr<sup>VI</sup>(N—B(C<sub>6</sub>F<sub>5</sub>)<sub>3</sub>)Sal<sup>CF<sub>3</sub></sup>]<sup>+</sup></b>	--	--	1.558 (+0.055)	174.5
<b>[Cr<sup>VI</sup>(N—B(C<sub>6</sub>F<sub>5</sub>)<sub>3</sub>)Sal<sup>tBu</sup>]<sup>+</sup></b>	--	--	1.554 (+0.049)	174.4
<b>[Cr<sup>V</sup>(N—B(C<sub>6</sub>F<sub>5</sub>)<sub>3</sub>)Sal<sup>NMe<sub>2</sub></sup>]<sup>•+b</sup></b>	-0.499 (+0.074)	1.552 (+0.108)	1.587 (+0.067)	173.7

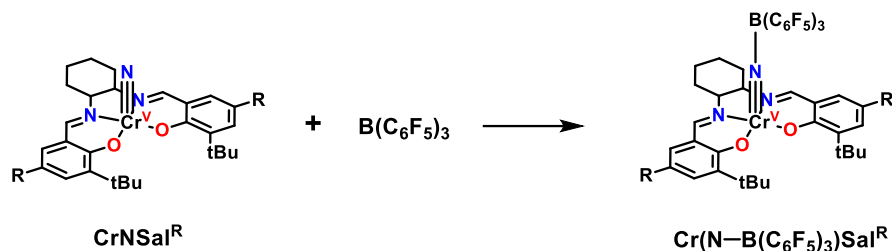
<sup>a</sup>See Chapter 2 for neutral nitride values and Chapter 3 for oxidized nitride values.

<sup>b</sup>Calculated value corresponds to broken-symmetry singlet solution.

Energetic analysis of the neutral and oxidized adducts were then employed to gain further insight into the observed reactivities. Table 4.5 denotes the energy for the reaction of neutral complexes with tris(pentafluorophenyl) borane depicted in Scheme 4.2 which can be calculated using Equation (1). The reactivity of borane with neutral complexes is predicted to be thermodynamically favourable consistent with experimentally observed adduct formation. The reactivity of borane with the CF<sub>3</sub> derivative is predicted to be the least favourable likely because this species is calculated to exhibit the smallest nitride partial charge due to the strong electron-withdrawing nature of the CF<sub>3</sub> substituent. The tBu and NMe<sub>2</sub> derivatives support this trend, with the NMe<sub>2</sub> substituent conferring the largest nitride negative charge and thus exhibiting the largest energy change.



**Scheme 4.2.** Reactivity of **CrNSal<sup>CF3</sup>**, **CrNSal<sup>tBu</sup>** and **CrNSal<sup>NMe2</sup>** with tris(pentafluorophenyl) borane.



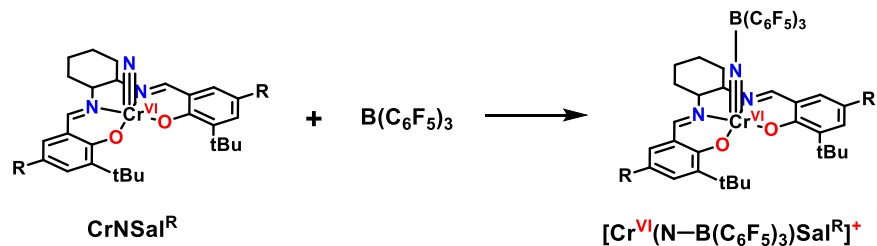
$$\Delta E_{\text{reaction}} = E_{\text{Cr}(\text{N}-\text{B}(\text{C}_6\text{F}_5)_3)\text{Sal}^{\text{R}}} - (E_{\text{CrNSal}^{\text{R}}} + E_{\text{B}(\text{C}_6\text{F}_5)_3}) \quad (1)$$

**Table 4.5.** Total energy change upon reactivity of **CrNSal<sup>R</sup>** with tris(pentafluorophenyl) borane.

Complex	$\Delta E_{\text{reaction}} / \text{kcal mol}^{-1}$
<b>Cr(N—B(C<sub>6</sub>F<sub>5</sub>)<sub>3</sub>)Sal<sup>CF3</sup></b>	-13.2
<b>Cr(N—B(C<sub>6</sub>F<sub>5</sub>)<sub>3</sub>)Sal<sup>tBu</sup></b>	- 20.2
<b>Cr(N—B(C<sub>6</sub>F<sub>5</sub>)<sub>3</sub>)Sal<sup>NMe2</sup></b>	- 21.3

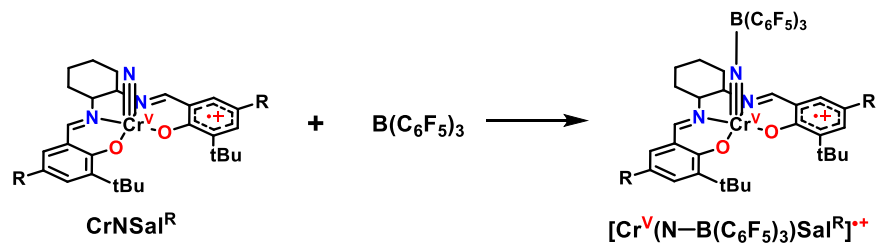
The reactivity of the Cr(VI) complexes with tris(pentafluorophenyl) borane depicted in Scheme 4.3 is calculated to be endothermic (Table 4.6) using Equation (2). Very little energy change is predicted for the reaction of **[Cr<sup>VI</sup>NSal<sup>tBu</sup>]<sup>+</sup>** with borane ( $\Delta E = + 0.1 \text{ kcal mol}^{-1}$ ), while adduct formation for **[Cr<sup>VI</sup>NSal<sup>CF3</sup>]<sup>+</sup>** is predicted to be considerably more endothermic ( $\Delta E = +7.3 \text{ kcal mol}^{-1}$ ). It is likely that this difference derives from partial charge predictions on the nitride, as the value for **[Cr<sup>VI</sup>NSal<sup>tBu</sup>]<sup>+</sup>** is calculated to be *ca.* 1.6 times larger than that of **[Cr<sup>VI</sup>NSal<sup>CF3</sup>]<sup>+</sup>**. Interestingly, calculations predict the reactivity of **[Cr<sup>V</sup>NSal<sup>NMe2</sup>]<sup>•+</sup>** with borane depicted in Scheme 4.4 to be considerably exothermic ( $\Delta E = - 11.4 \text{ kcal mol}^{-1}$ ). These results are consistent with UV-vis-NIR data that suggest adduct formation occurs readily for **[Cr<sup>V</sup>NSal<sup>NMe2</sup>]<sup>•+</sup>** and the neutral complexes, while no reactivity is observed for **[Cr<sup>VI</sup>NSal<sup>CF3</sup>]<sup>+</sup>** and **[Cr<sup>VI</sup>NSal<sup>tBu</sup>]<sup>+</sup>**.

**Scheme 4.3.** Reactivity of  $[\text{Cr}^{\text{VI}}\text{NSal}^{\text{CF}_3}]^+$  and  $[\text{Cr}^{\text{VI}}\text{NSal}^{\text{tBu}}]^+$  with tris(pentafluorophenyl) borane ( $\text{R} = \text{CF}_3, \text{tBu}$ ).



$$\Delta E_{\text{reaction}} = E_{[\text{Cr}^{\text{VI}}(\text{N}-\text{B}(\text{C}_6\text{F}_5)_3)\text{Sal}^{\text{R}}]^+} - (E_{\text{CrNSal}^{\text{R}}} + E_{\text{B}(\text{C}_6\text{F}_5)_3}) \quad (2)$$

**Scheme 4.4.** Reactivity of  $[\text{Cr}^{\text{V}}\text{NSal}^{\text{NMe}_2}]^{\bullet+}$  with tris(pentafluorophenyl) borane ( $\text{R} = \text{NMe}_2$ ).



$$\Delta E_{\text{reaction}} = E_{[\text{Cr}^{\text{V}}(\text{N}-\text{B}(\text{C}_6\text{F}_5)_3)\text{Sal}^{\text{R}}]^{\bullet+}} - (E_{\text{CrNSal}^{\text{R}}} + E_{\text{B}(\text{C}_6\text{F}_5)_3}) \quad (3)$$

**Table 4.6.** Total energy change upon reactivity of oxidized complexes with tris(pentafluorophenyl) borane.

Complex	$\Delta E_{\text{reaction}} / \text{kcal mol}^{-1}$
$[\text{Cr}^{\text{VI}}(\text{N}-\text{B}(\text{C}_6\text{F}_5)_3)\text{Sal}^{\text{CF}_3}]^+$	+ 7.3
$[\text{Cr}^{\text{VI}}(\text{N}-\text{B}(\text{C}_6\text{F}_5)_3)\text{Sal}^{\text{tBu}}]^+$	+ 0.1
$[\text{Cr}^{\text{V}}(\text{N}-\text{B}(\text{C}_6\text{F}_5)_3)\text{Sal}^{\text{NMe}_2}]^{\bullet+}$	- 11.4

### 4.3. Discussion and Summary

Overall, this chapter describes the reactivity differences between neutral and oxidized Cr nitride salen complexes associated with locus the of oxidation. Nucleophilicity is observed to be a general property for neutral compounds as expected for nitride ligands bound to an early transition metal ion. This was shown by their reactivity with the Lewis acidic tris(pentafluorophenyl) borane monitored by UV-vis-NIR and EPR experiments. The nitride is calculated to have a considerable partial charge value of ca. -0.4 and is the most likely site of electrophilic attack (compared to a partial charge of -0.11 for the dimethyl amino N in **CrNSal<sup>NMe2</sup>** for example).<sup>284</sup> The nitride fragment also features the least sterically hindered environment for interaction with the bulky borane.

Metal-based oxidation results in a loss of nitride nucleophilicity. **[Cr<sup>VI</sup>NSal<sup>CF3</sup>]<sup>+</sup>** and **[Cr<sup>VI</sup>NSal<sup>tBu</sup>]<sup>+</sup>** do not react with the borane as shown by UV-vis-NIR experiments. DFT calculations predict a significant decrease in negative partial charge due to the enhanced covalency of the Cr—N triple bond. In addition, NBO calculations predict significant stabilization of  $\pi$  bonding MO's, and reactivity of Cr(VI) complexes with the borane are predicted to be endothermic. A similar result was reported in the literature for rhenium nitride complexes in 1982 by Dehnicke. The addition of trihalide boranes to **Re<sup>V</sup>NCI<sub>2</sub>(PEt<sub>2</sub>Ph)** afforded N—B adducts, while no reactivity with boranes was observed for the independently prepared **[ReN<sup>VI</sup>Cl<sub>4</sub>]<sup>-</sup>** analogue.<sup>285,286</sup> It should be noted however that this account was purely observational and no rationale was discussed. The ancillary ligands in this example are not held constant and may also impart additional reactivity effects. This trend in nucleophilicity holds for the reverse case as well. Hanack *et al.* have reported a tungsten nitride phthalocyanine complex **W<sup>V</sup>N(Pc)** that is initially unreactive towards trimethylsilyl chloride, however reduction to the W(IV) analogue using KC<sub>8</sub> affords nucleophilic properties where a Si—N adduct is formed between the nitride and silyl species.<sup>54</sup>

Herein, ligand-based oxidation was not found to inhibit nucleophilic reactivity of the nitride. The addition of 1 equivalent of borane to **[Cr<sup>V</sup>NSal<sup>NMe2</sup>]<sup>•+</sup>** affords significant changes in the absorption spectrum and is attributed to N—B adduct formation. Furthermore, the addition of borane to a solution of **[Cr<sup>V</sup>NSal<sup>NMe2</sup>]<sup>•+</sup>** was analyzed by frozen solution EPR and results in an enhancement of the **CrNSal<sup>NMe2</sup>** and **[Cr<sup>V</sup>NSal<sup>NMe2</sup>]<sup>••2+</sup>** signal intensities. Although not confirmed, it is possible that borane

coordination to both neutral and bis-oxidized species enhances corresponding signals by inhibiting aggregation and through-space interactions. On the basis of this assumption, it would be rather unsurprising that  $[\text{Cr}^{\text{V}}\text{NSal}^{\text{NMe}_2}]^{\cdot+}$  reacts with borane in this scenario. Reactivity of this complex was also extensively studied using DFT calculations. Minimal changes in nitride partial charge and  $\pi$  orbital energies in comparison to Cr(VI) species are consistent with the retention of nucleophilicity. Furthermore, energetic analysis predicts that the reaction of  $[\text{Cr}^{\text{V}}\text{NSal}^{\text{NMe}_2}]^{\cdot+}$  with borane is exothermic.

In summary, this chapter outlines the feasibility of modulating reactivity in oxidized Cr nitride salen complexes through ligand electronic effects, demonstrating the importance of metal oxidation state on nitride nucleophilicity. Additional efforts are needed to further characterize the nature of the N—B interaction for  $[\text{Cr}^{\text{V}}\text{NSal}^{\text{NMe}_2}]^{\cdot+}$  experimentally.

## 4.4. Experimental

### 4.4.1. Materials

All chemicals were of the highest quality grade and purified whenever necessary. Tris(pentafluorophenyl) borane was purchased from Sigma-Aldrich and used without further purification. Dichloromethane was dried by refluxing over calcium hydride and distilled prior to use. The tris(2,4-dibromophenyl)aminium hexafluoroantimonate radical oxidant  $[\text{N}(\text{C}_6\text{H}_3\text{Br}_2)_3][\text{SbF}_6]$  was synthesized according to published protocols.<sup>276</sup>

### 4.4.2. Instrumentation

Electronic spectra were obtained using a Cary 5000 spectrophotometer equipped with custom designed immersion fiber-optic probes with 0.1 and 1 cm path lengths. Constant temperatures were maintained with an FTS Multi-Cool Low Temperature Bath and solvent contraction was accounted for. All electron paramagnetic resonance spectra were recorded on a Bruker EMXplus spectrometer operating with a premium X-band microwave bridge and an HS resonator. EPR spectra were simulated using the EasySpin package in Matlab.<sup>238</sup>

#### 4.4.3. Reactivity Studies of Complexes with Tris(pentafluorophenyl) Borane monitored by Electronic Absorption Spectroscopy

*Neutral Species.* Under an inert atmosphere at 233 K, a total of 100  $\mu\text{L}$  containing tris(pentafluorophenyl) borane (15.8 mM in dry  $\text{CH}_2\text{Cl}_2$ ) was added in 20  $\mu\text{L}$  aliquots to 3.5 mL complex (0.45 mM in dry  $\text{CH}_2\text{Cl}_2$ ). Absorption spectra were collected immediately after each aliquot was added. Room temperature studies revealed identical spectral features.

*Oxidized Species.* Under an inert atmosphere at 233 K, 100  $\mu\text{L}$  of tris(pentafluorophenyl) borane (15.8 mM in dry  $\text{CH}_2\text{Cl}_2$ ) was added immediately to 3.5 mL complex (0.45 mM in dry  $\text{CH}_2\text{Cl}_2$ ). Absorption spectra were collected immediately upon addition. Titration of 1 equivalent borane into  $[\text{Cr}^{\text{V}}\text{NSal}^{\text{NMe}_2}]^{\bullet+}$  was facilitated by adding four successive 0.25  $\mu\text{L}$  aliquots of borane solution (15.8 mM in dry  $\text{CH}_2\text{Cl}_2$ ) into 3.5 mL complex (0.45 mM in dry  $\text{CH}_2\text{Cl}_2$ ). Spectra were taken immediately after addition of each aliquot.

#### 4.4.4. Reactivity Studies of Complexes with Tris(pentafluorophenyl) Borane monitored by Electronic Paramagnetic Resonance Spectroscopy

*Neutral Species.* Under an inert atmosphere, a 1 mL solution of tris(pentafluorophenyl) borane (1.0 mM in dry  $\text{CH}_2\text{Cl}_2$ ) was added to a 1 mL solution of complex (1.0 mM in dry  $\text{CH}_2\text{Cl}_2$ ) and allowed to stir for 1 hour at room temperature. A slight colour change for all compounds was noticed immediately upon mixing and persisted for the duration of the stirring. A small sample was transferred to a capillary and placed in an EPR tube for solution EPR analysis (298 K). A portion of the stock solution was diluted and analyzed by UV-vis to ensure spectra matched previously recorded UV-vis data.

*Oxidized Species.* Under an inert atmosphere, 100  $\mu\text{L}$  of tris(pentafluorophenyl) borane (20 mM in dry  $\text{CH}_2\text{Cl}_2$ ) was added to a 4 mL solution of electrochemically generated  $[\text{Cr}^{\text{V}}\text{NSal}^{\text{NMe}_2}]^{\bullet+}$  (0.5 mM in dry  $\text{CH}_2\text{Cl}_2$ ) and allowed to stir for 20 minutes at 253 K. An immediate colour change from pink to purple was noticed upon addition and persisted for the duration of the stirring. A 40  $\mu\text{L}$  portion of the stock solution was transferred to a capillary and placed in an EPR tube for solution EPR analysis (298 K). A

200  $\mu\text{L}$  portion of the stock as also diluted to 400  $\mu\text{L}$  (0.25 mM final concentration). 250  $\mu\text{L}$  of this solution was then pipetted into an EPR tube and frozen for analysis at 100 K.

#### 4.4.5. Theoretical Analysis

Geometry optimizations were all performed using the Gaussian 16 program (Revision A.03)<sup>241</sup> employing the B3LYP functional in combination with the 6-31g\* basis set.<sup>242</sup> Frequency calculations performed on the same functional/basis set confirmed optimized structures were at a global minimum. Single point calculations for Mulliken charge analysis as well as NBO calculations<sup>282,287</sup> were performed using the B3P86 functional and the TZVP basis set of Ahlrichs.<sup>245,246</sup> All calculations apart from the optimization of neutral and oxidized adducts employed a polarizable continuum model (PCM) for  $\text{CH}_2\text{Cl}_2$  ( $\epsilon=8.93$ ) for all atoms.<sup>242,247,248</sup> The PCM model resulted in convergence errors for the **CrNSal**<sup>CF<sub>3</sub></sup> adduct. Thus, all neutral and oxidized adducts were optimized in the gas-phase, and single point calculations for spin density and energetic analysis employed a PCM for  $\text{CH}_2\text{Cl}_2$ .

## Chapter 5. Ongoing and Future Directions

### 5.1. Thesis Summary

This thesis presents the synthesis, oxidation and nucleophilic reactivity of a series of chromium nitride complexes employing non-innocent salen ligands. Through combined experimental and computational techniques, investigation of electronic structure was possible, allowing for a description of reactivity based on the oxidation locus. Outlined below is the ongoing and future work that build on the results described in the previous chapters.

### 5.2. Chapter 2 and Chapter 3

Chapter 2 outlines the synthesis and characterization of **CrNSal<sup>CF<sub>3</sub></sup>**, **CrNSal<sup>tBu</sup>** and **CrNSal<sup>NMe<sub>2</sub></sup>**, while Chapter 3 details the oxidation of these complexes. Strong evidence is provided supporting metal-based oxidation for complexes bearing the electron-withdrawing CF<sub>3</sub> and moderately electron-donating tBu *para*-R substituents, while ligand radical formation is supported upon substitution with the strongly electron-donating NMe<sub>2</sub> substituent. Although the oxidized complexes are stable in solution at room temperature, they decomposed upon attempted isolation in the solid state. Additional experiments could be conducted to provide further evidence for the assigned oxidation states, provided the samples remain in solution.

#### 5.2.1. Variable Temperature Evans Method on [Cr<sup>V</sup>NSal<sup>NMe<sub>2</sub></sup>]<sup>•+</sup>

Spectroscopic and theoretical investigations of oxidized **CrNSal<sup>NMe<sub>2</sub></sup>** support formation of a ligand radical. Frozen solution EPR measurements (20 K) suggest the presence of considerable magnetic coupling between the Cr(V) *d*<sup>1</sup> metal center and ligand radical to afford [Cr<sup>V</sup>NSal<sup>NMe<sub>2</sub></sup>]<sup>•+</sup> as an EPR silent species. Unfortunately, the current data cannot unambiguously discriminate whether this is the result of a ferromagnetic interaction with a large zero-field splitting (ZFS) component,<sup>161,269,270</sup> or whether the coupling is antiferromagnetic affording a diamagnetic species.<sup>158,271</sup> Magnetic susceptibility measurements *via* Evans Method reveals a magnetic moment of  $\mu_{\text{eff}} = 2.82$  (2 unpaired electrons) suggesting the formation of a triplet (*S* = 1) species at room temperature (Fig.

5.1). Interestingly, density functional theory (DFT) calculations predict the broken-symmetry singlet structure to be lower in energy by 0.2 kcal mol<sup>-1</sup> in comparison to the triplet. We questioned whether the experimentally measured spin state at room temperature corresponds to a populated ( $S = 1$ ) excited state, with a singlet ground state as predicted by DFT. Variable temperature (VT) Evans Method experiments in the 198 – 298 K range (in CD<sub>2</sub>Cl<sub>2</sub>) should be conducted in order to probe this further.

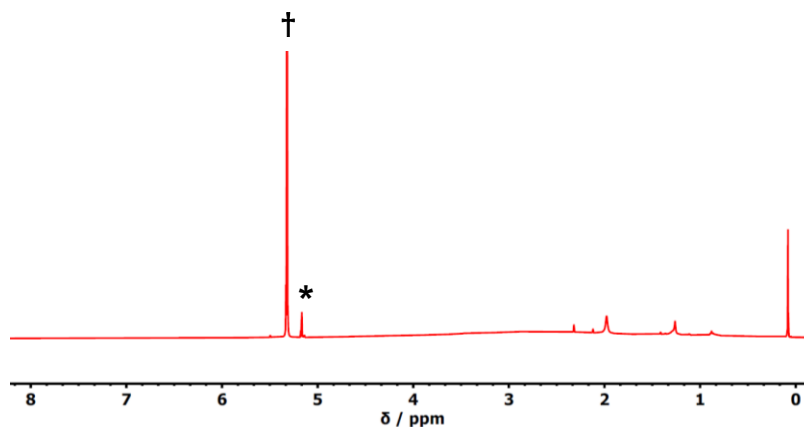


**Figure 5.1.** <sup>1</sup>H NMR analysis of **[Cr<sup>V</sup>NSal<sup>NMe2</sup>]<sup>•+</sup>** at 298 K in CD<sub>2</sub>Cl<sub>2</sub> oxidized using AgSbF<sub>6</sub> (0.65 V vs F<sub>c</sub><sup>+</sup>/F<sub>c</sub>).<sup>266</sup> \* Denotes the solvent peak. † Denotes the paramagnetically shifted solvent peak used as a reference for magnetic susceptibility *via* Evans Method.

Evans Method measures the downfield NMR shift of an inert reference (typically the solvent) due to the presence of a dissolved paramagnetic material in order to determine the magnetic moment of that material.<sup>288</sup> This is accomplished using an NMR tube insert where the reference sample (contained in the inner tube) is immersed in a solution containing the dissolved paramagnetic material (outer tube). The difference in chemical shift ( $\Delta\delta$ ) is used to obtain the molar susceptibility ( $\chi_m$ ) using Equation 1, which can then be used to determine the effective magnetic moment ( $\mu_{eff}$ ) in Equation 2 (where  $M_a$  and  $c_A$  represent the molar mass and concentration of the paramagnetic material, and  $\chi_d$  is the diamagnetic correction factor). If a weakly antiferromagnetically-coupled electronic structure is the ground state for **[Cr<sup>V</sup>NSal<sup>NMe2</sup>]<sup>•+</sup>**, then a VT Evans Method experiment could show a decrease in  $\mu_{eff}$  with decreasing temperature.<sup>289–293</sup> Subsequent



measurements from low to high temperature should also be conducted in order to confirm the reversibility of any change in  $\mu_{eff}$ .

$$\chi_m = \frac{3M_a\Delta\delta}{4\pi c_A 10^6} - \chi^d \quad (1)$$

$$\mu_{eff} = 2.83\sqrt{\chi_m T} \quad (2)$$

### 5.2.2. Infrared Spectroscopy

Infrared (IR) spectroscopy studies are ongoing and can be used to further probe the Cr oxidation state by monitoring changes in the nitride stretching frequencies. The solution IR spectra of **CrNSal<sup>NMe2</sup>** and **CrNSal<sup>tBu</sup>** feature a moderately intense band at 1020 cm<sup>-1</sup> assigned to the Cr—N stretching frequency,<sup>227,294,295</sup> while this band is observed as a shoulder at 1029 cm<sup>-1</sup> for **CrNSal<sup>CF3</sup>** (Fig. 5.2A and Table 5.1). Interestingly, oxidation results in a loss of these features (Fig. 5.2B), with new bands observed at slightly higher energy in the [**Cr<sup>VI</sup>NSal<sup>tBu</sup>**]<sup>•+</sup> and [**Cr<sup>V</sup>NSal<sup>NMe2</sup>**]<sup>•+</sup> spectra (1110 and 1050 cm<sup>-1</sup> respectively) likely corresponding to the nitride stretch in the oxidized versions. Unfortunately, the [**Cr<sup>VI</sup>NSal<sup>CF3</sup>**]<sup>•+</sup> spectrum contains intense absorptions in the energy region that the new nitride stretch is expected to occur, making characterization of this band difficult. Interestingly however, [**Cr<sup>VI</sup>NSal<sup>tBu</sup>**]<sup>•+</sup> features a larger shift in the nitride stretch ( $\Delta E = + 90$  cm<sup>-1</sup>) in comparison to [**Cr<sup>V</sup>NSal<sup>NMe2</sup>**]<sup>•+</sup> ( $\Delta E = + 30$  cm<sup>-1</sup>) in-line with a stronger Cr—N bond for the Cr(VI) derivative in agreement with DFT results outlined in Section 4.1.3. Additional experiments are needed to confirm whether these new frequencies at higher energy correspond to the new nitride stretching vibrations. The nitride IR stretching vibrations could be further probed through labelling experiments where samples containing 50% <sup>15</sup>N labelled nitride are prepared. IR measurements on the labelled samples are expected to result in a splitting of the nitride stretching frequency, with the Cr—<sup>15</sup>N stretch occurring at slightly lower energy.<sup>296,297</sup> Oxidation of this sample should thus result in a shift of *both* the <sup>14</sup>N and <sup>15</sup>N nitride bands, confirming the assignment of the new peaks at higher energy.

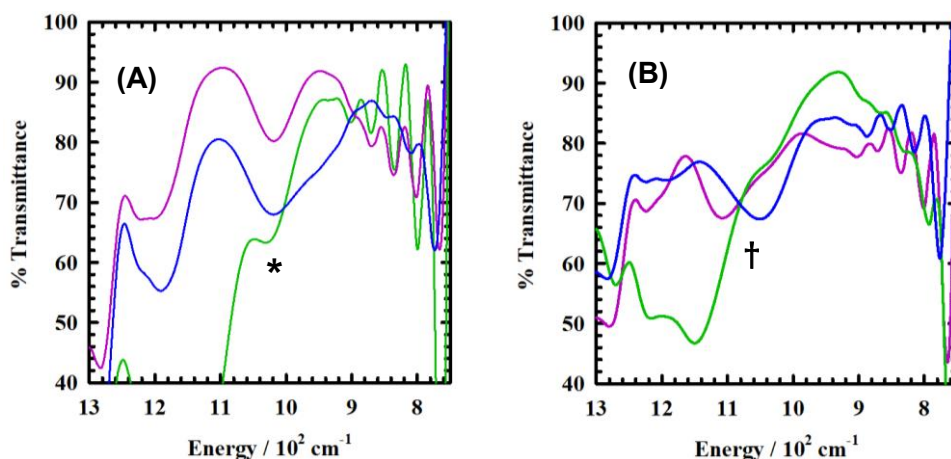


**Figure 5.2.** Solution IR spectra showing the nitride stretching frequency of **(A)** neutral (\*) and **(B)** oxidized (†) **CrNSal<sup>CF3</sup>** (green), **CrNSal<sup>tBu</sup>** (purple), and **CrNSal<sup>NMe2</sup>** (blue). Compounds were oxidized using  $[\text{N}(\text{C}_5\text{H}_3\text{Br}_2)_3][\text{SbF}_6]$ . Conditions: 0.5 mM,  $\text{CH}_2\text{Cl}_2$ . See Appendix D – Fig. D1 & D2 for full spectra.

**Table 5.1.** Tentative assignment of nitride stretching frequencies of neutral and oxidized **CrNSal<sup>CF3</sup>**, **CrNSal<sup>tBu</sup>**, and **CrNSal<sup>NMe2</sup>** in  $\text{cm}^{-1}$ . Bracketed values correspond to the difference (oxidized – neutral).

Compound	$\nu_{\text{Cr}-\text{N}}$ (neutral)	$\nu_{\text{Cr}-\text{N}}$ (oxidized)
<b>CrNSal<sup>CF3</sup></b>	1029	--
<b>CrNSal<sup>tBu</sup></b>	1020	1110 (90)
<b>CrNSal<sup>NMe2</sup></b>	1020	1050 (30)

### 5.2.3. X-ray Absorption Spectroscopy

X-ray absorption spectroscopy (XAS) studies can be conducted on frozen solution samples and could be useful in further probing the Cr oxidation state. The pre-edge region (resulting from  $1s \rightarrow 3d$  transitions) is highly sensitive to metal local geometry and electronic structure in transition metal complexes.<sup>298–300</sup> An increase in the pre-edge energy can thus be correlated to an increase in oxidation state. Neutral complexes should first be analyzed in order to provide baseline data for comparison to oxidized samples. There have been numerous reports of the characterization of Cr(V) complexes by XAS.<sup>301–304</sup> In one example by Hodgson, an intense pre-edge absorption feature centred at ~ 5990 eV was found to increase by 1 eV upon a change of oxidation state from Cr(IV) to Cr(V)

for high-valent oxo and nitrido porphyrin complexes.<sup>304</sup> Herein, the oxidation of **CrNSal**<sup>CF<sub>3</sub></sup> and **CrNSal**<sup>tBu</sup> to Cr(VI) is expected to deliver a corresponding increase in the pre-edge energy by *ca.* 1 eV.<sup>305,306</sup> Additionally, the XAS spectrum of an oxidized sample of **CrNSal**<sup>NMe<sub>2</sub></sup> should exhibit a similar pre-edge energy in comparison to the neutral form.

## 5.3. Chapter 4

Chapter 4 outlines the reactivities of **CrNSal**<sup>CF<sub>3</sub></sup>, **CrNSal**<sup>tBu</sup> and **CrNSal**<sup>NMe<sub>2</sub></sup> as well as oxidized versions. Nucleophilicity was determined to be a general property for neutral compounds as evidenced by their interaction with tris(pentafluorophenyl) borane. UV-vis-NIR experiments suggest that nucleophilicity is conserved upon formation of **[Cr<sup>V</sup>NSal<sup>NMe<sub>2</sub></sup>]<sup>•+</sup>**, while no reactivity with borane is observed for **[Cr<sup>VI</sup>NSal<sup>CF<sub>3</sub></sup>]<sup>+</sup>** and **[Cr<sup>VI</sup>NSal<sup>tBu</sup>]<sup>+</sup>**.

### 5.3.1. X-ray Crystallography

Additional experiments should be conducted in order to confirm whether reactivity between **[Cr<sup>V</sup>NSal<sup>NMe<sub>2</sub></sup>]<sup>•+</sup>** and tris(pentafluorophenyl) borane involves N—B interaction to afford the corresponding nitride adduct **[Cr<sup>V</sup>(N—B(C<sub>6</sub>F<sub>5</sub>)<sub>3</sub>)Sal<sup>NMe<sub>2</sub></sup>]<sup>•+</sup>**. The isolation of suitable X-ray quality crystals for **[Cr<sup>V</sup>NSal<sup>NMe<sub>2</sub></sup>]<sup>•+</sup>** has been unsuccessful and remains an ongoing challenge. Future work should continue in this regard and should also focus on X-ray crystallographic studies of **[Cr<sup>V</sup>(N—B(C<sub>6</sub>F<sub>5</sub>)<sub>3</sub>)Sal<sup>NMe<sub>2</sub></sup>]<sup>•+</sup>**. Ideally, adduct formation can affect crystal packing/morphology and potentially enhance single-crystal growth for solid-state characterization. Coordination sphere metrical parameters are expected to exhibit a significant degree of asymmetry about the equatorial plane consistent with radical localization.<sup>161,174,180,184</sup> It is possible that adduct formation could affect the degree of localization, however a strongly delocalized ligand radical is not likely formed based on the absence of characteristic sharp and intense near-infrared intervalence charge transfer (IVCT) bands in the absorption spectrum (Section 4.1.1).<sup>249,258,259</sup>

### 5.3.2. Reactivity Profile of Cr Complexes with Tris(pentafluorophenyl) Borane

Density functional theory was utilized to predict changes in partial charges and Cr—N bonding parameters, as well as provide information on the relative energetics of adduct formation. These calculations sufficiently accounted for the experimentally observed reactivity differences of tris(pentafluorophenyl) borane with Cr(VI) and ligand radical complexes. Furthermore, optimizations provided insight into the predicted geometries of adducts. Future work in this regard should focus on probing the nature of the N—B interaction using theory, as this can provide information on the molecular orbitals involved and further inform on the reactivity profiles of neutral complexes and  $[\text{Cr}^{\text{V}}\text{NSa}^{\text{NMe}_2}]^{.+}$  with Lewis acids. DFT can be used to obtain the energy for structures optimized at various N—B distances ( $r$ ), allowing for the construction of a reaction profile. The interaction is expected to follow a Lennard-Jones potential curve typically exhibited by Lewis acid-base adduct formation,<sup>307–309</sup> however calculations could also predict the presence of a transition state (Fig. 5.3).

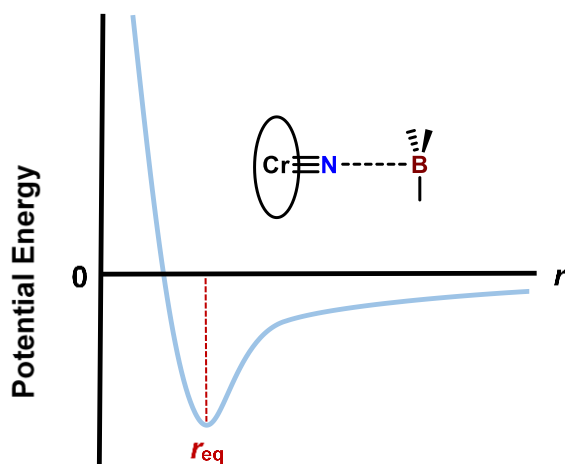


**Figure 5.3.** Lennard-Jones-type reaction profile for the N—B interaction.  $r_{\text{eq}}$  represents the equilibrium N—B distance in adducts.

A number of reports on metal nitrides suggest that the nitride lone pair is too low in energy to be involved in reactivity, and conclude that Cr—N  $\pi$  bonding orbitals are instead likely responsible for reactivity.<sup>36,38</sup> In this work, DFT calculations predicted that

the lone pair is ca. 230 kcal mol<sup>-1</sup> lower in energy than the  $\pi$  bonding interactions in agreement with this assignment, however optimizations predict a linear Cr—N—B bond angle (ca. 175 °) predicting involvement of the lone pair in the adduct. Future work should be geared at probing this further using DFT calculations. Reaction profiles can be constructed *via* optimization of the reactants at a series of constant N—B distances. These potential energy surface (PES) calculations can inform whether a bent interaction is favoured at greater distances, with a linear conformation stabilized as  $r_{eq}$  is approached (Fig. 5.4). Natural bond order (NBO) calculations conducted on each reaction coordinate can be used to visualize and provide information on the orbitals involved in reactivity. This will allow for a better understanding of the N—B interaction and whether a change from bent to linear approach of the borane is associated with a transition state.

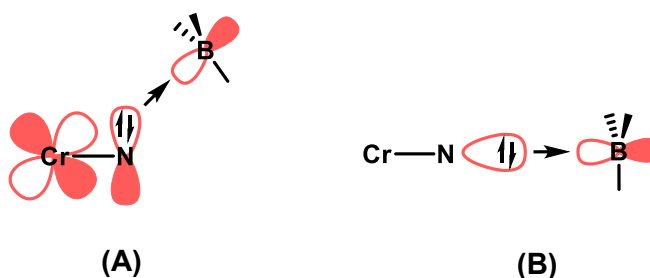


**Figure 5.4.** Interaction of filled Cr-nitride molecular orbitals with the empty borane p orbital. **(A)** A bent approach suggests involvement of the Cr—N  $\pi$  bonding orbitals in adduct formation. **(B)** A linear approach suggests involvement of the nitride lone pair in adduct formation.

### 5.3.3. Reactivity of [Cr<sup>VI</sup>NSal<sup>CF3</sup>]<sup>+</sup> and [Cr<sup>VI</sup>NSal<sup>tBu</sup>]<sup>+</sup> with Nucleophiles

Experimental results suggest that [Cr<sup>VI</sup>NSal<sup>CF3</sup>]<sup>+</sup> and [Cr<sup>VI</sup>NSal<sup>tBu</sup>]<sup>+</sup> do not react with tris(pentafluorophenyl) borane upon metal-based oxidation. This was rationalized by DFT calculations that predict a decrease in the nitride partial charge and lowering of the Cr—N molecular orbital (MO) manifold. Future work should focus on exploring whether metal-based oxidation affords an electrophilic nitride that reacts with nucleophiles such as phosphines.

In 2000, Brown *et al.* discussed charge effects on the reaction rate between neutral and cationic rhenium(V) oxo complexes with triphenylphosphine (Fig. 5.5A and 5.5B

respectively).<sup>310</sup> This was accomplished by substitution of the anionic tris(pyrazolyl)borate ligand for the neutral tris(pyrazolyl)methane ligand. It was reasoned that this 1-atom modification in the tris(pyrazolyl) backbone would afford a change in charge without significant perturbation of other steric or electronic properties. Kinetic measurements determined that formation of the Re(III)-phosphine adduct proceeded 1000 times *faster* for the cationic complex in comparison to the neutral analogue.

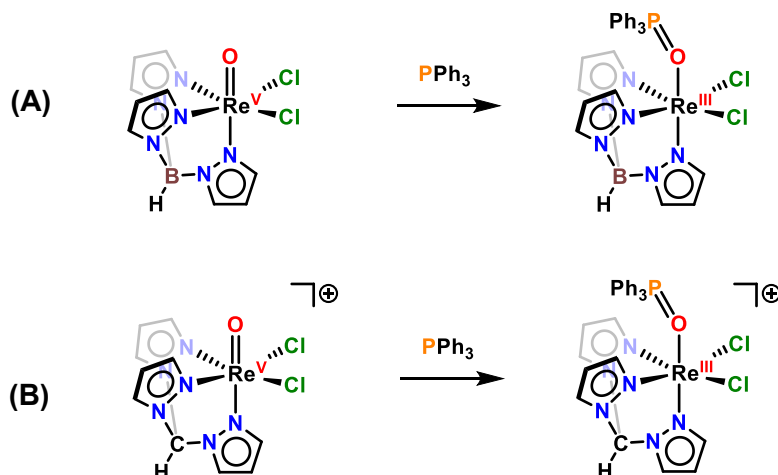


**Figure 5.5.** Reactivity of **(A)** neutral and **(B)** cationic Re(V) oxo complexes by triphenyl phosphine.

The observed reaction rates were rationalized by considering the effect of charge on the molecular orbitals (MO) involved in the reaction. Increasing the overall charge has the effect of decreasing the energy of all molecular orbitals. In particular, the energy of the  $\text{Re}-\text{O} \pi^*$  MO is lowered, which is the site of nucleophilic attack by the phosphine lone pair (Fig. 5.6).<sup>310</sup> Thus, the reactivity with phosphine is more favourable in the cationic complex due to enhanced electrophilicity of the oxo ligand, and the rate is greater. Due to the isoelectronic nature of oxo and nitride ligands, it stands to reason that this effect should also be observed for nitride complexes. Indeed, the  $\text{M}-\text{N} \pi^*$  orbitals have been cited as key reaction terminals in various electrophilic nitride complexes.<sup>37,57,71,311</sup>

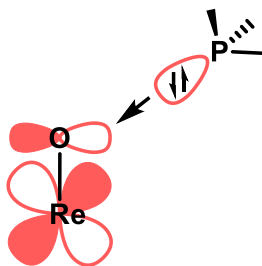


**Figure 5.6.** The orbitals involved in the reactivity of Re(V) oxo complexes by Brown include the Re—O  $\pi^*$  combination and phosphine lone pair.<sup>310</sup>

Similar to the charge effect discussed by Brown, all three **CrNSal<sup>R</sup>** complexes were oxidized to a mono-cation, suggesting an overall increase in electrophilic reactivity. However, the locus of oxidation (metal vs. ligand) is expected to affect the relative reaction rates with phosphine. DFT calculations outlined in Section 4.1.3 predict that formation of **[Cr<sup>VI</sup>NSal<sup>CF3</sup>]<sup>+</sup>** and **[Cr<sup>VI</sup>NSal<sup>tBu</sup>]<sup>+</sup>** results in greater stabilization of the Cr—N bonding orbitals energies (as well as the  $\sigma$  bonding orbitals and nitride lone pairs) in comparison to **[Cr<sup>V</sup>NSal<sup>NMe2</sup>]<sup>•+</sup>**. Analysis of the Cr—N  $\pi^*$  antibonding combinations (as well as the  $\sigma^*$  MOs) in Table 5.2 reveals that these orbitals also lower in energy upon oxidation, making them more energetically suited for reactivity with nucleophiles. The stabilization of the  $\pi^*$  orbitals in **[Cr<sup>VI</sup>NSal<sup>CF3</sup>]<sup>+</sup>** and **[Cr<sup>VI</sup>NSal<sup>tBu</sup>]<sup>+</sup>** is more pronounced in comparison to **[Cr<sup>V</sup>NSal<sup>NMe2</sup>]<sup>•+</sup>** ( $\Delta E_{\pi^*}$  in kcal mol<sup>-1</sup>: CF<sub>3</sub>: - 58.01 > tBu: - 41.42 >> NMe<sub>2</sub>: - 14.96) suggesting greater electrophilic properties for Cr(VI).

**Table 5.2.** Relative energies of  $\pi^*$  and  $\sigma^*$  antibonding interactions in kcal mol<sup>-1</sup>. Bracketed values correspond to the difference (oxidized – neutral values).<sup>a</sup>

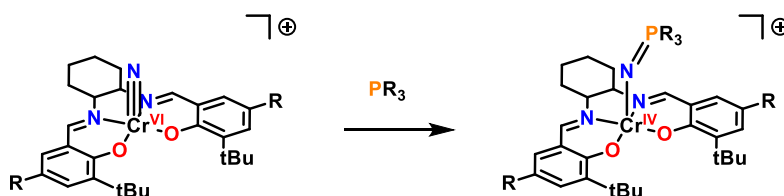
Compound	$\pi^*$	$\sigma^*$
CrNSal <sup>CF3</sup>	7.42	39.92
CrNSal <sup>tBu</sup>	13.57	45.90
CrNSal <sup>NMe2</sup>	14.63	46.81
[Cr <sup>VI</sup> NSal <sup>CF3</sup> ] <sup>+</sup>	- 50.59 (- 58.01)	- 26.76 (- 66.68)
[Cr <sup>VI</sup> NSal <sup>tBu</sup> ] <sup>+</sup>	- 27.85 (- 41.42)	-7.08 (- 52.98)
[Cr <sup>V</sup> NSal <sup>NMe2</sup> ] <sup>+,b</sup>	-0.33 (- 14.96)	32.24 (- 14.57)

<sup>a</sup>Values are obtained from the same NBO calculations discussed in Section 4.1.3.

<sup>b</sup>Calculated value corresponds to the broken-symmetry singlet structure. See Appendix D – Fig. D3-D8 for visualization of molecular orbitals.

Phosphine reactivity should be initially explored as this reaction is often used as an indicator of nitride electrophilicity (Fig. 5.7).<sup>7</sup> UV-vis and <sup>31</sup>P NMR can provide a straightforward approach to monitoring the reactivity. Neutral compounds should be tested as well, however these species are nucleophilic and are not expected to react with phosphines. The ability to turn on Cr nitride electrophilicity *via* oxidation is of current interest to further explore the reactivity of these interesting systems in 2-electron pathways. Depending on the results with phosphine, reactivity with other nucleophilic small molecules such as CO,<sup>63,312</sup> isocyanides,<sup>22,313</sup> carbenes,<sup>314</sup> and alkenes,<sup>71,72,105,315</sup> could be pursued.

**Scheme 5.1.** Potential reactivity of [Cr<sup>VI</sup>NSal<sup>CF3</sup>]<sup>+</sup> and [Cr<sup>VI</sup>NSal<sup>tBu</sup>]<sup>+</sup> with phosphines (R = alkyl, aryl).





In summary, although metal-based oxidation results in a loss of nucleophilicity, DFT calculations suggest that the Cr(VI) species will exhibit enhanced electrophilic properties at the nitride relative to the ligand radical and neutral complexes. The nucleophilic reactivities of **CrNSal<sup>R</sup>** derivatives as well as **[Cr<sup>V</sup>NSal<sup>NMe2</sup>]<sup>•+</sup>** have been discussed, and future endeavors in studying Cr(VI) will serve to broaden the scope of reactivity tuning of Cr nitride salen complexes through ligand electronics.

## 5.4. Conclusion

This thesis demonstrates that the locus of oxidation in Cr nitride salen complexes can be influenced through the modulation of *para*-R phenoxide substituents of varying electron donating abilities. This led to remarkable reactivity differences at the nitride, where nucleophilicity was lost upon metal-based oxidation and conserved upon formation of a ligand radical. These differences were rationalized by DFT analysis of the complexes. In all, this work can serve to further our understanding of the interesting nature of metal nitride triple bonds, and how ligand and metal electronic effects can be exploited to influence reactivity.

## 5.5. Experimental

### 5.5.1. Materials

All chemicals were of the highest quality grade and purified whenever necessary. Dichloromethane was dried by refluxing over calcium hydride and distilled prior to use. The tris(2,4-dibromophenyl)aminium hexafluoroantimonate radical oxidant **[N(C<sub>6</sub>H<sub>3</sub>Br<sub>2</sub>)<sub>3</sub>][SbF<sub>6</sub>]** was synthesized according to published protocols.<sup>276</sup>

### 5.5.2. Instrumentation

IR spectra were recorded on a PerkinElmer UTAR Two FT-IR Spectrometer using a 1 mm Specac transmission cell.

### 5.5.3. Theoretical Analysis

Geometry optimizations were all performed using the Gaussian 16 program (Revision A.03)<sup>241</sup> employing the B3LYP functional in combination with the 6-31g\* basis set.<sup>242</sup> Frequency calculations performed on the same functional/basis set confirmed optimized structures were at a global minimum. Single point and NBO calculations<sup>282,287</sup> were performed using the B3P86 functional and the TZVP basis set of Ahlrichs.<sup>245,246</sup> All calculations employed a polarizable continuum model (PCM) for CH<sub>2</sub>Cl<sub>2</sub> ( $\epsilon=8.93$ ) for all atoms.<sup>242,247,248</sup>

## References

- (1) Fritzsche, J.; Struve, H. *J. Prakt. Chem.* **1847**, 41, 103.
- (2) Eklund, P.; Kerdsonpanya, S.; Alling, B. *J. Mater. Chem. C* **2016**, 4 (18), 3905–3914.
- (3) Quintela, C. X.; Podkaminer, J. P.; Luckyanova, M. N.; Paudel, T. R.; Thies, E. L.; Hillsberry, D. A.; Tenne, D. A.; Tsymbal, E. Y.; Chen, G.; Eom, C.-B.; Rivadulla, F. *Adv. Mater.* **2015**, 27 (19), 3032–3037.
- (4) Pan, Z.; Sun, H.; Zhang, Y.; Chen, C. *Phys. Rev. Lett.* **2009**, 102 (5), 55503.
- (5) Dehnicke, K.; Strähle, J. *Angew. Chemie Int. Ed. English* **1981**, 20 (5), 413–426.
- (6) Dehnicke, K.; Strähle, J. *Angew. Chemie Int. Ed. English* **1992**, 31 (8), 955–978.
- (7) Smith, J. M. *Reactive Transition Metal Nitride Complexes*; Progress in Inorganic Chemistry; 2014.
- (8) MacKay, B. A.; Fryzuk, M. D. *Chem. Rev.* **2004**, 104 (2), 385–402.
- (9) Erisman, J. W.; Sutton, M. A.; Galloway, J.; Klimont, Z.; Winiwarter, W. *Nat. Geosci.* **2008**, 1 (10), 636–639.
- (10) Chatt, J.; Dilworth, J. R.; Richards, R. L. *Chem. Rev.* **1978**, 78 (6), 589–625.
- (11) MacLeod, K. C.; Holland, P. L. *Nat. Chem.* **2013**, 5 (7), 559–565.
- (12) Schlögl, R. *Handbook of Heterogeneous Catalysis*, 2nd ed.; Ertyl, G., Knözinger, H., Weitkamp, J., Eds.; Wiley-VCH, 2008.
- (13) Mortensen, J. J.; Hansen, L. B.; Hammer, B.; Nørskov, J. K. *J. Catal.* **1999**, 182 (2), 479–488.
- (14) Sippel, D.; Rohde, M.; Netzer, J.; Trncik, C.; Gies, J.; Grunau, K.; Djurdjevic, I.; Decamps, L.; Andrade, S. L. A.; Einsle, O. *Science (80-. )*. **2018**, 359 (6383), 1484 LP – 1489.

- (15) Skubi, K. L.; Holland, P. L. *Biochemistry* **2018**, *57* (26), 3540–3541.
- (16) Burgess, B. K.; Lowe, D. J. *Chem. Rev.* **1996**, *96* (7), 2983–3012.
- (17) Hoffman, B. M.; Lukoyanov, D.; Yang, Z.-Y.; Dean, D. R.; Seefeldt, L. C. *Chem. Rev.* **2014**, *114* (8), 4041–4062.
- (18) Yandulov, D. V.; Schrock, R. R. *Science* (80-. ). **2003**, *301*, 76–78.
- (19) Arashiba, K.; Kinoshita, E.; Kuriyama, S.; Eizawa, A.; Nakajima, K.; Tanaka, H.; Yoshizawa, K.; Nishibayashi, Y. *J. Am. Chem. Soc.* **2015**, *137* (17), 5666–5669.
- (20) Anderson, J. S.; Rittle, J.; Peters, J. C. *Nature* **2013**, *501* (7465), 84–87.
- (21) Del Castillo, T. J.; Thompson, N. B.; Peters, J. C. *J. Am. Chem. Soc.* **2016**, *138* (16), 5341–5350.
- (22) Scepaniak, J. J.; Bontchev, R. P.; Johnson, D. L.; Smith, J. M. *Angew. Chemie Int. Ed.* **2011**, *50* (29), 6630–6633.
- (23) Scepaniak, J. J.; Fulton, M. D.; Bontchev, R. P.; Duesler, E. N.; Kirk, M. L.; Smith, J. M. *J. Am. Chem. Soc.* **2008**, *130* (32), 10515–10517.
- (24) Scepaniak, J. J.; Margarit, C. G.; Harvey, J. N.; Smith, J. M. *Inorg. Chem.* **2011**, *50* (19), 9508–9517.
- (25) Thompson, N. B.; Green, M. T.; Peters, J. C. *J. Am. Chem. Soc.* **2017**, *139* (43), 15312–15315.
- (26) Sabenya, G.; Lázaro, L.; Gamba, I.; Martin-Diaconescu, V.; Andris, E.; Weyhermüller, T.; Neese, F.; Roithova, J.; Bill, E.; Lloret-Fillol, J.; Costas, M. *J. Am. Chem. Soc.* **2017**, *139* (27), 9168–9177.
- (27) Bucinsky, L.; Breza, M.; Lee, W.-T.; Hickey, A. K.; Dickie, D. A.; Nieto, I.; DeGayner, J. A.; Harris, T. D.; Meyer, K.; Krzystek, J.; Ozarowski, A.; Nehrkorn, J.; Schnegg, A.; Holdack, K.; Herber, R. H.; Telser, J.; Smith, J. M. *Inorg. Chem.* **2017**, *56* (8), 4751–4768.
- (28) Maity, A. K.; Murillo, J.; Metta-Magaña, A. J.; Pinter, B.; Fortier, S. *J. Am. Chem.*

Soc. **2017**, 139 (44), 15691–15700.

- (29) Ballhausen, C. J.; Gray, H. B. *Inorg. Chem.* **1962**, 1 (1), 111–122.
- (30) Winkler, J. R.; Gray, H. B. In *Molecular Electronic Structures of Transition Metal Complexes I. Structure and Bonding*; Springer, Berlin, Heidelberg, 2012; pp 17–28.
- (31) Nugent, W. A.; Mayer, J. M. *Metal-ligand Multiple Bonds*; John Wiley & Sons: New York, 1988.
- (32) Gray, H. B. *Chem. Int.* **2019**, 41 (4), 16–19.
- (33) Gray, H. B.; Winkler, J. R. *Acc. Chem. Res.* **2018**, 51 (8), 1850–1857.
- (34) Ray, K.; Heims, F.; Pfaff, F. F. *Eur. J. Inorg. Chem.* **2013**, 2013 (22-23), 3784–3807.
- (35) O'Halloran, K. P.; Zhao, C.; Ando, N. S.; Schultz, A. J.; Koetzle, T. F.; Piccoli, P. M. B.; Hedman, B.; Hodgson, K. O.; Bobyr, E.; Kirk, M. L.; Knottenbelt, S.; Depperman, E. C.; Stein, B.; Anderson, T. M.; Cao, R.; Geletii, Y. V.; Hardcastle, K. I.; Musaev, D. G.; Neiwert, W. A.; Fang, X.; Morokuma, K.; Wu, S.; Kögerler, P.; Hill, C. L. *Inorg. Chem.* **2012**, 51 (13), 7025–7031.
- (36) Grant, L. N.; Pinter, B.; Kurogi, T.; Carroll, M. E.; Wu, G.; Manor, B. C.; Carroll, P. J.; Mindiola, D. J. *Chem. Sci.* **2017**, 8 (2), 1209–1224.
- (37) Eikey, R. A.; Abu-omar, M. M. *Coord. Chem. Rev.* **2003**, 243, 83–124.
- (38) Thompson, R.; Tran, B. L.; Ghosh, S.; Chen, C. H.; Pink, M.; Gao, X.; Carroll, P. J.; Baik, M. H.; Mindiola, D. J. *Inorg. Chem.* **2015**, 54 (6), 3068–3077.
- (39) Ju Chang Kim; Byung Min Lee; Jong, I. S. *Polyhedron* **1995**, 14 (15), 2145–2149.
- (40) Crevier, T. J.; Bennett, B. K.; Soper, J. D.; Bowman, J. A.; Dehestani, A.; Hrovat, D. A.; Lovell, S.; Kaminsky, W.; Mayer, J. M. *J. Am. Chem. Soc.* **2001**, 123 (6), 1059–1071.
- (41) Bendix, J.; Anthon, C.; Schau-Magnussen, M.; Brock-Nannestad, T.; Vibenholt, J.; Rehman, M.; Sauer, S. P. A. *Angew. Chemie Int. Ed.* **2011**, 50 (19), 4480–4483.

- (42) Sceats, E. L.; Figueroa, J. S.; Cummins, C. C.; Loening, N. M.; Van der Wel, P.; Griffin, R. G. *Polyhedron* **2004**, 23 (17), 2751–2768.
- (43) Fairhurst, S. A.; Hughes, D. L.; Ibrahim, S. K.; Abasq, M.-L.; Talarmin, J.; Queiros, M. A.; Fonseca, A.; Pickett, C. J. *J. Chem. Soc. Dalt. Trans.* **1995**, No. 12, 1973–1984.
- (44) Kim, J. C.; Rees, W. S.; Goedken, V. L. *Inorg. Chem.* **1995**, 34 (9), 2483–2486.
- (45) Powell, K. R.; Perez, P. J.; Luan, L.; Feng, S. G.; White, P. S.; Brookhart, M.; Templeton, J. L. *Organometallics* **1994**, 13 (5), 1851–1864.
- (46) Abram, U.; Voigt, A.; Kirmse, R. *Polyhedron* **2000**, 19 (14), 1741–1748.
- (47) Leung, W.-H.; Chan, E. Y. Y.; Lai, T. C. Y.; Wong, W.-T. *J. Chem. Soc. Dalt. Trans.* **2000**, No. 1, 51–56.
- (48) Marshman, R. W.; Shapley, P. A. *J. Am. Chem. Soc.* **1990**, 112 (23), 8369–8378.
- (49) Walstrom, A.; Fan, H.; Pink, M.; Caulton, K. G. *Inorganica Chim. Acta* **2010**, 363 (3), 633–636.
- (50) H. Doerrer, L.; J. Graham, A.; L. H. Green, M. *J. Chem. Soc. Dalt. Trans.* **1998**, No. 23, 3941–3946.
- (51) Hagenbach, A.; Abram, U. *Zeitschrift für Anorg. und Allg. Chemie* **2005**, 631 (12), 2303–2305.
- (52) Abram, U.; Schulz Lang, E.; Abram, S.; Wegmann, J.; R. Dilworth, J.; Kirmse, R.; Derek Woollins, J. *J. Chem. Soc. Dalt. Trans.* **1997**, No. 4, 623–630.
- (53) Abram, U. *Zeitschrift für Anorg. und Allg. Chemie* **1999**, 625 (6), 839–841.
- (54) Verma, S.; Hanack, M. *Zeitschrift für Anorg. und Allg. Chemie* **2003**, 629 (5), 880–892.
- (55) Ritter, S.; Abram, U. *Inorganica Chim. Acta* **1995**, 231 (1), 245–248.
- (56) Refosco, F.; Tisato, F.; Moresco, A.; Bandoli, G. *J. Chem. Soc. Dalt. Trans.* **1995**,

No. 21, 3475–3482.

- (57) Berry, J. F. *Comments Inorg. Chem.* **2009**, 30 (1–2), 28–66.
- (58) Zolnhofer, E. M.; Käß, M.; Khusniyarov, M. M.; Heinemann, F. W.; Maron, L.; van Gastel, M.; Bill, E.; Meyer, K. *J. Am. Chem. Soc.* **2014**, 136 (42), 15072–15078.
- (59) Sieh, D.; Schöffel, J.; Burger, P. *Dalt. Trans.* **2011**, 40 (37), 9512–9524.
- (60) Vreeken, V.; Siegler, M. A.; de Bruin, B.; Reek, J. N. H.; Lutz, M.; van der Vlugt, J. I. *Angew. Chemie Int. Ed.* **2015**, 54 (24), 7055–7059.
- (61) Scheibel, M. G.; Askevold, B.; Heinemann, F. W.; Reijerse, E. J.; de Bruin, B.; Schneider, S. *Nat. Chem.* **2012**, 4 (7), 552–558.
- (62) Scheibel, M. G.; Wu, Y.; Stückl, A. C.; Krause, L.; Carl, E.; Stalke, D.; de Bruin, B.; Schneider, S. *J. Am. Chem. Soc.* **2013**, 135 (47), 17719–17722.
- (63) Askevold, B.; Nieto, J. T.; Tussupbayev, S.; Diefenbach, M.; Herdtweck, E.; Holthausen, M. C.; Schneider, S. *Nat. Chem.* **2011**, 3 (7), 532–537.
- (64) Pipes, D. W.; Bakir, M.; Vitols, S. E.; Hodgson, D. J.; Meyer, T. J. *J. Am. Chem. Soc.* **1990**, 112 (14), 5507–5514.
- (65) Coia, G. M.; Demadis, K. D.; Meyer, T. J. *Inorg. Chem.* **2000**, 39 (10), 2212–2223.
- (66) El-Samanody, E.-S.; Demadis, K. D.; Meyer, T. J.; White, P. S. *Inorg. Chem.* **2001**, 40 (15), 3677–3686.
- (67) Buhr, J. D.; Taube, H. *Inorg. Chem.* **1979**, 18 (8), 2208–2212.
- (68) Che, C.-M.; Lam, H.-W.; Tong, W.-F.; Lai, T.-F.; Lau, T.-C. *J. Chem. Soc. Chem. Commun.* **1989**, No. 24, 1883–1884.
- (69) Ware, D. C.; Taube, H. *Inorg. Chem.* **1991**, 30 (24), 4605–4610.
- (70) Demadis, K. D.; Meyer, T. J.; White, P. S. *Inorg. Chem.* **1997**, 36 (25), 5678–5679.
- (71) Maestri, A. G.; Cherry, K. S.; Toboni, J. J.; Brown, S. N. *J. Am. Chem. Soc.* **2001**,

123 (30), 7459–7460.

- (72) Brown, S. N. *Journal of the American Chemical Society*. 1999, pp 9752–9753.
- (73) Huynh, M. H. V; Jameson, D. L.; Meyer, T. J. *Inorg. Chem.* **2001**, 40 (20), 5062–5063.
- (74) Bennett, B. K.; Saganic, E.; Lovell, S.; Kaminsky, W.; Samuel, A.; Mayer, J. M. *Inorg. Chem.* **2003**, 42 (13), 4127–4134.
- (75) Fang, G.-S.; Huang, J.-S.; Zhu, N.; Che, C.-M. *Eur. J. Inorg. Chem.* **2004**, 2004 (6), 1341–1348.
- (76) Yi; Lam, T. C. H.; Sau, Y.-K.; Zhang, Q.-F.; Williams, I. D.; Leung, W.-H. *Inorg. Chem.* **2007**, 46 (17), 7193–7198.
- (77) Besson, C.; Geletii, Y. V; Villain, F.; Villanneau, R.; Hill, C. L.; Proust, A. *Inorg. Chem.* **2009**, 48 (19), 9436–9443.
- (78) Schendzielorz, F. S.; Finger, M.; Volkmann, C.; Würtele, C.; Schneider, S. *Angew. Chemie Int. Ed.* **2016**, 55 (38), 11417–11420.
- (79) Du Bois, J.; Tomooka, C. S.; Hong, J.; Carreira, E. M. *J. Am. Chem. Soc.* **1997**, 119 (13), 3179–3180.
- (80) Bois, J. Du; Tomooka, C. S.; Hong, J.; Carreira, E. M.; Day, M. W. *Angew. Chemie Int. Ed. English* **1997**, 36 (15), 1645–1647.
- (81) Du Bois, J.; Tomooka, C. S.; Hong, J.; Carreira, E. M. *Acc. Chem. Res.* **1997**, 30 (9), 364–372.
- (82) Minakata, S.; Nishimura, M.; Takahashi, T.; Oderaotoshi, Y.; Komatsu, M. *Tetrahedron Lett.* **2001**, 42 (51), 9019–9022.
- (83) Nishimura, M.; Minakata, S.; Takahashi, T.; Oderaotoshi, Y.; Komatsu, M. *J. Org. Chem.* **2002**, 67 (7), 2101–2110.
- (84) Ho, C.-M.; Lau, T.-C.; Kwong, H.-L.; Wong, W.-T. *J. Chem. Soc. Dalt. Trans.* **1999**, No. 15, 2411–2414.



- (85) Ostovic, D.; Bruice, T. C. *Acc. Chem. Res.* **1992**, *25* (7), 314–320.
- (86) Borovik, A. S. *Chem. Soc. Rev.* **2011**, *40*, 1870.
- (87) Gunay, A.; Theopold, K. H. *Chem. Rev.* **2010**, *110* (2), 1060–1081.
- (88) Groves, J. T.; Takahashi, T. *J. Am. Chem. Soc.* **1983**, *105* (7), 2073–2074.
- (89) Bottomley, L. A.; Neely, F. L. *J. Am. Chem. Soc.* **1988**, *110* (20), 6748–6752.
- (90) Pérez, F. R.; Belmar, J.; Moreno, Y.; Baggio, R.; Peña, O. *New J. Chem.* **2005**, *29* (2), 283–287.
- (91) Du Bois, J.; Hong, J.; Carreira, E. M.; Day, M. W. *J. Am. Chem. Soc.* **1996**, *118* (4), 915–916.
- (92) Minakata, S.; Ando, T.; Nishimura, M.; Ryu, I.; Komatsu, M. *Angew. Chemie Int. Ed.* **1998**, *37* (24), 3392–3394.
- (93) Leung, S. K.-Y.; Huang, J.-S.; Liang, J.-L.; Che, C.-M.; Zhou, Z.-Y. *Angew. Chemie Int. Ed.* **2003**, *42* (3), 340–343.
- (94) Yiu, S.-M.; Lam, W. W. Y.; Ho, C.-M.; Lau, T.-C. *J. Am. Chem. Soc.* **2007**, *129* (4), 803–809.
- (95) Musch Long, A. K.; Yu, R. P.; Timmer, G. H.; Berry, J. F. *J. Am. Chem. Soc.* **2010**, *132* (35), 12228–12230.
- (96) Henning, H.; Hofbauer, K.; Handke, K.; Stich, R. *Angew. Chemie Int. Ed. English* **1997**, *36* (4), 408–410.
- (97) Long, A. K. M.; Timmer, G. H.; Pap, J. S.; Snyder, J. L.; Yu, R. P.; Berry, J. F. *J. Am. Chem. Soc.* **2011**, *133* (33), 13138–13150.
- (98) Hojilla Atienza, C. C.; Bowman, A. C.; Lobkovsky, E.; Chirik, P. J. *J. Am. Chem. Soc.* **2010**, *132* (46), 16343–16345.
- (99) Thomson, R. K.; Cantat, T.; Scott, B. L.; Morris, D. E.; Batista, E. R.; Kiplinger, J. L. *Nat. Chem.* **2010**, *2* (9), 723–729.

- (100) Schlangen, M.; Neugebauer, J.; Reiher, M.; Schröder, D.; López, J. P.; Haryono, M.; Heinemann, F. W.; Grohmann, A.; Schwarz, H. *J. Am. Chem. Soc.* **2008**, *130* (13), 4285–4294.
- (101) Bordwell, F. G.; Cheng, J.; Ji, G. Z.; Satish, A. V; Zhang, X. *J. Am. Chem. Soc.* **1991**, *113* (26), 9790–9795.
- (102) Bordwell, F. G.; Cheng, J. P.; Satish, A. V; Twyman, C. L. *J. Org. Chem.* **1992**, *57* (24), 6542–6546.
- (103) Man, W. L.; Lam, W. W. Y.; Kwong, H. K.; Yiu, S. M.; Lau, T. C. *Angew. Chemie - Int. Ed.* **2012**, *51*, 9101–9104.
- (104) Parker, V. D. *J. Am. Chem. Soc.* **1992**, *114* (19), 7458–7462.
- (105) Man, W. L.; Lam, W. W. Y.; Yiu, S. M.; Lau, T. C.; Peng, S. M. *J. Am. Chem. Soc.* **2004**, *126* (47), 15336–15337.
- (106) Golubkov, G.; Gross, Z. *J. Am. Chem. Soc.* **2005**, *127* (10), 3258–3259.
- (107) Chang, C. J.; Low, D. W.; Gray, H. B. *Inorg. Chem.* **1997**, *95*, 1285–1286.
- (108) Woo, L. K. *Chem. Rev.* **1993**, *93*, 1125–1136.
- (109) Birk, T.; Bendix, J. *Inorg. Chem.* **2003**, *42* (23), 7608–7615.
- (110) Cozzi, P. G. *Chem. Soc. Rev.* **2004**, *33* (7), 410–421.
- (111) Clarke, R. M.; Herasymchuk, K.; Storr, T. *Coord. Chem. Rev.* **2017**, *352*, 67–82.
- (112) Jørgensen, C. K. *Coord. Chem. Rev.* **1966**, *1* (1), 164–178.
- (113) Chirik, P. J. *Inorg. Chem.* **2011**, *50* (20), 9737–9740.
- (114) *The PyMOL Molecular Graphics System*, 2.0.; Schrodinger, LLC.
- (115) Denisov, I. G.; Makris, T. M.; Sligar, S. G.; Schlichting, I. *Chem. Rev.* **2005**, *105* (6), 2253–2278.
- (116) Rittle, J.; Green, M. T. *Science* (80-. ). **2010**, *330* (6006), 933 LP – 937.

- (117) Whittaker, M. M.; DeVito, V. L.; Asher, S. A.; Whittaker, J. W. *J. Biol. Chem.* **1989**, *264* (13), 7104–7106.
- (118) Whittaker, M. M.; Whittaker, J. W. *J. Biol. Chem.* **1990**, *265* (17), 9610–9613.
- (119) Whittaker, J. W. *Chem. Rev.* **2003**, *103* (6), 2347–2364.
- (120) Lyaskovskyy, V.; de Bruin, B. *ACS Catal.* **2012**, *2* (2), 270–279.
- (121) Que, L.; Tolman, W. B. *Nature* **2008**, *455* (7211), 333–340.
- (122) Chirila, A.; Das, B. G.; Kuijpers, P. F.; Sinha, V.; de Bruin, B. *Non-Noble Metal Catalysis*. February 4, 2019, pp 1–31.
- (123) Dzik, W. I.; van der Vlugt, J. I.; Reek, J. N. H.; de Bruin, B. *Angew. Chemie Int. Ed.* **2011**, *50* (15), 3356–3358.
- (124) Dzik, W. I.; Zhang, X. P.; de Bruin, B. *Inorg. Chem.* **2011**, *50* (20), 9896–9903.
- (125) Chirik, P. J.; Wieghardt, K. *Science (80-. )*. **2010**, *327* (5967), 794 LP – 795.
- (126) Bouwkamp, M. W.; Bowman, A. C.; Lobkovsky, E.; Chirik, P. J. *J. Am. Chem. Soc.* **2006**, *128* (41), 13340–13341.
- (127) Bart, S. C.; Chłopek, K.; Bill, E.; Bouwkamp, M. W.; Lobkovsky, E.; Neese, F.; Wieghardt, K.; Chirik, P. J. *J. Am. Chem. Soc.* **2006**, *128* (42), 13901–13912.
- (128) van der Vlugt, J. I. *Chem. – A Eur. J.* **2019**, *25* (11), 2651–2662.
- (129) Bagh, B.; Broere, D. L. J.; Sinha, V.; Kuijpers, P. F.; van Leest, N. P.; de Bruin, B.; Demeshko, S.; Siegler, M. A.; van der Vlugt, J. I. *J. Am. Chem. Soc.* **2017**, *139* (14), 5117–5124.
- (130) Nguyen, A. I.; Zarkesh, R. A.; Lacy, D. C.; Thorson, M. K.; Heyduk, A. F. *Chem. Sci.* **2011**, *2* (1), 166–169.
- (131) Matsumoto, T.; Chang, H.-C.; Wakizaka, M.; Ueno, S.; Kobayashi, A.; Nakayama, A.; Taketsugu, T.; Kato, M. *J. Am. Chem. Soc.* **2013**, *135* (23), 8646–8654.

- (132) Smith, A. L.; Hardcastle, K. I.; Soper, J. D. *J. Am. Chem. Soc.* **2010**, *132* (41), 14358–14360.
- (133) van der Meer, M.; Rechkemmer, Y.; Peremykin, I.; Hohloch, S.; van Slageren, J.; Sarkar, B. *Chem. Commun.* **2014**, *50* (76), 11104–11106.
- (134) Ren, Y.; Cheaib, K.; Jacquet, J.; Vezin, H.; Fensterbank, L.; Orio, M.; Blanchard, S.; Desage-El Murr, M. *Chem. – A Eur. J.* **2018**, *24* (20), 5086–5090.
- (135) Blackmore, K. J.; Ziller, J. W.; Heyduk, A. F. *Inorg. Chem.* **2005**, *44* (16), 5559–5561.
- (136) Haneline, M. R.; Heyduk, A. F. *J. Am. Chem. Soc.* **2006**, *128* (26), 8410–8411.
- (137) Wong, J. L.; Sánchez, R. H.; Logan, J. G.; Zarkesh, R. A.; Ziller, J. W.; Heyduk, A. F. *Chem. Sci.* **2013**, *4* (4), 1906–1910.
- (138) Mukherjee, C.; Weyhermüller, T.; Bothe, E.; Chaudhuri, P. *Inorg. Chem.* **2008**, *47* (7), 2740–2746.
- (139) Shaw, S.; White, J. D. *Chem. Rev.* **2019**, *119* (16), 9381–9426.
- (140) Canali, L.; C. Sherrington, D. *Chem. Soc. Rev.* **1999**, *28* (2), 85–93.
- (141) Katsuki, T. *ChemInform* **2003**, *34* (18).
- (142) Che, C.-M.; Huang, J.-S. *Coord. Chem. Rev.* **2003**, *242* (1), 97–113.
- (143) McGarrigle, E. M.; Gilheany, D. G. *Chemical Reviews*. 2005, pp 1563–1602.
- (144) Darensbourg, D. J. *Chem. Rev.* **2007**, *107* (6), 2388–2410.
- (145) Irie, R.; Noda, K.; Ito, Y.; Matsumoto, N.; Katsuki, T. *Tetrahedron Lett.* **1990**, *31* (50), 7345–7348.
- (146) Jacobsen, E. N.; Zhang, W.; Muci, A. R.; Ecker, J. R.; Deng, L. *J. Am. Chem. Soc.* **1991**, *113* (18), 7063–7064.
- (147) Baleizão, C.; Garcia, H. *Chem. Rev.* **2006**, *106* (9), 3987–4043.

- (148) Matsumoto, K.; Saito, B.; Katsuki, T. *Chem. Commun.* **2007**, No. 35, 3619–3627.
- (149) Łępicka, K.; Pieta, P.; Francius, G.; Walcarius, A.; Kutner, W. *Electrochim. Acta* **2019**, *315*, 75–83.
- (150) Miyasaka, H.; Saitoh, A.; Abe, S. *Coord. Chem. Rev.* **2007**, *251* (21), 2622–2664.
- (151) Freire, C.; Nunes, M.; Pereira, C.; Fernandes, D. M.; Peixoto, A. F.; Rocha, M. *Coord. Chem. Rev.* **2019**, *394*, 104–134.
- (152) Wezenberg, S. J.; Kleij, A. W. *Angew. Chemie Int. Ed.* **2008**, *47* (13), 2354–2364.
- (153) Kaczmarek, M. T.; Zabiszak, M.; Nowak, M.; Jastrzab, R. *Coord. Chem. Rev.* **2018**, *370*, 42–54.
- (154) Erxleben, A. *Inorganica Chim. Acta* **2018**, *472*, 40–57.
- (155) Ning, Y.; Huo, Y.; Xue, H.; Du, Y.; Yao, Y.; Sedgwick, A. C.; Lin, H.; Li, C.; Jiang, S.-D.; Wang, B.-W.; Gao, S.; Kang, L.; Sessler, J. L.; Zhang, J.-L. *J. Am. Chem. Soc.* **2020**, *142* (22), 10219–10227.
- (156) Thomas, F. *Eur. J. Inorg. Chem.* **2007**, *2007* (17), 2365.
- (157) Asami, K.; Tsukidate, K.; Iwatsuki, S.; Tani, F.; Karasawa, S.; Chiang, L.; Storr, T.; Thomas, F.; Shimazaki, Y. *Inorg. Chem.* **2012**, *51* (22), 12450–12461.
- (158) Pratt, R. C.; Stack, T. D. P. *J. Am. Chem. Soc.* **2003**, *125* (29), 8716–8717.
- (159) Lyons, C. T.; Stack, T. D. P. *Coord. Chem. Rev.* **2013**, *257* (2), 528–540.
- (160) Pratt, R. C.; Stack, T. D. P. *Inorg. Chem.* **2005**, *44* (7), 2367–2375.
- (161) Orio, M.; Jarjays, O.; Kanso, H.; Philouze, C.; Neese, F.; Thomas, F. *Angew. Chemie Int. Ed.* **2010**, *49* (29), 4989–4992.
- (162) Wang, Y.; DuBois, J. L.; Hedman, B.; Hodgson, K. O.; Stack, T. D. P. *Science* (80-. ). **1998**, *279* (5350), 537 LP – 540.
- (163) Butsch, K.; Günther, T.; Klein, A.; Stirnat, K.; Berkessel, A.; Neudörfl, J. *Inorganica*

*Chim. Acta* **2013**, 394, 237–246.

- (164) Wang, Y.; Stack, T. D. P. *J. Am. Chem. Soc.* **1996**, 118 (51), 13097–13098.
- (165) Campbell, E. J.; Nguyen, S. T. *Tetrahedron Lett.* **2001**, 42 (7), 1221–1225.
- (166) Pratt, R. C.; Lyons, C. T.; Wasinger, E. C.; Stack, T. D. P. *J. Am. Chem. Soc.* **2012**, 134 (17), 7367–7377.
- (167) Saint-Aman, E.; Me'nage, S.; Pierre, J.-L.; Defrancq, E.; Gellon, G. *New J. Chem.* **1998**, 22 (5), 393–394.
- (168) Chiang, L.; Wasinger, E. C.; Shimazaki, Y.; Young, V.; Storr, T.; Stack, T. D. P. *Inorganica Chim. Acta* **2018**, 481, 151–158.
- (169) Clarke, R. M.; Storr, T. *Dalt. Trans.* **2014**, 43 (25), 9380–9391.
- (170) Andrez, J.; Guidal, V.; Scopelliti, R.; Pécaut, J.; Gambarelli, S.; Mazzanti, M. *J. Am. Chem. Soc.* **2017**, 139 (25), 8628–8638.
- (171) Kochem, A.; Kanso, H.; Baptiste, B.; Arora, H.; Philouze, C.; Jarjayes, O.; Vezin, H.; Luneau, D.; Orio, M.; Thomas, F. *Inorg. Chem.* **2012**, 51 (20), 10557–10571.
- (172) Clarke, R. M.; Hazin, K.; Thompson, J. R.; Savard, D.; Prosser, K. E.; Storr, T. *Inorg. Chem.* **2016**, 55 (2), 762–774.
- (173) Dunn, T. J.; Chiang, L.; Ramogida, C. F.; Hazin, K.; Webb, M. I.; Katz, M. J.; Storr, T. *Chem. – A Eur. J.* **2013**, 19 (29), 9606–9618.
- (174) Shimazaki, Y.; Stack, T. D. P.; Storr, T. *Inorg. Chem.* **2009**, 48 (17), 8383–8392.
- (175) Kurahashi, T.; Fujii, H. *J. Am. Chem. Soc.* **2011**, 133 (21), 8307–8316.
- (176) Storr, T.; Wasinger, E. C.; Pratt, R. C.; Stack, T. D. P. *Angew. Chemie Int. Ed.* **2007**, 46 (27), 5198–5201.
- (177) Storr, T.; Verma, P.; Pratt, R. C.; Wasinger, E. C.; Shimazaki, Y.; Stack, T. D. P. *J. Am. Chem. Soc.* **2008**, 130 (46), 15448–15459.

- (178) Shimazaki, Y.; Tani, F.; Fukui, K.; Naruta, Y.; Yamauchi, O. *J. Am. Chem. Soc.* **2003**, *125* (35), 10512–10513.
- (179) Chiang, L.; Herasymchuk, K.; Thomas, F.; Storr, T. *Inorg. Chem.* **2015**, *54* (12), 5970–5980.
- (180) Chiang, L.; Kochem, A.; Jarjayes, O.; Dunn, T. J.; Vezin, H.; Sakaguchi, M.; Ogura, T.; Orio, M.; Shimazaki, Y.; Thomas, F.; Storr, T. *Chem. – A Eur. J.* **2012**, *18* (44), 14117–14127.
- (181) Clarke, R. M.; Storr, T. *J. Am. Chem. Soc.* **2016**, *138* (47), 15299–15302.
- (182) Chiang, L.; Clarke, R. M.; Herasymchuk, K.; Sutherland, M.; Prosser, K. E.; Shimazaki, Y.; Storr, T. *Eur. J. Inorg. Chem.* **2016**, *2016* (1), 49–55.
- (183) Chiang, L.; Allan, L. E. N.; Alcantara, J.; Wang, M. C. P.; Storr, T.; Shaver, M. P. *Dalt. Trans.* **2014**, *43* (11), 4295–4304.
- (184) Herasymchuk, K.; Chiang, L.; Hayes, C. E.; Brown, M. L.; Ovens, J. S.; Patrick, B. O.; Leznoff, D. B.; Storr, T. *Dalt. Trans.* **2016**, *45*, 12576–12586.
- (185) Qin, Z.; Thomas, C. M.; Lee, S.; Coates, G. W. *Angew. Chemie Int. Ed.* **2003**, *42* (44), 5484–5487.
- (186) Thomas, F.; Jarjayes, O.; Duboc, C.; Philouze, C.; Saint-Aman, E.; Pierre, J.-L. *Dalt. Trans.* **2004**, No. 17, 2662–2669.
- (187) Asami, K.; Takashina, A.; Kobayashi, M.; Iwatsuki, S.; Yajima, T.; Kochem, A.; van Gastel, M.; Tani, F.; Kohzuma, T.; Thomas, F.; Shimazaki, Y. *Dalt. Trans.* **2014**, *43* (5), 2283–2293.
- (188) Kochem, A.; Jarjayes, O.; Baptiste, B.; Philouze, C.; Vezin, H.; Tsukidate, K.; Tani, F.; Orio, M.; Shimazaki, Y.; Thomas, F. *Chem. – A Eur. J.* **2012**, *18* (4), 1068–1072.
- (189) Oshita, H.; Shimazaki, Y. *Chem. – A Eur. J.* **2020**, *n/a* (n/a).
- (190) Jacobsen, E. N.; Zhang, W.; Guler, M. L. *J. Am. Chem. Soc.* **1991**, *113* (17), 6703–6704.

- (191) Palucki, M.; Finney, N. S.; Pospisil, P. J.; Güler, M. L.; Ishida, T.; Jacobsen, E. N. *J. Am. Chem. Soc.* **1998**, *120* (5), 948–954.
- (192) Darensbourg, D. J.; Mackiewicz, R. M.; Phelps, A. L.; Billodeaux, D. R. *Acc. Chem. Res.* **2004**, *37* (11), 836–844.
- (193) Darensbourg, D. J.; Mackiewicz, R. M.; Rodgers, J. L.; Fang, C. C.; Billodeaux, D. R.; Reibenspies, J. H. *Inorg. Chem.* **2004**, *43* (19), 6024–6034.
- (194) Man, W. L.; Lam, W. W. Y.; Lau, T. C. *Acc. Chem. Res.* **2014**, *47* (2), 427–439.
- (195) Zhang, W.; Loebach, J. L.; Wilson, S. R.; Jacobsen, E. N. *J. Am. Chem. Soc.* **1990**, *112* (7), 2801–2803.
- (196) Jacobsen, E. N.; Deng, L.; Furukawa, Y.; Martínez, L. E. *Tetrahedron* **1994**, *50* (15), 4323–4334.
- (197) Irie, R.; Noda, K.; Ito, Y.; Matsumoto, N.; Katsuki, T. *Tetrahedron: Asymmetry* **1991**, *2* (7), 481–494.
- (198) Chang, S.; Galvin, J. M.; Jacobsen, E. N. *J. Am. Chem. Soc.* **1994**, *116* (15), 6937–6938.
- (199) Srinivasan, K.; Michaud, P.; Kochi, J. K. *J. Am. Chem. Soc.* **1986**, *108* (9), 2309–2320.
- (200) Khavrutskii, I. V.; Musaev, D. G.; Morokuma, K. *Proc. Natl. Acad. Sci. U. S. A.* **2004**, *101* (16), 5743 LP – 5748.
- (201) Samsel, E. G.; Srinivasan, K.; Kochi, J. K. *J. Am. Chem. Soc.* **1985**, *107* (25), 7606–7617.
- (202) Linker, T. *Angew. Chemie Int. Ed. English* **1997**, *36* (19), 2060–2062.
- (203) Bandini, M.; Cozzi, P. G.; Melchiorre, P.; Morganti, S.; Umani-Ronchi, A. *Org. Lett.* **2001**, *3* (8), 1153–1155.
- (204) Jacobsen, E. N. *Acc. Chem. Res.* **2000**, *33* (6), 421–431.



- (205) Martinez, L. E.; Leighton, J. L.; Carsten, D. H.; Jacobsen, E. N. *J. Am. Chem. Soc.* **1995**, *117* (21), 5897–5898.
- (206) Hansen, K. B.; Leighton, J. L.; Jacobsen, E. N. *J. Am. Chem. Soc.* **1996**, *118* (44), 10924–10925.
- (207) Konsler, R. G.; Karl, J.; Jacobsen, E. N. *J. Am. Chem. Soc.* **1998**, *120* (41), 10780–10781.
- (208) Coates, G. W.; Moore, D. R. *Angew. Chemie Int. Ed.* **2004**, *43* (48), 6618–6639.
- (209) Paddock, R. L.; Nguyen, S. T. *J. Am. Chem. Soc.* **2001**, *123* (46), 11498–11499.
- (210) Darensbourg, D. J.; Moncada, A. I. *Inorg. Chem.* **2008**, *47* (21), 10000–10008.
- (211) Darensbourg, D. J.; Yeung, A. D. *Polym. Chem.* **2015**, *6* (7), 1103–1117.
- (212) Darensbourg, D. J.; Yarbrough, J. C. *J. Am. Chem. Soc.* **2002**, *124* (22), 6335–6342.
- (213) Darensbourg, D. J.; Yarbrough, J. C.; Ortiz, C.; Fang, C. C. *J. Am. Chem. Soc.* **2003**, *125* (25), 7586–7591.
- (214) Eberhardt, R.; Allmendinger, M.; Rieger, B. *Macromol. Rapid Commun.* **2003**, *24* (2), 194–196.
- (215) Adam, W.; Hajra, S.; Herderich, M.; Saha-Möller, C. R. *Org. Lett.* **2000**, *2* (18), 2773–2776.
- (216) Müller, J.; Kikuchi, A.; Bill, E.; Weyhermüller, T.; Hildebrandt, P.; Ould-Moussa, L.; Wieghardt, K. *Inorganica Chim. Acta* **2000**, *297* (1), 265–277.
- (217) Sokolowski, A.; Bothe, E.; Bill, E.; Weyhermüller, T.; Wieghardt, K. *Chem. Commun.* **1996**, No. 14, 1671–1672.
- (218) Akiko Hori; Takehiro Ozawa; Hironobu Yoshida; Yohko Imori; Yoshihiko Kuribayashi; Emiko Nakano; Nagao Azuma. *Inorganica Chim. Acta* **1998**, *281* (2), 207–213.

- (219) Odom, A. L.; Cummins, C. C.; Protasiewicz, J. D. *J. Am. Chem. Soc.* **1995**, 117 (24), 6613–6614.
- (220) Groves, J. T.; Takahashi, T.; Butler, W. M. *Inorg. Chem.* **1983**, 22 (6), 884–887.
- (221) Che, C. M.; Ma, J. X.; Wong, W. T.; Lai, T. F.; Poon, C. K. *Inorg. Chem.* **1988**, 27 (14), 2547–2548.
- (222) Meyer, K.; Bendix, J.; Bill, E.; Weyhermüller, T.; Wieghardt, K. *Inorg. Chem.* **1998**, 37 (20), 5180–5188.
- (223) Niemann, A.; Bossek, U.; Haselhorst, G.; Wieghardt, K.; Nuber, B. *Inorg. Chem.* **1996**, 35 (4), 906–915.
- (224) Groves, J. T.; Takahashi, T.; Butler, W. M. *Inorg. Chem.* **1983**, 22 (6), 884–887.
- (225) Arshankow, S. I.; Poznjak, A. L. *Zeitschrift für Anorg. und Allg. Chemie* **1981**, 481 (10), 201–206.
- (226) Bottomley, L. A.; Neely, F. L. *Inorg. Chem.* **1997**, 36 (24), 5435–5439.
- (227) Birk, T.; Bendix, J. *Inorg. Chem.* **2003**, 42 (23), 7608–7615.
- (228) Bendix, J. *J. Am. Chem. Soc.* **2003**, 125 (44), 13348–13349.
- (229) Groves, J. T.; Haushalter, R. C. *J. Chem. Soc. Chem. Commun.* **1981**, No. 22, 1165–1166.
- (230) Brock-Nannestad, T.; Hammershøi, A.; Schau-Magnussen, M.; Vibenholt, J.; Bendix, J. *Inorg. Chem. Commun.* **2011**, 14 (1), 251–253.
- (231) Hedegaard, E. D.; Schau-Magnussen, M.; Bendix, J. *Inorg. Chem. Commun.* **2011**, 14 (5), 719–721.
- (232) Bendix, J.; Birk, T.; Weyhermüller, T. *Dalt. Trans.* **2005**, No. 16, 2737–2741.
- (233) Azuma, N.; Ozawa, T.; Tsuboyama, S. *J. Chem. Soc. Dalt. Trans.* **1994**, No. 18, 2609–2613.

- (234) Buchler, J. W.; Dreher, C.; Lay, K.-L.; Raap, A.; Gersonde, K. *Inorg. Chem.* **1983**, 22 (6), 879–884.
- (235) Azuma, N.; Imori, Y.; Yoshida, H.; Tajima, K.; Li, Y.; Yamauchi, J. *Inorganica Chim. Acta* **1997**, 266 (1), 29–36.
- (236) Du Bois, J.; Hong, J.; Carreira, E. M.; Day, M. W. *J. Am. Chem. Soc.* **1996**, 118 (4), 915–916.
- (237) Herwig, W.; Zeiss, H. *J. Org. Chem.* **1958**, 23 (9), 1404.
- (238) Stoll, S.; Schweiger, A. *J. Magn. Reson.* **2006**, 178 (1), 42–55.
- (239) Sheldrick, G. M. *SHELXT v2014*; Bruker AXS Inc: Madison, WI.
- (240) Hu, C. B.; Sheldrick, G. M.; Dittrich, B. *J. Appl. Crystallogr.* **2011**, 44, 1281–1284.
- (241) Frisch, M. J. *et al. Gaussian 16*; Gaussian Inc: Wallingford, CT, USA, 2016.
- (242) Becke, A. D. *J. Chem. Phys.* **1993**, No. 98, 5648–5652.
- (243) Dunn, T. J.; Ramogida, C. F.; Simmonds, C.; Paterson, A.; Wong, E. W. Y.; Chiang, L.; Shimazaki, Y.; Storr, T. *Inorg. Chem.* **2011**, 50 (14), 6746–6755.
- (244) Dunn, T. J.; Chiang, L.; Ramogida, C. F.; Webb, M. I.; Savard, D.; Sakaguchi, M.; Ogura, T.; Shimazaki, Y.; Storr, T. *Dalt. Trans.* **2012**, 41 (26), 7905–7914.
- (245) Schäfer, A.; Horn, H.; Ahlrichs, R. *J. Chem. physicse* **1992**, No. 97, 2571–2577.
- (246) Schäfer, A.; Huber, C.; Ahlrichs, R. *J. Chem. Phys.* **1994**, 100 (8), 5829–5835.
- (247) Barone, V.; Cossi, M.; Tomasi, J. *J. Comput. Chem.* **1998**, 19 (4), 404–417.
- (248) Tomasi, J.; Mennucci, B.; Cancès, E. *J. Mol. Struct. THEOCHEM* **1999**, 464 (1), 211–226.
- (249) D'Alessandro, D. M.; Keene, F. R. *Chem. Soc. Rev.* **2006**, 35 (5), 424–440.
- (250) Kaim, W.; Klein, A.; Glöckle, M. *Acc. Chem. Res.* **2000**, 33 (11), 755–763.

- (251) Demadis, K. D.; Hartshorn, C. M.; Meyer, T. J. *Chem. Rev.* **2001**, 101 (9), 2655–2686.
- (252) Creutz, C.; Taube, H. *J. Am. Chem. Soc.* **1969**, 91 (14), 3988–3989.
- (253) Robin, M. B.; Day, P. *Adv. Inorg. Chem. Radiochem.* **1968**, 10, 247.
- (254) Balzani, V.; Juris, A.; Venturi, M.; Campagna, S.; Serroni, S. *Chem. Rev.* **1996**, 96 (2), 759–834.
- (255) Launay, J.-P. *Chem. Soc. Rev.* **2001**, 30 (6), 386–397.
- (256) Brunschwig, B. S.; Creutz, C.; Sutin, N. *Chem. Soc. Rev.* **2002**, 31 (3), 168–184.
- (257) Hush, N. S. *Progress in Inorganic Chemistry*. January 1, 1967, pp 391–444.
- (258) Parthey, M.; Kaupp, M. *Chem. Soc. Rev.* **2014**, 43 (14), 5067–5088.
- (259) Kaim, W. *Coord. Chem. Rev.* **2011**, 255 (21), 2503–2513.
- (260) Flanagan, J. B.; Margel, S.; Bard, A. J.; Anson, F. C. *J. Am. Chem. Soc.* **1978**, 100 (13), 4248–4253.
- (261) Haim, A. *Progress in Inorganic Chemistry*. January 1, 1983, pp 273–357.
- (262) Kalyanasundaram, K.; Nazeeruddin, M. K. *Inorganica Chim. Acta* **1994**, 226 (1), 213–230.
- (263) Ward, M. D. *Chem. Soc. Rev.* **1995**, 24 (2), 121–134.
- (264) Kiernicki, J. J.; Cladis, D. P.; Fanwick, P. E.; Zeller, M.; Bart, S. C. *J. Am. Chem. Soc.* **2015**, 137 (34), 11115–11125.
- (265) Richardson, D. E.; Taube, H. *Coord. Chem. Rev.* **1984**, 60, 107–129.
- (266) Connelly, N. G.; Geiger, W. E. *Chem. Rev.* **1996**, 96 (2), 877–910.
- (267) Shimazaki, Y.; Yamauchib, O. *Indian J. Chem. - Sect. A Inorganic, Phys. Theor. Anal. Chem.* **2011**, 50, 383–394.

- (268) Golubkov, G.; Gross, Z. *Angew. Chemie Int. Ed.* **2003**, 42 (37), 4507–4510.
- (269) Dei, A.; Gatteschi, D.; Pardi, L.; Barra, A. L.; Brunel, L. C. *Chem. Phys. Lett.* **1990**, 175 (6), 589–592.
- (270) Berreau, L. M.; Mahapatra, S.; Halfen, J. A.; Houser, R. P.; Young Victor G., J.; Tolman, W. B. *Angew. Chemie Int. Ed.* **1999**, 38 (1-2), 207–210.
- (271) Balaghi, S. E.; Safaei, E.; Chiang, L.; Wong, E. W. Y.; Savard, D.; Clarke, R. M.; Storr, T. *Dalt. Trans.* **2013**, 42 (19), 6829–6839.
- (272) Soda, T.; Kitagawa, Y.; Onishi, T.; Takano, Y.; Shigeta, Y.; Nagao, H.; Yoshioka, Y.; Yamaguchi, K. *Chem. Phys. Lett.* **2000**, 319 (3), 223–230.
- (273) Kitagawa, Y. Saito, T., Ed.; IntechOpen: Rijeka, 2018; p Ch. 7.
- (274) Chiang, L.; Savard, D.; Shimazaki, Y.; Thomas, F.; Storr, T. *Inorg. Chem.* **2014**, 53 (11), 5810–5819.
- (275) Gorelsky, S. I. *AOMix: Program for Molecular Orbital Analysis*; University of Ottawa, Canada, 2007.
- (276) Murata, Y.; Cheng, F.; Kitagawa, T.; Komatsu, K. *J. Am. Chem. Soc.* **2004**, 126 (29), 8874–8875.
- (277) Noviandri, I.; Brown, K. N.; Fleming, D. S.; Gulyas, P. T.; Lay, P. A.; Masters, A. F.; Phillips, L. *J. Phys. Chem. B* **1999**, 103 (32), 6713–6722.
- (278) Spuhler, P.; Lein, M.; Frenking, G. *Zeitschrift für Anorg. und Allg. Chemie* **2003**, 629 (5), 803–815.
- (279) Bachler, V. *J. Comput. Chem.* **2005**, 26 (6), 532–551.
- (280) Hedegård, E. D.; Bendix, J.; Sauer, S. P. A. *J. Mol. Struct. THEOCHEM* **2009**, 913 (1), 1–7.
- (281) Mulliken, R. S. *J. Chem. Phys.* **1955**, 23 (10), 1833–1840.
- (282) Weinhold, F.; Landis, C. R.; Glendening, E. D. *Int. Rev. Phys. Chem.* **2016**, 35 (3),

399–440.

- (283) Johnson, S. I.; Heins, S. P.; Klug, C. M.; Wiedner, E. S.; Bullock, R. M.; Raugei, S. *Chem. Commun.* **2019**, 55 (35), 5083–5086.
- (284) Beaumier, E. P.; Billow, B. S.; Singh, A. K.; Biros, S. M.; Odom, A. L. *Chem. Sci.* **2016**, 7 (4), 2532–2536.
- (285) Chatt, J.; Heaton, B. T. *J. Chem. Soc. A Inorganic, Phys. Theor.* **1971**, No. 0, 705–707.
- (286) Kafitz, W.; Weller, F.; Dehnicke, K. *Zeitschrift für Anorg. und Allg. Chemie* **1982**, 490 (1), 175–181.
- (287) Weinhold, F. *J. Comput. Chem.* **2012**, 33 (30), 2363–2379.
- (288) Evans, D. F. *J. Chem. Soc.* **1959**, No. 0, 2003–2005.
- (289) Baker, M. V.; Field, L. D.; Hambley, T. W. *Inorg. Chem.* **1988**, 27 (16), 2872–2876.
- (290) Johnson, B. J.; Antholine, W. E.; Lindeman, S. V.; Mankad, N. P. *Chem. Commun.* **2015**, 51 (59), 11860–11863.
- (291) Heider, S.; Petzold, H.; Teucher, G. *Eur. J. Inorg. Chem.* **2013**, 2013 (13), 2382–2388.
- (292) De, S.; Tewary, S.; Garnier, D.; Li, Y.; Gontard, G.; Lisnard, L.; Flambard, A.; Breher, F.; Boillot, M.-L.; Rajaraman, G.; Lescouëzec, R. *Eur. J. Inorg. Chem.* **2018**, 2018 (3–4), 414–428.
- (293) Schlamp, S.; Dankhoff, K.; Weber, B. *New J. Chem.* **2014**, 38 (5), 1965–1972.
- (294) Yandulov, D. V.; Schrock, R. R. *J. Am. Chem. Soc.* **2002**, 124 (22), 6252–6253.
- (295) Hill, C. L.; Hollander, F. J. *J. Am. Chem. Soc.* **1982**, 104 (25), 7318–7319.
- (296) Andris, E.; Navrátil, R.; Jašík, J.; Sabenya, G.; Costas, M.; Srnc, M.; Roithová, J. *Chem. – A Eur. J.* **2018**, 24 (20), 5078–5081.

- (297) Betley, T. A.; Peters, J. C. *J. Am. Chem. Soc.* **2004**, 126 (20), 6252–6254.
- (298) Westre, T. E.; Kennepohl, P.; DeWitt, J. G.; Hedman, B.; Hodgson, K. O.; Solomon, E. I. *J. Am. Chem. Soc.* **1997**, 119 (27), 6297–6314.
- (299) DuBois, J. L.; Mukherjee, P.; Stack, T. D. P.; Hedman, B.; Solomon, E. I.; Hodgson, K. O. *J. Am. Chem. Soc.* **2000**, 122 (24), 5775–5787.
- (300) Kapre, R. R.; Bothe, E.; Weyhermüller, T.; DeBeer George, S.; Muresan, N.; Wieghardt, K. *Inorg. Chem.* **2007**, 46 (19), 7827–7839.
- (301) Codd, R.; Levina, A.; Zhang, L.; Hambley, T. W.; Lay, P. A. *Inorg. Chem.* **2000**, 39 (5), 990–997.
- (302) Levina, A.; Zhang, L.; Lay, P. A. *Inorg. Chem.* **2003**, 42 (3), 767–784.
- (303) Levina, A.; Codd, R.; Foran, G. J.; Hambley, T. W.; Maschmeyer, T.; Masters, A. F.; Lay, P. A. *Inorg. Chem.* **2004**, 43 (3), 1046–1055.
- (304) Penner-Hahn, J. E.; Benfatto, M.; Hedman, B.; Takahashi, T.; Doniach, S.; Groves, J. T.; Hodgson, K. O. *Inorg. Chem.* **1986**, 25 (13), 2255–2259.
- (305) Pantelouris, A.; Modrow, H.; Pantelouris, M.; Hormes, J.; Reinen, D. *Chem. Phys.* **2004**, 300 (1), 13–22.
- (306) Kapre, R.; Ray, K.; Sylvestre, I.; Weyhermüller, T.; DeBeer George, S.; Neese, F.; Wieghardt, K. *Inorg. Chem.* **2006**, 45 (9), 3499–3509.
- (307) Almas, Q. L.; Pearson, J. K. *ACS Omega* **2018**, 3 (1), 608–614.
- (308) Staubitz, A.; Robertson, A. P. M.; Sloan, M. E.; Manners, I. *Chem. Rev.* **2010**, 110 (7), 4023–4078.
- (309) Rokob, T. A.; Hamza, A.; Stirling, A.; Pápai, I. *J. Am. Chem. Soc.* **2009**, 131 (5), 2029–2036.
- (310) Seymore, S. B.; Brown, S. N. *Inorg. Chem.* **2000**, 39 (2), 325–332.
- (311) Smith, J. M. *Prog. Inorg. Chem.* **2014**, 58, 417.

- (312) Tran, B. L.; Pink, M.; Gao, X.; Park, H.; Mindiola, D. J. *J. Am. Chem. Soc.* **2010**, 132 (5), 1458–1459.
- (313) Kwong, H.-K.; Man, W.-L.; Xiang, J.; Wong, W.-T.; Lau, T.-C. *Inorg. Chem.* **2009**, 48 (7), 3080–3086.
- (314) Leung, C.-F.; Wong, T.-W.; Lau, T.-C.; Wong, W.-T. *Eur. J. Inorg. Chem.* **2005**, 2005 (4), 773–778.
- (315) Maestri, A. G.; Taylor, S. D.; Schuck, S. M.; Brown, S. N. *Organometallics* **2004**, 23 (8), 1932–1946.



## Appendix A. Supplementary Material for Chapter 2

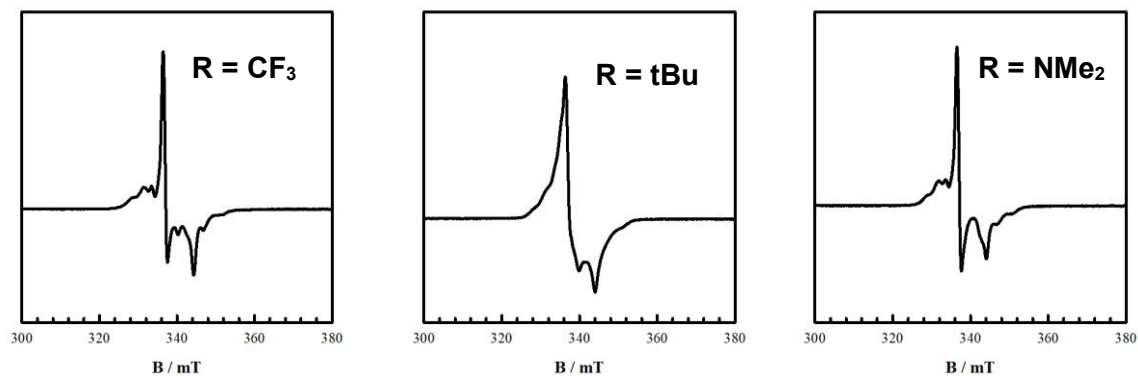


**Figure A1.** Low temperature EPR spectrum of  $\text{CrNSal}^{\text{CF}_3}$ ,  $\text{CrNSal}^{\text{tBu}}$ , and  $\text{CrNSal}^{\text{NMe}_2}$  in dichloromethane in the absence of TBAP. Conditions: 0.33 mM complex; 0.1 M TBAP; freq. = 9.38 GHz; power = 2.0 mW; mod. freq. = 100 kHz; mod. amp. = 6 GHz;  $T = 77 \text{ K}$ .

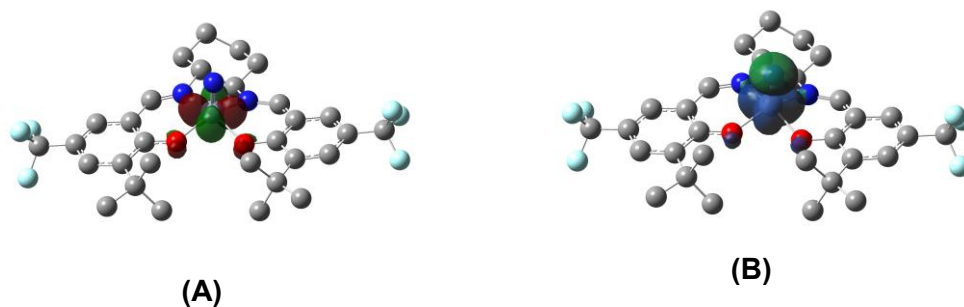


**Figure A2.** (A) SOMO and (B) spin density plots for  $\text{CrNSal}^{\text{CF}_3}$ .

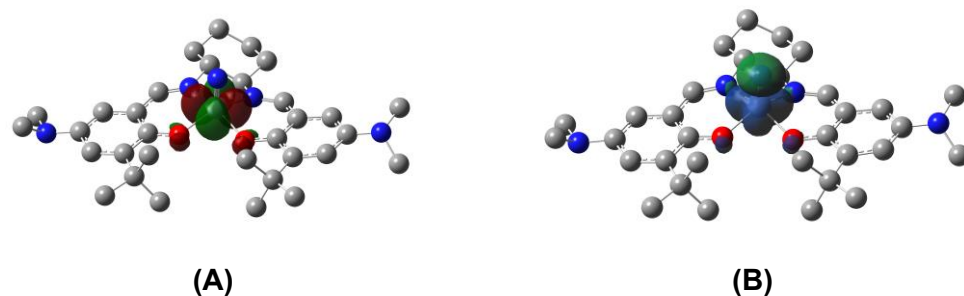


**Figure A3.** (A) SOMO and (B) spin density plots for  $\text{CrNSal}^{\text{NMe}_2}$ .

## Computational Data

**Table A1.** Optimized coordinates for **CrNSal<sup>NMe2</sup>** in Å.

Atom	X	Y	Z
O	-1.3505	-0.69235	0.050258
O	1.345336	-0.69063	-0.14032
N	-1.31743	2.042904	0.255584
N	1.261752	2.030092	-0.14322
C	-3.89752	-4.30263	-0.24632
C	-1.86823	-3.32753	-1.3081
C	-2.09486	-3.40785	1.219131
C	-2.8445	-3.18316	-0.11655
C	-2.66294	-0.59423	-0.0098
C	-3.47675	-1.77633	-0.1197
C	-4.84983	-1.61318	-0.2369
C	-5.51722	-0.36102	-0.23473
C	-4.73011	0.771151	-0.12432
C	-3.31899	0.67084	-0.01799
C	-2.59385	1.905825	0.071971
C	-0.68385	3.372174	0.371135
C	0.591148	3.305137	-0.48942
C	2.550469	1.901652	-0.23162
C	3.297732	0.689235	-0.05806
C	4.711198	0.80694	-0.02769
C	5.5154	-0.31576	0.045585
C	4.865066	-1.57762	0.047369
C	3.49135	-1.75827	-0.02837
C	2.657068	-0.58545	-0.05966
C	2.880465	-3.17405	-0.06151
C	1.929844	-3.37234	1.142819
C	2.109293	-3.36739	-1.38977
C	3.95251	-4.28052	0.012261
H	-4.45271	-4.24273	-1.18979
H	-4.61857	-4.29186	0.579362

H	-3.38992	-5.27359	-0.22601
H	-2.3999	-3.20183	-2.25956
H	-1.06907	-2.58756	-1.25529
H	-1.41766	-4.32793	-1.30523
H	-2.79323	-3.36838	2.06413
H	-1.32225	-2.65317	1.373212
H	-1.61937	-4.39669	1.222341
H	-5.46657	-2.49462	-0.35927
H	-5.1723	1.761737	-0.10903
H	-3.20243	2.805929	-0.01795
H	0.266667	3.210146	-1.53721
H	5.139918	1.802951	-0.0604
H	5.497088	-2.45265	0.131031
H	1.489163	-4.37672	1.111597
H	1.122284	-2.63997	1.136023
H	2.479649	-3.27659	2.087206
H	1.653244	-4.36492	-1.41878
H	1.319036	-2.62357	-1.50133
H	2.789909	-3.28417	-2.24616
H	3.458788	-5.25816	-0.024
H	4.654105	-4.23597	-0.82894
H	4.528339	-4.23835	0.944191
H	3.143799	2.78087	-0.48477
H	-0.36732	3.462706	1.420669
C	-1.53577	4.594959	0.014642
H	-2.41276	4.652157	0.669247
H	-1.903	4.505105	-1.01722
C	-0.70361	5.880227	0.15994
H	-1.31227	6.74374	-0.13182
H	-0.44052	6.023372	1.217113
C	0.575927	5.822568	-0.68303
H	0.309379	5.801871	-1.749
H	1.175286	6.726952	-0.52752
C	1.426741	4.584796	-0.35094

H	2.291699	4.557036	-1.02223
H	1.812712	4.655406	0.675366
N	0.208229	0.569466	2.042525
Cr	0.031138	0.5511	0.528332
N	-6.92658	-0.32962	-0.4038
N	6.928323	-0.26558	0.170372
C	-7.70729	-1.11012	0.558667
H	-7.74142	-0.63627	1.5557
H	-8.73393	-1.20996	0.191284
H	-7.29275	-2.11299	0.674043
C	-7.5187	0.977519	-0.64367
H	-8.57066	0.8429	-0.91403
H	-7.47948	1.64774	0.234655
H	-7.01133	1.472307	-1.47734
C	7.511239	1.047228	0.401859
H	8.571516	0.923472	0.643522
H	7.441303	1.721628	-0.47134
H	7.020299	1.531373	1.25132
C	7.692831	-1.03259	-0.8151
H	7.695422	-0.55408	-1.81061
H	8.729875	-1.12123	-0.47518
H	7.288336	-2.04012	-0.92446

**Table A2.** Optimized coordinates for **CrNSal<sup>tBu</sup>** in Å.

Atom	X	Y	Z
Cr	0.04088	0.59203	-0.5377
O	1.34312	-0.6593	0.14391
N	1.25777	2.06883	0.16433
C	2.65459	-0.5542	0.1061
O	-1.3531	-0.6531	-0.0916
N	-1.3113	2.08547	-0.2935
C	3.49099	-1.7234	0.09375
N	0.24593	0.61518	-2.0473

C	4.86799	-1.5322	0.07175
H	5.49782	-2.413	0.04344
C	5.52031	-0.274	0.08961
C	4.70479	0.83793	0.14163
H	5.12633	1.83749	0.18043
C	3.29276	0.72369	0.13926
C	2.88341	-3.1411	0.10386
C	2.05823	-3.3409	1.39798
H	2.70136	-3.2527	2.28238
H	1.60912	-4.342	1.40778
H	1.25813	-2.6035	1.47628
C	1.9847	-3.3406	-1.1398
H	1.18034	-2.6053	-1.1711
H	1.5388	-4.343	-1.1247
H	2.57511	-3.2499	-2.0599
C	3.96097	-4.2443	0.0724
H	4.57704	-4.1966	-0.8331
H	3.46886	-5.2234	0.08297
H	4.62499	-4.2017	0.94367
C	7.05693	-0.2062	0.06247
C	7.57183	1.24528	0.09174
H	7.21934	1.81958	-0.7728
H	8.66734	1.24882	0.06724
H	7.25987	1.77009	1.00217
C	7.58269	-0.8774	-1.2289
H	8.6788	-0.845	-1.2564
H	7.20462	-0.3618	-2.1193
H	7.27982	-1.9279	-1.296
C	7.63337	-0.9462	1.29327
H	7.29016	-0.4814	2.2249
H	8.72967	-0.9119	1.27969
H	7.33485	-1.9998	1.31432
C	2.54212	1.93653	0.29305
H	3.12981	2.8137	0.56577

C	0.58138	3.34654	0.49112
H	0.23339	3.25525	1.53163
C	0.5666	5.86397	0.67792
H	0.27703	5.84599	1.73791
H	1.17073	6.76698	0.53347
C	-0.6942	5.92199	-0.1928
H	-1.3078	6.78681	0.08418
H	-0.4079	6.06295	-1.2442
C	-0.6734	3.41365	-0.3982
H	-0.3335	3.50071	-1.4406
C	1.4224	4.62411	0.36711
H	1.83027	4.69115	-0.6509
H	2.27271	4.59696	1.05679
C	-1.5315	4.63821	-0.0636
H	-1.9218	4.55085	0.95988
H	-2.3934	4.69532	-0.7379
C	-2.5913	1.94922	-0.142
H	-3.2023	2.84934	-0.0698
C	-3.318	0.71415	-0.0657
C	-4.7283	0.81116	0.02436
H	-5.1628	1.80597	0.01953
C	-5.5283	-0.3105	0.10981
C	-4.8604	-1.5599	0.10669
H	-5.4764	-2.4486	0.16877
C	-3.4827	-1.7331	0.02999
C	-2.6646	-0.5547	-0.0567
C	-2.8545	-3.1417	0.03159
C	-2.0608	-3.3605	-1.2792
H	-2.7295	-3.3085	-2.1473
H	-1.5929	-4.3529	-1.275
H	-1.2779	-2.6106	-1.4005
C	-1.9198	-3.2972	1.25485
H	-1.124	-2.5517	1.24068
H	-1.4624	-4.2946	1.25503

H	-2.4854	-3.1872	2.18849
C	-3.9141	-4.2593	0.11791
H	-4.6053	-4.2425	-0.7328
H	-4.5026	-4.203	1.04121
H	-3.4082	-5.2313	0.11044
C	-7.0631	-0.2605	0.20243
C	-7.5958	1.18469	0.19162
H	-7.2161	1.76499	1.04053
H	-8.6894	1.17545	0.26006
H	-7.3265	1.71114	-0.7313
C	-7.6814	-1.0107	-1.0016
H	-7.383	-0.5444	-1.9477
H	-8.7765	-0.9898	-0.9422
H	-7.3707	-2.0605	-1.0326
C	-7.527	-0.9346	1.51588
H	-7.1182	-0.4126	2.38895
H	-7.21	-1.9815	1.57235
H	-8.6213	-0.9144	1.58894

**Table A3.** Optimized coordinates for **CrNSal<sup>CF3</sup>** in Å.

Atom	X	Y	Z
O	-1.3606	-0.6376	0.06193
N	-1.3236	2.09252	0.2929
C	-2.6627	-0.552	0.01705
F	-7.4781	-0.9878	-1.221
F	-7.5432	-0.8279	0.93968
F	-7.4536	0.97726	-0.2748
F	7.49891	-1.0417	-1.1389
F	7.52561	-0.5594	0.97413
F	7.41103	1.04111	-0.4982
O	1.3543	-0.6678	-0.0526
N	1.24879	2.07103	-0.1645
C	-3.4638	-1.743	-0.1285

N	0.19555	0.6525	2.06499
C	-4.84	-1.5889	-0.1867
H	-5.4672	-2.4659	-0.2914
C	-5.488	-0.3362	-0.126
C	-4.732	0.80563	-0.0064
H	-5.2104	1.7796	0.03149
C	-3.3254	0.71844	0.06911
C	-2.8111	-3.1352	-0.225
C	-1.9855	-3.4226	1.05216
H	-1.5207	-4.4134	0.9791
H	-2.631	-3.4196	1.93871
H	-1.1972	-2.6835	1.1958
C	-1.9034	-3.1927	-1.4774
H	-1.1209	-2.434	-1.437
H	-2.493	-3.0389	-2.3894
H	-1.4257	-4.1774	-1.5484
C	-3.8594	-4.2582	-0.3602
H	-3.3428	-5.2221	-0.4233
H	-4.467	-4.1538	-1.2668
H	-4.5322	-4.304	0.50427
C	-6.9845	-0.2875	-0.1709
C	-2.6046	1.95445	0.15987
H	-3.222	2.85284	0.10926
C	-0.6821	3.41426	0.41439
H	-0.342	3.48504	1.45812
C	-1.5342	4.64758	0.09476
H	-2.3992	4.69822	0.76622
H	-1.923	4.57639	-0.9312
C	-0.6946	5.92735	0.24586
H	-1.3029	6.79945	-0.02
H	-0.4128	6.05219	1.30066
C	0.57077	5.87775	-0.619
H	1.1771	6.77663	-0.4584
H	0.28665	5.87911	-1.681



C	1.41906	4.62878	-0.3246
H	2.27487	4.6129	-1.0083
H	1.82207	4.67567	0.69672
C	0.57575	3.35413	-0.4737
H	0.22797	3.28375	-1.5168
C	2.52735	1.92873	-0.3377
H	3.10931	2.79932	-0.6448
C	3.28464	0.72318	-0.1835
C	4.6903	0.83666	-0.256
H	5.14326	1.81681	-0.3701
C	5.47623	-0.2876	-0.1777
C	4.86182	-1.5522	-0.0412
H	5.51411	-2.4152	0.01567
C	3.48967	-1.7352	0.01474
C	2.65454	-0.5599	-0.0555
C	2.8758	-3.1403	0.16207
C	2.0422	-3.2115	1.46458
H	2.67998	-3.0449	2.34088
H	1.58897	-4.2055	1.56301
H	1.24463	-2.4679	1.47373
C	1.9858	-3.4522	-1.0645
H	2.58007	-3.4431	-1.9864
H	1.17776	-2.7273	-1.1647
H	1.54362	-4.4506	-0.9601
C	3.95524	-4.2388	0.24286
H	4.57249	-4.2828	-0.6623
H	3.46515	-5.2125	0.35118
H	4.6168	-4.1082	1.10729
C	6.97161	-0.2059	-0.2114
Cr	0.02863	0.59986	0.55838

---

## Appendix B. Supplementary Material for Chapter 3

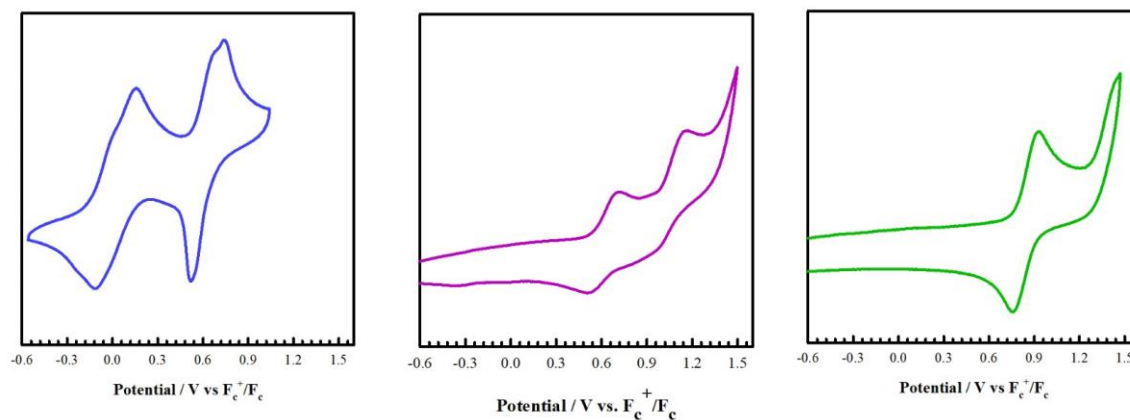


**Figure B1.** Additional redox processes for complexes. Blue:  $\text{CrNSal}^{\text{NMe}_2}$ ; purple:  $\text{CrNSal}^{\text{tBu}}$ ; green:  $\text{CrNSal}^{\text{CF}_3}$ . Conditions: 1.0 mM complex; 0.1 M  $n\text{Bu}_4\text{NClO}_4$ ; scan rate: 100 mV/s;  $T = 298\text{ K}$ ;  $\text{CH}_2\text{Cl}_2$ .

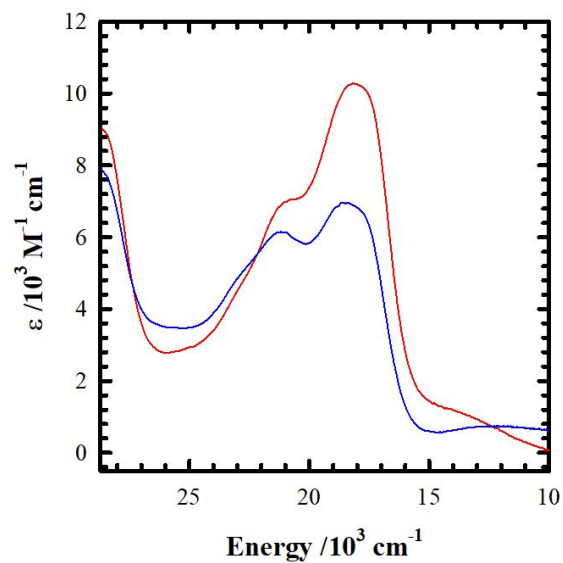


**Figure B2.** Comparison of UV-vis spectra of  $[\text{Cr}^{\text{V}}\text{NSal}^{\text{NMe}_2}]^{\bullet+}$  (blue) and  $[\text{Cr}^{\text{V}}\text{NSal}^{\text{NMe}_2}]^{\bullet\bullet 2+}$  (red).

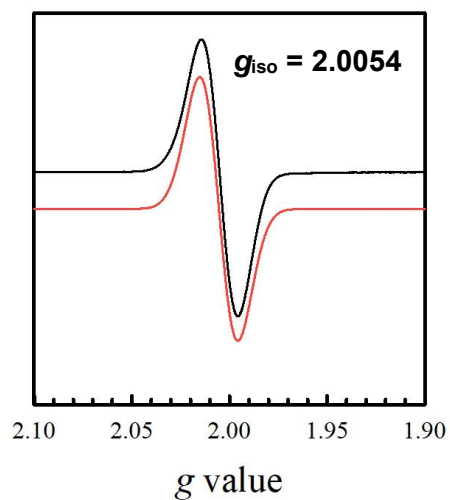


**Figure B3.** EPR of  $[\text{Cr}^{\text{V}}\text{NSal}^{\text{NMe}_2}]^{2+}$  (black) and simulation (red). Conditions: 0.45 mM complex; 0.1 M TBAP; freq. = 9.4 GHz; power = 2.0 mW; mod. freq. = 100 kHz; mod. amp. = 6 GHz; T = 20 K.

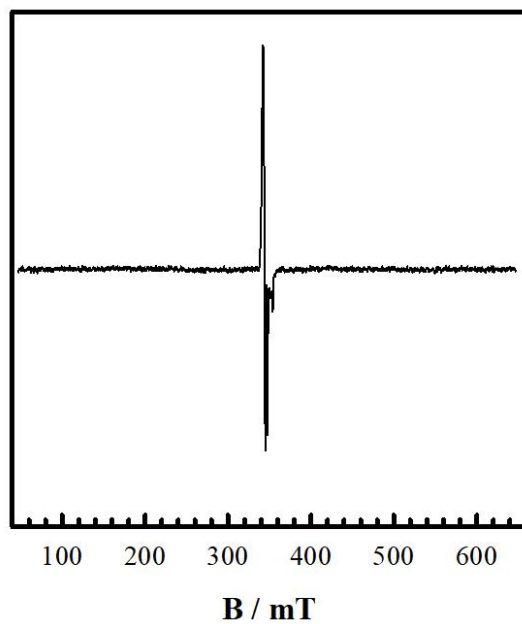


**Figure B4.** Full EPR spectrum of  $[\text{Cr}^{\text{V}}\text{NSal}^{\text{NMe}_2}]^{2+}$ . Conditions: 0.45 mM complex; 0.1 M TBAP; freq. = 9.4 GHz; power = 2.0 mW; mod. freq. = 100 kHz; mod. amp. = 2 GHz; T = 9 K.

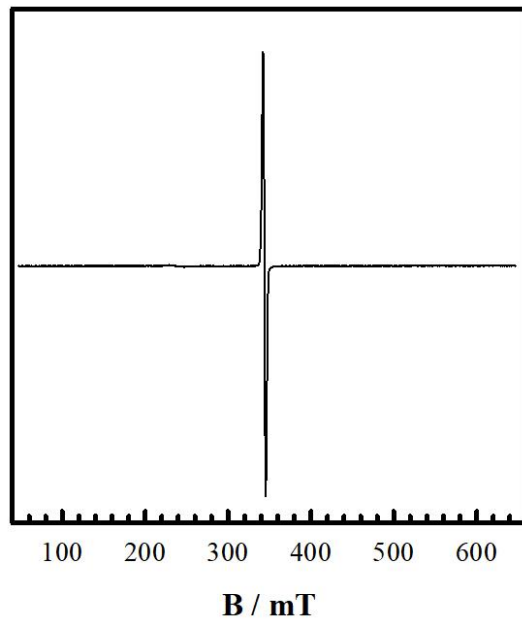


**Figure B5.** Full EPR spectrum of  $[\text{Cr}^{\text{V}}\text{NSal}^{\text{NMe}_2}]^{2+}$ . Conditions: 0.45 mM complex; 0.1 M TBAP; freq. = 9.4 GHz; power = 2.0 mW; mod. freq. = 100 kHz; mod. amp. = 2 GHz; T = 20 K.

## Computational Data

**Table B1.** Optimized coordinates for  $[\text{Cr}^{\text{V}}\text{NSaI}^{\text{NMe}_2}]^{+}$  in Å.

Atom	X	Y	Z
O	-1.335	-0.6557	-0.0653
O	1.39714	-0.7014	-0.0627
N	-1.353	2.05404	0.24637
N	1.23289	2.05878	-0.1834
C	-3.8093	-4.3122	-0.4715
C	-1.8964	-3.2035	-1.6149
C	-1.9196	-3.4705	0.91167
C	-2.7767	-3.1738	-0.3423
C	-2.6583	-0.5953	-0.061
C	-3.4417	-1.7889	-0.2018
C	-4.8237	-1.6565	-0.2248
C	-5.5214	-0.4253	-0.1109
C	-4.7541	0.72317	0.00376
C	-3.3389	0.65236	0.02454
C	-2.6344	1.89928	0.11006
C	-0.7254	3.38716	0.35896
C	0.53853	3.33124	-0.5192
C	2.5112	1.95156	-0.3018
C	3.28961	0.73894	-0.1265
C	4.66872	0.88077	-0.1238
C	5.5162	-0.2517	-0.0355
C	4.89941	-1.5446	-0.0055
C	3.54023	-1.744	-0.0278
C	2.67312	-0.5689	-0.0609
C	2.94404	-3.1618	0.00752
C	2.08978	-3.3343	1.28846
C	2.0795	-3.3948	-1.2563
C	4.03686	-4.2496	0.02792
H	-4.4367	-4.2051	-1.364
H	-4.4638	-4.3792	0.40531

H	-3.2778	-5.2663	-0.5579
H	-2.5083	-3.0415	-2.5107
H	-1.1214	-2.4361	-1.582
H	-1.4106	-4.1822	-1.7122
H	-2.5485	-3.5028	1.80958
H	-1.1487	-2.7128	1.05699
H	-1.4308	-4.4472	0.80884
H	-5.4215	-2.5477	-0.3623
H	-5.2158	1.70019	0.09361
H	-3.2582	2.7909	0.05525
H	0.20324	3.21281	-1.5602
H	5.0884	1.87647	-0.1947
H	5.5451	-2.4079	0.03888
H	1.66505	-4.3445	1.31051
H	1.26914	-2.6174	1.32999
H	2.70796	-3.2099	2.18523
H	1.66595	-4.4096	-1.2332
H	1.25042	-2.6894	-1.3158
H	2.6868	-3.3004	-2.1644
H	3.55539	-5.2326	0.04402
H	4.67572	-4.2125	-0.8621
H	4.67285	-4.1839	0.91817
H	3.09243	2.82992	-0.5813
H	-0.3999	3.48065	1.40518
C	-1.5918	4.60138	0.00784
H	-2.4566	4.65492	0.67797
H	-1.9755	4.49975	-1.0166
C	-0.7683	5.89448	0.13083
H	-1.3902	6.74909	-0.1577
H	-0.4893	6.04845	1.18216
C	0.49624	5.84286	-0.7342
H	0.21242	5.8106	-1.7951
H	1.09055	6.75278	-0.5956
C	1.36635	4.61682	-0.4064

H	2.21739	4.59205	-1.0953
H	1.76981	4.70024	0.61192
N	0.11597	0.58236	2.00648
Cr	-0.0168	0.57626	0.49191
N	-6.9322	-0.4163	-0.1875
N	6.86636	-0.1179	0.00858
C	-7.6517	-1.3299	0.7026
H	-7.658	-0.9768	1.74824
H	-8.6886	-1.4168	0.36315
H	-7.2092	-2.3267	0.68347
C	-7.5747	0.88678	-0.2707
H	-8.6379	0.74065	-0.4825
H	-7.4924	1.4768	0.65981
H	-7.141	1.46907	-1.089
C	7.48892	1.21058	-0.0074
H	8.56863	1.09567	0.05996
H	7.25141	1.73874	-0.9364
H	7.14722	1.80694	0.84423
C	7.73762	-1.2955	0.0862
H	7.59697	-1.9396	-0.7874
H	8.77409	-0.9661	0.11163
H	7.53004	-1.8706	0.99423

**Table B2.** Optimized coordinates for  $[\text{Cr}^{\text{VI}}\text{NSal}^{\text{tBu}}]^+$  in Å.

Atom	X	Y	Z
O	-1.3778	-0.5205	0.78763
O	1.22441	-0.5357	-0.2485
N	-1.241	2.09058	0.48645
N	1.23143	2.09685	-0.1199
C	-4.0072	-4.1083	0.90028
C	-1.781	-3.4947	-0.0374
C	-2.3967	-2.8818	2.351
C	-2.9159	-3.0184	0.89798

C	-2.6368	-0.4953	0.3582
C	-3.4519	-1.6637	0.39727
C	-4.7558	-1.5234	-0.0749
C	-5.3352	-0.3177	-0.537
C	-4.5368	0.81236	-0.4983
C	-3.1961	0.74094	-0.0642
C	-2.4718	1.96742	0.08999
C	-0.6099	3.41393	0.65928
C	0.57023	3.40543	-0.3217
C	2.50292	1.94751	-0.3163
C	3.23592	0.71405	-0.2399
C	4.64466	0.77489	-0.3065
C	5.4084	-0.3788	-0.3358
C	4.70652	-1.6055	-0.3359
C	3.31776	-1.7414	-0.3071
C	2.56741	-0.5371	-0.2355
C	2.64385	-3.1271	-0.3235
C	1.85341	-3.3292	0.99183
C	1.71053	-3.2393	-1.5532
C	3.6707	-4.2739	-0.4218
H	-4.3899	-4.316	-0.1052
H	-4.8521	-3.8455	1.54685
H	-3.5763	-5.0394	1.28326
H	-2.1552	-3.6424	-1.0573
H	-0.9595	-2.7775	-0.0747
H	-1.3793	-4.4511	0.31708
H	-3.2039	-2.565	3.02173
H	-1.5804	-2.1616	2.43121
H	-2.03	-3.8532	2.7023
H	-5.3818	-2.4062	-0.0799
H	-4.9227	1.78137	-0.794
H	-3.0391	2.87643	-0.1024
H	0.15441	3.39325	-1.3396
H	5.10827	1.75483	-0.3275



H	5.29554	-2.513	-0.3655
H	1.35835	-4.3071	0.98506
H	1.08749	-2.5648	1.1344
H	2.53027	-3.2997	1.85362
H	1.21579	-4.2175	-1.5572
H	0.93785	-2.4682	-1.5552
H	2.28687	-3.1494	-2.4816
H	3.13386	-5.2283	-0.4412
H	4.27061	-4.2153	-1.3369
H	4.34947	-4.2984	0.43815
H	3.08634	2.82526	-0.5907
H	-0.2033	3.41442	1.67894
C	-1.482	4.6578	0.48153
H	-2.3111	4.64547	1.19813
H	-1.9131	4.68359	-0.5279
C	-0.6123	5.91104	0.68932
H	-1.2261	6.80566	0.53912
H	-0.2585	5.94079	1.72861
C	0.58669	5.92577	-0.268
H	0.22703	6.02221	-1.3014
H	1.21698	6.80014	-0.073
C	1.44594	4.65327	-0.1473
H	2.23569	4.6819	-0.9053
H	1.93254	4.61701	0.8364
N	0.64232	0.66558	2.01787
Cr	0.07506	0.56238	0.62736
C	-6.7918	-0.308	-1.0279
C	6.94581	-0.3757	-0.3754
C	-7.2379	1.09411	-1.4832
H	-7.1946	1.8226	-0.6654
H	-6.6261	1.46781	-2.3123
H	-8.2753	1.05227	-1.8316
C	-7.726	-0.7673	0.11746
H	-8.7669	-0.7679	-0.2262

H	-7.4901	-1.7801	0.46065
H	-7.6523	-0.0931	0.97825
C	-6.9329	-1.2759	-2.2275
H	-6.6662	-2.3038	-1.9599
H	-7.9699	-1.2838	-2.5825
H	-6.2908	-0.9659	-3.0598
C	7.49158	-1.1097	0.87309
H	7.14991	-2.1492	0.92013
H	8.58761	-1.1209	0.85361
H	7.17272	-0.608	1.79385
C	7.51895	1.05386	-0.385
H	7.19026	1.61956	-1.2645
H	7.23345	1.61439	0.51255
H	8.61293	1.00948	-0.4118
C	7.43179	-1.1014	-1.6529
H	7.09178	-2.1418	-1.6903
H	7.06813	-0.595	-2.5543
H	8.52746	-1.1097	-1.6861

**Table B3.** Optimized coordinates for  $[\text{Cr}^{\text{VI}}\text{NSal}^{\text{CF}_3}]^+$  in Å.

Atom	X	Y	Z
O	-1.3822	-0.5251	0.74465
O	1.24245	-0.5324	-0.2805
N	-1.2396	2.08754	0.46678
N	1.23248	2.09279	-0.1519
C	-3.9801	-4.1346	0.84076
C	-1.7759	-3.4873	-0.1288
C	-2.347	-2.9282	2.28594
C	-2.8935	-3.0401	0.84097
C	-2.65	-0.4995	0.34888
C	-3.4502	-1.6809	0.3798
C	-4.7663	-1.5441	-0.055
C	-5.3252	-0.3205	-0.4656

C	-4.5625	0.82774	-0.4334
C	-3.2166	0.74865	-0.0312
C	-2.4825	1.97292	0.11645
C	-0.6032	3.41054	0.63785
C	0.56684	3.40082	-0.3533
C	2.50318	1.95093	-0.3423
C	3.24331	0.71859	-0.2588
C	4.64735	0.78396	-0.3056
C	5.37726	-0.3865	-0.3237
C	4.71284	-1.6243	-0.3341
C	3.32421	-1.7516	-0.3214
C	2.58194	-0.5389	-0.2586
C	2.64656	-3.134	-0.3538
C	1.84391	-3.3427	0.95288
C	1.72733	-3.2345	-1.595
C	3.67606	-4.2787	-0.4492
H	-4.3828	-4.3208	-0.1611
H	-4.8116	-3.8913	1.5118
H	-3.5369	-5.0719	1.19235
H	-2.1701	-3.6157	-1.1435
H	-0.9589	-2.765	-0.1672
H	-1.3619	-4.4481	0.19745
H	-3.1428	-2.6306	2.97841
H	-1.5329	-2.2055	2.36646
H	-1.9681	-3.9045	2.60885
H	-5.4081	-2.4156	-0.0654
H	-4.9868	1.78757	-0.7067
H	-3.0535	2.88537	-0.0439
H	0.14451	3.38021	-1.3679
H	5.14035	1.74977	-0.325
H	5.32067	-2.5191	-0.366
H	1.35062	-4.3209	0.93387
H	1.07487	-2.5812	1.09309
H	2.51168	-3.3181	1.82157

H	1.23118	-4.2115	-1.6093
H	0.95537	-2.4625	-1.6022
H	2.31422	-3.1407	-2.516
H	3.14001	-5.2328	-0.4807
H	4.28466	-4.2136	-1.3581
H	4.34517	-4.3088	0.41795
H	3.08393	2.83028	-0.6156
H	-0.1898	3.40714	1.6547
C	-1.4769	4.65434	0.46782
H	-2.2966	4.64447	1.19514
H	-1.9198	4.67704	-0.5367
C	-0.6045	5.90777	0.66324
H	-1.2208	6.80113	0.51752
H	-0.2397	5.94006	1.69852
C	0.58317	5.92061	-0.3075
H	0.21281	6.01454	-1.3372
H	1.21605	6.79478	-0.1211
C	1.44446	4.649	-0.192
H	2.22513	4.67517	-0.9593
H	1.94121	4.61623	0.78667
N	0.62688	0.6606	1.98
Cr	0.07472	0.55039	0.58613
C	-6.7466	-0.2931	-0.9557
C	6.88047	-0.3586	-0.297
F	-7.5593	-1.0322	-0.1674
F	-6.8508	-0.8038	-2.2057
F	-7.246	0.96008	-0.9957
F	7.37162	0.84145	-0.6736
F	7.36344	-0.614	0.94208
F	7.41101	-1.2925	-1.1187

---

## Appendix C. Supplementary Material for Chapter 4

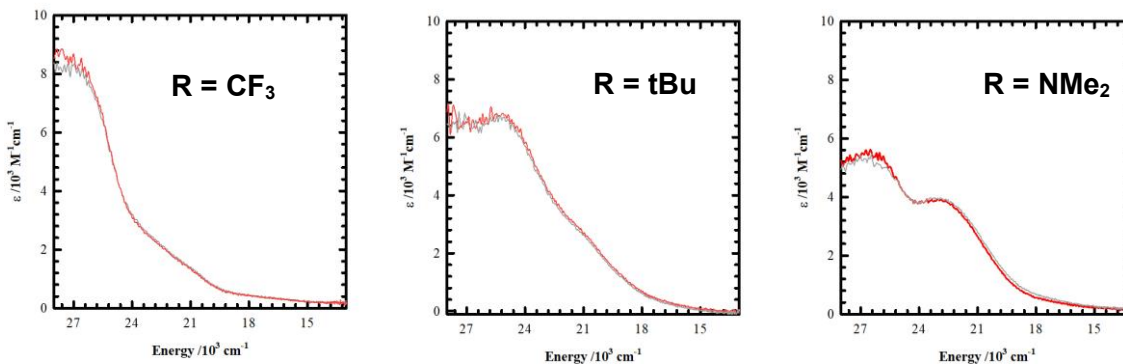


**Figure C1.** Addition of 1 equivalent tris(pentafluorophenyl) borane to neutral complexes (red) followed by an addition of a second equivalent (grey). Conditions: 0.45 mM complex;  $T = 233\text{ K}$ ;  $\text{CH}_2\text{Cl}_2$ .

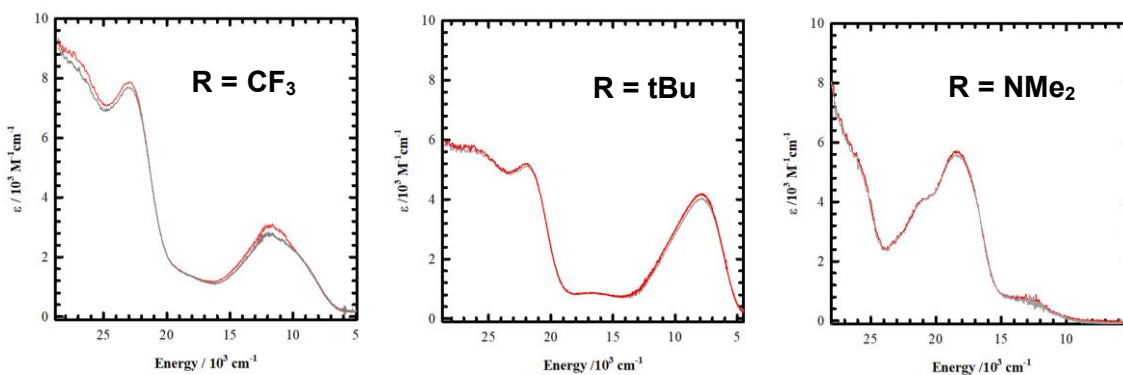


**Figure C2.** Addition of 1 equivalent tris(pentafluorophenyl) borane to oxidized complexes (red) followed by an addition of a second equivalent (grey). Conditions: 0.45 mM complex;  $T = 233\text{ K}$ ;  $\text{CH}_2\text{Cl}_2$ .

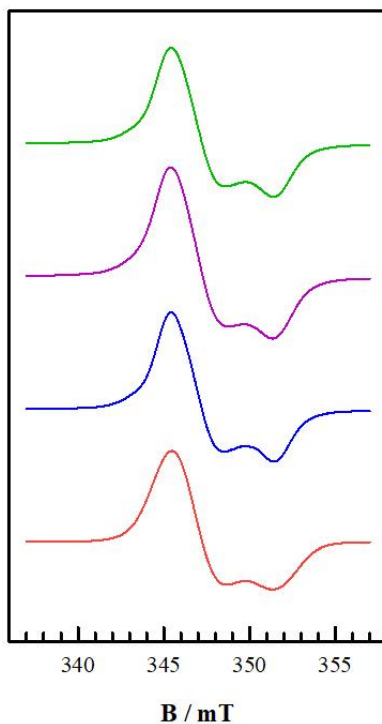


**Figure C3.** Frozen EPR of **CrNSal<sup>R</sup>** with 1 equivalent tris(pentafluorophenyl) borane. Green: R = CF<sub>3</sub>; purple R = tBu; blue: R = NMe<sub>2</sub>; red: simulation. Fitted parameter values are identical for all compounds:  $g_{\perp} = 1.9888$ ,  $g_{\parallel} = 1.9580$ ,  $A^{53\text{Cr}} = 55.71$  MHz,  $A^{14\text{N}} = 16.55$  MHz. Conditions: 0.25 mM complex; freq. = 9.6364 GHz; power = 2.0 mW; mod. freq. = 100 kHz; mod. amp. = 0.6 mT; T = 100 K.

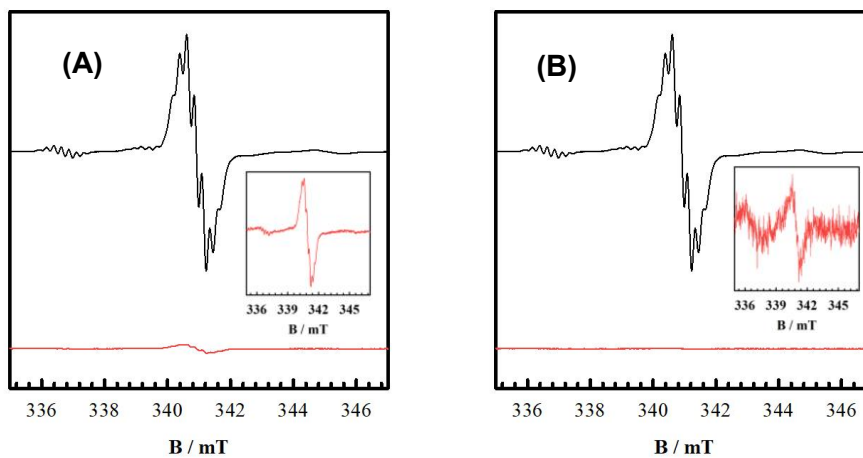


**Figure C4. (A)** Solution EPR analysis of concentration matched samples of **CrNSal<sup>NMe2</sup>** (black) and **[Cr<sup>V</sup>NSal<sup>NMe2</sup>]<sup>•+</sup>** with 1 equivalent of tris(pentafluorophenyl) borane (red). Inset represents a magnification of the signal in red. **(B)** Solution EPR of concentration matched samples of **CrNSal<sup>NMe2</sup>** (black) and **[Cr<sup>V</sup>NSal<sup>NMe2</sup>]<sup>••2+</sup>** (red). Inset represents a magnification of the signal in red. Conditions: 0.50 mM complex; freq. = 9.428 GHz; power = 2.0 mW; mod. freq. = 100 kHz; mod. amp. = 0.6 mT; T = 298 K.

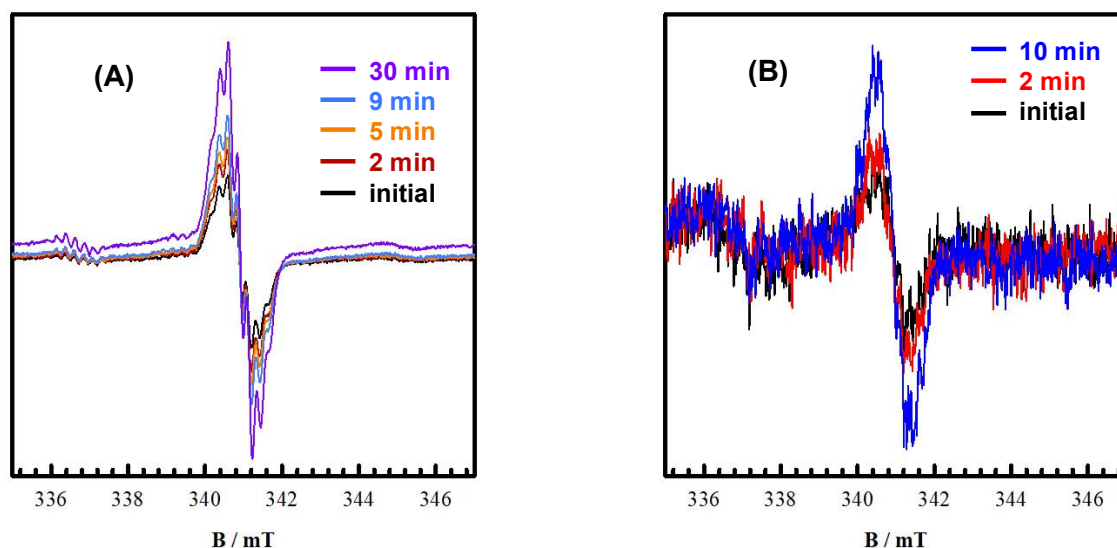


**Figure C5.** Time-dependant solution EPR analysis of  $[\text{Cr}^{\text{V}}\text{NSal}^{\text{NMe}_2}]^+ \cdot$  (A) and  $[\text{Cr}^{\text{V}}\text{NSal}^{\text{NMe}_2}]^{..2+}$  (B) depicts the decomposition of these complexes back to neutral  $\text{CrNSal}^{\text{NMe}_2}$ . Conditions: 0.50 mM complex; freq. = 9.427 GHz; power = 2.0 mW; mod. freq. = 100 kHz; mod. amp. = 0.6 mT; T = 298 K.

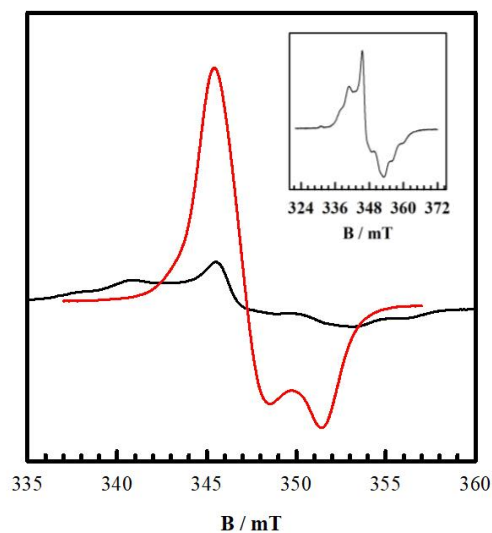


**Figure C6.** EPR of concentration matched samples of  $\text{CrNSal}^{\text{NMe}_2}$  (black) and  $\text{CrNSal}^{\text{NMe}_2}$  with 1 equivalent tris(pentafluorophenyl) borane added (red). Inset: magnified signal of  $\text{CrNSal}^{\text{NMe}_2}$ . Conditions: 0.3 mM complex; freq. = 9.388 GHz; power = 2.0 mW; mod. freq. = 100 kHz; mod. amp. = 6 GHz; T = 100 K.

## NBO Analysis

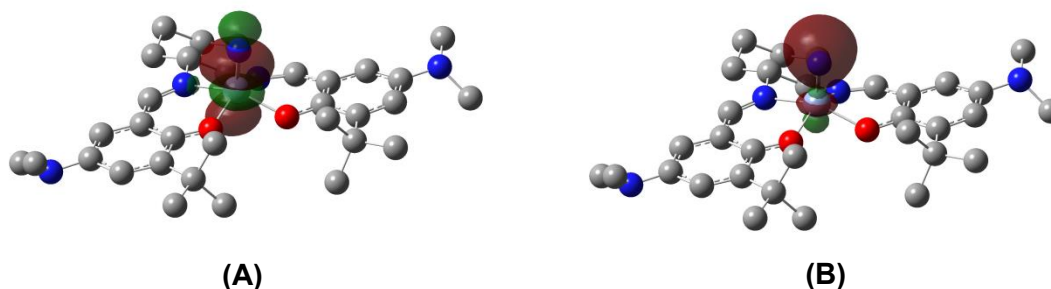


**Figure C7.** Visualization of the alpha orbitals of the Cr—N  $\sigma$  interaction **(A)** and lone pair **(B)** for  $\text{CrNSal}^{\text{NMe}_2}$ .

**Table C1.** Analysis of  $\text{CrNSal}^{\text{NMe}_2}$  – alpha orbitals.

$\pi$ bond		$\pi$ bond		$\sigma$ bond		Lone pair
N	Cr	N	Cr	N	Cr	N
42.44 %	57.56 %	42.60 %	57.40 %	53.33 %	46.67 %	90.28 %
s	s	s	s	s	s	s
0.06 %	2.60 %	0.00 %	0.03 %	18.59 %	6.21 %	81.37 %
p	p	p	p	p	p	p
99.77 %	8.73 %	99.84 %	4.29 %	81.33 %	2.80 %	18.63 %
d	d	d	d	d	d	d
0.17 %	88.65 %	0.16 %	95.68 %	0.08 %	90.99 %	0.00 %

**Table C2.** Analysis of  $\text{CrNSal}^{\text{NMe}_2}$  – beta orbitals.

$\pi$ bond		$\pi$ bond		$\sigma$ bond		Lone pair
N	Cr	N	Cr	N	Cr	N
58.06 %	41.94 %	58.59 %	41.41 %	60.77 %	39.23 %	91.41 %
s	s	s	s	s	s	s
0.13 %	1.73 %	0.00 %	0.03 %	25.93 %	7.14 %	73.95 %
p	p	p	p	p	p	p
99.74 %	9.90 %	99.87 %	5.91 %	74.01 %	3.31 %	36.04 %
d	d	d	d	d	d	d
0.13 %	88.46 %	0.12 %	94.05 %	0.06 %	89.55 %	0.00 %



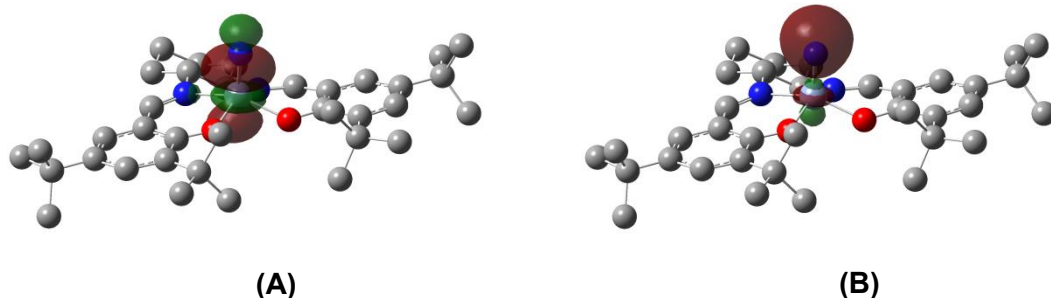


**Figure C8.** Visualization of the alpha orbitals of the Cr—N  $\sigma$  interaction **(A)** and lone pair **(B)** for **CrNSal<sup>tBu</sup>**.

**Table C3.** Analysis of **CrNSal<sup>tBu</sup>** – alpha orbitals.

$\pi$ bond		$\pi$ bond		$\sigma$ bond		Lone pair
N	Cr	N	Cr	N	Cr	N
42.35 %	57.65 %	42.49 %	57.51 %	53.30 %	46.70 %	90.27 %
s	s	s	s	s	s	s
0.06 %	2.59 %	0.00 %	0.03 %	18.48 %	6.22 %	81.53 %
p	p	p	p	p	p	p
99.77 %	8.67 %	99.83 %	4.27 %	81.48 %	2.79 %	18.47 %
d	d	d	d	d	d	d
0.17 %	88.74 %	0.16 %	95.71 %	0.08 %	90.99 %	0.00 %

**Table C4.** Analysis of **CrNSal<sup>NMe2</sup>** – beta orbitals.

$\pi$ bond		$\pi$ bond		$\sigma$ bond		Lone pair
N	Cr	N	Cr	N	Cr	N
58.03 %	41.97 %	58.54 %	41.46 %	60.76 %	39.24 %	91.40 %
s	s	s	s	s	s	s
0.13 %	1.72 %	0.00 %	0.03 %	25.77 %	7.14 %	74.12 %
p	p	p	p	p	p	p
99.75 %	9.73 %	99.87 %	5.89 %	74.17 %	3.29 %	25.88 %
d	d	d	d	d	d	d
0.13 %	88.55 %	0.12 %	94.08 %	0.06 %	89.57 %	0.00 %

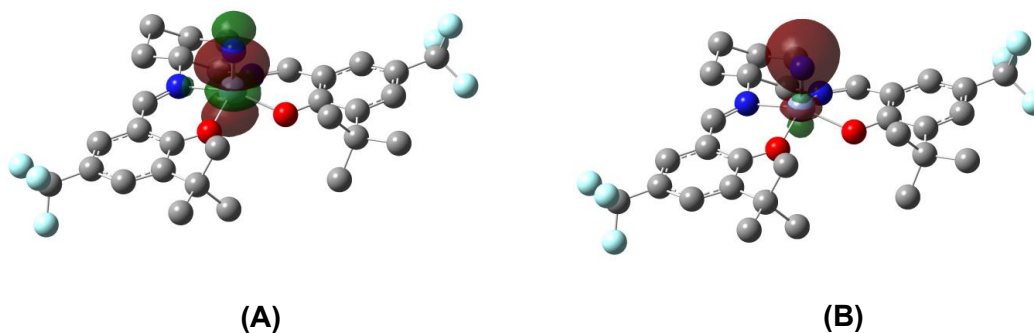


**Figure C9.** Visualization of the alpha orbitals of the Cr—N  $\sigma$  interaction **(A)** and lone pair **(B)** for  $\text{CrNSal}^{\text{CF}_3}$ .

**Table C5.** Analysis of  $\text{CrNSal}^{\text{CF}_3}$  – alpha orbitals.

$\pi$ bond		$\pi$ bond		$\sigma$ bond		Lone pair
N	Cr	N	Cr	N	Cr	N
41.89 %	58.11 %	42.03 %	57.97 %	53.14 %	46.86 %	90.23 %
s	s	s	s	s	s	s
0.05 %	2.54 %	0.00 %	0.03 %	17.88 %	6.24 %	82.09 %
p	p	p	p	p	p	p
99.77 %	8.45 %	99.83 %	4.17 %	82.04 %	2.76 %	17.91 %
d	d	d	d	d	d	d
0.17 %	89.01 %	0.17 %	95.80 %	0.08 %	91.00 %	0.00 %

**Table C6.** Analysis of  $\text{CrNSal}^{\text{CF}_3}$  – beta orbitals.

$\pi$ bond		$\pi$ bond		$\sigma$ bond		Lone pair
N	Cr	N	Cr	N	Cr	N
57.73 %	42.27 %	58.26 %	41.74 %	60.70 %	39.30 %	91.38 %
s	s	s	s	s	s	s
0.12 %	1.69 %	0.00 %	0.04 %	25.18 %	7.19 %	74.71 %
p	p	p	p	p	p	p
99.75 %	9.53 %	99.87 %	5.79 %	74.75 %	3.21 %	25.28 %
d	d	d	d	d	d	d
0.13 %	88.79 %	0.13 %	94.17 %	0.07 %	89.60 %	0.00 %

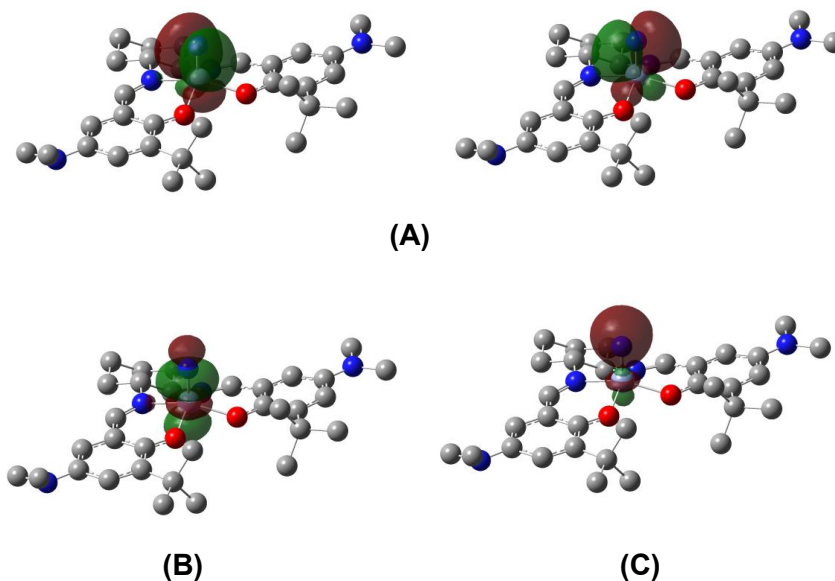


**Figure C10.** Visualization of the alpha orbitals involved in the Cr—N  $\pi$  interactions (A),  $\sigma$  interaction (B) and lone pair (C) for  $[\text{Cr}^{\text{V}}\text{NSal}^{\text{NMe}_2}]^{+\bullet}$ .

**Table C7.** Analysis of  $[\text{Cr}^{\text{V}}\text{NSal}^{\text{NMe}_2}]^{+\bullet}$  – alpha orbitals.

$\pi$ bond		$\pi$ bond		$\sigma$ bond		Lone pair
N	Cr	N	Cr	N	Cr	N
41.68 %	58.32 %	42.29 %	57.71 %	53.27 %	46.73 %	90.31 %
s	s	s	s	s	s	s
0.04 %	2.45 %	0.00 %	0.05 %	17.98 %	6.37 %	82.01 %
p	p	p	p	p	p	p
99.79 %	8.26 %	99.83 %	4.35 %	81.94 %	2.80 %	17.88 %
d	d	d	d	d	d	d
0.17 %	89.29 %	0.17 %	95.60 %	0.08 %	90.83 %	0.00 %

**Table C8.** Analysis of  $[\text{Cr}^{\text{V}}\text{NSal}^{\text{NMe}_2}]^{+\bullet}$  – beta orbitals.

$\pi$ bond		$\pi$ bond		$\sigma$ bond		Lone pair
N	Cr	N	Cr	N	Cr	N
57.00 %	43.00 %	57.91 %	42.09 %	60.66 %	39.34 %	91.34 %
s	s	s	s	s	s	s
0.22 %	1.37 %	0.03 %	0.36 %	24.70 %	7.20 %	75.07 %
p	p	p	p	p	p	p
99.65 %	8.09 %	99.84 %	7.27 %	75.25 %	3.22 %	24.92 %
d	d	d	d	d	d	d
0.13 %	90.54 %	0.13 %	92.37 %	0.07 %	89.58 %	0.00 %

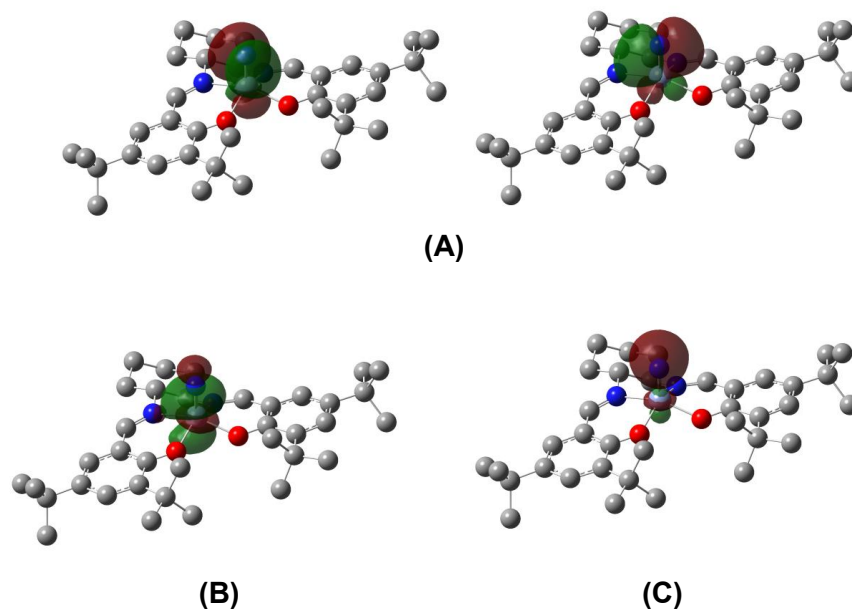


**Figure C11.** Visualization of the Cr—N  $\pi$  interactions **(A)**,  $\sigma$  interaction **(B)** and lone pair **(C)** for  $[\text{Cr}^{\text{VI}}\text{NSal}^{\text{tBu}}]^+$ .

**Table C9.** Analysis of  $[\text{Cr}^{\text{VI}}\text{NSal}^{\text{tBu}}]^+$  orbitals.

$\pi$ bond		$\pi$ bond		$\sigma$ bond		Lone pair
N	Cr	N	Cr	N	Cr	N
46.04 %	53.96 %	46.78 %	53.22 %	56.89 %	43.11 %	--
s	s	s	s	s	s	s
0.07 %	1.93 %	0.01 %	0.20 %	19.75 %	10.28 %	80.19 %
p	p	p	p	p	p	p
99.76 %	7.61 %	99.83 %	7.31 %	80.17 %	3.02 %	19.80 %
d	d	d	d	d	d	d
0.17 %	90.46 %	0.17 %	92.49 %	0.08 %	86.69 %	0.00 %

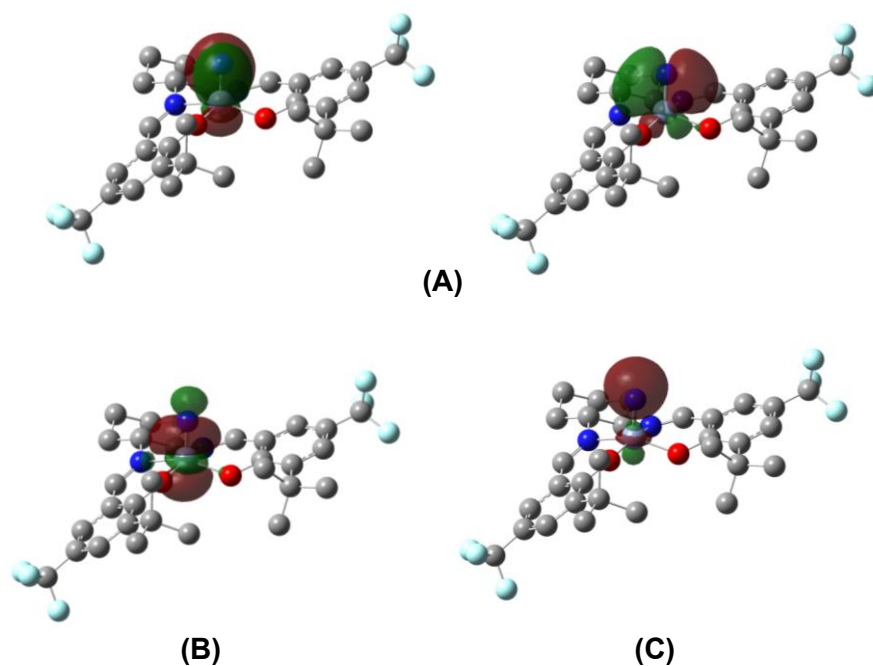


**Figure C12.** Visualization of the Cr—N  $\pi$  interactions **(A)**,  $\sigma$  interaction **(B)** and lone pair **(C)** for  $[\text{Cr}^{\text{VI}}\text{NSal}^{\text{CF}_3}]^+$ .

**Table C10.** Analysis of  $[\text{Cr}^{\text{VI}}\text{NSal}^{\text{CF}_3}]^+$ .

$\pi$ bond		$\pi$ bond		$\sigma$ bond		Lone pair
N 44.42 %	Cr 55.58 %	N 47.41 %	Cr 52.59 %	N 56.54 %	Cr 43.46 %	N --
s 0.42 %	s 1.65 %	s 0.02 %	s 0.00 %	s 20.14 %	s 13.57 %	s 79.44 %
p 99.40 %	p 6.55 %	p 99.81 %	p 17.16 %	p 79.78 %	p 1.44 %	p 20.55 %
d 0.18 %	d 91.80 %	d 0.17 %	d 82.84 %	d 0.08 %	d 84.99 %	d 0.00 %

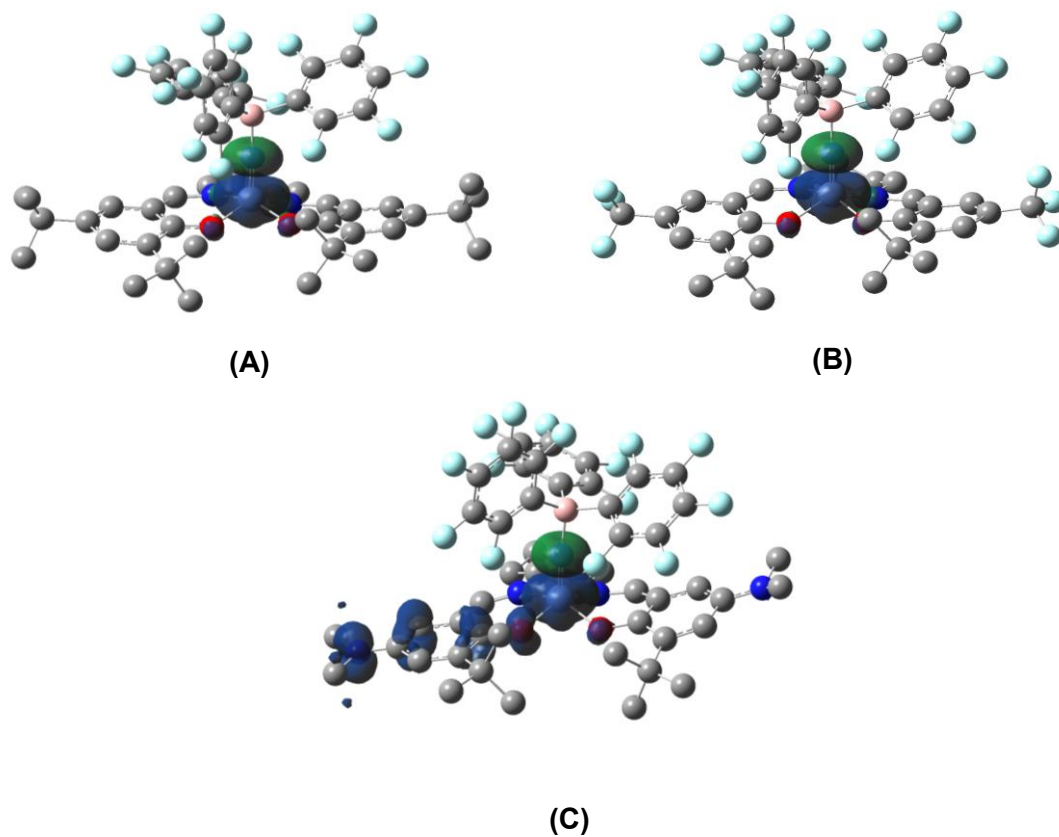


**Figure C13.** Spin density plots for (A)  $\text{Cr}(\text{N}-\text{B}(\text{C}_6\text{F}_5)_3)\text{Sal}^{\text{tBu}}$ , (B)  $\text{Cr}(\text{N}-\text{B}(\text{C}_6\text{F}_5)_3)\text{Sal}^{\text{CF}_3}$ , (C) triplet  $[\text{Cr}^{\text{V}}(\text{N}-\text{B}(\text{C}_6\text{F}_5)_3)\text{Sal}^{\text{NMe}_2}]^{\bullet+}$ .

## Appendix D. Supplementary Material for Chapter 5

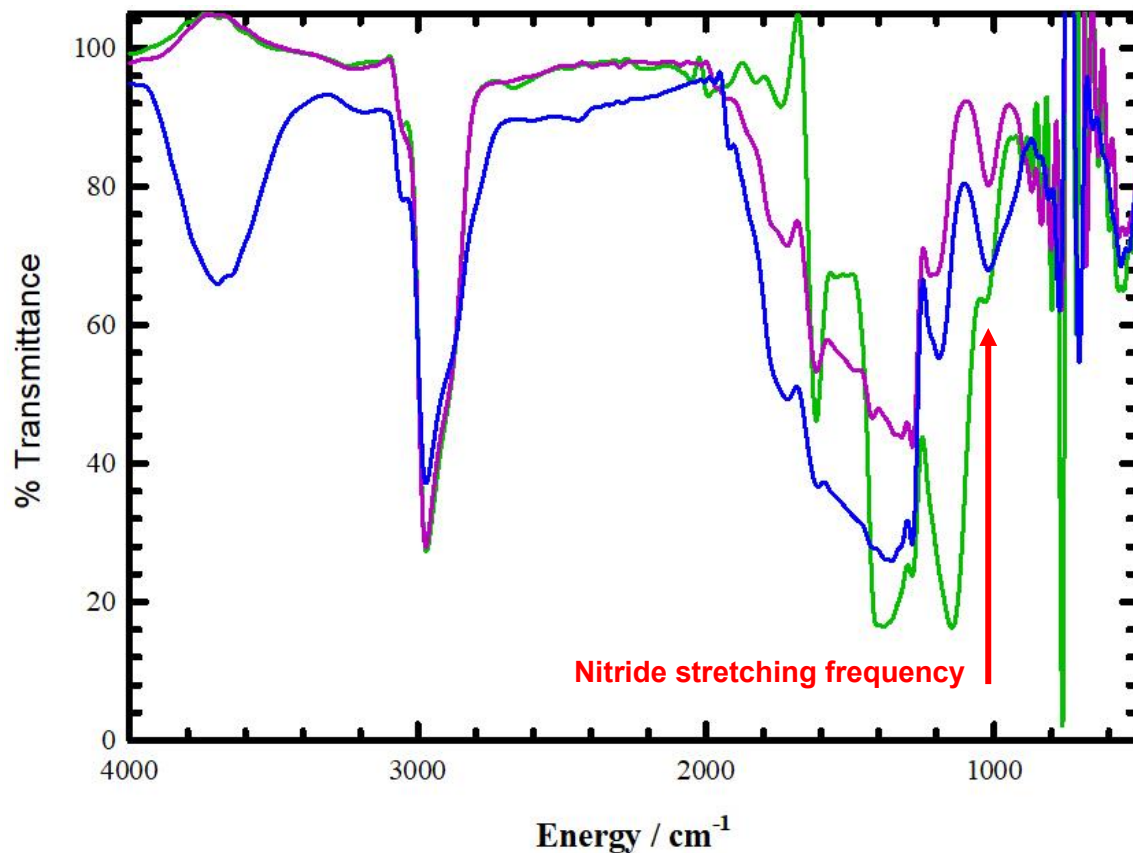


**Figure D1.** Full IR spectra of  $\text{CrNSal}^{\text{CF}_3}$  (green),  $\text{CrNSal}^{\text{tBu}}$  (purple), and  $\text{CrNSal}^{\text{NMe}_2}$  (blue). Conditions: 0.5 mM,  $\text{CH}_2\text{Cl}_2$ .

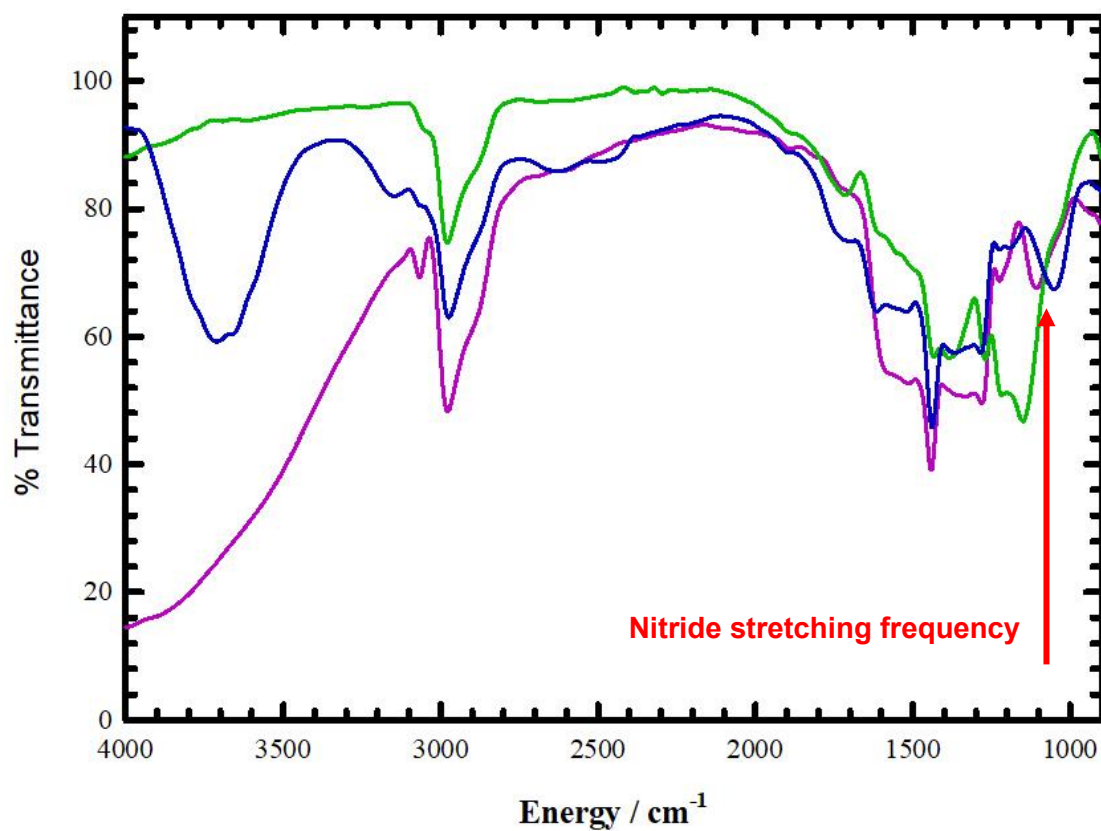


**Figure D2.** Full IR spectra of  $[\text{Cr}^{\text{VI}}\text{NSal}^{\text{CF}_3}]^+$  (green),  $[\text{Cr}^{\text{VI}}\text{NSal}^{\text{tBu}}]^+$  (purple), and  $[\text{Cr}^{\text{V}}\text{NSal}^{\text{NMe}_2}]^+$  (blue). Complexes were oxidized using  $[\text{N}(\text{C}_5\text{H}_3\text{Br}_2)_3]^+[\text{SbF}_6]^-$ . Conditions: 0.5 mM,  $\text{CH}_2\text{Cl}_2$ .



## NBO Analysis

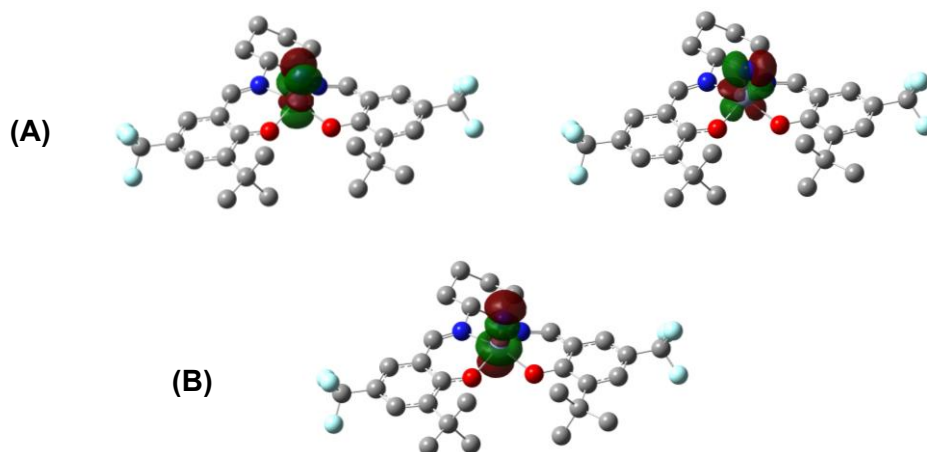


**Figure D3.** NBO analysis of CrNSal<sup>CF3</sup>. **(A)** Visualization of the alpha orbitals of the Cr—N  $\pi^*$  interaction in the xz and yz planes. **(B)** Visualization of the alpha orbital of the Cr—N  $\sigma^*$  interaction.

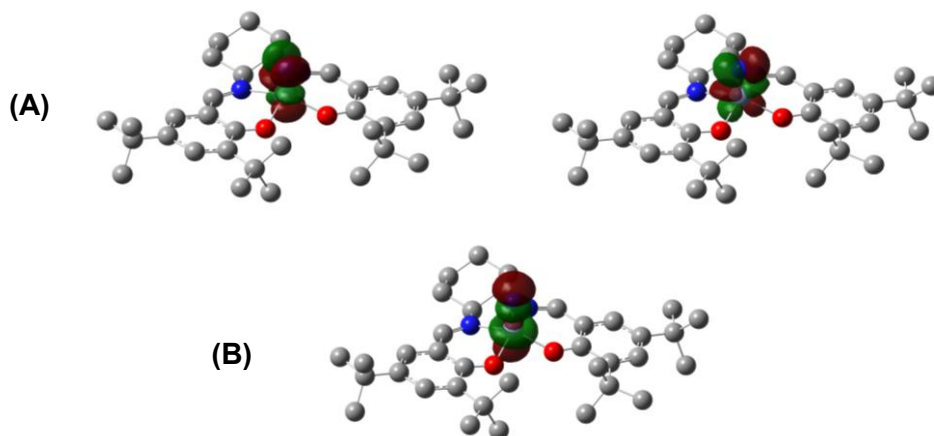


**Figure D4.** NBO analysis of CrNSal<sup>tBu</sup>. **(A)** Visualization of the alpha orbitals of the Cr—N  $\pi^*$  interaction in the xz and yz planes. **(B)** Visualization of the alpha orbital of the Cr—N  $\sigma^*$  interaction.

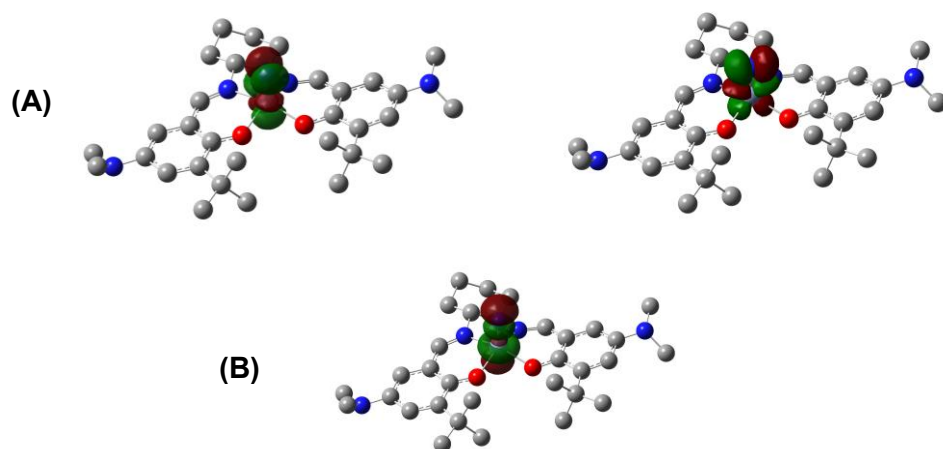


**Figure D5.** NBO analysis of  $\text{CrNSal}^{\text{NMe}_2}$ . **(A)** Visualization of the alpha orbitals of the Cr—N  $\pi^*$  interaction in the xz and yz planes. **(B)** Visualization of the alpha orbital of the Cr—N  $\sigma^*$  interaction.

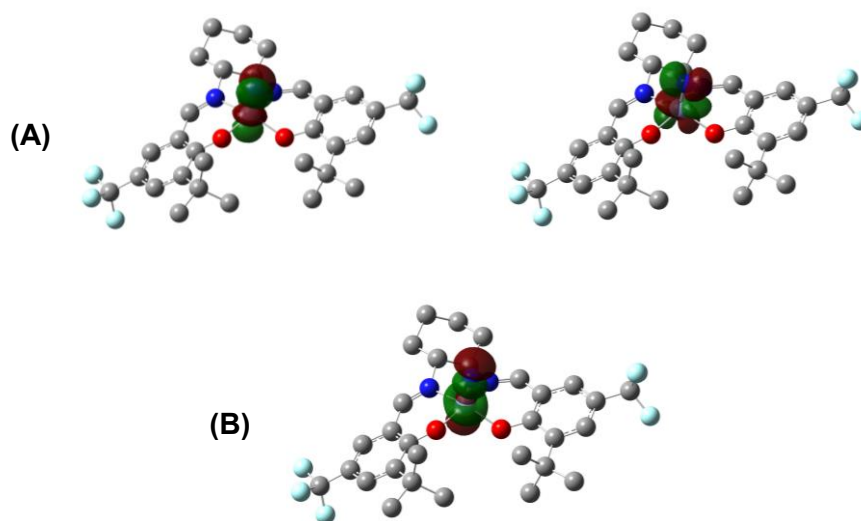


**Figure D6.** NBO analysis of  $[\text{Cr}^{\text{VI}}\text{NSal}^{\text{CF}_3}]^+$ . **(A)** Visualization of the of the Cr—N  $\pi^*$  interaction in the xz and yz planes. **(B)** Visualization of the of the Cr—N  $\sigma^*$  interaction.

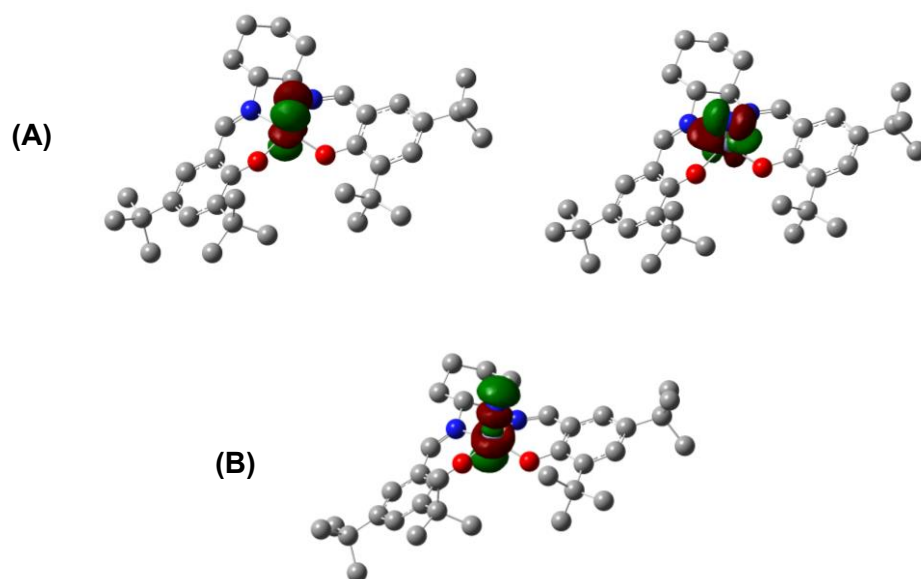


**Figure D7.** NBO analysis of  $[\text{Cr}^{\text{VI}}\text{NSal}^{\text{tBu}}]^+$ . **(A)** Visualization of the of the Cr—N  $\pi^*$  interaction in the xz and yz planes. **(B)** Visualization of the of the Cr—N  $\sigma^*$  interaction.

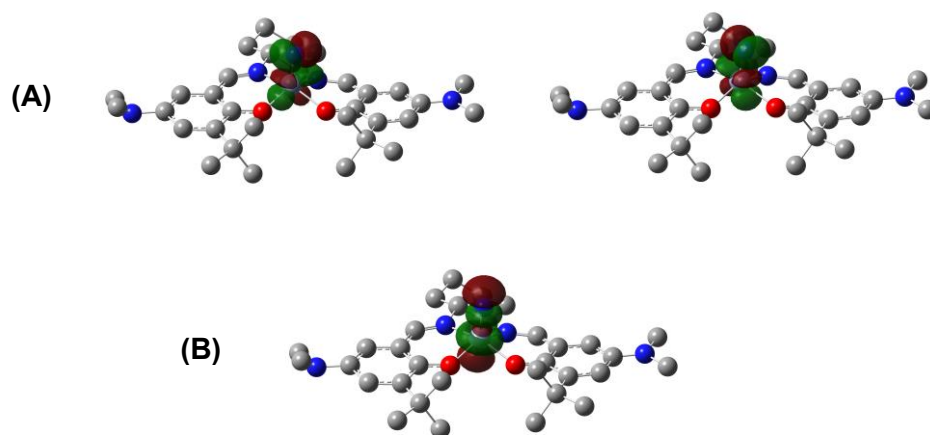


**Figure D8.** NBO analysis of  $[\text{Cr}^{\text{V}}\text{NSal}^{\text{NMe}_2}]^+$ . **(A)** Visualization of the alpha orbitals of the Cr—N  $\pi^*$  interaction in the xz and yz planes. **(B)** Visualization of the alpha orbital of the Cr—N  $\sigma^*$  interaction.